14 March 2014 | $10

Science

The Small World of Surface Tension

AAAS

pages 1177 & 1190

page 1206

EDITORIAL

1177 Time for New Schizophrenia Rx
Steven E. Hyman
>> News story p. 1190

NEWS OF THE WEEK

1182 A roundup of the week's top stories

NEWS & ANALYSIS

1185 Ukraine's Science Reformers Seize the Moment

1186 The Future Is Flat in White House's 2015 Spending Request
Budget Lows, Highs, and Dreams

1188 Cancer Genes Help HIV Persist, Complicating Cure Efforts

1189 How Earth Can Cool Without Plunging Into a Deep Freeze
>> Science Express Report by K. Maher and C. P. Chamberlain

NEWS FOCUS

1190 Talking Back to Madness
>> Editorial p. 1177

1194 Water's Tough Skin
>> Video

LETTERS

1199 Conserving Carnivores: More than Numbers
K. A. Alexander and C. E. Sanderson

Conserving Carnivores: Politics in Play
G. Chapron and J. V. López-Bao

Obscuring Gender Bias with "Choice"
A. L. Conner et al.

Response
B. L. Benderly

BOOKS *ET AL.*

1201 Girls Coming to Tech!
A. S. Bix, reviewed by M. Klawe

1202 Celestial Sleuth
D. W. Olson, reviewed by E. L. Altschuler

POLICY FORUM

1203 The Parable of Google Flu: Traps in Big Data Analysis
D. Lazer et al.
>> Science Podcast

PERSPECTIVES

1206 Simplicity amid Complexity
I. Held

1207 Internal mRNA Methylation Finally Finds Functions
T. W. Nilsen

1208 Stirring the Simmering "Designer Baby" Pot
T. H. Murray

1210 Where Do Batteries End and Supercapacitors Begin?
P. Simon et al.

1212 Getting Rid of a Persistent Troublemaker to Cure Hepatitis
A. Shlomai and C. M. Rice
>> Research Article p. 1221

1213 Society, Where None Intrudes
H. C. J. Godfray
>> Report p. 1240

ON THE WEB THIS WEEK

>> *Science* Podcast
On this week's show: avoiding big data traps and a roundup of shorts from our daily news site.

>> Find More Online
Check out *Science* Express, the weekly podcast, videos, daily news, our research journals, and *Science* Careers at **www.sciencemag.org**.

COVER

Surface tension supports a water strider. At small scales, the influence of surface tension can exceed that of gravity, affecting everything from how small animals urinate to how water ferns stay buoyant and how pathogens spread from a sneeze or cough. *Science* explores the small world of surface tension in a News Focus on page 1194.

Photo: © Hideta Nagai/National Geographic Society/Corbis

DEPARTMENTS

1175 This Week in *Science*
1178 Editors' Choice
1180 *Science* Staff
1270 New Products
1271 *Science* Careers

Published by AAAS

RESEARCH ARTICLES

1215 Structures of Cas9 Endonucleases Reveal RNA-Mediated Conformational Activation
M. Jinek et al.
Binding of a guide RNA triggers structural changes in a set of DNA-cleaving enzymes.
Research Article Summary; for full text: http://dx.doi.org/10.1126/science.1247997

1216 Ligand-Controlled C(sp^3)–H Arylation and Olefination in Synthesis of Unnatural Chiral α–Amino Acids
J. He et al.
Two different ligands can be used in succession to tune the reactivity of a palladium catalyst.

1221 Specific and Nonhepatotoxic Degradation of Nuclear Hepatitis B Virus cccDNA
J. Lucifora et al.
Cytokine induction renders viral DNA vulnerable and eliminates infection.
>> Perspective p. 1212

REPORTS

1228 Free-Standing Single-Atom-Thick Iron Membranes Suspended in Graphene Pores
J. Zhao et al.
The pores in a graphene membrane stabilize the formation of two-dimensional iron sheets.

1232 Main-Group Compounds Selectively Oxidize Mixtures of Methane, Ethane, and Propane to Alcohol Esters
B. G. Hashiguchi et al.
Lead and thallium salts are surprisingly selective and efficient oxidants of the constituents of natural gas.

1237 Changes in Seismic Anisotropy Shed Light on the Nature of the Gutenberg Discontinuity
C. Beghein et al.
The Gutenberg discontinuity is distinct from the lithosphere-asthenosphere boundary.

1240 Lethal Interactions Between Parasites and Prey Increase Niche Diversity in a Tropical Community
M. A. Condon et al.
Incorrect fly-host choice in parasitoid wasps creates multidimensional niches, generating high levels of hidden diversity.
>> Perspective p. 1213

1244 Structure of Human RNase L Reveals the Basis for Regulated RNA Decay in the IFN Response
Y. Han et al.
The crystal structure of an interferon-induced ribonuclease shows how it selects and shreds its RNA targets.

1249 Selective Methylation of Histone H3 Variant H3.1 Regulates Heterochromatin Replication
Y. Jacob et al.
The specificity of a histone methyltransferase for a histone variant maintains heterochromatin through cell division.

1253 Vertebrate Limb Bud Formation Is Initiated by Localized Epithelial-to-Mesenchymal Transition
J. Gros and C. J. Tabin
Cell state change, rather than differential proliferation, initiates limb formation during development.

1256 The *stum* Gene Is Essential for Mechanical Sensing in Proprioceptive Neurons
B. S. Desai et al.
The *stumble* gene in flies is required in neurons that sense joint angles.

1260 Complement Is Activated by IgG Hexamers Assembled at the Cell Surface
C. A. Diebolder et al.
Hexameric platforms of antibodies on the cell surface trigger the complement cascade.

1264 Dlk1 Promotes a Fast Motor Neuron Biophysical Signature Required for Peak Force Execution
D. Müller et al.
The fast versus slow profile of motor neurons is controlled by expression of a membrane protein.

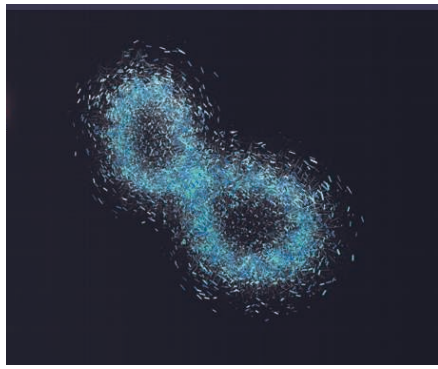

pages 1212 & 1221

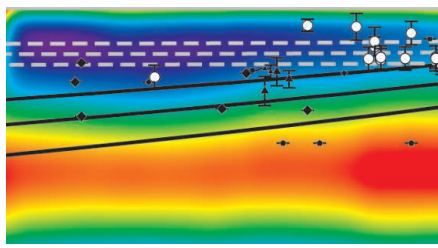

page 1237

SCIENCE (ISSN 0036-8075) is published weekly on Friday, except the last week in December, by the American Association for the Advancement of Science, 1200 New York Avenue, NW, Washington, DC 20005. Periodicals Mail postage (publication No. 484460) paid at Washington, DC, and additional mailing offices. Copyright © 2013 by the American Association for the Advancement of Science. The title SCIENCE is a registered trademark of the AAAS. Domestic individual membership and subscription (51 issues): $153 ($74 allocated to subscription). Domestic institutional subscription (51 issues): $1282; Foreign postage extra: Mexico, Caribbean (surface mail) $55; other countries (air assist delivery) $85. First class, airmail, student, and emeritus rates on request. Canadian rates with GST available upon request, GST #1254 88122. Publications Mail Agreement Number 1069624. **Printed in the U.S.A.**

Change of address: Allow 4 weeks, giving old and new addresses and 8-digit account number. **Postmaster:** Send change of address to AAAS, P.O. Box 96178, Washington, DC 20090–6178. **Single-copy sales:** $10.00 current issue, $15.00 back issue prepaid includes surface postage; bulk rates on request. **Authorization to photocopy** material for internal or personal use under circumstances not falling within the fair use provisions of the Copyright Act is granted by AAAS to libraries and other users registered with the Copyright Clearance Center (CCC) Transactional Reporting Service, provided that $30.00 per article is paid directly to CCC, 222 Rosewood Drive, Danvers, MA 01923. The identification code for *Science* is 0036-8075. *Science* is indexed in the *Reader's Guide to Periodical Literature* and in several specialized indexes.

Hexing Complement

Complement activation is an immediate and potent immune defense mechanism, but how immunoglobulin G (IgG) antibodies activate complement at the molecular level is poorly understood. Using high-resolution crystallography, **Diebolder *et al.*** (p. 1260) show that human IgGs form hexameric structures by interacting with neighboring IgG molecules, and the complex then activates complement. Thus, IgG molecules and the complement system can coexist in the blood because complement activation will only be triggered after IgG senses a surface antigen and starts to aggregate.

Light Alkanes, Heavy Metals

Hydraulic fracturing, or fracking, has rapidly increased the supply of natural gas and has motivated methods to convert its constituents into commodity chemicals. **Hashiguchi *et al.*** (p. 1232) have found that lead and thallium salts are both efficient and selective oxidants, not only for methane, but for ethane and propane as well. In trifluoroacetic acid solvent, the alkanes are cleanly oxidized to the trifluoroacetate esters of their respective alcohols and 1,2-diols. Building on earlier discoveries, this work paves the way to developing methods that reduce our dependence on petroleum for industrial feedstocks.

Cas9 Solved

Clustered regularly interspaced short palindromic repeats (CRISPR)–associated (Cas) loci allow prokaryotes to identify and destroy invading DNA. Not only important to bacteria, the universal value of Cas endonuclease specificity has also resulted in Cas9 being exploited as a tool for genome editing. **Jinek *et al.*** (p. 1215, published online 6 February) determined the 2.6 and 2.2 angstrom resolution crystal structures of two Cas9 enzymes to reveal a common structural core with distinct peripheral elaborations. The enzymes are autoinhibited, undergo large conformational changes on binding RNA, and have channels lined with basic residues that are candidates for an RNA-DNA binding groove. Based on these and other insights from the structures, this work provides important revelations both for the CRISPR mechanism and for genome editing.

A Palladium 1-2 Punch

Methods to replace carbon-hydrogen bonds directly with carbon-carbon bonds offer enticing prospects for streamlining the synthesis of organic compounds. The trouble is that it is hard to select any particular C-H bond and to avoid making complex mixtures of products. **He *et al.*** (p. 1216) report that a pair of powerful pyrimidine ligands induces a palladium catalyst to add aryl groups selectively to amino acid derivatives. One ligand promotes addition of a single aryl group to the β-carbon center; the other appends a second, potentially different aryl group to the same carbon—all in the same flask.

Iron in Graphene

Carbon or other covalently bonded materials, like boron nitride, can form two-dimensional sheets because of the strong bonding between the atoms. In contrast, metals share electrons in a three-dimensional delocalized way, and this could preclude the formation of thin stable sheets. Nevertheless, **Zhao *et al.*** (p. 1228) observed pure iron membranes suspended across the pores in a graphene sheet. This phenomenon was discovered when an iron chloride solution, used to process the graphene, decomposed to form pure iron films across the pores.

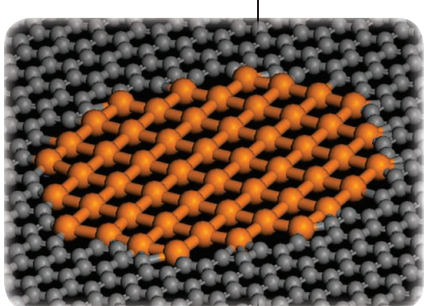

G Below Sea

Rheological differences between Earth's lithosphere and asthenosphere help drive plate tectonics. Geophysical analyses repeatedly reveal a seismic Gutenberg (G) discontinuity at 40- to 100-kilometer depth in oceanic plates, although the origin of this boundary remains enigmatic. **Beghein *et al.*** (p. 1237, published online 27 February) found that vertical stratification of anisotropy aligned with the depths of the G discontinuity, but not with the lithosphere-asthenosphere boundary. It appears that the G discontinuity forms when there are geophysical changes in the mantle, such as dehydration beneath mid-ocean ridges.

Where Do You Want Your Leg?

Initiation of limb formation is the key to understanding limb-cell specification and patterning during development. **Gros and Tabin** (p. 1253) show that a localized epithelial-to-mesenchymal transition triggers the formation of the limb. Finding that limbs initiate through cell-state change, and not through differential proliferation, redefines questions such as how limb buds are placed on the body plan.

Touchy-Feely Genes

All animals need accurate proprioceptive sensation to control motor function. **Desai *et al.*** (p. 1256) identified a *Drosophila* mutant with impaired walking coordination. The affected gene, *stumble* (*stum*), is conserved throughout the animal kingdom and expressed in a subpopulation of multidendritic neurons. *stum*-expressing neurons are found proximal to leg joints, and if the angle of the joint shifts, dendritic stretching occurs that in turn elevates cellular calcium. Therefore, it looks as if *stum* is a transducer for mechanical stimuli.

Quick, Quick, Slow

The slow muscles of postural stability and the fast muscles of running and jumping are driven by motor neurons that are differentiated by fast and slow biophysical properties. By retrograde labeling of mouse and chick muscle fibers, **Müller *et al.*** (p. 1264) characterized the developmental distinctions between fast and slow motor neurons. A transmembrane protein, when over- or under-expressed, was discovered to drive specification of the motor neurons and a downstream effector specified some, but not all, of the biophysical attributes.

CREDITS (TOP TO BOTTOM): JOOST BAKKER; ZHAO *ET AL.*

Downloaded from www.sciencemag.org on March 14, 2014

Additional summaries

Clearance of Chronic Virus

The family of mRNA-editing enzymes, APOBEC, restricts hepatitis B virus (HBV) replication. **Lucifora *et al.*** (p. 1221, published online 20 February; see the Perspective by **Shlomai and Rice**) provide evidence that specific APOBECs mediate the anti-HBV effects of host cytokines, which in turn apparently induce nuclear deaminase activity without damaging host cells. Thus, there may be potential in these findings for developing a therapeutic route to curing chronic HBV infection.

Hidden Diversity

Why are there so many species in the tropics? Niche partitioning by highly specialized plant species seems to be the main generator of high diversity. **Condon *et al.*** (p. 1240; see the Perspective by **Godfray**) show that niche partitioning can also be generated by interactions between plant resources and parasites, resulting in hyperdiverse communities. The cryptic diversity of 14 neotropical fly pollinators and 18 of their highly specific wasp parasites induced mortality partitions between multiple narrow niches. The extreme specificity of the wasp-fly relationships was initially only revealed by molecular analysis.

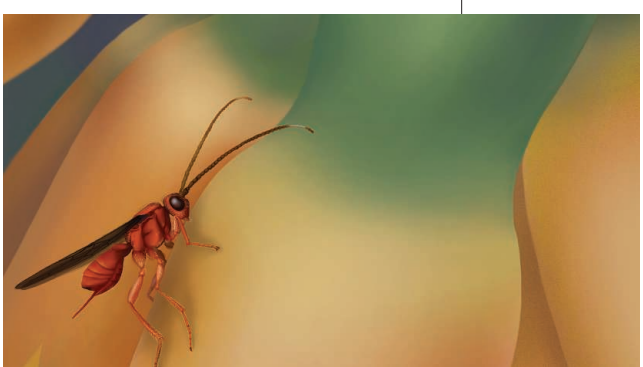

CREDIT: TAINA LITWAK/SYSTEMATIC ENTOMOLOGY LABORATORY, USDA

Crossed Homodimer

Our cells respond to infection by releasing interferons, which protect neighboring cells, in part through the cleavage of intracellular RNA by a protein kinase family receptor, RNase L. RNase L is activated by 2′,5′-linked oligoadenylates (the second messenger 2-5 A), sensors of pathogen- and damage-associated RNA. **Han *et al.*** (p. 1244, published online 27 February) report crystal structures of human RNase L in complexes with 2-5 A, nucleotides, and an 18-nucleotide oligomer RNA target.

Making a Histone Mark

The covalent marks on histones (the principal components of chromatin) play a critical role in the regulation of gene expression. Somehow these marks are preserved when a cell in a tissue divides so that the daughter cells maintain the gene expression program and tissue identity of the parent cell. **Jacob *et al.*** (p. 1249) show that the *Arabidopsis* histone methylase ATXR5 is specific for the replication-dependent histone variant H3.1 and maintains the repressive histone H3 lysine-27 methyl mark on the H3.1 variant during genome replication, thus, preserving cell-type–specific regions of heterochromatin and gene repression through cell division and beyond.

Steven E. Hyman is director of the Stanley Center for Psychiatric Research at the Broad Institute of Harvard and the Massachusetts Institute of Technology in Cambridge, MA, and a professor in the Department of Stem Cell and Regenerative Biology at Harvard University, Cambridge, MA. E-mail: seh@harvard.edu

Time for New Schizophrenia Rx

LAST MONTH, THE BATTLE AGAINST FOUR MAJOR DISEASES RECEIVED SOME GOOD NEWS. THE U.S. National Institutes of Health (NIH) and 10 of the world's largest pharmaceutical companies decided that instead of working ineffectively in silos, they would work together to discover therapies for Alzheimer's disease, type 2 diabetes, rheumatoid arthritis, and lupus. This initiative—the Accelerating Medicines Partnership (AMP)—recognizes that progress toward new therapies for common chronic diseases increasingly requires large-scale collaborative efforts that range from the need to grapple with heterogeneous polygenic disease phenotypes to the validation of biomarkers in large populations. What is disappointing is that, at least for the time being, the consortium dropped schizophrenia from its list, despite vast unmet medical need and substantial, albeit still recent, scientific advances. Was schizophrenia deemed too risky to pursue? If innovative partnerships such as the AMP are not willing to take on common and serious but otherwise neglected disorders such as schizophrenia, then the scientific community will have to find new ways of pooling intellectual and financial resources to address them.

Schizophrenia is a severe and disabling brain disorder that also creates enormous costs and challenges for caregivers and for society. Antipsychotic drugs that partially treat hallucinations and delusions were discovered in the early 1950s but have serious side effects and leave entirely untreated schizophrenia's characteristic cognitive impairments and "negative" symptoms such as blunting of emotion, loss of motivation, and impoverishment of thought and speech. The past six decades have witnessed many commercially successful antipsychotic drugs, but no new mechanisms of action and no gains in efficacy since the early 1960s. Cognitive behavioral therapies show promise, but even when combined with current medications, individuals with schizophrenia live with profound limitations resulting from diminished control over thought, emotion, and behavior. Many pharmaceutical companies have exited psychiatry in recent years because of high failure rates in clinical trials, only rudimentary understanding of disease mechanisms, and the lack of treatment biomarkers. Under these circumstances, patients and families would have scant hope for the arrival of better drug treatments.

Much about this grim scientific picture has changed in the past 5 years. New genomic technologies, combined with global collaborations to identify study participants and collect samples, have permitted the identification of a large and rapidly growing number of alleles associated with schizophrenia, bipolar disorder, and autism. Molecular pathways involved in neuronal function are emerging from the data and are beginning to suggest drug targets. Animal and in vitro models in which to investigate hundreds of gene variants of small effect remain works in progress. However, promising tools have emerged here too. For molecular and cellular analyses, stem cell technologies make possible the generation of human neurons in vitro. When combined with remarkable new genome engineering tools, these approaches permit the study of individual risk alleles, multiple alleles in molecular pathways, and the correction of risk alleles in neurons derived from patient samples. Studies at neural circuit levels are yet more challenging, but one can even envision transgenic nonhuman primate disease models with the genome engineering tools at hand. Proposals to the AMP have focused on advancing the genetic analysis of schizophrenia; improving in vitro human neuronal models to study disease-associated alleles; and a project to identify biomarkers, modeled on the early stages of the successful Alzheimer's Disease Neuroimaging Initiative.

Perhaps recent exits by companies from psychiatry made schizophrenia too great a reach for the AMP, despite continued strong support from NIH leadership. It is precisely when new knowledge opens challenging but real possibilities to make major advances in health that partnerships such as the AMP seem most warranted. The scientific community, including industry, academia, patient groups, and government, must find ways of sharing financial risk while developing effective and well-governed partnerships. Otherwise, important basic science investments will go untranslated while patients and society continue to bear painful and costly burdens.

– Steven E. Hyman

10.1126/science.1252603

CREDITS: (LEFT) MARIA NEMCHUK, THE BROAD INSTITUTE OF MIT AND HARVARD; (RIGHT) JOHNNY GRIM/FLICKR

Downloaded from www.sciencemag.org on March 14, 2014

Published by AAAS

EDITED BY KRISTEN MUELLER AND JESSE SMITH

PALEONTOLOGY

Whales in the Desert

Mass strandings of whales have long puzzled observers, who wonder about the causes of such simultaneous and often large-scale mortality events. These events are not new, however, and recent road development in the Atacama region of Chile serendipitously revealed a large and unique collection of marine vertebrate fossils that may shed some light on the phenomenon. Pyenson *et al*. report that the site, Cerro Ballena, dates to the Late Miocene period and consists of over 40 skeletons of marine vertebrates, including rorqual and sperm whales, seals, predatory fishes, and fascinating, now completely extinct, species such as walrus-whales and aquatic sloths. Four distinct time horizons exist within the site, indicating that the mass strandings occurred repeatedly, and the relatively complete condition of the skeletons suggests that the death site was protected from scavengers and other forces that would distribute the bones. Based on the diverse array of species involved, and the repeated occurrence of the strandings, harmful algal blooms may have been to blame. The assemblage at Cerro Ballena provides both a vivid picture of a rich but now past marine environment and insight into a phenomenon that is often still a mystery. An associated open-access Web site allows readers to learn more about the site and fossils. — SNV

Proc. R. Soc. London Ser. B **281**, 20133316 (2014).

PSYCHOLOGY

Me Me Me

What makes me me, and not you? Is it my corpus of autobiographical memories? Is it my concordance of wants and desires, which may themselves have been birthed and shaped by my personality traits? Or is it my sense of right and wrong? Strohminger and Nichols opt for the last and demonstrate in a series of studies that morality constitutes the largest part of self. Capacities and traits were grouped into psychological categories representing lower-level functions, such as perception and sensation; everyday automatic cognitive functions, such as identifying objects and riding a bike; or distinctive individual preferences, such as liking broccoli and valuing honesty. Then, online Americans were asked which were associated most closely with personal identities or, alternatively, the extent to which a person would change if that particular capacity or trait were lost. Throughout, attributes closer to morality were deemed to be more essential to one's identity. In a futuristic scenario set in 2049, when asked what part of Jim the accountant's brain would need to be transplanted into a recipient body in order to resurrect Jim, the part supporting moral judgment was chosen most. — GJC

Cognition **131**, 159 (2014).

CELL BIOLOGY

A Complicated Death

Much is known about signaling mechanisms that cause cells to undergo cell death or apoptosis, but it can be hard to know how the many steps play out to determine whether a particular cell lives or dies. Kallenberger *et al*. therefore undertook a combination of mathematical modeling and experiments on single cells to elucidate how cultured human cells responded to activation of the Fas death receptor. The receptor causes activation of the protease caspase-8, which undergoes multiple cleavage events that control both its activity and substrate preference. Caspase activity in single cells was measured by monitoring fluorescently tagged substrates. This revealed the kinetics of caspase activation and the variability in cell responses. Unexpectedly, a slower rate of cell death in cells exposed to higher concentrations of CD95 ligand was observed. Such a complicated caspase cleavage scheme may enable important characteristics such as switch-like behavior that

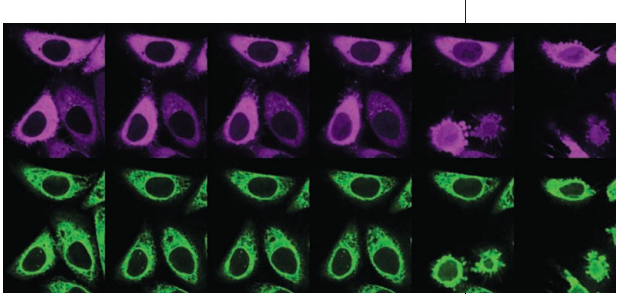

CREDITS (TOP TO BOTTOM): ADAM METALLO/SMITHSONIAN INSTITUTION; S. KALLENBERGER *ET AL.*, *SCIENCE SIGNALING* **7**, 316 (11 MARCH 2014)

Downloaded from www.sciencemag.org on March 14, 2014

Published by AAAS

does not cause cell death in response to low amounts of signal (but shows autoamplification when strongly activated) and a timer mechanism to shut the system down. — LBR

Sci. Signal. **7**, ra23 (2014).

CHEMISTRY

Process of Elimination

Transition metals such as rhodium and palladium (Pd) often catalyze reactions through a pair of processes termed oxidative addition and reductive elimination. Effectively, the metal inserts itself between two bonded atoms, and then after some rearrangements or substitutions in the coordination sphere, a different bond forms via the reverse process. Pérez-Temprano *et al.* explored the factors underlying which bonds form most readily by reductive elimination from Pd(IV). They prepared a complex with fluoride, tosyl-substituted nitrogen (NHTs), and aryl as well as alkyl carbon ligands, and then measured a ratio of alkyl C-F, C-C, and alkyl C-N bonded products of roughly 5:3:1. By adding an $(NHTs)^-$ salt to the reaction mixture, the authors could shift the ratio almost completely in favor of the C-N elimination pathway. Kinetic studies implicated a mechanism in which dissociation of $(NHTs)^-$ from Pd leads to a transient five-coordinate intermediate common to all three product channels, with the C-N pathway proceeding stepwise via subsequent attack by the nitrogen anion at carbon. The results could help to optimize synthetic protocols for C-N bond formation. — JSY

J. Am. Chem. Soc. **136**, 10.1021/ja411433f (2014).

MICROFLUIDICS

Paper Power

Paper-based microfluidic devices offer much promise for instrument-free medical diagnostics that can perform complex analytical functions while being easy to manipulate and use. Such devices require miniaturized power sources that are compatible with the paper technology and can be disposed of with minimum environmental impact. Esquivel *et al.* explore the use of fuel cells for powering such devices. They have developed a microfluidic fuel cell that exploits the capillary flow in the paper test strip without requiring external pumps. Both the KOH electrolyte and the methanol fuel are stored within the paper strip; when water is added, the fuel cell starts to generate power. The proof-of-concept prototypes reported by the authors meet the power needs of commercially available rapid tests that are powered by button-cell batteries. Integrated with a lateral flow test, the fuel cells can use the sample under analysis (e.g., blood) to generate the power needed for the analysis itself (e.g., glucose levels in the blood). The test strips are similar in construction to the lateral flow strips used in medical diagnostics and should thus be comparatively easy to incorporate into the manufacturing process. — JFU

Energy Environ. Sci. 10.1039/C3EE44044C (2014).

MATERIALS SCIENCE

Thermally Stable Reflections

A simple thermostat exploits the difference in the thermal expansion of two metal films to sense temperature changes and trigger the heating or cooling system on or off as needed. In some cases, though, the change in dimension with temperature is a problem; for example, a satellite built on Earth has to be engineered to allow for the shrinking of the parts that will occur when it reaches the low temperatures found in outer space. A few materials exist that show either limited or negative thermal expansion, including complex metal oxides, silica glasses, and an iron-nickel alloy, but these materials may be brittle or operate only over a narrow temperature range. One route to creating a material with a tailorable coefficient of thermal expansion (CTE) is to create an engineered structure. Yamamoto *et al.* created a periodic lattice composed of hexagonal plates of aluminum combined with a frame of titanium, which has a lower CTE, to make a thin-film material. When heated, the expansion of the aluminum is accommodated by stretching and bending of the titanium, in such a way that the connection points stay stationary. The samples were tested from room temperature to 185°C and showed a very low and slightly negative CTE. The authors envision using this architecture for making an array of mirrors, and demonstrate this capability by showing that the reflected image quality remained constant over the test temperature range. — MSL

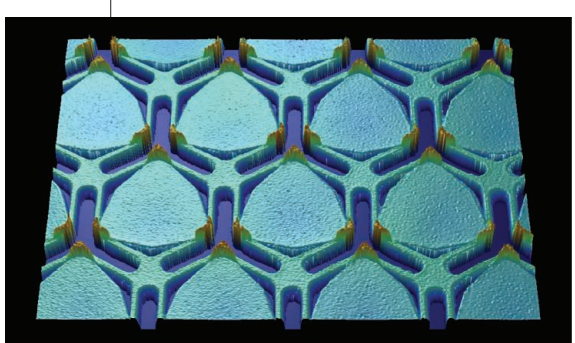

CREDIT: NAMIKO YAMAMOTO

Adv. Mater. 10.1002/adma.201304997 (2014).

Published by AAAS

AROUND THE WORLD

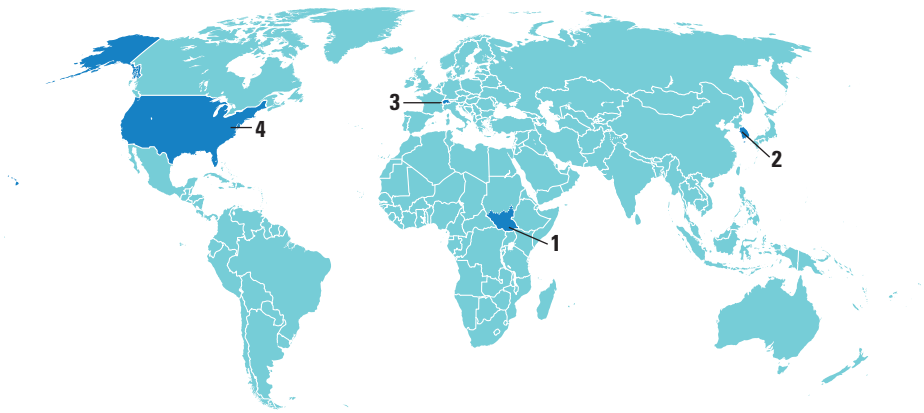

Put to use. A South Sudanese woman receives the oral cholera vaccine earlier this month.

Juba **1**

Cholera Vaccine Stash Deployed

The World Health Organization (WHO) is putting its new stockpile of oral cholera vaccines to use for the first time. Some 140,000 people in refugee camps in war-torn South Sudan are expected to receive the vaccine by the end of March. There is no cholera in South Sudan at the moment, but the impoverished country has been considered at risk since fighting broke out between the government and opposition forces in December. The vaccines will be administered by Doctors Without Borders.

Just how useful cholera vaccines are has been hotly debated; some have argued they are impractical and distract from the need to provide clean water and sanitation (*Science*, 17 August 2012, p. 785). But in 2012, WHO decided to assemble a 2-million-dose stockpile for use in emergency situations. The vaccine will first be offered in relatively secure refugee camps in Juba, the capital, and in the centrally located Lakes state, but the program may be expanded to other areas later.

NOTED

>Serbian government officials prompted scientific outrage with plans to **relocate Nikola Tesla's ashes** from a museum in Belgrade to a burial site at the city's Church of Saint Sava. Critics of the move, planned for July, say the prolific inventor was not a believer and that his remains belong at the Nikola Tesla Museum—their home since 1957—rather than the world's largest Orthodox church. The Facebook page "Leave Tesla Alone" has garnered more than 37,000 "likes."

Cheonan, South Korea **2**

Avian Flu Claims Research Flock

Korea's premier poultry research center was forced to cull its 11,000 hens and 5000 ducks last week after an outbreak of the deadly new avian influenza strain H5N8. Researchers at the National Institute of Animal Science (NIAS) made every effort to keep the Cheonan campus, 85 kilometers south of Seoul, virus-free. But on 3 March, 30 dead ducks were confirmed to be infected, and staff immediately culled the rest. Researchers predict that it will take nearly 2 years to reconstitute the flocks—used to study breed improvement and husbandry techniques—from birds kept at other facilities.

The incident highlights the difficulty of protecting poultry farms from circulating avian influenza. Officials are investigating three possible routes the virus could have taken onto campus: wild birds, NIAS vehicles, and supply deliveries, said Lee Jun-Won, deputy agriculture minister, at a press conference, where he promised "to hold those responsible accountable."

Since the strain emerged in central South Korea in January, it has spread virtually nationwide and outbreaks are still being reported. There have been no reports of human infections. **http://scim.ag/_H5N8**

Geneva, Switzerland **3**

WHO Proposes Halving Recommended Sugar Intake

The World Health Organization (WHO) last week released draft guidelines that halve the maximum amount of sugar it recommends people consume. The current recommendation states that sugars should make up less than 10% of daily energy intake. That includes both sugar that manufacturers or consumers add to food and sugar naturally present in honey or fruit juices. The draft suggests a further reduction to less than 5% of total energy—about 25 grams per day for an adult with a normal body mass index. But it calls this a "conditional recommendation," and says that there is "a need for substantial debate and involvement of stakeholders before this recommendation can be adopted as policy."

WHO will accept comments on the draft until 31 March, and many food companies are likely to voice strong opposition. (A single can of sugar-sweetened soda would exceed the daily recommended intake.) "If pressure comes to the organization, we are very well equipped to resist that type of pressure," said Francesco Branca, WHO's director of nutrition for health and development, at a press conference.

CREDITS (TOP TO BOTTOM): JM LOPEZ/AFP/GETTY IMAGES/NEWSCOM; GETTY IMAGES/ISTOCKPHOTO

Downloaded from www.sciencemag.org on March 14, 2014

Published by AAAS

Washington, D.C. 4

House Science Panel Takes Up Controversial NSF Bill

A highly partisan bill affecting research and education programs at the National Science Foundation (NSF) and other federal agencies is advancing in the U.S. House of Representatives. Introduced this week by Representative Lamar Smith (R–TX), who chairs the House science committee, the legislation would alter NSF's peer-review process, reduce funding for social science research, and create a new office within NSF to oversee federal science education programs. "To remain globally competitive, we need to make sure our priorities are funded and that taxpayer dollars are spent wisely," Smith said in a statement before his panel took up the measure, titled the Frontiers in Innovation, Research, Science, and Technology (FIRST) Act.

Science lobbyists and Democrats have sharply criticized the bill, saying its authorized spending levels are too low and its approach to managing research unwise. "[T]he bill does little to close this nation's innovation deficit, [and] it also does some things to widen it," said the Association of American Universities, a group of 62 research-intensive institutions.
http://scim.ag/_FIRST

NEWSMAKERS

Climate Scientist Breaks Into the Geology Club

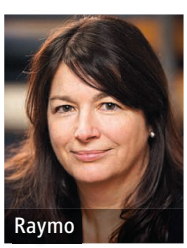
Raymo

Geologist and climate scientist **Maureen Raymo** joins the likes of Charles Darwin as this year's winner of the British Wollaston Medal, becoming the first female honoree in the prize's 183-year history. Raymo, 54, will receive the medal—cast in the platinum-group metal palladium discovered by chemist William Hyde Wollaston—at the Geological Society of London's annual meeting in June.

Like her Wollaston-winning predecessor, 19th century glaciologist Louis Agassiz, Raymo has focused on Earth's ice ages. Early in her career, she proposed that the rise of the Himalayas and the Tibetan Plateau 40 million years ago drove Earth from a "hothouse" climate into its present "icehouse" climate, an idea bolstered in this week's issue of *Science* (see p. 1189). She also helped explain why Earth's ice ages switched from a 40,000-year pacing to today's 100,000-year pacing. Now, after decades spent mostly at a desk, she has gone into the field to sort out how much the accumulation of glacial ice lowered sea level 3 million years ago. Given her early training in geology, she says, "I feel right at home."

Cardiologist and University President to Lead Smithsonian

For the first time, a physician will take the helm at the U.S. Smithsonian Institution. In mid-2015, **David Skorton**, president of Cornell University since 2006, will become secretary of the 168-year-old organization, whose 19 museums, zoo, and nine research centers are partially federally funded. Trained as a cardiologist, Skorton specialized in treating congenital heart disorders and developing better 3D imaging techniques. After 26 years as a professor at the University of Iowa, he served as its president from 2003 to 2006.

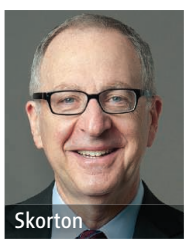
Skorton

Since moving to Cornell, Skorton has helped raise $5 billion and won a stiff competition to build a high-tech college campus in New York City that blends technology training, on-the-job experience, and entrepreneurship. At the press conference this week announcing his appointment, Skorton stressed the importance of arts and humanities: "A life in medicine has taught me that we will not solve our thorniest problems or meet our toughest challenges as a society through science alone."
http://scim.ag/Skorton

THEY SAID IT

"I already knew I wanted to become a scientist, but that afternoon I learned from Carl the kind of person I wanted to become."

—Astrophysicist and science communicator Neil deGrasse Tyson, on his first meeting at age 17 with Carl Sagan, during the debut episode of the 13-part update to Sagan's classic 1980 documentary series *Cosmos*.

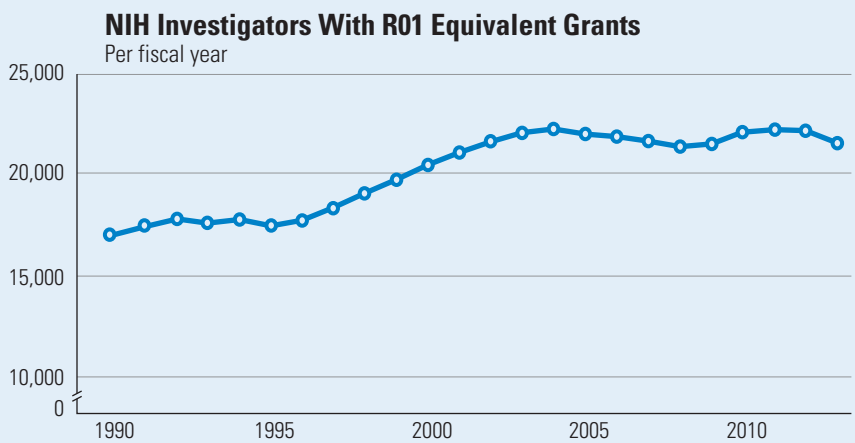

Has the Cull Begun in Biomedicine?

New data show that after remaining more or less steady for a decade, the number of investigators with National Institutes of Health (NIH) funding dropped last year from 22,116 to 21,511, a loss of 605 researchers. That's according to data for the agency's bread-and-butter R01 equivalent grants (above, excludes stimulus funding). Another analysis by the American Society for Biochemistry and Molecular Biology (ASBMB) pegs the drop at 1001. The decline, which came the same year that sequestration took a 5% bite from NIH's $31 billion budget, suggests a contraction in the number of labs supported by NIH. "Is this a wise culling of the herd," asks ASBMB President Jeremy Berg, "or is this a destructive loss of productive investigators and talent?"
http://scim.ag/NIHdrop

CREDITS (TOP TO BOTTOM): COURTESY OF CORNELL UNIVERSITY PHOTOGRAPHY; (DATA SOURCE) NIH OFFICE OF EXTRAMURAL RESEARCH; J. HENRY FAIR

Published by AAAS

Random Sample

Font of Knowledge

Fourteen-year-old Suvir Mirchandani says the U.S. government could save hundreds of millions of dollars simply by changing the font of its printed documents, and he's got numbers to prove it. When Mirchandani started sixth grade at Dorseyville Middle School in Pittsburgh, Pennsylvania, he noticed that teachers were handing out a lot more homework in a wide array of fonts. Wondering if the school could save money by opting for less ink-hungry varieties, he collected a week's worth of printed handouts, designed a test document to model their character frequencies, and ran it through ink coverage software using various fonts. He found that switching to the svelte Garamond font would save the school district nearly $21,000 a year. "It was shocking," says Peter Pinko, the school's science coach, who worked with him on the project. "It surprised the [district] business manager."

Mirchandani submitted the findings to the *Journal of Emerging Investigators*, which publishes research by middle and high school students. Its editors—graduate students at Harvard University—suggested he scale the study up to the federal government. When the Government Printing Office didn't respond to his information request in time, he used public documents, including the 2014 budget and an Internal Revenue Service form, to run the analysis. His conclusion: An across-the-board switch to Garamond could save roughly $234 million a year. He hopes the study will influence font choice for teachers and bureaucrats alike but isn't holding his breath. "I'm aware that people are resistant to change," he says. Now a high school freshman, Mirchandani wants to pursue a career in computer science or environmental science.

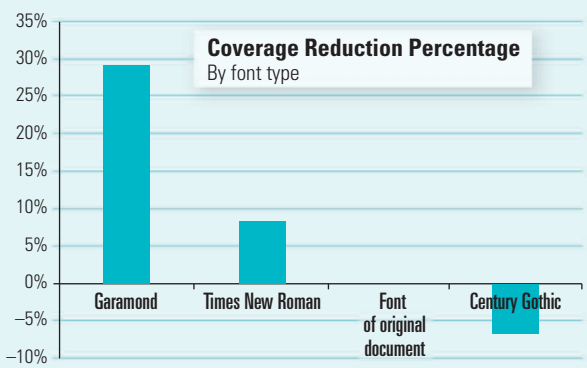

BY THE NUMBERS

13% Proportion of animal rights extremist acts between 2000 and 2012 that targeted universities, down from 61% between 1990 and 1999. Meanwhile, incidents involving individual homes and property have risen from 9% to 46% of the total, according to a new Federation of American Societies for Experimental Biology guide. **http://scim.ag/_FASEB**

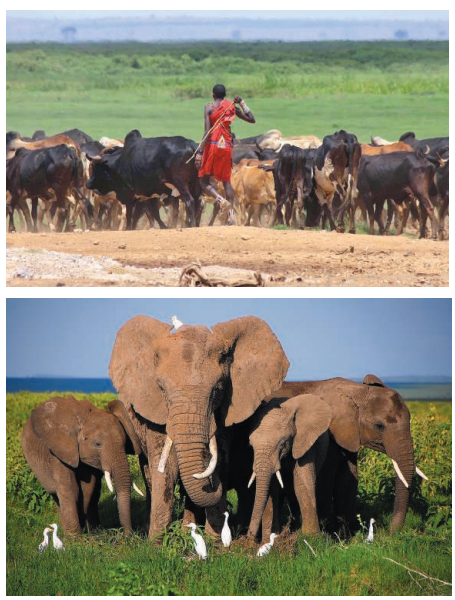

Sounds risky. Elephants have learned to recognize and fear the voices of Maasai hunters (*top*).

CREDITS: (LEFT, TOP TO BOTTOM) ADAPTED FROM S. MIRCHANDANI AND P. PINKO, *JOURNAL OF EMERGING INVESTIGATORS* (10 MAY 2013 AND 6 MARCH 2014); (RIGHT, PHOTOS TOP TO BOTTOM) GRAEME SHANNON; KAREN MCCOMB

FINDINGS

Sight by Sound Upturns Brain Model

A computer program that uses sound to give "sight" to the blind challenges the prevailing view of how the brain is organized. The system, called vOICe, scans images and converts shapes into sound by assigning higher sound frequencies to higher points in space. For example, a diagonal line stretching upward from left to right becomes a series of ascending tones.

The developers—neuroscientists from the Hebrew University of Jerusalem—tested vOICe on people who were born blind. Despite having no visual memories, they could "see" a person's exact posture represented in sound after 70 hours of training, the team reported last week in *Current Biology*.

Brain imaging then revealed activity in the area of their visual cortices responsible for recognizing body shapes in sighted people—a surprising find, the researchers say, because this area shouldn't fully develop without visual experiences. Because a traditional sensory-organized brain model can't explain the results, they argue that the brain is arranged according to tasks rather than senses. **http://scim.ag/_sight**

Elephants Know Subtleties Of Human Voice

Elephants can tell certain human languages apart and even determine our gender and relative age, according to new research in Kenya's Amboseli National Park. There, Maasai pastoralists sometimes spear elephants in protest of park policies or retaliation for tusking and trampling of people or cattle. To find out if the animals could distinguish Maasai voices from those of Kamba farmers in the area, Karen McComb, a behavioral ecologist at the University of Sussex, and colleagues used concealed loudspeakers to play recordings of people in the two ethnic groups speaking their respective languages.

As the team reported on 10 March in the *Proceedings of the National Academy of Sciences*, elephant family groups were more likely to retreat and bunch together in response to adult male Maasai voices than adult male Kamba voices. They were much less fearful of the voices of Maasai women or boys. Young elephants likely learn this sensitivity by watching, the researchers say, in a dramatic example of a human threat changing natural behaviors. **http://scim.ag/elevoice**

Published by AAAS

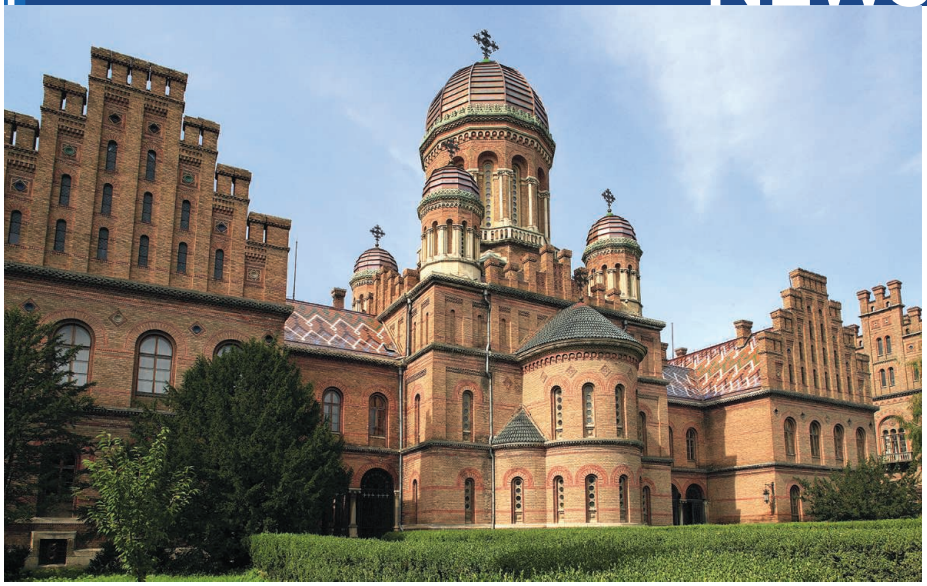

Unshackled. Law would give Chernivtsi National University and other Ukrainian universities autonomy.

EASTERN EUROPE

Ukraine's Science Reformers Seize the Moment

While chaos mounted in southern Ukraine last week, with Russian forces overrunning Crimea and the region threatening to secede, a handful of science leaders huddled in Kyiv, Ukraine's capital, plotting a revolution of their own. Their aim: reinvigorate a scientific community that has been adrift since Soviet times.

Gathered in the Verkhovna Rada, Ukraine's parliament, on 6 March, the luminaries reviewed draft legislation that would transform the nation's science and higher education system. The two bills would set up a competitive grant system, root out moribund institutions, give greater autonomy to universities, and make it easier to ship reagents and biological samples into and out of Ukraine. "We have a historic chance to revitalize science," says molecular biologist Nataliya Shulga, chief executive of the Ukrainian Science Club, a think tank in Kyiv.

Their window of opportunity, which opened with the ouster of the pro-Russian government of Viktor Yanukovych last month, may be fleeting. Backers are angling to get the laws—one on S&T and a second on higher education—on the books before presidential elections on 25 May, after which the Rada may have new priorities. Science could slip off the Rada's radar even before then, if Crimea careens out of control. "The situation is tense and unpredictable," says neuroscientist Oleg Krishtal, director of the Bogomoletz Institute of Physiology in Kyiv and a longtime advocate of radical reforms.

Ukrainian science has been in a downward spiral since the Soviet Union's collapse in 1991. That year, Ukraine spent roughly $700 million on S&T, or 0.9% of its gross domestic product; the 2014 S&T budget, in contrast, stood at just $475 million—and that was before the depths of Ukraine's penury became known.

As spending shriveled over the years, scientific vitality withered. In 2007, the Ukrainian Science Club set out to determine how many Ukrainian researchers are "internationally visible," says Krishtal, the club's president. Of the nation's estimated 82,000 scientists, "we found that only a few hundred" are known outside Ukraine, he says. "It was a shock."

Yet there was little impetus for change—until now. The ouster of Yanukovych's government, which spurned calls for educational reform, has raised hopes. Equally important, reformists have one of their own in the Rada: Liliya Hrynevych, an educator elected in 2012. "We need to reinvent the system," says Hrynevych, who heads the Rada's Committee on Science and Education.

One target for reform is how the scarce government science funding is doled out. A mere 7% is disbursed competitively, Hrynevych says. "Bureaucrats allocate the rest." The science law would establish a National Research Fund to distribute state science funding based on merit-based review. And to better focus scarce resources, the science law mandates a nationwide audit to identify intellectually "dead" institutes.

The proposed science law also aims to ease the passage of research materials across the border. "Biomedical science in Ukraine is controlled by customs," Shulga says. For starters, she explains, you "can't ship anything on dry ice." And ordering reagents is often an adventure. For instance, a Bogomoletz team last year placed a €216 order for 250 milligrams of ultrapure sucrose for isolation of membrane peptides. A customs officer refused to believe that sugar could cost so much and demanded that the scientists apply for an import license. "We have many more stories like that," Shulga says. The draft law calls for a team of customs officers specially trained to deal with science-related imports and exports.

The second law, on higher education, would unfetter universities from stifling state controls. "Universities need more freedom, and independent funding sources," says Vladimir Konovalchuk, an agricultural science expert at Bridges, a consulting firm in Kyiv. The law would give universities autonomy to run their own affairs, free professors from onerous ministry requirements on lecturing hours, and mandate access for all researchers in Ukraine to scientific literature databases such as the Web of Science.

Leading the charge. Rada deputy Liliya Hrynevych.

The full Rada has already received the higher education bill, while the S&T bill should be ready for consideration later this month. The interim science and education minister, Serhiy Kvit, has been a proponent of education reform and backs the legislation, Shulga says. Hrynevych, meanwhile, says she's "working with all [Rada] factions to ensure support for the reforms."

Although Crimea is casting a shadow, Hrynevych sees a more prosaic threat to her efforts to overhaul the system—and one that will require help from abroad to overcome. "Reforms need money, which we do not have."

–RICHARD STONE

CREDITS (TOP TO BOTTOM): © ISIFA IMAGE SERVICE S.R.O./ALAMY; COURTESY OF LILIYA HRYNEVYCH

Published by AAAS

U.S. SCIENCE FUNDING

The Future Is Flat in White House's 2015 Spending Request

The 2015 budget request that President Barack Obama sent to Congress last week sounded a bit like one of those Hollywood previews shown at the multiplex. It invited its audience to imagine an alternative world. In it, scientists get 1650 additional grants from the National Institutes of Health (NIH) and the National Science Foundation (NSF), agricultural researchers get a new $20 million biosafety laboratory, and there's a new $1 billion fund aimed at preparing for global warming. It all could become real, the White House argued, if lawmakers would allow the government to spend about $56 billion more than permitted under a budget agreement that sets the spending rules for the upcoming fiscal year.

Alas, for the research community, the White House's wish list will probably end up like a fantasy film, because Congress isn't likely to go along. Instead, the more realistic portions of the president's $3.9 trillion request depict a gloomier future for federal science funding: essentially flat or declining budgets at major basic research agencies, with a few bright or bleak spots for certain fields (see box, below, and table, next page).

Frozen out. NASA's Stratospheric Observatory for Infrared Astronomy, an aircraft-mounted telescope, would be grounded if Congress agrees with President Barack Obama's 2015 budget request.

That scenario isn't sitting well with research advocates. These funding levels "jeopardize our global leadership in science," said Mary Woolley, CEO and president of Research!America, a prominent lobbying group in Alexandria, Virginia, in a statement. "We simply cannot sustain our nation's research ecosystem … with anemic funding."

Obama administration science officials say they did the best they could under strict 2015 spending limits imposed by an agreement that lawmakers reached this past December to end a government shutdown and trim long-term deficits (*Science*, 20 December 2013, p. 1426). That deal limited total discretionary spending in 2015 to about $1 trillion, split roughly between civilian and defense programs. (The remaining $2.9 trillion goes to mandatory entitlement programs, such as Medicare and interest payments on debt.) Research would get about one of every eight of those discretionary dollars, administration officials note. Still, "all of us would have preferred more," said White House science adviser John Holdren during the budget unveiling on 4 March.

Overall, the core request for the fiscal year that begins on 1 October includes $135.4 billion for R&D, spread across numerous agencies. That number, if approved by Congress, would represent a 1.2% increase over current R&D spending, the White House estimates. But

Budget Lows, Highs, and Dreams

On the chopping block.

- **NASA's Stratospheric Observatory for Infrared Astronomy (SOFIA)**, a Boeing 747 outfitted with a 2.5-meter infrared telescope, which has cost some $1.25 billion to build.
- **The Department of Energy's (DOE's) fusion research program**, down 17.6% to $416 million, would result in reduced operations at fusion reactors based at U.S. universities.
- **One science laboratory operated by the National Oceanic and Atmospheric Administration.** (The agency hadn't named it as *Science* went to press.)

Due for a raise.

- **DOE's Advanced Research Projects Agency – Energy** gets a 16.1% boost to $325 million. But Congress may not back expanding efforts to push high-risk, high-payoff energy technologies to market.
- **The U.S. Department of Agriculture (USDA)** gets $75 million for three new "innovation institutes" that would work on biomanufacturing and bioproducts, pollination and pollinator health, and antimicrobial resistance studies.
- Three research agencies get better-than-average increases: **DARPA** a 4.9% increase to $2.92 billion; the **National Institute of Standards and Technology research labs** a 4.6% increase to $680 million; and **the U.S. Geological Survey** a 4% increase to $1.07 billion.

If we only had more money.

The White House's $56 billion OSGI "wish list" includes an extra $5.3 billion for research, if Congress agrees.

- $2.1 billion for military R&D;
- $1 billion for a Climate Resilience Fund; one-third goes to research on adapting to a warmer world;
- $970 million for NIH, enough for some 650 additional grants;
- $886 million for NASA;
- $552 million for NSF, which could support 1000 additional awards;
- $20 million for USDA to consolidate two aging labs in Athens, Georgia, which handle potentially dangerous biological agents into a single, modern facility.

CREDIT: NASA/JIM ROSS

Downloaded from www.sciencemag.org on March 14, 2014

Published by AAAS

the increase would not keep pace with the forecast inflation rate of 1.7% for 2015, analysts note, meaning that spending would actually erode.

Within the R&D total, budgets for applied research and development would rise slightly and basic science would drop by 0.5%, or $331 million, to $32.1 billion. The biggest basic science funders would see little new money or cuts, while the picture is brighter for some smaller programs.

Many, if not all, of these numbers are likely to be remolded in Congress. And lawmakers also will decide whether they want to back any of the additional $5.3 billion in science-related spending that the White House included on its $56 billion wish list, officially known as the Opportunity, Growth, and Security Initiative (OGSI). The initiative is a political gesture, meant to highlight how Congress could rise above the discretionary spending cap without adding to the deficit. Lawmakers could raise one-half of the extra OGSI money by raising taxes on retirement accounts held by the affluent, the White House proposes, and more by reshaping farm and unemployment insurance programs. The extra money would allow Congress to add $970 million to the NIH budget, the White House notes, enough for some 650 new grants, and give other science agencies hefty raises.

Key legislators, however, say that the steps needed to raise the money are out of the question. The OGSI concept is "extremely disappointing" because it busts the spending cap, and won't fly in the Republican-controlled House of Representatives, declared Representative Harold "Hal" Rogers (R–KY), who chairs that body's spending panel. And Senator Barbara Mikulski (D–MD), who leads the Senate's spending panel, has promised to adhere to the discretionary cap, suggesting any additional science spending would have to come through cuts to other existing programs. Researchers probably won't know the final outcome until after congressional elections in November.

In the meantime, researchers are taking a closer look at the request's details. At NIH, a 0.7% increase to $30.36 billion would support 9326 new and competing grants, 329 more than this year. That number comes on the heels of news that the total number of principal investigators supported by NIH shrank by as many as 1000 in 2013 (see p. 1183). NIH's request is "status quo when the last thing we need is status quo," said Jennifer Zeitzer, director of legislative affairs for the Federation of American Societies for Experimental Biology in Bethesda, Maryland.

A few NIH programs would gain. The agency wants to spend $100 million, up from $40 million, on its share of the Brain Research through Advancing Innovative Neurotechnologies (BRAIN) Initiative. BRAIN is a brain-mapping project that the administration launched last year with $100 million from several agencies and wants to double in 2015. And NIH would add $50 million to the Common Fund, the pot of money within the NIH director's office for cross-cutting initiatives. The pot would grow to $583 million, of which some $30 million would be used for high-risk, cutting-edge projects selected using a process similar to that pioneered by the Defense Advanced Research Projects Agency. Instead of taking a year or more to review and select proposals, an NIH program manager would identify "a bold, innovative strategy to tackle a really important problem," then handpick academic and industry partners, said NIH Director Francis Collins.

How Science Fared ($ Billions)

	2014	2015 request	% change
National Institutes of Health	30.151	30.362	0.7%
National Science Foundation	7.172	7.255	1.2%
Research	5.809	5.807	0.0%
Education	0.847	0.890	5.1%
DOE Office of Science	5.066	5.111	0.9%
Basic Energy	1.712	1.807	5.5%
Bio/Environmental	0.610	0.628	3.0%
Fusion	0.505	0.416	-17.6%
High Energy Physics	0.797	0.744	-6.6%
Nuclear Physics	0.569	0.594	4.3%
ARPA-E	0.280	0.325	16.1%
NIST S&T labs	0.65	0.68	4.6%
USGS	1.032	1.073	4.0%
NASA	17.647	17.461	-1.1%
Science office	5.151	4.972	-3.5%
USDA Agricultural Research	1.268	1.241	-2.1%
National Institute of Food & Ag	0.790	0.843	6.7%
Ag/Food Research Initiative	0.316	0.325	2.8%
Innovation institutes		0.075	N/A
NOAA Operations/Research	3.287	3.376	2.7%
DOD S&T	12.009	11.515	-4.1%
DARPA	2.779	2.915	4.9%
DHS R&D	1.032	0.876	-15.1%

At NSF, acting Director Cora Marrett told reporters this week that NSF's requested 1.2% increase, to $7.23 billion, should be viewed in the context of how well the agency did this year compared with its peers. "Our 4% increase in 2014 represents a better situation than obtained for a number of other agencies," she noted.

Marrett also said she's not disappointed that the request—which includes no increase for NSF's research accounts—is the smallest jump in years. "Single-year budget figures can be misleading," she said. "One really ought to look out over a period of time."

That longer time frame, however, is exactly what bothers science lobbyists. NSF's budget hasn't kept pace with inflation since 2010, says Sam Rankin of the American Mathematical Society in Washington, D.C., despite promises from Congress and the White House for a decade long doubling of NSF's budget. He and others hope to convince appropriators to reverse that erosion, which amounts to $345 million, by taking money from other federal programs.

At the Department of Energy's Office of Science, the nation's single largest funder of physical science, spending would rise 0.9% to $5.11 billion. The biggest winner is advanced computing research, up 13.2% to $541 million, primarily aimed at upgrading supercomputers used by energy and other researchers. In contrast, the fusion program would take a 17.6% cut to $416 million, while high-energy physics spending would fall 6.6% to $744 million.

–DAVID MALAKOFF

With reporting by Yudhijit Bhattacharjee, Adrian Cho, Jocelyn Kaiser, Eli Kintisch, Jeffrey Mervis, Kelly Servick, and Erik Stokstad.

CREDIT: WHITE HOUSE OFFICE OF MANAGEMENT AND BUDGET

Published by AAAS

HIV/AIDS

Cancer Genes Help HIV Persist, Complicating Cure Efforts

BOSTON—Upbeat headlines from a major HIV/AIDS conference* here focused on an HIV-infected baby that started antiviral treatment 4 hours after birth and now has no detectable virus, raising hopes that it has been cured. But perhaps the most eye-opening finding at the meeting struck a cautionary note, revealing how HIV quietly persists in the body even when the infection appears to have been vanquished. That work also raises ominous questions about the risk of cancer in people on HIV drugs long-term.

The celebrated infant, from Long Beach, California, mirrors the famous case of the "Mississippi baby" revealed at this same meeting last year (*Science*, 8 March 2013, p. 1134). That child, now 3, also was started on antiretroviral drugs shortly after birth, but now has been off treatment for 23 months without any sign of the virus returning. In the new case, which made the front page of *The New York Times*, the 9-month-old child remains on treatment. "It's premature to get excited," says virologist Douglas Richman of the University of California, San Diego.

One reason Richman and others are so cautious is that the AIDS virus is something like the proverbial cockroach that survives a nuclear blast. HIV can hide deep inside cells, weaving its DNA into human chromosomes, impervious to drugs and immune attack as long as it remains dormant. Pools of these latently infected cells, or reservoirs, can survive for decades and have become the bane of attempts to cure HIV infection.

At the meeting, two studies detailed a novel mechanism that would help explain how reservoirs persist. The riddle addressed by the new work is this: In HIV-infected people on powerful treatment that completely shuts down the production of new viruses, why don't all of their infected cells disappear within a few years as the long-lived immune cells die off? One possibility is that some infected cells still produce new HIVs that manage to dodge antiretroviral drugs and infect virgin cells, constantly refilling the pool. Evidence suggests this occasionally occurs, particularly in tissue that drugs have difficulty reaching (*Science*, 23 December 2011, p. 1614), but many researchers doubt that it happens routinely. A more likely explanation, they believe, is that the infected cells make copies of themselves, a cloning process known as homeostatic proliferation.

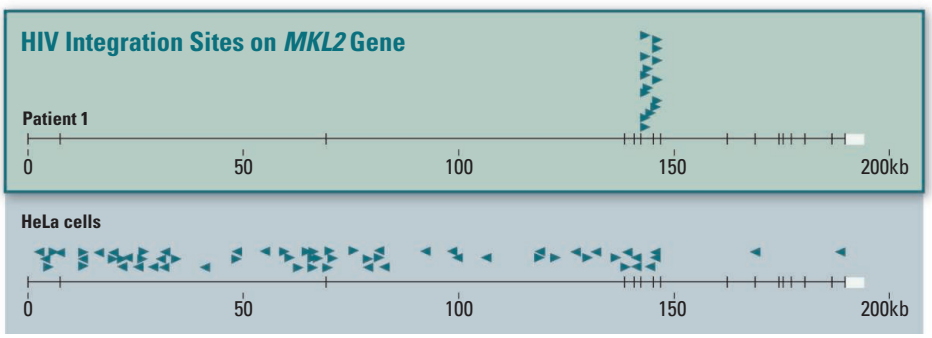

Selective advantage. An HIV-infected patient on long-term antiretrovirals has cells with the viral DNA repeatedly integrated in a small region of a cancer gene, but in a control experiment (*bottom*) the virus has no such preference.

The two new studies examined blood cells taken at different points in time from a total of eight HIV-infected people who had received antiretroviral treatment for up to 14 years. All told, the researchers determined the precise locations at which the HIV DNA had integrated in more than 2500 instances.

When a person becomes infected with HIV, the virus makes billions of copies of itself that go on to infect new cells. In the genome of each new cell, the virus integrates its genetic material largely at random, with the result that viral DNA can be found at millions of different sites across the population of cells. But that's not what the researchers found in their long-term patients. Clinical virologist Thor Wagner of the University of Washington (UW), Seattle, explained how in three of them, 40% of the integration sites were identical in two cells or more. That suggested that infected cells were duplicating themselves, keeping the viral DNA in its original integration site.

"Homeostatic proliferation has been a theory for a long time," says Wagner, who works with the well-known team of pediatrician Lisa Frenkel and virologist James Mullins. "We think this is the best proof yet that it occurs." Anne-Mieke Vandamme, an epidemiological virologist at the Rega Institute for Medical Research in Leuven, Belgium, agrees, saying, "these were very, very exciting data."

A team led by Stephen Hughes, director of the National Cancer Institute's HIV Drug Resistance Program in Frederick, Maryland, found roughly the same things in its five patients. "The integration sites we saw are not random," Hughes says. Indeed, in one person, about half of the infected blood cells had HIV DNA integrated at the exact same place in the human DNA.

A form of natural selection probably explains the dominance of a few integration sites. The researchers suggest that clones in the reservoir gain an evolutionary advantage if HIV has integrated in their genome at sites that speed up cell growth—a first step toward cancer. Hughes's group dramatically showed this with one patient who had 15 separate integrations in a relatively short stretch of one cancer gene (see illustration).

Although a growing body of evidence reveals higher rates of cancers in HIV-infected people who receive long-term treatment, the causes have been difficult to pin down because of the effects of age, antiretroviral drugs, and other confounding factors. "I would suspect that this may be linked to why people with HIV have more cancers, but we haven't yet proven that," says Frenkel, also of UW Seattle.

Wagner says both groups' findings call into question the "kick and kill" strategy that attempts to purge the reservoir. Several research groups are testing drugs that aim to kick the transcription process into gear and force latently infected cells to produce virus; the idea is that the infected cells will die as they release virus, while antiretrovirals will mop up the freed HIVs. Wagner, however, worries that kicking cells will simply crank up homeostatic proliferation. "I think you need strategies to directly target the infected cells," he says.

The cancer connection may hold a clue. Much cancer research today attempts to selectively eliminate cancer cells and not harm healthy ones, but applying that strategy to HIV is a tall order. "I don't know what the solution is going to be," Wagner says.

–JON COHEN

*Conference on Retroviruses and Opportunistic Infections, 3–6 March.

Downloaded from www.sciencemag.org on March 14, 2014

CREDIT: ADAPTED FROM STEPHEN HUGHES/NATIONAL CANCER INSTITUTE

Published by AAAS

Reactive. In Iceland, fast-eroding mountains create young soils rich in fresh, easily weathered minerals.

PALEOCLIMATE

How Earth Can Cool Without Plunging Into a Deep Freeze

Earth obviously has a decent thermostat; life has thrived here uninterrupted for 3 billion years and more. But researchers have been arguing for decades about how it works—particularly when something resets the temperature. Forty million years ago, for example, the planet began slipping from a "hothouse" climate to that of an "icehouse." Geoscientists have suspected that the rising of the Himalayas triggered the chill by speeding up processes that suck carbon dioxide from the atmosphere. But nobody could explain what kept the planet from spiraling into a pole-to-pole ice age. Now, a geochemical model published online this week in *Science* suggests that Earth's temperature controls have built-in restraints, rooted in the chemistry of rock and flowing water (http://scim.ag/geoMaher).

The model is the work of geochemists Katherine Maher—who has a degree in civil and environmental engineering—and C. Page Chamberlain of Stanford University in California. They approached Earth's climate control system as an industrial chemical reactor, with rock, air, and flowing water taking the place of pipes, vats, and valves. Volcanoes supply carbon dioxide that, being a greenhouse gas, can warm climate. But the gas also dissolves in water, turning into carbonic acid that can dissolve rock. The products of this acid weathering then run down rivers to the sea, where microscopic animals combine them with more carbon dioxide from the air to build hard skeletons. Those end up buried beneath the sea floor after the animals die.

By pulling carbon dioxide out of the atmosphere and burying it, geoscientists agree, this vast web of reactions keeps the greenhouse gas from building up and turning Earth into a torrid hell like Venus. Mountains are a key actor. You might guess that most of the dissolved rock carried by the Amazon River, for example, comes from the waterlogged Amazon Basin, where water spends lots of time. In fact, almost all of it comes from the Andes. Even though water speeds through the soil there, the rapidly eroding, still-rising mountains supply fresh, easily weathered minerals that eclipse any contributions from the depleted basin soils.

So the uplift of mountains ought to rev up rock weathering and turn down the thermostat. In the early 1990s, climate scientist Maureen Raymo of the Lamont-Doherty Earth Observatory in Palisades, New York, and her colleagues proposed that's what happened 40 million years ago: The rise of the Himalayas and the Tibetan Plateau increased erosion and thus acid weathering, drew down atmospheric carbon dioxide, and cooled the climate. But critics asked how the process could have stabilized before driving climate into a deep, permanent icehouse—and nobody had a good answer.

Your choice. Geochemist Katherine Maher holds a young, dark soil that water can easily weather and an older, less reactive one already well weathered.

Maher and Chamberlain tried a new approach. Where previous geochemical models had simply plugged in assumptions about how fast weathering works, their simulations included detailed weathering processes. The results showed that the impact of weathering depends crucially on two factors: how long water remains in contact with fresh, easily weathered rock in the soil, and how long it takes for water to take on the maximum load of dissolved material that chemical thermodynamics allows.

The model shows how the accelerated erosion that accompanies the rise of great mountains like the Andes recycles more carbon to the sea floor and cools the globe. But the thermodynamic load limit caps just how much even the fastest mountain building can cool climate. So does another factor: temperature. Lower temperature fosters slower weathering reactions. As a result, global cooling slows weathering all across the continents and reins in cooling due to mountain building. That answers earlier criticism that the Himalayan scenario would have threatened the planet with runaway cooling.

"They have a great idea," says geochemical modeler Robert Berner, who is a professor emeritus at Yale University. "They're doing a much more sophisticated job than we did and made it a much more interesting story." Putting the details of weathering together with mountain building reconciles past modeling inconsistencies, says geochemical modeler Lee Kump of Pennsylvania State University, University Park, who calls the work "elegant and straightforward."

Now, Kump says, fieldworkers know which measurements, such as how water moves through a drainage basin, they need to improve. With more realistic inputs to models, researchers could further build their confidence that their simulations of the geochemical reactor match the real world of water, gas, and rock.

–RICHARD A. KERR

CREDITS (TOP TO BOTTOM): KATHERINE MAHER; MATTHEW ROTHE

Downloaded from www.sciencemag.org on March 14, 2014

Published by AAAS

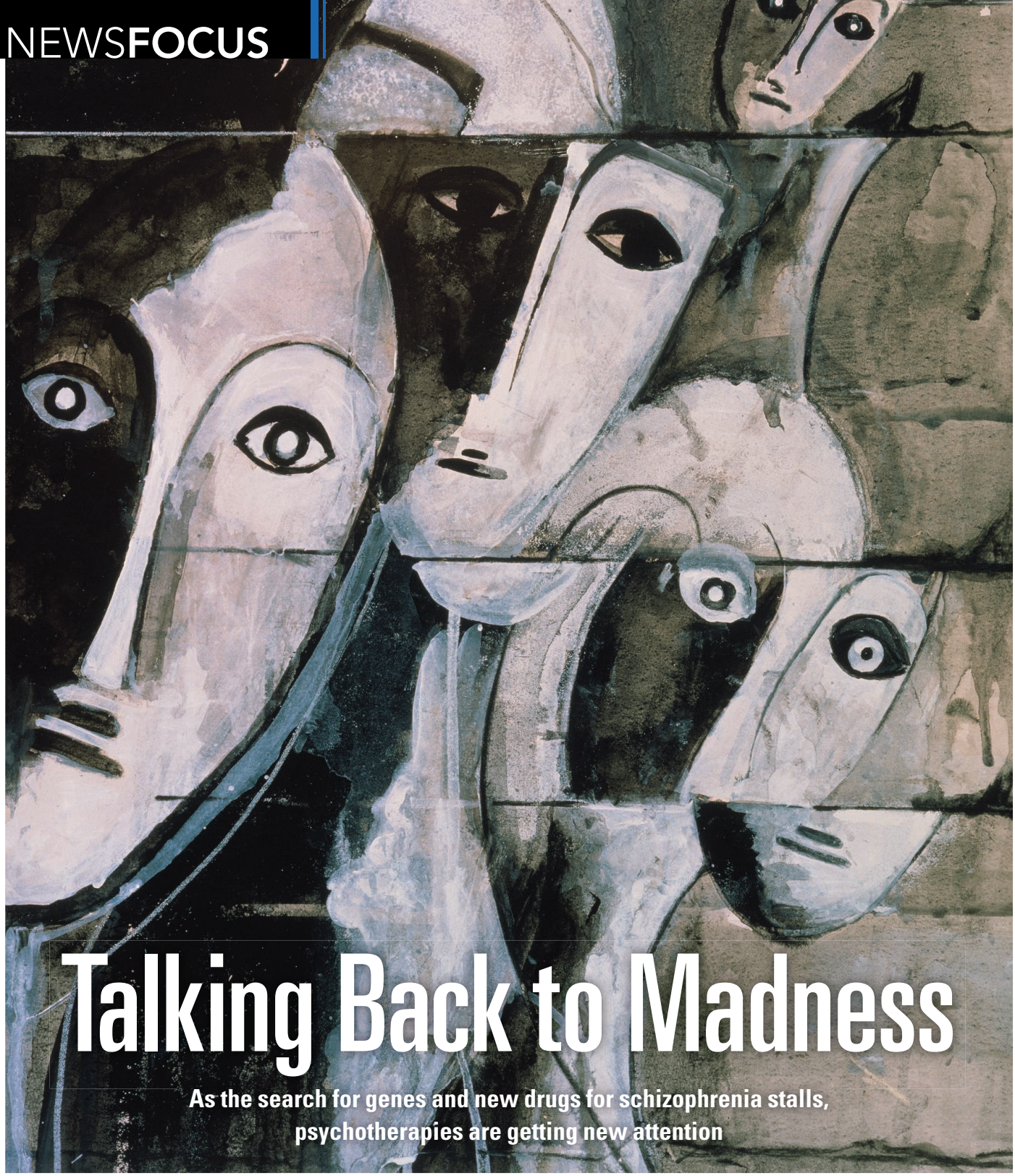

Talking Back to Madness

As the search for genes and new drugs for schizophrenia stalls, psychotherapies are getting new attention

NEW YORK CITY AND NEWCASTLE, U.K.— Terry was 13, a lonely African-American boy growing up in a troubled home in Detroit, when he first heard the voices. They were ugly and mean. The voices said he was no good, that no one loved him, and that he should kill himself. So he tried his best: When he was 15, he took 30 Valium pills and had to have his stomach pumped. Then the voices commanded him to kill his father. They told him exactly how to do it—put rat poison in his food. Fortunately, some other, gentler voices intervened and told him not to.

After high school, Terry began attending university in Detroit, but that didn't last long. Still haunted by the voices, he was soon addicted to heroin, and his marriage ended in divorce. In 1980, he moved to New York, looking for a new start. He got a job at a doughnut shop, then at a community center, but eventually the voices got worse and so did his drug habit. He found another woman to be with, but she

CREDIT: L. WILLIAMS/SCIENCE SOURCE

Downloaded from www.sciencemag.org on March 14, 2014

Published by AAAS

Waking nightmare. People suffering from schizophrenia often have hallucinations, delusions, and severe emotional problems.

was also taking drugs, and eventually abandoned Terry and their two daughters.

Terry (not his real name), now 60, is telling me his story over lunch at a restaurant on 42nd Street, across from Grand Central Terminal. He's tall and stocky, with kind eyes and a gentle sense of humor that mask his tortured soul. But things are better for Terry now. About 14 years ago, he met the psychotherapist he credits with saving his life. During a drug-fueled crisis, with the ugly voices raging in his head, his eldest daughter checked him into New York Methodist Hospital in Brooklyn, where psychologist Jessica Arenella was working. "I was there 6 weeks," Terry says. "She would sit by my bedside, listening to me rambling on."

Four years later he was hospitalized again, just when Arenella was about to go into private practice. She suggested that he start seeing her. "I said, 'You're a white bitch, how the hell can you help me?' " Terry recalls. "She said, 'I may be a white bitch, but I can back my play with you.' She was tough."

Terry has been seeing Arenella for psychotherapy sessions for the past decade. The voices haven't entirely gone away, he says, but she has taught him how to live with them, and how to follow the gentle voices and ignore the nasty ones. "Without Jessica, I wouldn't have made it," Terry says.

Terry is suffering from schizoaffective disorder, one of a number of so-called schizophrenia spectrum disorders. By treating his psychosis with "talk" psychotherapy, Arenella, along with a small number of other psychologists and psychiatrists, is bucking a decades-old trend, in which antipsychotic drugs have long been seen as the first line of defense against the illnesses. In a radical departure, Arenella and other advocates of psychological approaches are engaging with patients' symptoms, such as hearing voices or experiencing hallucinations or paranoid fantasies, and taking them seriously rather than dismissing them or relying on medication to stamp them out.

A number of clinical trials of these techniques have shown modest but measurable effects on symptoms such as hallucinations and delusions. One of these, a short-term approach called cognitive behavioral therapy (CBT), has been recommended since 2002 by health authorities in the United Kingdom for all new cases of schizophrenia, and long-term psychotherapy has been adopted as standard treatment in a number of Scandinavian communities. It's generally combined with traditional drug treatment, but one study, published earlier this year, suggests that CBT could substitute for antipsychotic drugs in some cases. "There is a strong possibility that psychological treatments are likely to be at least as effective as drugs, and they are certainly preferred by patients," says Peter Tyrer, a psychiatrist at Imperial College London.

Nevertheless, the idea that schizophrenia, long regarded as a disease of the brain, can be treated psychologically remains very controversial, and some are not swayed by the recent clinical trials. "These studies have no more credibility than studies of homeopathy," says Keith Laws, a psychologist at the University of Hertfordshire in Hatfield, U.K., and co-author of a recent meta-analysis concluding that CBT has only a very small effect on psychotic symptoms.

A Sample of Recent Clinical Trials

Year and authors	Subjects	Treatment type	Results
2010 Lynch *et al.*	Meta-analysis of nine trials with schizophrenia patients	CBT vs. counseling, "befriending," psycho-education, and other psychological interventions	CBT not more effective in reducing symptoms or preventing relapse
2011 Seikkula *et al.*	117 patients having first episode of psychosis	Family therapy and intense community support	81% recovery rate after 24 months
2011 Wykes *et al.*	Meta-analysis of 40 studies of remediation for cognitive problems	Cognitive remediation therapy	Moderate effectiveness
2012 Van der Gaag *et al.*	201 people at high risk of psychosis	CBT + TAU vs. TAU	Significant reduction in transition to psychosis after 18 months
2012 Grant *et al.*	60 "low-functioning" schizophrenia patients with severe social/emotional problems	CBT + TAU vs. TAU	Moderate to strong improvement after 18 months
2012 Rosenbaum *et al.*	269 patients having first episode of schizophrenia	Psychodynamic therapy + TAU vs. TAU	Significant improvement in symptoms after 24 months
2012 Jones *et al.*	Cochrane review of 20 previous trials	CBT vs. other "talking" therapy treatments	CBT not better on symptoms but better on relieving distress
2014 Jauhar *et al.*	Meta-analysis of 52 previous studies	CBT	CBT has "small" effect on symptoms
2014 Turner *et al.*	Meta-analysis of 48 previous studies	CBT, "befriending," cognitive remediation, etc.	CBT significantly more effective
2014 Morrison *et al.*	74 people with psychotic symptoms but not taking medication	CBT + TAU vs. TAU	Moderate reduction of symptoms after 18 months

CBT = cognitive behavioral therapy **TAU** = treatment as usual

Jury still out. Psychological treatments for psychosis have shown moderately positive results in many, but by no means all, published studies.

DATA SOURCE: M. BALTER/*SCIENCE*

Stress and vulnerability

About 1% of people worldwide fall victim to schizophrenia or a related disorder over their lifetimes. They may suffer both "positive" symptoms, such as hallucinations and delusions, and "negative" symptoms, such as emotional withdrawal and severe inability to focus on daily tasks.

Most schizophrenia experts subscribe to the stress-vulnerability model of the disorder, in which some individuals have a greater predisposition—either because of genes, childhood trauma, or environmental factors—to psychosis than others. In vulnerable people, psychotic episodes are often set off by some sort of stressful event, usually in the late teens or early adulthood.

Published by AAAS

But past psychological approaches, such as psychoanalysis, have shown limited success in treating the disease. Sigmund Freud, the founder of psychoanalysis, eventually gave up on using it to treat psychotic patients, although a number of later post-Freudian psychiatrists continued to use it with sporadic success. When antipsychotic drugs arrived in the 1950s, with their clear ability to dampen the worst psychotic symptoms, psychotherapy became increasingly marginalized.

Drugs have serious side effects, however, and at least 50% of patients either refuse or fail to take them, according to recent studies. Moreover, the search for genes behind schizophrenia and other mental illnesses, which might lead to new drug therapies, has failed to produce any smoking guns and has led only to the discovery of a large number of genetic variants, each conferring a very small additional risk. "We're trying to fix something, but we don't know what's broken," says Brian Koehler, a psychologist at New York University in New York City who also sees schizophrenia patients in private practice.

Now, psychological treatments are gaining ground again. Most advocates of psychotherapies insist they are not claiming that schizophrenia is purely a psychological malady caused by a dysfunctional family background. "We're looking for a much more nuanced form of psychiatry that doesn't reject biology, but that is able to situate the biology within the realm of lived human experience, which is socially and culturally determined," says psychiatrist Pat Bracken, director of mental health at Bantry General Hospital in Ireland.

Today's psychotherapists use two main approaches to treat schizophrenia. The first, called psychodynamic therapy, is derived from earlier psychoanalytic techniques but discards older Freudian ideas that sexual repression is behind psychosis. Instead, it focuses on both childhood experiences and the way that psychotic symptoms unconsciously serve a useful function for the patient, for example, by masking unbearably painful thoughts and feelings.

Psychodynamic sessions typically go on for many years, as in Terry's case, and scientific evidence for their benefits is limited. Although anecdotal stories of success abound, advocates of psychodynamic therapy increasingly recognize the importance of rigorous trials. "We live in an evidence-based era, we can't duck out of that," says Brian Martindale, a U.K.-based psychiatrist and chair of the International Society for Psychological and Social Approaches to Psychosis.

"There's always a little bit of truth at the heart of the delusion."

—DOUGLAS TURKINGTON, NEWCASTLE UNIVERSITY

The gold standard for medical evidence is the randomized controlled trial, and these have been difficult to design for psychodynamic treatment. For one, the treatment is lengthy and costly, and few patients receive it—thus making adequate sample sizes difficult to assemble. But one influential study, led by psychiatrist Bent Rosenbaum of the University of Copenhagen and published in the journal *Psychiatry* in 2012, did find signs that it is effective. Rosenbaum's study compared 150 patients receiving what is often called treatment as usual (TAU)—including meetings, education about their condition, and low doses of antipsychotic medication—with 119 patients who also received intense psychodynamic therapy. After 2 years, both groups had improved, but the psychodynamic cohort achieved markedly greater reductions in psychotic symptoms.

Still, questions remain about whether such improvements last after the treatment ends, and whether they are really due to the treatment or, as psychiatrist Richard Warner of the University of Colorado, Boulder, puts it, "because they had contact with a human being who was kind and interested in them."

The second approach, CBT, is a shorter, more pragmatic method that takes patients through a series of guided steps designed to explore alternative interpretations of what he or she is experiencing, with the goal of changing both outlook and behavior. CBT, which has proven effective for depression and anxiety disorders, typically takes months rather than years, and it has shown more clear-cut effectiveness.

"There's always a little bit of truth at the heart of the delusion," explains Douglas Turkington, a CBT pioneer at Newcastle University in the United Kingdom. "If someone has a funny idea we call a delusion, you have to talk about it and put it on the table," says Ross Tappen, a psychologist at the Manhattan Psychiatric Center in New York City.

And if delusions are taken seriously, Tappen adds, they can often be treated. "A delusion is the psychological equivalent of an inoperable tumor that is out of control and takes over your normal functioning," he says. "What therapy does, at its best, is to shrink the psychological tumor."

Sandy's CBT

An invisible companion, named John, had been tormenting Sandy (a pseudonym) since he was 10. John would talk and sing loudly, often during the night, keeping him awake. Once, John told Sandy to put the wrong answer on a school exam, and he obeyed. When Sandy, who lives in Britain's Greater Manchester area, was 18, doctors referred him to the Psychosis Research Unit in Manchester, a joint program of the University of Manchester and local mental health services. There he came under the care of psychologist Paul Hutton.

Sandy was convinced that John was real and had nearly complete control over his life. He declined to take medication, but did agree to undergo a series of CBT sessions. Hutton, now at the University of Edinburgh, was able to figure out that John made Sandy feel less lonely, and also that John was helpful in some situations, taking his side during Sandy's frequent arguments with his parents. But having John in his life convinced Sandy that he was "weird."

Hutton encouraged Sandy to avoid trying to push John away and instead let him come and go as he pleased. Sandy was also

CREDIT: COURTESY OF DOUGLAS TURKINGTON

Published by AAAS

taught to test how much control John really had over him with so-called mindfulness exercises in which he remained detached during John's exhortations. Meanwhile, Hutton gave Sandy educational materials indicating that having invisible friends was normal, and that he was not really weird at all. Each week, Sandy was asked to rate how convinced he was that John was real, how often John appeared, and for how long.

With these numbers steadily dropping, by week 4 Sandy agreed to get rid of John entirely. After week 11, he had done so, and the psychotic episode seemed to be over—at least for the time being, as Hutton described in a case study first published online in 2011 in *Behavioural and Cognitive Psychotherapy.*

Hutton concedes that Sandy is "at the positive end of the spectrum" of CBT successes, because he was fairly young and his hallucinations were "very amenable … to the sort of well-tested approaches we use." But he adds that he often sees "fairly dramatic responses" to CBT.

As early as 2000, Turkington and others published a study of 90 patients in the *Archives of General Psychiatry* showing that while 9 months of either CBT or a sympathetic support technique called befriending could improve both positive and negative schizophrenia symptoms, only the CBT group maintained its improvement 9 months after the trial had ended.

In 2012, another team confirmed that CBT could be effective for so-called negative symptoms of schizophrenia, such as emotional distance, apathy, and social withdrawal, which are usually much harder to treat.

And the most recent CBT trial, published last month in *The Lancet*, concludes that CBT might serve as a substitute for antipsychotic drugs in some cases, rather than just an adjunct to them as in most clinical studies (see *Science*NOW, http://scim.ag/schizCBT). In this study, 74 schizophrenia spectrum patients who were being treated in Manchester and Newcastle, and who had declined to take drugs, were randomized by computer into two groups, one receiving TAU and the other TAU plus CBT.

After 18 months, the CBT group showed moderately better scores on various tests for psychotic symptoms; indeed, CBT performed about as well as antipsychotic drugs do when compared with placebos, meaning that CBT could substitute for drugs in some situations—especially those in which patients are refusing to take them anyway.

Clinical psychologist Anthony Morrison of the University of Manchester, who led the study, stresses that a drug-free approach might be appropriate only for patients who are relatively high-functioning and have not shown any risk to themselves or others. Nevertheless, the results are "utterly convincing," says Max Birchwood, a psychologist at the University of Warwick in Coventry, U.K.

Other researchers, however, are deeply skeptical of the claims for CBT. In January, a team led by Laws and psychiatrist Peter McKenna, now at the University of Barcelona, concluded in a meta-analysis in *The British Journal of Psychiatry* that past trials of CBT for schizophrenia were seriously flawed. The study found that the differences between treatment and control groups were very small, and that these were reduced further when sources of bias—such as inadequate blinding or masking—were controlled for. "The UK government's continued vigorous advocacy of this form of treatment … might be considered puzzling," the authors wrote, adding that "claims that CBT is effective against these symptoms of the disorder are no longer tenable."

"It may be a placebo effect, but I will go for all the placebo effect I can get. I'll take it."

—JESSICA ARENELLA, PSYCHOLOGIST

Arenella, who treats Terry and some of her other patients with a combination of psychodynamic and CBT approaches, says that in the end it doesn't matter whether talk therapies work because of the theory behind them or just because someone is taking the patient and their symptoms seriously. "It may be a placebo effect, but I will go for all the placebo effect I can get," she says. "I'll take it."

In the end, the spread of talk therapies for psychosis could be limited by a scarcity of resources, and of therapists willing to try them. Treating such clients is very stressful and seldom financially rewarding. "A lot of people don't want to take these patients," Arenella says. "Working with them is scary. People get violent, people get hurt, computers get thrown to the ground, ceiling tiles get pulled out." And Martindale says that "contact with madness is very disturbing; it conjures up all sorts of feelings."

Government agencies and insurance companies can help by covering such treatments, even though they are more expensive in the long run than drugs, say Arenella and others. They are worth trying, Bracken says. "I have a lot of patients whom I would say recovered from psychosis. I see people who move on with their lives, get their quality of life back, are able to live independently." Indeed, the popular notion that a schizophrenia diagnosis is a life sentence of mental illness is not borne out by the statistics: In one typical study, published in the *American Journal of Psychiatry* in 2004, researchers found that nearly 50% of first-episode schizophrenia or schizoaffective disorder patients were symptom-free after 5 years.

"But many people don't get there no matter what we do," Bracken says, "until that spark in them finally says, 'I want my life back.' "

My lunch with Terry was coming to an end, so I pulled out my American Express card to pay the bill. Terry was still smiling, although he looked very tired from telling me his story over the previous 2 hours. As I paid up, I told him about a meeting I had just attended in San Francisco on psychological approaches to psychosis, as part of my reporting for this story.

"I'd like to fly to San Francisco and take people out to lunch with my own American Express card," Terry said. "I'd like to get married again, or have a girlfriend. I'm going to get all that. It's going to happen because, like I told Jessica, I'm not going to settle for anything less."

–MICHAEL BALTER

CREDIT: HARRY POCIUS

Published by AAAS

Water's Tough Skin

Surface tension is a force to be reckoned with, especially if you are small

An ant could step off a cliff and land unharmed. But if it dips a leg in a raindrop, the insect can be caught in a life-threatening morass, all because of the surface tension of water. The result of polar interactions among water molecules, surface tension is what draws a water droplet into a sphere. It creates an elastic surface that can deform without breaking—think of a water strider oaring its way across the surface of a pond. At the same time, it enables water to cling like quicksand to an ant unlucky enough to blunder in. Creatures of our size barely acknowledge surface tension's existence, but for the tiny, "it becomes a dominant force," says David Hu, a mechanical engineer at the Georgia Institute of Technology in Atlanta.

Because of surface tension, a rat can't pee a steady stream, but instead must slowly push out urine drop by drop. (It can take 10 minutes for a single drop to fall.) Surface tension thwarts juvenile flying fish: When they try to escape into the air like the larger adults, they sometimes bounce off the underside of the water's surface layer. Dew forming on a mosquito's wing will cause the wing to fold up, grounding the insect until the wing dries out.

Physicists have a pretty good understanding of how surface tension arises. The clingy water molecules attempt to minimize their connections with other types of molecules. So when something deforms the water surface, the displaced water molecules work to return to their minimum-energy configuration—unless the intruder itself attracts water molecules, in which case the water clings like glue. But biologists have tended to ignore the air-water interface, Hu says. His own eyes were opened a decade ago when he began to study how water striders skate so effortlessly along the surfaces of ponds. Using dyes and high-speed video, Hu and his colleagues found that by vigorously rowing along the surface, striders cre-

CREDIT: © DAVID EBENER/EPA/CORBIS

Downloaded from www.sciencemag.org on March 14, 2014

Published by AAAS

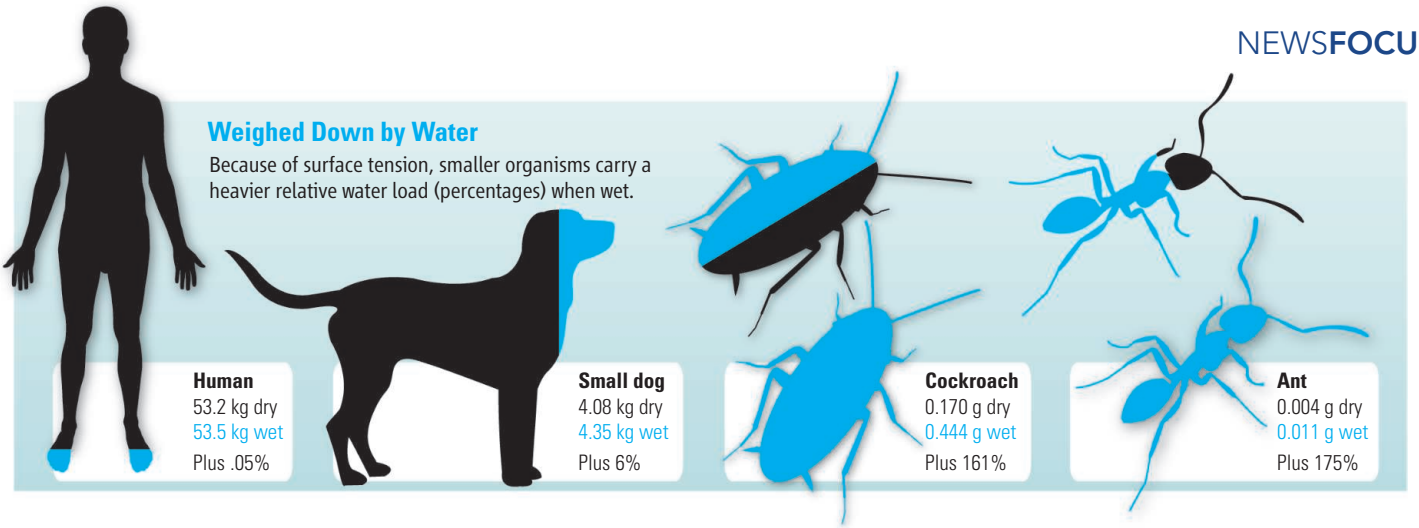

ate swirls that help propel them forward, all without rupturing the water surface. "That work was the trigger of academic interest in surface tension in biology," says Ho-Young Kim, a mechanical engineer at Seoul National University.

Hu has since looked at other phenomena involving air-water interfaces—how dogs shake to dry off, how mosquitoes cope with rain (*Science*, 8 June 2012, p. 1216), and how animals pee—disparate phenomena "linked by common equations and modeling ideas," he says. Since then, other researchers have recognized the power of surface tension to explain form and behavior on the small scale. And while humans, unlike ants, don't have to worry about being trapped because of surface tension, it's still relevant to our lives. For example, our lungs secrete a chemical inside their air-filled sacs to lower the surface tension there, which allows us to breathe without the sacs collapsing when we exhale. Surface tension also allows human and agricultural pathogens to travel long distances in tiny, lightweight droplets.

Some of the most eye-catching new findings were on display at "Shaking, dripping and drinking: surface-tension phenomena in organismal biology," a symposium that Hu helped organize at the annual meeting of the Society for Integrative and Comparative Biology in Austin in January. "The sheer dazzling diversity of biological phenomena to which surface tension is relevant is mind-blowing," says Steven Vogel, a biomechanist at Duke University in Durham, North Carolina.

Giving plants "muscles"

Plants lack muscles, but findings presented at the symposium showed that for some, surface tension can substitute. "When there's a change in surface tension, you get motion," explains Rachel Levy, a mathematician at Harvey Mudd College in Claremont, California. "It creates motion in ways you don't expect."

Consider *Erodium*, a group of flowers whose fruit resemble a bird beak. Inside that beak, each seed develops a centimeter-long awn—a rodlike "tail" that serves two purposes. Initially, inside the fruit, the awn is stretched out. When the fruit dries and cracks open, the freed awn spontaneously coils, releasing its stored energy and sending the seed a half-meter from the parent plant. After the seed lands, the awn winds up during the day and unwinds at night, screwing the seed into the ground bit by bit—a millimeter or so a day.

Kim has found that surface tension drives the process. Normally, surface tension causes water droplets to ball up to minimize the air-water interface, he explains. But when those droplets meet a surface that has a greater attraction for the molecules of water than water itself, they will spread out and wet it. He found that the awns of *Erodium* and of *Pelargonium*, another group of plants with self-burying seeds, consist mostly of fibers of lignin and pectin, both water-loving molecules. At times of day when humidity is high, the fibers quickly absorb moisture. "The wet tissues swell and become straight from [an] initially dry, coiled configuration," Kim explains. When humidity drops, the fibers dry out, the tissues shrink, and the awn coils up again.

Kim mounted seeds from both groups of plants onto a force sensor and increased the humidity to measure the force they generated as they tried to uncoil. He also tested the burying potential of the force by watching awns drive their seeds into "soils" of glass beads of different sizes. The force "is just enough to dig into the soil," Kim reported in January.

It might also be enough to propel a microrobot. Today's microrobots all require electrical tethers, because no battery is both sufficiently powerful and small enough to be carried on board. Eventually Kim wants to equip robots with humidity-driven "muscles" that won't require external power. "But first we need to know how the biology works," he says.

A raincoat for a leaf

A floating fern, *Salvinia molesta*, forms meter-thick beds at the surface of ponds and slow-moving rivers. Native to South America, it's become invasive around the world, clogging waterways and disrupting aquatic ecosystems. But what attracted Wilhelm Barthlott to this prolific plant was its ability to keep submerged leaves coated with a thin layer of air. The film of air gives the leaves a silvery sheen and enables the plant to carry out photosynthesis and gas exchange underwater. It also makes the fern buoyant, so it will quickly bob to the surface if an opening appears, filling in any gaps before other species can get established.

Dig in. As the awn of a *Pelargonium* seed dries, it coils, generating force needed to bury the seed.

CREDITS (TOP TO BOTTOM): (DATA SOURCE) DAVID HU; (ILLUSTRATION) C. SMITH/*SCIENCE*; WONJONG JUNG

Published by AAAS

Engineers want to create similar air layers on the hulls of ships to reduce drag and fuel consumption. But to date, they have not been able to generate a layer that lasts. So Barthlott, a biologist emeritus at the University of Bonn in Germany, and his colleagues decided to see how *Salvinia* does it. Studying the microscopic structure of the leaf surface, they discovered hundreds of regularly spaced clumps of 2-millimeter-long hairs, four per clump. The clumps resemble eggbeaters: The hairs in each clump flare out midway up but reconnect at their tips. Along most of their length, the hairs are coated with hydrophobic, or water-repellent, wax, while the tips are waxless and hydrophilic—they attract water. Surface tension pins the air-water interface to the tips so that the air layer resists disruption by turbulence in water. The interface is "a bit like a tent where the hairs are the poles," said Matthias Mayser, a biologist with an engineering background at the University of Liège in Belgium who worked with Barthlott. "The water stays on top of the air."

The plant also repels rain, Mayser explained. "It would be impossible to establish an air layer upon submergence if the room in between the hairs was already filled by water from rain." By filming drops falling on the *Salvinia* leaf surface, he observed that "the [drop's] surface tension keeps the drop in a spherical form and prevents water from penetrating" between the hairs. That keeps the leaf's silvery sheath of air intact.

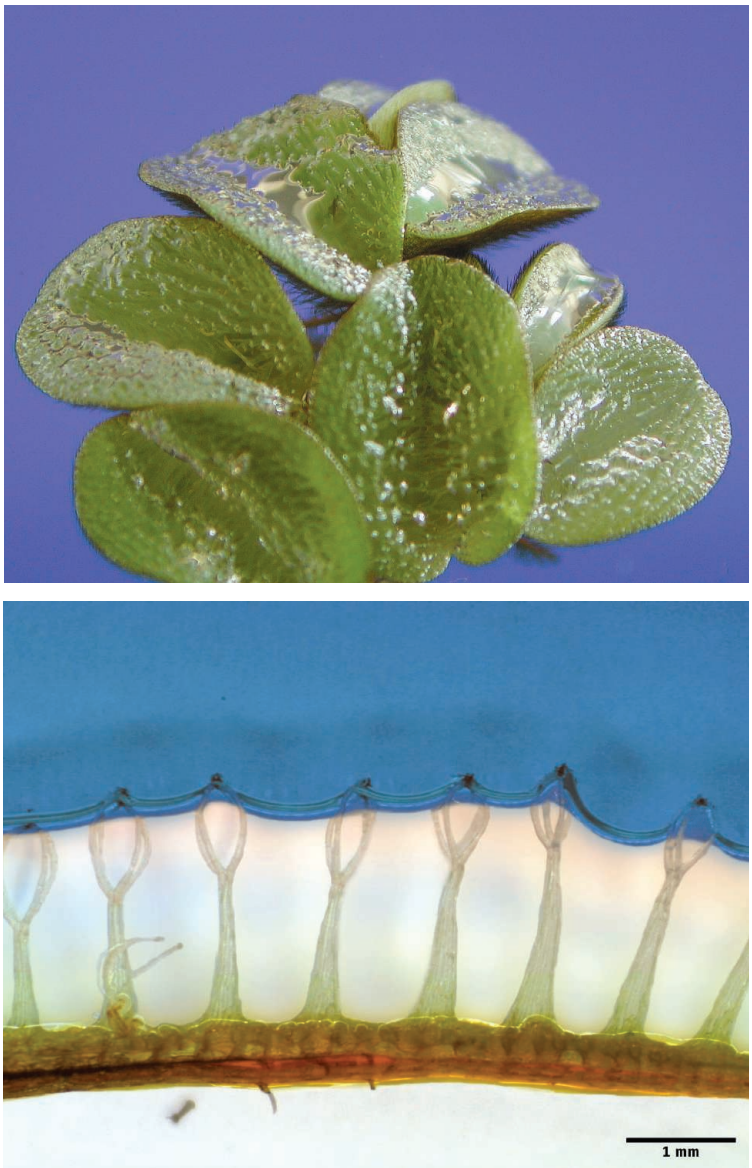

Airtight. Hairs that keep water suspended above a layer of air (*lower image*) help give a floating fern its silvery sheen.

Flying low among the lilies

Galerucella nymphaeae, or water lily beetles, spend most of their time munching water lily leaves. But as Manu Prakash watched them on a Massachusetts pond one day, he noticed a strange behavior. Flying from leaf to leaf, the beetles skimmed the water surface, never lifting off. Prakash, a physicist at Stanford University in California, wondered whether surface tension plays a role in this peculiar flight mode.

He and his graduate student Haripriya Mukundarajan filmed water lily beetles as they flew and took a close look at their anatomy with an electron microscope. They saw that each apple seed–sized beetle was covered with hairs. Further tests showed that the hairs made the insect superhydrophobic. Only the claws at the end of each leg were hairless and hydrophilic. Prakash suspected that the beetle's body and legs would be repelled from the water surface, but the claws would tend to stick to the water.

The film revealed that as the beetle flies, it drags the claws of four of its six legs in the water, raising only the middle two legs. "If there was no surface tension, the moment the wings generate lift, the beetle would pop off the water," Prakash explained at the meeting. But the claws tether the beetle to the water, while the rest of its body is repelled by the water surface. "So the beetle bounces up and down," he said.

Although erratic, skimming the water is a more efficient way for the beetle to travel from leaf to leaf than full-fledged flight would be. To take off into the air would be a waste of time and energy. The only downside is that if the beetle goes too fast—it normally flies about 0.5 meters per second—it catches up with the ripples it creates as it moves, which slows it down. But Prakash thinks the beetles, like water striders, are a textbook example of how evolution has put surface tension to work. "There's so much stuff that you see when you are sitting on a pond."

Germs go airborne

Surface tension may keep some beetles water-bound, but it also helps pathogens take flight. Each cough or sneeze launches bacteria and viruses skyward in a cloud of droplets whose sizes are determined in part by surface tension, says Lydia Bourouiba. Through high-speed video, mathematical modeling, and lab experiments, this applied mathematician from the Massachusetts Institute of Technology in Cambridge is working out details of such airborne pathogens with an eye toward curbing the spread of disease.

Some researchers believe respiratory viruses generally don't travel far after a cough or sneeze, arguing that they are mostly carried in large droplets that land within a meter or two. Others contend that it's the smaller droplets, which are airborne for much longer, that underlie transmission. But very few researchers have studied how pathogens are actually transported from place to place, says James Hughes, a medical epidemiologist at Emory University in Atlanta. "Even the sizes of the droplets emitted remain debated," Bourouiba says. Surface tension, by governing the shapes and sizes of drops and bubbles, as well as how quickly they burst, influences how far they travel.

CREDITS (TOP TO BOTTOM): MATTHIAS MAYSER AND WILHELM BARTHLOTT; ERIK SCHNEIDER, MATTHIAS MAYSER, AND WILHELM BARTHLOTT

Published by AAAS

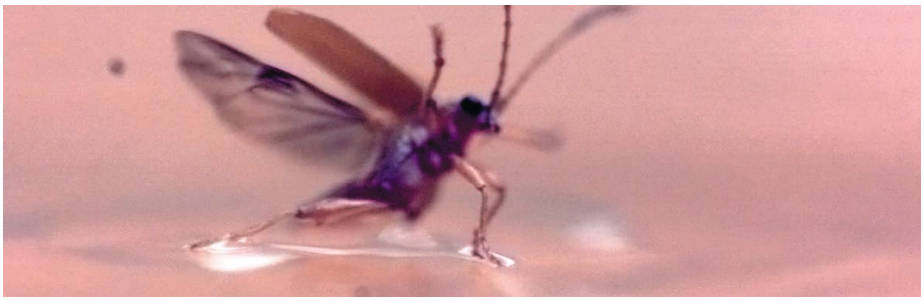

Skimming low. This water lily beetle remains tethered to the water surface as it flies to a new leaf.

By filming coughs, sneezes, and bursting bubbles and closely examining the cloud of droplets emitted, she has characterized their sizes and the flight distances. She used these observations to help come up with a mathematical model that assesses how buoyancy and momentum interact to determine how far the droplet cloud launched by a cough or sneeze can travel. The model shows that coughing can spread pathogens 200 times farther than other models had predicted, she reported at the meeting. Smaller droplets can waft up to 6 meters.

Temperature and humidity should also influence droplets' lifetimes, and Bourouiba says her model can account for their effects as well. That could prove useful for understanding what environmental conditions promote a pathogen's spread. "Here's somebody that comes from a totally different background and discipline who is applying her expertise and know-how to an important public health issue," Hughes says.

Bourouiba and her colleagues have put their approach to work to understand the spread of *Clostridium difficile*, which can cause severe and persistent diarrhea. The bacterial infection affects about a half-million people a year, particularly in hospitals or long-term care facilities. Outbreaks can be hard to stop because the bacterium produces spores that last for months, and hospitals find it everywhere, including suspended in the air. But how does it get airborne? High-pressure flush toilets, Bourouiba reported at the meeting and in a paper posted to the arXiv preprint server in October.

She mounted a camera to the sides of toilet seats; with special lighting, filming at up to 2000 frames per second, she was able to visualize water droplets erupting with each flush. While a substantial portion of the airborne droplets were large enough to sink back onto the toilet seat or other nearby surfaces, many were so small that they remained suspended, she said. As with the visualizations of coughs and sneezes, she used these observations to develop another mathematical model, one that predicts the range and spread of droplets spewing from the toilet.

Certain cleaning products actually worsen the problem, she says, by reducing the surface tension of the water in the toilet bowl, which allows more small droplets to escape. "This is important," she said, "because current mitigation strategies in hospitals only focus on bleaching surfaces, thus effectively ignoring the aerosol problem." The modeling may give "us enough information to design intervention strategies," she said, such as increasing surface tension with water additives.

Achoo. Following a sneeze, high-speed video and image processing visualized a waterfall of large droplets (*left*) and a lingering cloud of small droplets (*right*) that can spread pathogens farther.

Bourouiba and Tristan Gilet, a fluid dynamics engineer at the University of Liège, are also looking at how the properties of water can spread plant diseases. Agricultural experts have long known that plant diseases flourish after rain, among them wheat leaf rust, which threatens global wheat crops. Bourouiba and Gilet wondered whether the raindrops themselves help disperse the pathogens living on leaves. They again enlisted high-speed video, studying natural and artificial leaves with a range of sizes and other properties.

Because leaves are somewhat hydrophobic, an impacting raindrop tends to form a discrete puddle instead of a thin film. That standing water can absorb pathogens. The videos showed that when another raindrop lands right next to a puddle, it splashes, launching part or all of the puddle from the leaf, Gilet reported at the meeting. "The second raindrop expels [the first] in a very efficient way." How far that water travels depends on the size and flexibility, or compliance, of the leaf. Small leaves, like a tomato's, bend and absorb the impact of the raindrop, dampening any splash. Big leaves resist the impact, so the splash can travel much farther, he said.

"The idea of rain generating disease in plants is pretty new," Hu says. "It spreads [pathogens] in a way the pathogen couldn't do itself." The importance of the effect will vary depending on the concentration of pathogens and the size of the ejected drop. But the research suggests that a wider spacing between plants could slow the spread of some diseases.

From insect locomotion to a strategy for boosting global crop yields: A simple physical phenomenon lets us not only understand the world of the very small; it may also help us cope better with the world at large. And that's what appeals to Hu. "I love that when I study surface tension dynamics I can draw on ideas from many disciplines: mathematics, biology, chemistry, physics, computer science, and engineering," he says. "We need all of these perspectives to understand the many ways surface tension impacts the world."

–ELIZABETH PENNISI

CREDITS (TOP TO BOTTOM): MANU PRAKASH AND HARIPRIYA MUKUNDARAJAN; LYDIA BOUROUIBA AND JOHN BUSH/MIT

Published by AAAS

LETTERS

edited by Jennifer Sills

Conserving Carnivores: More than Numbers

IN THEIR REVIEW "STATUS AND ECOLOGICAL EFFECTS OF THE WORLD'S largest carnivores" (10 January, DOI: 10.1126/science.1241484), W. J. Ripple *et al*. assess threats to carnivores and urge that minimum population densities be maintained for persistence of large carnivores, biodiversity, and ecosystem structure. We argue that carnivore conservation is not just a numbers game. Life history strategy (including number of offspring, life span, and diet) and behavioral ecology (behavior that evolves from ecological pressures) of the species in question should also guide management approaches.

For example, in social species, group survival can be critically dependent on maintaining a certain number of individuals within the group (*1*) [to enable cooperative hunting, for example (*2*)]. Consideration of such a threshold, and the risks of falling below it, are often absent from carnivore management programs. Yet this factor may explain the pattern of higher extinction rates in social carnivores, relative to solitary carnivores (*3*). The important contrast between the number of individuals in a population and the number needed to sustain social group persistence could also explain Ripple *et al*.'s observation that solitary pumas are more successful than group-living gray wolves under similar conditions. Indeed, it is thought that the slowed recolonization rates for the gray wolf (*Canis lupis*) in the U.S. Greater Yellowstone ecosystem were due to a lack of mates with which dispersing animals could create new breeding units (*4*).

Diet plays an important role as well. With the exception of one herbivorous panda, only large carnivore species (≥2.4 kg) categorized as strict meat eaters are listed by the International Union for the Conservation of Nature (IUCN) as critically endangered, endangered, or threatened (*5*). In contrast, all insectivores are classified as least-concern. An exclusive meat diet may signal particular vulnerability to human conflict, which is associated with increased likelihood of livestock depredation and/or increased human perceptions of risk. Infectious disease may also present a particular threat to social carnivores as a consequence of increased contact between individuals, disease mortality, and loss of individuals below some critical threshold (*6*).

We urge consideration of life history strategy and social behavior in the development of carnivore management strategy.

KATHLEEN A. ALEXANDER* AND CLAIRE E. SANDERSON

Department of Fisheries and Wildlife Conservation, Virginia Tech University, Blacksburg, VA 24061, USA and CARACAL, Centre for Conservation of African Resources: Animals, Communities, and Land Use, Kasane, Botswana.

*Corresponding author. E-mail: kathyalx@vt.edu

References

1. W. C. Allee, *Animal Aggregations: A Study in General Sociology* (Univ. of Chicago Press, Chicago, 1931).
2. F. Courchamp, D. W. Macdonald, *Anim. Conserv.* **4**, 169 (2001).
3. J. Muñoz-Durán, *Evol. Ecol. Res.* **4**, 963 (2002).
4. A. Hurford, M. Hebblewhite, M. A. Lewis, *Theor. Popul. Biol.* **70**, 244 (2006).
5. The IUCN Red List of Threatened Species (www.iucnredlist.org/).
6. C. E. Sanderson, S. E. Jobbins, K. A. Alexander, *Popul. Ecol.* 1 (October 2013).

Conserving Carnivores: Politics in Play

IN THEIR REVIEW "STATUS AND ECOLOGICAL effects of the world's largest carnivores" (10 January, DOI: 10.1126/science.1241484), W. J. Ripple *et al*. propose the creation of a Global Large Carnivore Initiative (GLCI) endorsed by bold commitments from politicians around the world. However, large carnivores deliver political services in addition to ecological services, and this complication may prevent a GLCI from gaining strong political commitment.

Conflicts involving the political response to large carnivores raise controversial questions about land-use and political economies. The animals serve as a powerful symbol to communicate difficulties (often those that they revealed but did not create) and to influence policies. Opposing the recovery of large carnivores or limiting their populations has therefore become an inexpensive way for politicians to pose as defenders of particular interest groups that they might otherwise ignore.

An illustrative example is the decline of sheep farming in France. French sheep farmers claim that wolf attacks threaten their livelihoods (*1*). However, this story overlooks political factors. In 1985, French Special Forces sank Greenpeace's flagship boat in Auckland harbor to prevent protests against nuclear tests. As part of the compensation, France agreed to not take measures that could hinder the import of New Zealand lambs into the European Union (*2*). This sudden end to France's protectionist standing has been a tough economic challenge for French sheep farming. Since the wolf naturally came back to France from Italy in 1992, some French politicians took the opportunity to stand for national sheep farming by dramatizing the impact of live-

CREDIT: PHOTOS.COM

Downloaded from www.sciencemag.org on March 14, 2014

stock attacks and opposing the wolf return, without addressing the ultimate market-based causes of sheep farming decline. In 2012, wolf-linked subsidies to sheep farming amounted to 8.8 € million (*3*), and data now reveal that sheep farming fares better in wolf regions (*4*).

There are strong political incentives to scapegoat large carnivores. We recommend developing a better understanding of the political ecology of large carnivore conservation.

GUILLAUME CHAPRON[1]* AND JOSÉ VICENTE LÓPEZ-BAO[1,2]

[1]Grimsö Wildlife Research Station, Swedish University of Agricultural Sciences, SE-73091 Riddarhyttan, Sweden. [2]Research Unit of Biodiversity (UO/CSIC/PA), Oviedo University, Mieres, 33600, Spain.

*Corresponding author. E-mail: gchapron@carnivoreconservation.org

References

1. S. Sayare, "As wolves return to French Alps, a way of life is threatened," *New York Times*, 4 September 2013, p. A4.
2. C. Harding, *Singapore Yearbook Int. Law* **10**, 99 (2006); http://cadair.aber.ac.uk/dspace/handle/2160/13189.
3. Ministère de l'Écologie de Développement Durable et de l'Énergie, Ministère de l'Agriculture de l'Agroalimentaire et de la Forêt, "Plan d'Action National Loup 2013–2017" (Paris, 2013); www.loup.developpement-durable.gouv.fr/IMG/pdf/130830_PLAN_LOUP_2013-2.pdf.
4. L. Garde, in *Loup et Élevage: S'Ouvrir à la Complexité: CERPAM—Centre d'Etudes et de Réalisations Pastorales Alpes Méditerranée*, L. Garde, Ed. (CERPAM, Manosque, France, 2007), pp. 14–20.

Obscuring Gender Bias with "Choice"

B. L. BENDERLY'S *SCIENCE* CAREERS ARTICLE "What is keeping women out of leadership jobs in academic medicine?"(7 January, http://scim.ag/1hmBHVl) about a recent report (*1*) misrepresents the study's findings and perpetuates gender biases by framing women's second-place standing in academic medicine as the result of personal choices rather than institutional barriers.

Benderly writes, "Women on medical faculties…may prefer teaching and treating patients to publishing research papers." Yet the report's authors clearly caution that their methods cannot detect whether personal preferences or professional obstacles drive women to the "clinician-educator track" instead of the "traditional tenure track." Benderly offers a similar caveat, but nevertheless concludes by asking whether women's service motivations explain their downshift to the clinician-educator track.

Social psychological research repeatedly demonstrates that institutionalized gender bias hinders women's progress in academic science (including medicine). In a recent experiment, for example, men and women science faculty evaluated a job application from a woman less favorably than the identical application from a man (*2*).

Studies also reveal how attributing workplace inequities to women's preferences distracts observers from unfair institutional practices. One recent article, for instance, showed that professional women who viewed their move to stay-at-home motherhood as a personal choice, as compared to new full-time moms who did not view their move as a choice, less often cited discrimination, harassment, and family-unfriendly policies as sources of gender inequality (*3*). In this same article, undergraduates who incidentally saw a book titled *Choosing to Leave: Women's Experiences Away from the Workforce* more firmly believed that gender discrimination is not a problem than did undergraduates who saw *Women at Home: Experiences Away from the Workforce.* Other studies similarly demonstrate that framing unequal outcomes as the result of individual choices, rather than of institutional or societal forces, deadens empathy and delays action (*4*, *5*).

To help end gender inequities, all publications must take greater care when reporting about women in science.

ALANA L. CONNER,[1]* KAREN S. COOK,[2,3,4] SHELLEY J. CORRELL,[2,5] HAZEL ROSE MARKUS,[1,6] CORINNE A. MOSS-RACUSIN,[7] CAROL B. MULLER,[8] JENNIFER L. RAYMOND,[9,10] CAROLINE SIMARD[10]

[1]Center for Social Psychological Answers to Real-World Questions (SPARQ), Stanford University, Stanford, CA 94305, USA. [2]Department of Sociology, Stanford University, Stanford, CA 94305, USA. [3]Institute for Research in the Social Sciences (IRiSS), Stanford, CA 94305, USA. [4]Office of the Vice Provost for Faculty Development and Diversity, Stanford University, Stanford, CA 94305, USA. [5]Michelle R. Clayman Institute for Research on Gender, Stanford University, Stanford, CA 94305, USA. [6]Department of Psychology, Stanford University, Stanford, CA 94305, USA. [7]Department of Psychology, Skidmore College, Saratoga Springs, NY 12866, USA. [8]Stanford WISE Ventures, Office of the Vice Provost for Faculty Development and Diversity and Office of the Vice Provost for Graduate Education, Stanford University, Stanford, CA 94305, USA. [9]Department of Neurobiology, Stanford University School of Medicine, Stanford, CA 94305, USA. [10]Office of Diversity and Leadership, Stanford University School of Medicine, Stanford, CA 94305, USA.

*Corresponding author. E-mail: alacon@stanford.edu

References

1. A. P. Mayer *et al.*, *Acad. Med.* **89**, 312 (2014).
2. C. A. Moss-Racusin, J. F. Dovidio, V. L. Brescoll, M. J. Graham, J. Handelsman, *Proc. Natl. Acad. Sci. U.S.A.* **109**, 16474 (2012).
3. N. M. Stephens, C. S. Levine, *Psych. Sci.* **22**, 1231 (2011).
4. K. Savani, N. M. Stephens, H. R. Markus, *Psych. Sci.* **22**, 795 (2011).
5. N. M. Stephens, M. G. Hamedani, H. R. Markus, H. B. Bergsieker, L. Eloul, *Psych. Sci.* **20**, 878 (2009).

Response

I BELIEVE THAT CONNER *ET AL*. MISREPRESENT my article and misconstrue my intentions in writing it. Along with them and *Science* Careers, I strongly deplore and oppose bias and discrimination of any kind in science. My colleagues and I work assiduously to help female (and male) scientists and aspiring scientists advance in the careers of their choosing.

In line with that goal, I report on research that helps scientists of both genders understand the career opportunities that currently exist so that they can make choices that maximize their chances of finding and prospering in positions that fit their values, goals, aspirations, and definitions of success. Research (*1*) reveals that scientists value and aspire to a wide range of career goals, with some of both genders desiring traditional academic careers leading to top institutional leadership positions and others desiring to pursue different career objectives both in and out of academe. Evidence both formal (*2*) and anecdotal also shows that many young scientists report feeling strong pressure from their professors and advisers to pursue traditional academic careers in preference to other types of work that they may prefer. The letter writers' use of the term "downshift" to describe a physician's choice to pursue a career of teaching and clinical practice rather than of academic research may in itself exemplify this type of bias.

Contrary to the Letter, I did not conclude—in the sense of arriving at a judgment—that "women's service motivations" keep them from traditional tenure-track careers. As Conner *et al*. acknowledge, I, like the study's (*3*) authors, do not know why women chose as they did. I suggested a possible explanation also mentioned by the authors and ended the article with the authors' own statement that the question "deserves further analysis." I do not believe that this misrepresents their work.

BERYL LIEFF BENDERLY

Science Careers Columnist

References

1. M. Roach, H. Sauermann, *Res. Pol*. **39**, 422 (2010).
2. H. Sauermann, M. Roach, *PLOS ONE* **7**, e36307 (2012).
3. A. P. Mayer *et al.*, *Acad. Med.* **89**, 312 (2014).

Letters to the Editor

Letters (~300 words) discuss material published in *Science* in the past 3 months or matters of general interest. Letters are not acknowledged upon receipt. Whether published in full or in part, Letters are subject to editing for clarity and space. Letters submitted, published, or posted elsewhere, in print or online, will be disqualified. To submit a Letter, go to www.submit2science.org.

Published by AAAS

WOMEN IN SCIENCE

Opening Doors to Engineering

Maria Klawe

Women studying engineering before the 1970s were subject to many annoying assumptions: They were just looking for a husband. Their interest in engineering implied they were unattractive and unfeminine. They didn't deserve to take up a man's spot since they would simply get married and waste their education. And in any case, they wouldn't be any good at engineering. In *Girls Coming to Tech!* Amy Sue Bix offers a fascinating account of how women's enrollment in American undergraduate engineering programs gradually rose and of the many challenges women encountered as students and then professionals.

Historian Bix (Iowa State University) begins by recounting how a handful of individual women "invaded" the masculine world of engineering education in the late 19th and early 20th centuries. A dramatic shift occurred during World War II, when labor shortages led to a government-industry-academia initiative to provide special accelerated engineering training programs for women. Although most of the graduates left technical careers after the war, their success at college and work challenged the belief that women were not capable of learning technical material. That success facilitated women's participation in regular engineering programs, but increases in women's enrollment remained low for many years. After peaking at 20.9% in 2002, women's percentage of bachelor degrees from U.S. engineering programs has slipped back to 18% to 19%. Doubts about whether they belong in engineering still discourage many young women.

Bix provides detailed case studies of three high-profile universities: MIT, Georgia Tech, and Caltech. Although MIT has been coeducational since the 1870s, until World War II female students seldom composed much more than 1% of the student body. Some faculty, administrators, and male students felt that an MIT education was wasted on women. With limited housing for women students, female applicants were evaluated more selectively than males. This barrier was initially addressed in 1960, when alumna Katherine McCormick donated $1.5 million to build the first on-campus women's dorm. But housing limits remained a de facto quota on the number of women admitted until 1969. The chief proponents of women's engineering education at MIT in the late 1960s and 1970s were a few of the first female faculty: Emily Wick, Mildred Dresselhaus, Vera Kistiakowsky, and Sheila Widnall. Together with female students, they worked to change the MIT environment, addressing sexual harassment and the many negative comments encountered in classroom and labs.

Girls Coming to Tech!
A History of American Engineering Education for Women

by Amy Sue Bix
MIT Press, Cambridge, MA, 2014. 372 pp. $34, £23.95. ISBN 9780262019545. Engineering Studies.

Although a public institution (unlike MIT and Caltech), Georgia Tech was all-male until 1952 (with the exception of special wartime programs for women). Women often expressed interest in enrolling in Georgia Tech's regular programs, because it was the only institution in the state offering engineering and architecture degrees and was more affordable than out-of-state schools. After being denied entrance in 1943, Anne Bonds began attending Alabama Polytechnic Institute (now Auburn University) but petitioned the University System Board of Regents to make Georgia Tech coeducational. Lobbying by the Georgia Federation of Business and Professional Women's Clubs and Blake Van Leer's arrival as president in 1944 started serious discussions about the feasibility of coeducation. This surprised most students, who strongly identified with the single-sex climate and the masculine nature of engineering. Although the 1885 act establishing Georgia Tech did not bar female students, in 1947 the regents declined a coeducation proposal, citing overcrowding and the lack of appropriate facilities (e.g., housing and bathrooms).

In 1952, the Atlanta Women's Chamber of Commerce urged the regents to end the ban on women. This time, the regents referred the petition to Van Leer, who then surveyed students, faculty, alumni, and administrators. The student council voted 13 to 9 in favor of admitting women, despite dissent from many students who felt a vast majority were against the change because it would result in lowered standards and impaired classroom discussions. Administrators, more positive, hoped that adding women would cushion the steep, post–GI Bill drop in enrollment. After much heated debate, the regents agreed to admit females, although with a number of caveats. Women could only major in programs not available at any other Georgia state university, and no courses were to be designed primarily for them.

Caltech's story has a different twist. Founded (1891) as Throop University, a coeducational institution for manual training and basic education from fifth grade through college, it reinvented itself several years later as all-male Throop College of Technology (with a mission of intellectual excellence) and then assumed its current name in 1921. In the 1960s, the undergraduates began lobbying the administration to admit women, believing that this would promote the "humanization of students." Students complained of a sterile curriculum and social wasteland that created "eunuchs of science." After a 1967 national survey of rising sophomores revealed that Caltech students were much less happy with campus life than those elsewhere, an ad hoc faculty committee examined student experiences during their first two years. The committee soon recommended that Caltech admit female undergraduates, arguing that discrimination against women is "morally unjustifiable." A student poll in

CREDIT: COURTESY MIT MUSEUM

On the leading edge of a wave. The 25 women who entered MIT's class of 1964 matched the graduation rate of their 874 male classmates.

The reviewer is at Harvey Mudd College, Claremont, CA 91711, USA. E-mail: klawe@hmc.edu

Downloaded from www.sciencemag.org on March 14, 2014

Published by AAAS

fall 1967 found 79% supported that change, and a month later the Faculty Board voted 50 to 10 to recommend to the administration and trustees to "proceed with all deliberate speed toward the admission of women undergraduates." In fall 1970, 30 women started at Caltech as first-year students; 27 completed their degrees.

Bix provides detailed descriptions of how each of the three institutions gradually realized that admitting a small number of female students was not enough to ensure that they thrived academically and socially. From today's perspective, it seems obvious that immersing young women in an intense, stressful curriculum accompanied by a deeply masculine culture in which some faculty and many students questioned their ability and motives—while limited access to housing and bathrooms added further inconvenience and isolation—would prove difficult for many. MIT, for example, had years when only half the female first-year students survived to become sophomores. Over time, each institution provided more support to improve the learning and social environments for female undergraduates and made raising the number of female engineering students to "critical mass" a priority. Today, females compose close to 50% of the undergraduates at MIT, and a higher percentage of them complete their degree than do males.

Harvey Mudd College has its own story of "girls coming to tech." Founded in 1955 as the "science and engineering" Claremont College, its initial board questioned whether it should be coeducational. One trustee asked the founding president, Joe Platt, "Who would marry a female mathematician?" Joe's answer was "I did!" As a compromise, Mudd opened coeducational but with female enrollment capped at 11% to ensure that there was no lowering of admission standards. The cap wasn't removed until 1971, when the percentage of female students was nearing the limit. When I arrived at Mudd in 2006, just under a third of our students were female. Today about 46%, and more than half (54%) of our engineering seniors, are. Just as at other institutions, this progress was gained through great work by faculty, staff, students, alumni, and trustees to create a learning community where everyone thrives.

As someone who has been the "first female to hold my position" for more than 25 years, I appreciate the level of care and detail that Bix invests in *Girls Coming to Tech!* Despite the topic being an area of intense interest for me, I learned a great deal from her account.

10.1126/science.1251167

ASTRONOMY

Reading Clues in the Sky

Eric L. Altschuler

Celestial Sleuth
Using Astronomy to Solve Mysteries in Art, History and Literature
by Donald W. Olson
Springer, New York, 2014. 373 pp. Paper, 39.99. ISBN 9781461484028. Springer-Praxis Books in Popular Astronomy.

While in medical school, I made a long journey from sunny California to a conference in frigid Montreal. My budget prevented me from attending the conference's night on the town event, so I opted for a neighborhood bookstore. Splurging on a hot chocolate, I settled down in the warmest spot in the store to read an article in *Sky & Telescope* magazine about a star in Shakespeare's *Hamlet* (*1*). Over the years, its author, Donald Olson, with colleagues and students, has published many *Sky & Telescope* articles that use astronomy to explore mysteries from history, art, and literature. Olson (a physicist at Texas State University) has now collected these and additional pieces in *Celestial Sleuth*.

The first section of this enjoyable and thought-provoking book explores where and when artists such as J. M. W. Turner, Claude Monet, Vincent van Gogh, and Edvard Munch painted some of their classic works. Olson discusses how astronomical events played crucial roles in battles of the United States Revolutionary and Civil Wars and World War II. In the section on celestial events that may have inspired passages in literature, we learn of Geoffrey Chaucer's astronomical prowess. Among the many astronomical references in James Joyce's *Ulysses*, Olson discovers an observation of an astronomical phenomenon that would not be reported in the scientific literature for 60 years.

Olson's methods are often deftly simple: e.g., cross-checking historical accounts and meteorological reports with recreations of the sky around the time under investigation. In some cases, Olson and collaborators travel to locations they are studying to see the sky for themselves. They also use understandings of the Moon's brightness patterns and effects on tides to great benefit.

Shakespeare's plays include many mentions of things astronomical: for example, comets, eclipses, conjunctions of planets, and that Venus can appear as a morning or evening star. And there is that star Bernardo sights in the opening scene of *Hamlet*:

> *Last night of all,*
> *When yond same star that's westward from the pole*
> *Had made his course t'illume that part of heaven*
> *Where now it burns, Marcellus and myself,*
> *The bell then beating one,*

Internal evidence in the play suggests November as the month. Prior suggestions for the identity of Bernardo's star include stars from the constellations Ursa Major, Ursa Minor, Vega, Deneb, and Capella. But as Olson and his team calculated, none of these constellations would appear west of the pole at 1 a.m. in the November sky of 16th-century Denmark. They note that the constellation Cassiopeia is in the right place, but none of its stars are particularly bright. However, a "new star" first observed in Europe in November 1572 did appear burning brightly in Cassiopeia—supernova 1572A, studied most extensively and famously by Danish astronomer Tycho Brahe. (Interestingly, the names "Rosenkrans" and "Guldensteren"—Rosencrantz and Guildenstern from the play?—appear in a portrait of Tycho surrounded by coats-of-arms of his relatives.) So Olson and colleagues conclude that Shakespeare was keenly interested in the striking astrophysical event.

If you love astronomy, art, history, or literature you will enjoy *Celestial Sleuth* and probably want to give it to teachers, students, friends, and family. Further, you may find Olson's ingenious methods seeping into your own next experiment or analysis.

References

1. D. W. Olson, M. S. Olson, R. L. Doescher, *Sky Telescope* **96**, 68 (1998).

10.1126/science.1252465

The reviewer is at the Department of Physical Medicine and Rehabilitation, Rutgers New Jersey Medical School, Newark, NJ 07103–2499, USA. E-mail: altschel@njms.rutgers.edu

Published by AAAS

BIG DATA

The Parable of Google Flu: Traps in Big Data Analysis

Large errors in flu prediction were largely avoidable, which offers lessons for the use of big data.

David Lazer,[1,2]* Ryan Kennedy,[1,3,4] Gary King,[3] Alessandro Vespignani[5,6,3]

In February 2013, Google Flu Trends (GFT) made headlines but not for a reason that Google executives or the creators of the flu tracking system would have hoped. *Nature* reported that GFT was predicting more than double the proportion of doctor visits for influenza-like illness (ILI) than the Centers for Disease Control and Prevention (CDC), which bases its estimates on surveillance reports from laboratories across the United States (*1*, *2*). This happened despite the fact that GFT was built to predict CDC reports. Given that GFT is often held up as an exemplary use of big data (*3*, *4*), what lessons can we draw from this error?

The problems we identify are not limited to GFT. Research on whether search or social media can predict *x* has become commonplace (*5*–*7*) and is often put in sharp contrast with traditional methods and hypotheses. Although these studies have shown the value of these data, we are far from a place where they can supplant more traditional methods or theories (*8*). We explore two issues that contributed to GFT's mistakes—big data hubris and algorithm dynamics—and offer lessons for moving forward in the big data age.

Big Data Hubris

"Big data hubris" is the often implicit assumption that big data are a substitute for, rather than a supplement to, traditional data collection and analysis. Elsewhere, we have asserted that there are enormous scientific possibilities in big data (*9*–*11*). However, quantity of data does not mean that one can ignore foundational issues of measurement and construct validity and reliability and dependencies among data (*12*). The core challenge is that most big data that have received popular attention are not the output of instruments designed to produce valid and reliable data amenable for scientific analysis.

The initial version of GFT was a particularly problematic marriage of big and small data. Essentially, the methodology was to find the best matches among 50 million search terms to fit 1152 data points (*13*). The odds of finding search terms that match the propensity of the flu but are structurally unrelated, and so do not predict the future, were quite high. GFT developers, in fact, report weeding out seasonal search terms unrelated to the flu but strongly correlated to the CDC data, such as those regarding high school basketball (*13*). This should have been a warning that the big data were overfitting the small number of cases—a standard concern in data analysis. This ad hoc method of throwing out peculiar search terms failed when GFT completely missed the nonseasonal 2009 influenza A–H1N1 pandemic (*2*, *14*). In short, the initial version of GFT was part flu detector, part winter detector. GFT engineers updated the algorithm in 2009, and this model has run ever since, with a few changes announced in October 2013 (*10*, *15*).

Although not widely reported until 2013, the new GFT has been persistently overestimating flu prevalence for a much longer time. GFT also missed by a very large margin in the 2011–2012 flu season and has missed high for 100 out of 108 weeks starting with August 2011 (see the graph). These errors are not randomly distributed. For example, last week's errors predict this week's errors (temporal autocorrelation), and the direction and magnitude of error varies with the time of year (seasonality). These patterns mean that GFT overlooks considerable information that could be extracted by traditional statistical methods.

Even after GFT was updated in 2009, the comparative value of the algorithm as a stand-alone flu monitor is questionable. A study in 2010 demonstrated that GFT accuracy was not much better than a fairly simple projection forward using already available (typically on a 2-week lag) CDC data (*4*). The comparison has become even worse since that time, with lagged models significantly outperforming GFT (see the graph). Even 3-week-old CDC data do a better job of projecting current flu prevalence than GFT [see supplementary materials (SM)].

Considering the large number of approaches that provide inference on influenza activity (*16*–*19*), does this mean that the current version of GFT is not useful? No, greater value can be obtained by combining GFT with other near–real-time health data (*2*, *20*). For example, by combining GFT and lagged CDC data, as well as dynamically recalibrating GFT, we can substantially improve on the performance of GFT or the CDC alone (see the chart). This is no substitute for ongoing evaluation and improvement, but, by incorporating this information, GFT could have largely healed itself and would have likely remained out of the headlines.

[1]Lazer Laboratory, Northeastern University, Boston, MA 02115, USA. [2]Harvard Kennedy School, Harvard University, Cambridge, MA 02138, USA. [3]Institute for Quantitative Social Science, Harvard University, Cambridge, MA 02138, USA. [4]University of Houston, Houston, TX 77204, USA. [5]Laboratory for the Modeling of Biological and Sociotechnical Systems, Northeastern University, Boston, MA 02115, USA. [6]Institute for Scientific Interchange Foundation, Turin, Italy. *Corresponding author. E-mail: d.lazer@neu.edu.

CREDIT: ADAPTED FROM AXEL KORES/DESIGN & ART DIRECTION/ISTOCKPHOTO.COM

Downloaded from www.sciencemag.org on March 14, 2014

Published by AAAS

Algorithm Dynamics

All empirical research stands on a foundation of measurement. Is the instrumentation actually capturing the theoretical construct of interest? Is measurement stable and comparable across cases and over time? Are measurement errors systematic? At a minimum, it is quite likely that GFT was an unstable reflection of the prevalence of the flu because of algorithm dynamics affecting Google's search algorithm. Algorithm dynamics are the changes made by engineers to improve the commercial service and by consumers in using that service. Several changes in Google's search algorithm and user behavior likely affected GFT's tracking. The most common explanation for GFT's error is a media-stoked panic last flu season (*1*, *15*). Although this may have been a factor, it cannot explain why GFT has been missing high by wide margins for more than 2 years. The 2009 version of GFT has weathered other media panics related to the flu, including the 2005–2006 influenza A/H5N1 ("bird flu") outbreak and the 2009 A/H1N1 ("swine flu") pandemic. A more likely culprit is changes made by Google's search algorithm itself.

The Google search algorithm is not a static entity—the company is constantly testing and improving search. For example, the official Google search blog reported 86 changes in June and July 2012 alone (SM). Search patterns are the result of thousands of decisions made by the company's programmers in various subunits and by millions of consumers worldwide.

There are multiple challenges to replicating GFT's original algorithm. GFT has never documented the 45 search terms used, and the examples that have been released appear misleading (*14*) (SM). Google does provide a service, Google Correlate, which allows the user to identify search data that correlate with a given time series; however, it is limited to national level data, whereas GFT was developed using correlations at the regional level (*13*). The service also fails to return any of the sample search terms reported in GFT-related publications (*13*, *14*).

Nonetheless, using Google Correlate to compare correlated search terms for the GFT time series to those returned by the CDC's data revealed some interesting differences. In particular, searches for treatments for the flu and searches for information on differentiating the cold from the flu track closely with GFT's errors (SM). This points to the possibility that the explanation for changes in relative search behavior is "blue team" dynamics—where the algorithm producing the data (and thus user utilization) has been modified by the service provider in accordance with their business model. Google reported in June 2011 that it had modified its search results to provide suggested additional search terms and reported again in February 2012 that it was now returning potential diagnoses for searches including physical symptoms like "fever" and "cough" (*21*, *22*). The former recommends searching for treatments of the flu in response to general flu inquiries, and the latter may explain the increase in some searches to distinguish the flu from the common cold. We document several other changes that may have affected GFT (SM).

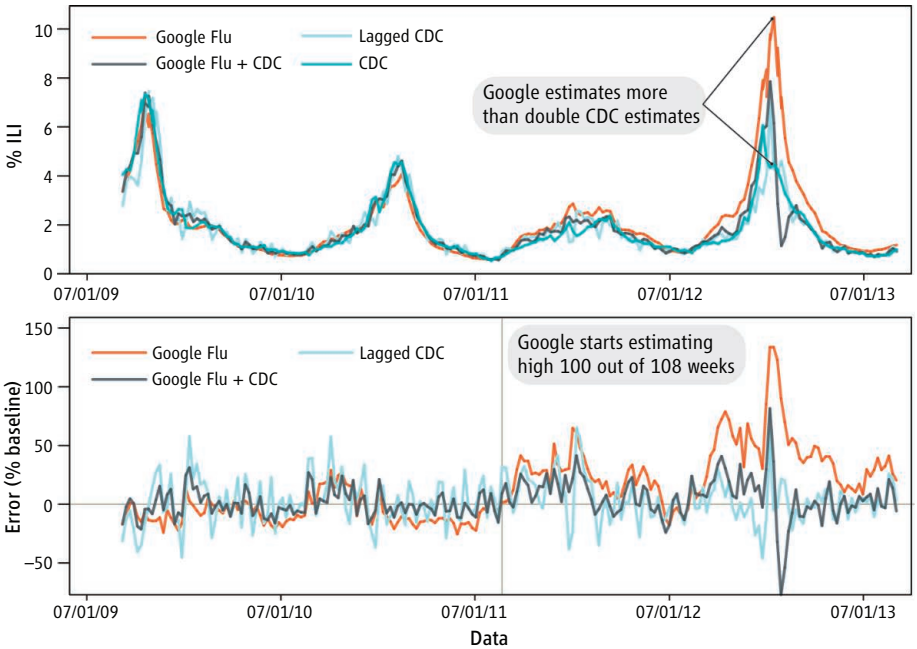

GFT overestimation. GFT overestimated the prevalence of flu in the 2012–2013 season and overshot the actual level in 2011–2012 by more than 50%. From 21 August 2011 to 1 September 2013, GFT reported overly high flu prevalence 100 out of 108 weeks. (**Top**) Estimates of doctor visits for ILI. "Lagged CDC" incorporates 52-week seasonality variables with lagged CDC data. "Google Flu + CDC" combines GFT, lagged CDC estimates, lagged error of GFT estimates, and 52-week seasonality variables. (**Bottom**) Error [as a percentage [[Non-CDC estmate)−(CDC estimate)]/(CDC) estimate)]. Both alternative models have much less error than GFT alone. Mean absolute error (MAE) during the out-of-sample period is 0.486 for GFT, 0.311 for lagged CDC, and 0.232 for combined GFT and CDC. All of these differences are statistically significant at $P < 0.05$. See SM.

In improving its service to customers, Google is also changing the data-generating process. Modifications to the search algorithm are presumably implemented so as to support Google's business model—for example, in part, by providing users useful information quickly and, in part, to promote more advertising revenue. Recommended searches, usually based on what others have searched, will increase the relative magnitude of certain searches. Because GFT uses the relative prevalence of search terms in its model, improvements in the search algorithm can adversely affect GFT's estimates. Oddly, GFT bakes in an assumption that relative search volume for certain terms is statically related to external events, but search behavior is not just exogenously determined, it is also endogenously cultivated by the service provider.

Blue team issues are not limited to Google. Platforms such as Twitter and Facebook are always being re-engineered, and whether studies conducted even a year ago on data collected from these platforms can be replicated in later or earlier periods is an open question.

Although it does not appear to be an issue in GFT, scholars should also be aware of the potential for "red team" attacks on the systems we monitor. Red team dynamics occur when research subjects (in this case Web searchers) attempt to manipulate the data-generating process to meet their own goals, such as economic or political gain. Twitter polling is a clear example of these tactics. Campaigns and companies, aware that news media are monitoring Twitter, have used numerous tactics to make sure their candidate or product is trending (*23*, *24*).

Similar use has been made of Twitter and Facebook to spread rumors about stock prices and markets. Ironically, the more successful we become at monitoring the behavior of people using these open sources of information, the more tempting it will be to manipulate those signals.

Published by AAAS

Transparency, Granularity, and All-Data

The GFT parable is important as a case study where we can learn critical lessons as we move forward in the age of big data analysis.

Transparency and Replicability. Replication is a growing concern across the academy. The supporting materials for the GFT-related papers did not meet emerging community standards. Neither were core search terms identified nor larger search corpus provided. It is impossible for Google to make its full arsenal of data available to outsiders, nor would it be ethically acceptable, given privacy issues. However, there is no such constraint regarding the derivative, aggregated data. Even if one had access to all of Google's data, it would be impossible to replicate the analyses of the original paper from the information provided regarding the analysis. Although it is laudable that Google developed Google Correlate ostensibly from the concept used for GFT, the public technology cannot be utilized to replicate their findings. Clicking the link titled "match the pattern of actual flu activity (this is how we built Google Flu Trends!)" will not, ironically, produce a replication of the GFT search terms (*14*). Oddly, the few search terms offered in the papers (*14*) do not seem to be strongly related with either GFT or the CDC data (SM)—we surmise that the authors felt an unarticulated need to cloak the actual search terms identified.

What is at stake is twofold. First, science is a cumulative endeavor, and to stand on the shoulders of giants requires that scientists be able to continually assess work on which they are building (*25*). Second, accumulation of knowledge requires fuel in the form of data. There is a network of researchers waiting to improve the value of big data projects and to squeeze more actionable information out of these types of data. The initial vision regarding GFT—that producing a more accurate picture of the current prevalence of contagious diseases might allow for life-saving interventions—is fundamentally correct, and all analyses suggest that there is indeed valuable signal to be extracted.

Google is a business, but it also holds in trust data on the desires, thoughts, and the connections of humanity. Making money "without doing evil" (paraphrasing Google's motto) is not enough when it is feasible to do so much good. It is also incumbent upon academia to build institutional models to facilitate collaborations with such big data projects—something that is too often missing now in universities (*26*).

Use Big Data to Understand the Unknown. Because a simple lagged model for flu prevalence will perform so well, there is little room for improvement on the CDC data for model projections [this does not apply to other methods to directly measure flu prevalence, e.g., (*20*, *27*, *28*)]. If you are 90% of the way there, at most, you can gain that last 10%. What is more valuable is to understand the prevalence of flu at very local levels, which is not practical for the CDC to widely produce, but which, in principle, more finely granular measures of GFT could provide. Such a finely granular view, in turn, would provide powerful input into generative models of flu propagation and more accurate prediction of the flu months ahead of time (*29*–*33*).

Study the Algorithm. Twitter, Facebook, Google, and the Internet more generally are constantly changing because of the actions of millions of engineers and consumers. Researchers need a better understanding of how these changes occur over time. Scientists need to replicate findings using these data sources across time and using other data sources to ensure that they are observing robust patterns and not evanescent trends. For example, it is eminently feasible to do controlled experiments with Google, e.g., looking at how Google search results will differ based on location and past searches (*34*). More generally, studying the evolution of socio-technical systems embedded in our societies is intrinsically important and worthy of study. The algorithms underlying Google, Twitter, and Facebook help determine what we find out about our health, politics, and friends.

It's Not Just About Size of the Data. There is a tendency for big data research and more traditional applied statistics to live in two different realms—aware of each other's existence but generally not very trusting of each other. Big data offer enormous possibilities for understanding human interactions at a societal scale, with rich spatial and temporal dynamics, and for detecting complex interactions and nonlinearities among variables. We contend that these are the most exciting frontiers in studying human behavior. However, traditional "small data" often offer information that is not contained (or containable) in big data, and the very factors that have enabled big data are enabling more traditional data collection. The Internet has opened the way for improving standard surveys, experiments, and health reporting (*35*). Instead of focusing on a "big data revolution," perhaps it is time we were focused on an "all data revolution," where we recognize that the critical change in the world has been innovative analytics, using data from all traditional and new sources, and providing a deeper, clearer understanding of our world.

References and Notes

1. D. Butler, *Nature* **494**, 155 (2013).
2. D. R. Olson *et al.*, *PLOS Comput. Biol.* **9**, e1003256 (2013).
3. A. McAfee, E. Brynjolfsson, *Harv. Bus. Rev.* **90**, 60 (2012).
4. S. Goel *et al.*, *Proc. Natl. Acad. Sci. U.S.A.* **107**, 17486 (2010).
5. A. Tumasjan *et al.*, in *Proceedings of the 4th International AAAI Conference on Weblogs and Social Media*, Atlanta, Georgia, 11 to 15 July 2010 (Association for Advancement of Artificial Intelligence, 2010), pp. 178.
6. J. Bollen *et al.*, *J. Comput. Sci.* **2**, 1 (2011).
7. F. Ciulla *et al.*, *EPJ Data Sci.* **1**, 8 (2012).
8. P. T. Metaxas *et al.*, in *Proceedings of PASSAT—IEEE Third International Conference on Social Computing*, Boston, MA, 9 to 11 October 2011 (IEEE, 2011), pp. 165; doi:10.1109/PASSAT/SocialCom.2011.98.
9. D. Lazer *et al.*, *Science* **323**, 721 (2009).
10. A. Vespignani, *Science* **325**, 425 (2009).
11. G. King, *Science* **331**, 719 (2011).
12. D. Boyd, K. Crawford *Inform. Commun. Soc.* **15**, 662 (2012).
13. J. Ginsberg *et al.*, *Nature* **457**, 1012 (2009).
14. S. Cook *et al.*, *PLOS ONE* **6**, e23610 (2011).
15. P. Copeland *et al.*, *Int. Soc. Negl. Trop. Dis.* **2013**, 3 (2013).
16. C. Viboud *et al.*, *Am. J. Epidemiol.* **158**, 996 (2003).
17. W. W. Thompson *et al.*, *J. Infect. Dis.* **194** (Suppl. 2), S82–S91 (2006).
18. I. M. Hall *et al.*, *Epidemiol. Infect.* **135**, 372 (2007).
19. J. B. S. Ong *et al.*, *PLOS ONE* **5**, e10036 (2010).
20. J. R. Ortiz *et al.*, *PLOS ONE* **6**, e18687 (2011).
21. Organizing lists of related searches, Google; http://insidesearch.blogspot.com/2011/06/organizing-lists-of-related-searches_16.html.
22. Improving health searches, because your health matters, Google; http://insidesearch.blogspot.com/2012/02/improving-health-searches-because-your.html.
23. E. Mustafaraj, P. Metaxas, in *Proceedings of the WebSci10*, Raleigh, NC, 26 and 27 April 2010 (Web Science Trust, 2010); http://journal.webscience.org/317/.
24. J. Ratkiewicz *et al.*, in *Proceedings of 5th International AAAI Conference on Weblogs and Social Media*, San Francisco, CA, 7 to 11 August 2011 (AAAI, 2011), p. 297–304.
25. G. King, *PS Polit. Sci. Polit.* **28**, 443 (1995).
26. P. Voosen, *Chronicle of Higher Education*, 13 September 2013; http://chronicle.com/article/Researchers-Struggle-to-Secure/141591/.
27. R. Lazarus *et al.*, *BMC Public Health* **1**, 9 (2001).
28. R. Chunara *et al.*, *Online J. Public Health Inform.* **5**, e133 (2013).
29. D. Balcan *et al.*, *Proc. Natl. Acad. Sci. U.S.A.* **106**, 21484 (2009).
30. D. L. Chao *et al.*, *PLOS Comput. Biol.* **6**, e1000656 (2010).
31. J. Shaman, A. Karspeck, *Proc. Natl. Acad. Sci. U.S.A.* **109**, 20425 (2012).
32. J. Shaman *et al.*, *Nat. Commun.* **4**, 2837 (2013).
33. E. O. Nsoesie *et al.*, *PLOS ONE* **8**, e67164 (2013).
34. A. Hannak *et al.*, in *Proceedings of the 22nd International World Wide Web Conference*, Rio de Janeiro, 13 to 17 May 2013 (Association for Computing Machinery, New York, 2013), pp. 527–538.
35. A. J. Berinsky *et al.*, *Polit. Anal.* **20**, 351–368 (2012).

Acknowledgments: This research was funded, in part, by NSF grant no. 1125095 Army Research Office (ARO) grant no. W911NF-12-1-0556, and, in part, by the Intelligence Advanced Research Projects Activity (IARPA) via Department of Interior National Business Center (DoI/NBC) contract D12PC00285. The views and conclusions contained herein are those of the authors and should not be interpreted as necessarily representing the official policies or endorsements, either expressed or implied, of the NSF ARO/IARPA, DoI/NBE, or the U.S. government. See SM for data and methods.

Supplementary Materials

www.sciencemag.org/content/343/6176/page/suppl/DC1

10.1126/science.1248506

Published by AAAS

CLIMATE CHANGE

Simplicity Amid Complexity

Despite the complexity of Earth's climate system, the influence of human activities on climate can be identified and predicted.

Isaac Held

We live in interesting times as we watch diverse effects of human activities on Earth's climate emerge from natural variability. In predicting the outcome of this evolving inadvertent experiment, climate science faces many challenges, some of which have been outlined in this series of *Science* Perspectives (*1*–*6*): reducing the uncertainty in climate sensitivity; explaining the recent slowdown in the rate of warming and its implications for understanding internal variability; uncovering the factors that control how and where the land will become drier as it warms; quantifying the cooling due to anthropogenic aerosols; explaining the curious evolution of atmospheric methane; and predicting changes in extreme weather. In addition to these challenges, the turbulent and chaotic atmospheric and oceanic flows seemingly limit predictability on various time scales. Is the climate system just too complex for useful prediction?

One response to the claim that multidecadal prediction is futile is to point to progress on each of these challenges (*1*–*6*). More fundamentally, an emphasis on complexity in the climate system must be balanced by recognition of emergent simplicity. The seasonal cycle provides a useful counterpoint. An individual year's temperature record is a consequence of chaotic weather superposed on a relatively simple and smooth underlying cycle. Watching temperatures change during a few weeks in the spring does not affect confidence that typical summer temperatures will eventually emerge. Climate models paint an analogous picture for the evolution of climate over decades to centuries: a superposition of internal variability and an externally forced component containing a natural part (solar variations and volcanoes) and a part due to human activities that, to first approximation, is a linear superposition of responses to different forcing agents such as CO_2, methane, and aerosols.

Unlike students of the seasonal cycle, students of climate change do not have the luxury of studying multiple realizations of their experiment, but can only observe the initial stages of a single realization. Thus, the attribution problem—the separation of the forced change from internal variability in observations and the partitioning of this forced component into parts due to different agents such as the well-mixed greenhouse gases or aerosols—is a tough challenge. But attribution leads directly to prediction of the forced response if the case can be made that the response is simple enough for past trends to strongly constrain future evolution.

Basing decisions on predictions of forced climate change is formally analogous to using knowledge of the normal climatological seasonal cycle to inform vacation plans, ignoring any weather predictions. Of course, we have much greater confidence in our knowledge of the climatological seasonal cycle than in predictions of forced climate change. The challenge to climate change research is to increase the credibility of the forced responses that theories and models predict, and to characterize internal variability well enough to appreciate which aspects of these forced response have already emerged from the background of internal variability and which are likely to emerge in the future. Any skill in predicting multidecadal internal variability on top of this forced response is icing on the cake.

Any strong nonlinearity in the forced response or abrupt shifts in the climate would provide special challenges. For example, suppose a model predicts distinctive atmospheric circulations and feedbacks to arise in an ice-free Arctic that have no close counterpart before that threshold is passed (*7*). What will provide credibility to a prediction of an abrupt forced climate change of this type, or the credibility of any prediction P that is not backed by attribution of recent trends? Paleoclimate reconstructions should provide some guidance and perhaps even close analogs. But, ultimately, it may just be necessary to rely on understanding the underlying physics. For example, suppose one can argue, based on this understanding, that some other aspect O of the climate depends on the same processes that come into play in the climate change P. If observations exist to evaluate the simulation of O, the result will be indirect evidence for P. This approach is being explored in several climate change contexts (*8*).

The models used to simulate the climate are themselves complex, chaotic dynamical systems. To work with them effectively requires not only the careful examination of alternative formulations of these comprehensive models but also the construction of a hierarchy of models in which elements of complexity are added sequentially. This approach is similar in spirit to that used in biology, where a hierarchy of model organisms—from bacteria to fruit fly to zebrafish to mouse to chimpanzee—is used to build an understanding of human biology (*9*).

A good example of the use of a hierarchy of models is provided by research on the

NOAA–Geophysical Fluid Dynamics Laboratory, Forrestal Campus, Princeton, NJ 08540, USA. E-mail: isaac.held@noaa.gov

CREDIT: PETER AND MARIA HOEY/WWW.PETERHOEY.COM

Published by AAAS

effect of the Antarctic ozone hole on the surface westerlies in the Southern Hemisphere. Observational studies showed that the westerlies shifted poleward by several degrees of latitude in recent decades, mainly in the Austral summer, and made a plausible connection to the development of the ozone hole (*10*). Comprehensive models provided important confirmation that the ozone hole does move the westerlies poleward (*11*). A variety of more idealized models are being used to explore the pathways through which changes in the stratosphere modify the surface winds, demonstrating that the poleward shift of the westerlies due to cooling of the polar stratosphere can be isolated from other parts of the climate problem and related to fundamental theories of atmospheric dynamics (*12*).

Increasing CO_2 concentrations also push the mid-latitude surface westerlies poleward in climate models, complicating both the quantitative attribution of the observed shift (*11*) and the predictions of how the westerlies will evolve in the future as the ozone hole heals and greenhouse gases continue to accumulate. However, both comprehensive and idealized climate models indicate that the effects on the westerlies of greenhouse gases and the ozone hole are linearly additive to a first approximation. An underlying simplicity in the forced climate change emerges here as well, making prediction plausible.

A creative tension between simulation and understanding, between accepting complexity and searching for simplicity, is present in many challenging scientific problems. Climate science provides an excellent example of this tension. The most advanced comprehensive climate models effectively represent the current ability to simulate the climate system, and it is natural and appropriate to take the output of those models as the basis for predicting the future climate. However, it is the understanding of these responses—an understanding that depends on the presence of an emergent simplicity in the forced response—which provides a level of confidence that justifies advising policy-makers and the public to pay heed to these predictions.

References

1. G. Hegerl, P. Stott, *Science* **343**, 844 (2014).
2. A. Clement, P. DiNezio, *Science* **343**, 976 (2014).
3. S. Sherwood, Q. Fu, *Science* **343**, 737 (2014).
4. D. Rosenfeld, S. Sherwood, R. Wood, L. Donner, *Science* **343**, 379 (2014).
5. E. G. Nisbet, E. J. Dlugokencky, P. Bousquet, *Science* **343**, 493 (2014).
6. G. A. Vecchi, G. Villarini, *Science* **343**, 618 (2014).
7. D. S. Abbott, E. Tziperman, *J. Atmos. Sci.* **66**, 519 (2009).
8. S. C. Sherwood, S. Bony, J.-L. Dufresne, *Nature* **505**, 37 (2014).
9. I. M. Held, *Bull. Am. Meteorol. Soc.* **86**, 1609 (2005).
10. D. W. J. Thompson, S. Solomon, *Science* **296**, 895 (2002).
11. S.-W. Son *et al.*, *J. Geophys. Res.* **115**, D00M07 (2010).
12. C. I. Garfinkel, D.-Y. Waugh, E. P. Gerber, *J. Clim.* **26**, 2077 (2013).

10.1126/science.1248447

MOLECULAR BIOLOGY

Internal mRNA Methylation Finally Finds Functions

Methylation of internal adenosine residues in messenger RNA (mRNA) modulates mRNA metabolism in both the nucleus and cytoplasm.

Timothy W. Nilsen

Modification of internal adenosines in messenger RNA (mRNA) by methylation of the N^6 position (m^6A) was first observed almost four decades ago. Early work demonstrated that the m^6A modification was quite common, occurring at an estimated frequency of three to five residues per mRNA. Nevertheless, the function, if any, of this modification remained enigmatic. The cloning in 1997 of a subunit of the RNA methylase complex (*1*) was followed by a period of fitful inactivity before the field reawakened in 2011 with the discovery of an enzyme, FTO (fat mass and obesity-associated protein), that was shown to catalyze the demethylation of internal m^6A residues (*2*). The existence of a demethylase and the demonstration that m^6A levels were raised when the enzyme was knocked down strongly suggested that at least some m^6A modifications were reversible and might be subject to dynamic regulation. Since then, a series of papers have appeared in rapid succession, together providing a wealth of unequivocal evidence for m^6A function. But these findings still have not led to a coherent picture of the number and variety of functions of the m^6A modification.

Two recent RNA "methylome" studies (*3*, *4*) provide a transcriptome-wide map of m^6A-modified mRNAs. Both report the presence of m^6A in about 7000 mRNAs, indicating that the modification is fairly promiscuous with regard to mRNA targets. However, methylation is highly selective when considering which specific sites are modified. Although both studies showed that methylation sites are largely confined to the consensus sequence Pu[G>A]m^6AC[A/C/U], only about 10% of sites conforming to this consensus are actually modified. Neither study was able to determine the stoichiometry of any specific modified site, nor could clusters of modified sites be identified. Both studies showed enrichment of modification sites near stop codons; however, one study saw enrichment in long internal exons while the other saw enrichment in 3′ untranslated regions. Additionally, one study found elevated levels of m^6A in the brain and the other study did not. The reasons for these discrepancies are not obvious. Nevertheless, both studies found that modification sites were well conserved between human and mouse transcriptomes—a finding strongly suggestive of biological function. Indeed, knockdown of the m^6A methylase (*3*) resulted in large-scale alterations in splicing patterns, consistent with a striking enrichment of m^6A modifications within alternatively spliced exons (see the figure), with constitutive

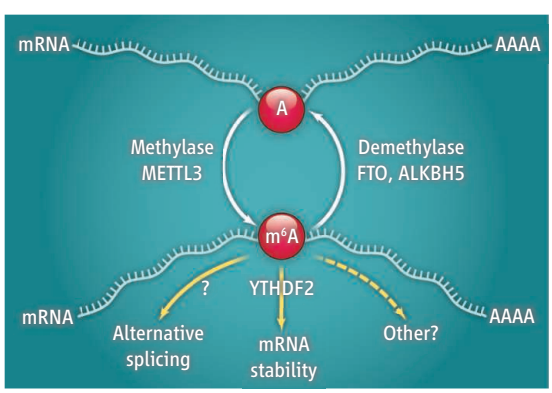

Methylating RNA regulates its function. A schematic diagram of the RNA m^6A methylation cycle. METTL3, methyltransferase-like 3.

Center for RNA Molecular Biology, Case Western Reserve University School of Medicine, 10900 Euclid Avenue, Cleveland, OH 44106, USA. E-mail: twn@case.edu

Published by AAAS

exons being correspondingly underenriched (*3*). How exactly the depletion of m^{6}A could alter splicing patterns is currently unknown.

A provocative study recently reported that inhibition of methylation by either a drug or knockdown of the m^{6}A methylase perturbed the circadian clock (*5*). When methylation was reduced by either treatment, the period of the clock was lengthened. By contrast, overexpression of the methylase caused a shorter period. Reduction of internal methylation resulted in a pronounced delay in export of mRNAs from the nucleus and, consequently, marked nuclear retention of those mRNAs. A second, perhaps related, phenomenon linked to inhibition of methylation was the widespread stabilization of mRNAs, in particular mRNAs encoding proteins known to be involved in the circadian clock. This observation may explain how the clock is perturbed when methylation is inhibited, but how specificity is achieved remains unknown. It is also unclear why overexpression of the methylase speeds up the clock; the methylation status of specific mRNAs was not examined.

Whereas these studies focused on the effects of inhibiting RNA methylation, another report examined the effect of a genetic null in an RNA demethylase. FTO, the first demethylase discovered, belongs to a family of enzymes that catalyze a wide range of oxidation reactions (*2*). Systematic study of these enzymes revealed that another family member, ALKBH5, was also a m^{6}A demethylase (*6*). Both FTO and ALKBH5 are localized to nuclei, and both colocalize with nuclear speckles, sites of concentrations of splicing factors. It is tempting to speculate that this localization is tied to the effects of methylation on splicing. Indeed, more than 3000 altered mRNA isoforms were observed when ALKBH5 was knocked down in tissue culture cells, indicating that splicing was affected. Despite this, mice null for ALKBH5 were anatomically normal and grew to adulthood. However, male mice lacking the demethylase were sterile, with gene expression and splicing massively altered in their testes. The sterility phenotype was manifested as a metaphase arrest during spermatogenesis. The tissue specificity of the phenomenon might be explained by the fact that ALKBH5 is more highly expressed in testes relative to other tissues, but perhaps the most puzzling observation is that deletion of the demethylase resulted in only a very modest increase in overall levels of m^{6}A in the testis.

The existence of a methylase and at least two demethylases coupled with phenotypes observed when either activity was altered strongly suggested that one or more factors recognize m^{6}A. A first step in identifying such factors has come from the demonstration that an RNA binding protein, YTHDF2, specifically recognizes m^{6}A-modified RNAs (*3*, *7*). In vivo cross-linking and immunoprecipitation showed that YTHDF2-bound RNAs were highly enriched for mRNAs known to be methylated (*7*). Moreover, a variety of approaches, including ribosome profiling and immunofluorescence microscopy, provided evidence that the binding of YTHDF2 to mRNA resulted in relocalization of the mRNA from translating ribosomes to cytoplasmic foci (P bodies) known to be enriched in RNA degradative activities. As a consequence, targeted mRNAs were destabilized, and the magnitude of destabilization correlated with the number of methylation sites in the mRNA. Knockdown of YTHDF2 led to an increase in mRNA stability for targeted transcripts.

Although these studies have provided new insight into the distribution and functional importance of the m^{6}A modification, several fundamental questions remain. Prime among these is how specificity of modification is achieved. Clearly, the sequence that constitutes the consensus site is not sufficient on its own, nor does secondary structure appear to play a role. If methylation is cotranscriptional, it may be possible that chromatin status could play a role in site selection. The function(s) of m^{6}A in nuclear RNA metabolism are also unclear. Although it is possible that nuclear factors recognize the modification, it seems equally plausible that modifications could function by preventing or altering the binding of some proteins. The importance or function of modifications in the vicinity of stop codons remains to be established, as does the importance of the FTO demethylase. Perhaps the most challenging question—and most difficult to answer—is how such a widespread modification has apparently quite specific effects. Are all modified sites equally important, or is only a small subset of them important? Hopefully, answers to at least some of these questions will emerge soon in this now fast-moving field.

References

1. J. A. Bokar, M. E. Shambaugh, D. Polayes, A. G. Matera, F. M. Rottman, *RNA* **3**, 1233 (1997).
2. G. Jia *et al.*, *Nat. Chem. Biol.* **7**, 885 (2011).
3. D. Dominissini *et al.*, *Nature* **485**, 201 (2012).
4. K. D. Meyer *et al.*, *Cell* **149**, 1635 (2012).
5. G. Zheng *et al.*, *Mol. Cell* **49**, 18 (2013).
6. J.-M. Fustin *et al.*, *Cell* **155**, 793 (2013).
7. X. Wang *et al.*, *Nature* **505**, 117 (2014).

10.1126/science.1249340

GENETICS

Stirring the Simmering "Designer Baby" Pot

Thomas H. Murray[1,2]

How much discretion should parents be granted in determining what sort of child they have?

In February 2014, the U.S. Food and Drug Administration's (FDA's) Cellular, Tissue, and Gene Therapies Advisory Committee met to consider the possibility of future clinical trials that would test mitochondrial manipulation technologies for two purposes: to treat infertility and to prevent the transmission of mitochondrial disease from women to their future children. This meeting focused on scientific, technological, and clinical issues. The FDA acknowledged "ethical and social policy issues related to genetic modification of eggs and embryos" but chose not to engage with them, at least not yet (*1*). Good ethics begins with good facts, but the effort by the FDA to get the facts straight is just the beginning, not the end, of the conversation we must have on the wisdom of mitochondrial manipulation and other reproductive technologies that potentially provide parents with more of a say about the children they have. Preventing a lethal disease is one thing; choosing the traits we desire is quite another.

The replacement of defective mitochondria involves placing nuclear DNA from the egg of a woman with a mitochondrial defect into a donated egg that has had its nuclear DNA removed, but contains healthy mitochondrial DNA. The egg can then be fertilized by artificial insemination. Daughters produced by this procedure could pass down the mitochondrial DNA to future offspring. Up to now, the United States has not allowed such genetic changes across generations.

[1]The Hastings Center, Garrison, New York, USA. [2]The Centre for Biomedical Ethics, National University of Singapore, Singapore 117597. E-mail: murrayt@thehastingscenter.org

Published by AAAS

The FDA's discussion about human testing of this procedure is stirring the pot of "designer baby" concerns that was recently agitated by the personal genomics and biotechnology company 23andMe. In September 2013, the company was granted a patent, "Gamete donor selection based on genetic calculations," that allows would-be parents "to select a donor and view other possible phenotype of the hypothetical child resulting from the recipient's and the donor's gametes, such as alcohol flush reaction, lactose tolerance, muscle performance, and any other appropriate phenotype…" (*2*). The company sought to reassure critics by stating that it was merely protecting intellectual property in its Family Traits Inheritance Calculator, described as "an engaging way … to see what kind of traits your child might inherit from you.… The tool offers people an enjoyable way to dip their toes into genetics" (*3*). 23andMe disavows any plans to offer donor gamete selection. The company, unwittingly, tapped into a simmering controversy over what it means to have a child in an era of increasing convergence among genetic, genomic, and reproductive technologies.

What makes the fuss stirred up by the 23andMe patent distinct from preimplantation genetic diagnosis (genetic profiling of embryos prior to implantation) and prenatal screening (procedures during pregnancy to detect health problems in the fetus) is its disconnection from the abortion debate. There is no existing embryo or fetus here. At stake is not whether to have a child, but how much discretion parents should exercise in determining what sort of child they have.

Of all the possible choices prospective parents might make, sex selection for nonmedical purposes has prompted the strongest policy response. It is prohibited in at least 36 countries, but not in the United States. (Israel bans the practice but makes exceptions for mental health or for parents with at least four children of the same sex.) Persistent passionate conflicts over the legal and moral status of embryos and fetuses have discouraged American legislators from proposing sensible regulation, lest they be drawn into the abortion debate. Surprisingly, there is no federal law forbidding reproductive human cloning. Efforts to pass legislation foundered when opponents insisted that cloning for research be likewise prohibited out of respect for embryos as persons.

In the absence of federal legislation, professional self-regulation has been the principal policy tool. However, this has led to conflicting guidance that reflects clashing ethical frameworks for thinking about parenthood in the genomic era. Take sex selection. The American College of Obstetrics and Gynecology's Committee on Ethics rejected all uses of sex selection except for sex-linked disorders. Its primary objection was that sex selection at any stage—even pre-conception—reinforces sex discrimination against women (*4*). The Ethics Committee of the American Society for Reproductive Medicine, by contrast, leaves open the door to sex selection for social reasons. It defers to the prospective parents: "It would not be unethical for parents to prefer that their firstborn or only child be of a particular gender because of the different meaning and companionship experiences that they expect to have" (*5*). The Committee showed similar deference on preimplantation genetic diagnosis, stating that for adult-onset conditions, its use is "ethically justified when the condition is serious and no safe, effective interventions are available." It also concluded that reproductive liberty arguments ethically allow for this test for "adult-onset conditions of lesser severity or penetrance." It does not address trait selection by this diagnosis, but the concept of reproductive liberty that suffuses the committee's guidelines grants wide discretion to parental preferences (*6*).

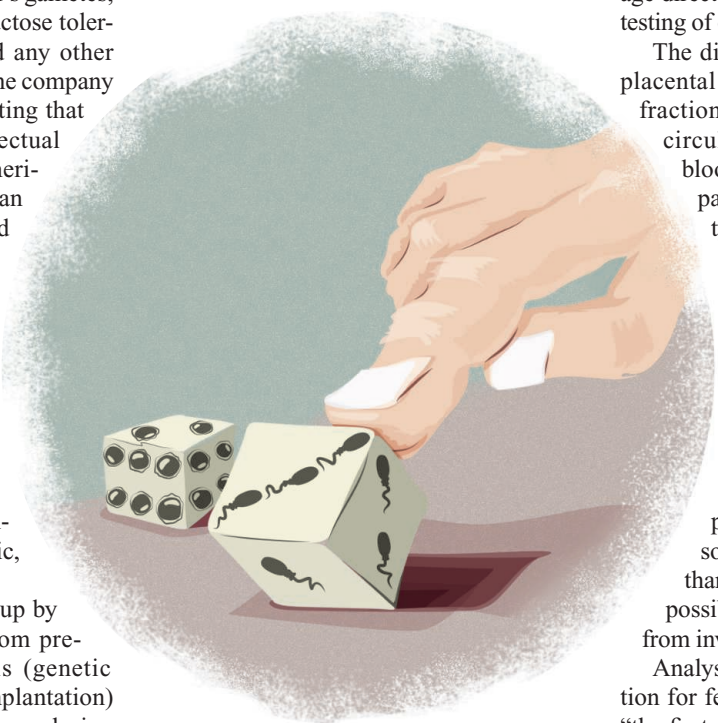

CREDIT: V. ALTOUNIAN/*SCIENCE*

By contrast, the American Academy of Pediatrics and the American College of Medical Genetics put children first in their report on genetic testing and screening of children: "Decisions about whether to offer genetic testing and screening should be driven by the best interest of the child." They counsel deferring testing for adult-onset conditions unless intervening would benefit the child's health. They also "strongly" discourage direct-to-consumer and home kit genetic testing of children (*7*).

The discovery that fetal DNA, likely of placental origin, constitutes a substantial fraction of the cell-free DNA (cfDNA) circulating in the pregnant woman's blood could allow future prospective parents another peek into the genotypes of potential offspring. Unlike amniocentesis and chorionic villus sampling, which are invasive procedures that increase the risk of spontaneous abortion, fetal cfDNA is available from a simple venipuncture. Using massively parallel sequencing for cfDNA, researchers screened a large and diverse sample of women for aneuploidy. False positive rates for trisomies 21 and 18 were much lower than with current screening methods, possibly sparing many pregnant women from invasive follow-up testing (*8*).

Analysis of cfDNA in maternal circulation for fetal aneuploidy screening is likely "the first of major steps toward the eventual application of whole fetal genome/whole fetal exome sequencing" (*9*). Indeed, it is now possible, using DNA from both parents (the father need only provide saliva) and the fetal cfDNA circulating in the mother's blood, to provide a reasonably accurate genome sequence for that fetus at 18.5 weeks gestational age. It is anticipated "that noninvasive analysis of inherited variation and de novo mutations in fetal genomes will facilitate prenatal diagnosis of both recessive and dominant Mendelian disorders" (*10*). A 2006 survey of in vitro fertilization clinics found that 77% of respondents foresaw whole-genome embryo screening as becoming routine for in vitro fertilization. In the same survey, 42% of clinics reported doing preimplantation genetic diagnosis for other than medical reasons, with nearly half (47%) of that group offering it in all circumstances (*11*). Little wonder, then, that people in other nations that prohibit sex selection for social reasons flock to the United States.

It is unrealistic to expect the U.S. policy lacuna over assisted reproductive technologies to be filled any time soon. Regula-

Published by AAAS

tion of preimplantation genetic diagnosis remains in a "state of suspended animation" (*12*). Professional self-regulation likely works well when the interested professions reflect a well-established public consensus. But when it comes to empowering parents to decide what sort of children they have beyond questions of serious childhood diseases, professional organizations cannot even agree on the appropriate ethical framework. Scholars have articulated alternatives: whether parental discretion should hold near-absolute sway (*13*); whether a child should have the prospect of "a decent chance of a happy life" (*14*); whether the welfare of the child-to-be should come first (*15*); and whether models emphasizing the deep interrelationship of parent and child should be considered (*16*).

Legislation, regulation, and professional guidelines depend on widely shared public values for their legitimacy. Technologies affecting reproduction have powerful resonance, as the response to the 23andMe patent confirms, even as the lives of children and their parents are affected far more by economic opportunity and security, education, and community resources.

Discussion of the ethics of mitochondrial manipulation cannot be postponed indefinitely. With little prospect of sensible legislation in the near term, and conflicting guidance from professional organizations, a national conversation about current and emerging technologies shaping the choices that parents will have is urgent. The UK conducted a similar exercise a decade ago that combined polling, focus groups, and the Internet (*17*). This is a task for the U.S. Presidential Commission for the Study of Bioethical Issues to pursue, given that its mission is to ensure that scientific research, health care delivery, and technological innovation are conducted in a socially and ethically responsible manner. It will not be easy to avoid the quicksand of the abortion debate, but it would be a great public service to provide a sober assessment of the choices that would-be parents increasingly face, and to encourage a respectful dialogue about the meaning of parenthood and the worth of a child so that parents and children can flourish together.

References

1. www.fda.gov/AdvisoryCommittees/Calendar/ucm380042.htm
2. A. Wojcick *et al*., U.S. Patent 8,543,339 (2013).
3. "A 23andMe Patent," The 23andMe Blog, available from http://blog.23andme.com/news/a-23andme-patent/.
4. Committee on Ethics, *Obstet. Gynecol.* **109**, 475 (2007).
5. Ethics Committee of the American Society for Reproductive Medicine, *Fertil. Steril.* **75**, 861 (2001).
6. Ethics Committee of the American Society for Reproductive Medicine, *Fertil. Steril.* **100**, 54 (2013).
7. M. E. Fallat *et al*., *Pediatrics* **131**, 620 (2013).
8. D. W. Bianchi *et al*., *N. Engl. J. Med.* **370**, 799 (2014).
9. A. R. Gregg *et al*, *J. Am. Coll. Med. Genet.* **15**, 395 (2013).
10. J. O. Kitzman *et al., Sci. Transl. Med*. **6**, 137ra76 (2012).
11. S. Baruch, D. Kaufman, K. L. Hudson, *Fertil. Steril.* **89**, 1053 (2008).
12. K. L. Hudson, *Fertil. Steril.* **85**, 1638 (2006).
13. J. A. Robertson, *J. Med. Ethics* **29**, 213 (2003).
14. B. Steinbock, R. McClamrock, *Hastings Cent. Rep.* **24**, 15 (1994).
15. J. Glover, *Choosing Children: Genes, Disability, and Design* (Clarendon, Oxford/New York, 2007).
16. T. H. Murray, *The Worth of a Child* (Univ. of California Press, Berkeley, 1996).
17. Human Fertilisation and Embryology Authority, Sex Selection: Options for Regulation (2003); available at www.hfea.gov.uk/cps/rde/xbcr/SID-3F57D79B-1FBD1F5D/hfea/Final_sex_selection_main_report.pdf.

10.1126/science.1248080

MATERIALS SCIENCE

Where Do Batteries End and Supercapacitors Begin?

Electrochemical measurements can distinguish between different types of energy storage materials and their underlying mechanisms.

Patrice Simon,[1] Yury Gogotsi,[2] Bruce Dunn,[3]

Batteries keep our devices working throughout the day—that is, they have a high energy density—but they can take hours to recharge when they run down. For rapid power delivery and recharging (i.e., high power density), electrochemical capacitors known as supercapacitors (*1*) are used. One such application is regenerative braking, used to recover power in cars and electric mass transit vehicles that would otherwise lose braking energy as heat. However, supercapacitors have low energy density.

Batteries and supercapacitors both rely on electrochemical processes, although separate electrochemical mechanisms determine their relative energy and power density. During the past 5 to 7 years, the energy storage field has witnessed a dramatic expansion in research directed at materials that might combine the high energy density of batteries with the long cycle life and short charging times of supercapacitors (*2*). However, the blurring of these two electrochemical approaches can cause confusion and may lead to unwarranted claims unless careful attention is paid to fundamental performance characteristics.

The electrochemical processes occurring in batteries and supercapacitors give rise to their different charge-storage properties. In lithium ion (Li^+) batteries, the insertion of Li^+ that enables redox reactions in bulk electrode materials is diffusion-controlled and can be slow. Supercapacitor devices, also known as electrical double-layer capacitors (EDLCs), store charge by adsorption of electrolyte ions onto the surface of electrode materials (see the figure, panels A to D). No redox reactions are required, so the response to changes in potential without diffusion limitations is rapid and leads to high power. However, the charge is confined to the surface, so the energy density of EDLCs is less than that of batteries (*3*). As shown in the figure, panels E to H, supercapacitors can be distinguished from batteries by both potentiostatic and galvanostatic methods. The different methods for achieving double-layer capacitance are characterized by classic rectangular cyclic voltammograms (panel E) and a linear time-dependent change in potential at a constant current (panel G). In batteries, the cyclic voltammograms are characterized by faradaic redox peaks, often with rather large voltage separation (greater than 0.1 to 0.2 V) between oxidation and reduction because of phase transitions (panel F) (*4*). The presence of two phases is indicated by the voltage plateau in galvanostatic experiments (panel H).

In the 1970s, Conway and others recognized that reversible redox reactions occurring at or near the surface of an appropriate electrode material lead to EDLC-like electrochemical features but the redox processes lead to much greater charge storage

[1]Université Paul Sabatier–Toulouse III, CIRIMAT UMR-CNRS 5085, and RS2E, FR CNRS 3459, 118 Route de Narbonne, 31062 Toulouse, France. [2]Department of Materials Science and Engineering and A. J. Drexel Nanomaterials Institute, Drexel University, Philadelphia, PA 19104, USA. [3]Department of Materials Science and Engineering and California NanoSystems Institute, University of California, Los Angeles, CA 90095, USA. E-mail: simon@chimie.ups-tlse.fr; gogotsi@drexel.edu; bdunn@ucla.edu

Published by AAAS

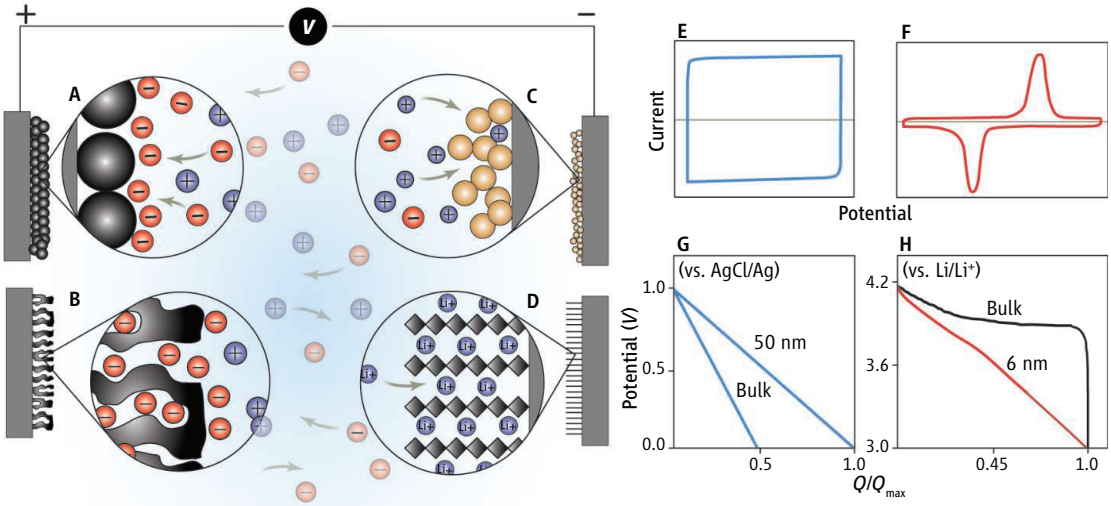

Comparing batteries and supercapacitors. (**A** to **D**) The different mechanisms of capacitive energy storage are illustrated. Double-layer capacitance develops at electrodes comprising (A) carbon particles or (B) porous carbon. The double layer shown here arises from adsorption of negative ions from the electrolyte on the positively charged electrode. Pseudocapacitive mechanisms include (C) redox pseudocapacitance, as occurs in hydrous RuO_2, and (D) intercalation pseudocapacitance, where Li^+ ions are inserted into the host material. (**E** to **H**) Electrochemical characteristics distinguish capacitor and battery materials. Cyclic voltammograms distinguish a capacitor material where the response to a linear change in potential is a constant current (E), as compared to a battery material, which exhibits faradaic redox peaks (F). Galvanostatic discharge behavior (where Q is charge) for a MnO_2 pseudocapacitor is linear for both bulk and nanoscale material (G) (*13*, *14*), but a $LiCoO_2$ nanoscale material exhibits a linear response while the bulk material shows a voltage plateau (H) (*8*).

(*5*). This pseudocapacitance represents a second mechanism for capacitive energy storage. The most widely known pseudocapacitors are RuO_2 and MnO_2; recently this list has expanded to other oxides, as well as nitrides and carbides, as different pseudocapacitance mechanisms have been identified (*6*). Pseudocapacitive materials hold the promise of achieving battery-level energy density combined with the cycle life and power density of EDLCs. To avoid further confusion with EDLCs, we propose that these materials be called oxide supercapacitors (nitride, carbide, etc.) to recognize that a substantial fraction of the charge storage arises from redox reactions. The use of this terminology requires identifying the charge storage mechanism, rather than basing the claim on the material type alone.

A second feature that blurs the distinction between batteries and supercapacitors is how their response changes when nanoscale materials are used. When battery materials are prepared in nanoscale forms, their power density increases because of the short transport paths for ions and electrons (*7*). However, increased power density does not necessarily transform nanoscale materials into oxide supercapacitors because their faradaic redox peaks and galvanostatic profiles remain battery-like (see the figure, panels F and H). At smaller dimensions (<10 nm), there are indications that traditional battery materials exhibit capacitor-like properties [e.g., $LiCoO_2$ shown in panel H of the figure (*8*); V_2O_5 may behave in a similar fashion (*9*)]. "Extrinsic" pseudocapacitance can emerge when a battery material is engineered at the nanoscale so that a large fraction of Li^+ storage sites are on the surface or near-surface region.

Pronounced redox peaks in the voltammetry can be an indication of pseudocapacitance, provided the peak voltage differences are small and remain so with increasing sweep rate (*5*). The kinetic information obtained from sweep voltammetry can also be used. For a redox reaction limited by semi-infinite diffusion, the peak current i varies as $v^{1/2}$; for a capacitive process, it varies as v. This relation is expressed as $i = av^b$ (*10*), with the value of b providing insight regarding the charge storage mechanism. Over a wide range of sweep rates v, the well-known battery material $LiFePO_4$ has $b \approx 0.5$, whereas $b \approx 1.0$ for the pseudocapacitor material Nb_2O_5 (*6*, *11*). In addition to diffusion-controlled behavior, low Coulombic efficiency and sluggish kinetics are indications that the material is not a supercapacitor. Thus, an electrode material or a device with well-separated redox peaks (panel F) and a discharge curve similar to the upper curve in panel H should not be considered a supercapacitor.

There is nothing inappropriate in using nanostructured battery materials in symmetric electrochemical cells or combined with a capacitive electrode (carbon) to make a hybrid energy storage device. However, it is misleading to test such a material or device at a low rate (for a supercapacitor, at least) and claim that it is a "high–energy density supercapacitor." Additionally, the use of low weight loadings or thin films of nanostructured battery materials leads to devices with moderate performance and limited cycle life (*12*). If the materials are to be considered for high-power devices, they need to be evaluated at the rates where supercapacitor devices are used (e.g., fully recharged in 1 min, referred to as a rate of 60C).

The prospect of developing materials with the energy density of batteries and the power density and cycle life of supercapacitors is an exciting direction that has yet to be realized. Whether to approach these goals by increasing the power density of battery materials or increasing the energy density of supercapacitors is one of the enticing features of the field. However, there needs to be clarity in the terminology used in combination with appropriate measurements and analyses. Proper evaluation of new materials and their charge storage mechanisms will facilitate progress in this important field of electrical energy storage.

References and Notes

1. J. R. Miller, P. Simon, *Science* **321**, 651 (2008).
2. F. Beguin, E. Frackowiak, Ed., *Supercapacitors: Materials, Systems and Applications* (Wiley-VCH, Weinheim, Germany, 2013).
3. P. Simon, Y. Gogotsi, *Acc. Chem. Res.* **46**, 1094 (2013).
4. B. E. Conway, *J. Electrochem. Soc.* **138**, 1539 (1991).
5. B. E. Conway, *Electrochemical Supercapacitors: Scientific Fundamentals and Technological Applications* (Springer, New York, 1999).
6. V. Augustyn *et al.*, *Nat. Mater.* **12**, 518 (2013).
7. A. S. Aricò, P. Bruce, B. Scrosati, J. M. Tarascon, W. van Schalkwijk, *Nat. Mater.* **4**, 366 (2005).
8. M. Okubo *et al.*, *J. Am. Chem. Soc.* **129**, 7444 (2007).
9. M. Sathiya, A. S. Prakash, K. Ramesha, J.-M. Tarascon, A. K. Shukla, *J. Am. Chem. Soc.* **133**, 16291 (2011).
10. H. Lindström *et al.*, *J. Phys. Chem. B* **101**, 7717 (1997).
11. J. Come, P. L. Taberna, S. Hamelet, C. Masquelier, P. Simon, *J. Electrochem. Soc.* **158**, A1090 (2011).
12. Y. Gogotsi, P. Simon, *Science* **334**, 917 (2011).
13. A. Boisset *et al.*, *J. Phys. Chem. C* **117**, 7408 (2013).
14. W. Shimizu, S. Makino, K. Takahashi, N. Imanishi, W. Sugimoto, *J. Power Sources* **241**, 572 (2013).

Acknowledgments: Supported by the FIRST (Y.G.) and MEEM (B.D.) Energy Frontier Research Centers (funded by the Office of Basic Energy Sciences, U.S. Department of Energy) and by European Research Council grant ERC-2011-AdG n°291543 (P.S.).

10.1126/science.1249625

CREDIT: ADAPTED FROM KRISTY JOST/DREXEL

Published by AAAS

VIROLOGY

Getting Rid of a Persistent Troublemaker to Cure Hepatitis

Eliminating the master genomic template of hepatitis B virus in infected liver cells through cytokine therapy may be a route to help cure chronic infection.

Amir Shlomai and Charles M. Rice

One of the major enigmas in hepatitis B virus (HBV) infection is the striking persistence of its episomal DNA [covalently closed circular DNA (cccDNA)], the viral transcriptional template sequestered in the nucleus of infected hepatocytes. Eradicating cccDNA is a requisite for virus elimination and cure, a desirable end point for the 400 million people chronically infected by HBV worldwide who are at a substantial risk for end-stage liver disease and liver cancer. Commonly used therapies suppress viral replication, but because they are ineffective at targeting the cccDNA pool, they often require lifelong administration to prevent viral rebound (*1*). Thus, the development of new drugs that efficiently and specifically target HBV cccDNA is a priority. On page 1221 of this issue, Lucifora *et al*. (*2*) uncover a mechanism that destroys cccDNA, which can be activated by two different approaches.

Fifteen years ago, a seminal study showed that HBV cccDNA could be cleared, without destruction of infected cells, from the livers of chimpanzees during acute infection (*3*). This challenged the prevailing concept that HBV infection was cleared exclusively by cell-mediated cytopathic mechanisms, and suggested the involvement of secreted cytokines, such as tumor necrosis factor–α (TNF-α) and interferon-γ (IFN-γ). Lucifora *et al*. show that IFN-α, a cytokine that has been used for decades to treat HBV infection, causes specific degradation of the nuclear cccDNA without detectable hepatotoxicity. Furthermore, a similar effect can be achieved by activating the lymphotoxin-β receptor (LTβR), a receptor engaged by members of the TNF cytokine superfamily.

Lucifora *et al*. found that IFN-α treatment of HBV-infected hepatocytes, or antibody-mediated activation of LTβR, resulted in extensive nucleotide changes [guanine (G) to adenine (A)] in cccDNA, a transition that is a hallmark of cytidine deamination. Remarkably, this deamination did not occur in cellular DNA, indicating that viral clearance might involve cccDNA-specific mechanisms.

That cytidine deamination blocks the HBV life cycle is neither new nor unexpected for a virus that replicates by reverse transcription (HBV replicates through an RNA intermediate, which is transcribed into complementary DNA using reverse transcriptase). In fact, HBV is inhibited by members of a cytidine deaminase family called apolipoprotein B mRNA editing enzyme, catalytic polypeptide-like 3 (APOBEC3). Initial studies suggested inhibitory mechanisms other than extensive genome editing (*4*). However, subsequent reports supported a role for APOBEC3-mediated hypermutation in the anti-HBV effect (*5*) and even suggested IFN-α as a stimulator of APOBEC3 expression in primary human hepatocytes (*6*). Lucifora *et al*. show that IFN-α or LTβR agonists trigger the expression of APOBEC3A or APOBEC3B, respectively, resulting in selective deamination and degradation of cccDNA. This effect is specific, because the HIV protein Vif, which blocks the action of all APOBEC3 proteins except for APOBEC3B, prevented the nucleotide changes in cccDNA induced by IFN-α and cccDNA degradation. This was not observed

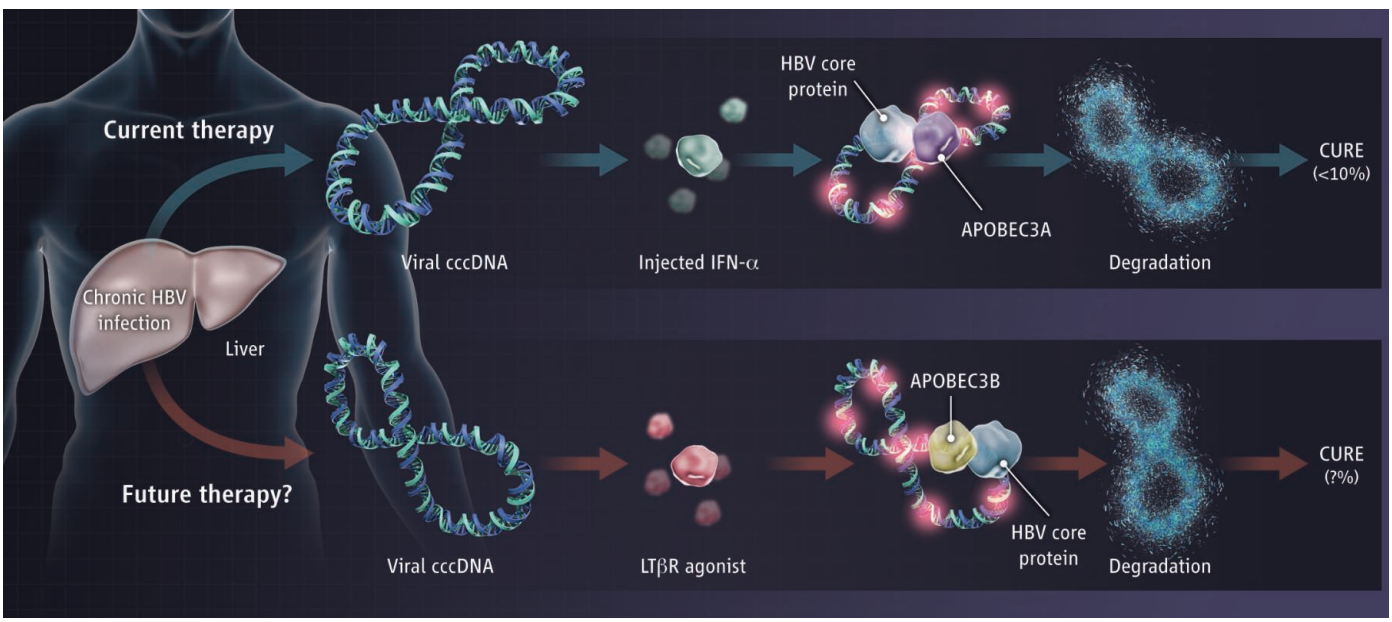

Destroying the master template. Treatment of HBV infection with IFN-α induces the expression of APOBEC3A, which interacts with HBV core protein that is associated with viral DNA (cccDNA) in the hepatocyte nucleus. APOBEC3A deaminates cccDNA, marking it for degradation. This mechanism of cccDNA degradation also occurs in response to activation of the LTβR, but involves APOBEC3B.

CREDIT: C. BICKEL/*SCIENCE*

Laboratory of Virology and Infectious Disease, Center for the Study of Hepatitis C, The Rockefeller University, 1230 York Avenue, New York, NY 10065, USA. E-mail: ricec@mail.rockefeller.edu

Published by AAAS

for changes in cccDNA induced by LTβR. Depletion of either APOBEC3A or APOBEC3B from infected liver cells abolished cccDNA degradation elicited by IFN-α or LTβR, respectively.

How might APOBEC3 enzymes selectively target cccDNA? Lucifora *et al*. implicate the HBV core protein, which binds to both cccDNA and APOBEC3A, thereby bringing them into close contact to promote cccDNA deamination and degradation (see the figure). Host genomic DNA, as well as HBV DNA that has integrated into the host genome, are spared.

What do these new findings mean for understanding HBV infection and improving treatment? In terms of resolution of infection, moderate cccDNA deamination occurred even without IFN-α, providing a possible explanation for the low frequency of spontaneous clearance seen in infected patients (2% of patients per year) (*7*). Still, the reason for the disappointing response to IFN-α–based HBV therapy remains unclear. The high concentrations of IFN-α used by Lucifora *et al*. to achieve maximal cccDNA degradation might suggest that clinically acceptable concentrations are not sufficient. Alternatively, the finding that the expression of APOBEC3A is only transient after IFN-α treatment in patients underscores the fact that hepatocytes rapidly become refractory to the cytokine (*8*). To explain the unexpected effect of APOBEC3 on double-stranded DNA, rather than on single-stranded DNA, the authors posit that transcription of viral RNA generates single-stranded HBV DNA that is accessible to APOBEC3 action. In this scenario, the repressive effect of IFN-α on HBV transcription (*9*) could antagonize APOBEC3-mediated cccDNA deamination and efficient elimination. Lucifora *et al*. also show that addition of potent nucleoside or nucleotide analogs that suppress viral replication enhance the effect of IFN-α on cccDNA. However, this does not mesh with the disappointing, albeit limited, clinical trial results obtained thus far (*10*). It may be that preexisting cccDNA is more resistant to that action of APOBEC compared to cccDNA that is newly generated by reverse transcription. Alternatively, the extent of deamination in response to IFN-α may be insufficient to irreversibly damage every molecule of cccDNA. However, combining newer analogs with IFNs that do not elicit a refractory state (*8*), or with LTβR agonists, may be worth testing.

Nonetheless, there is much about the IFN-α/LTβR-APOBEC3 mechanism that is mysterious. The amount of APOBEC3A or APOBEC3B expression (at the transcript level) did not always positively correlate with cccDNA degradation. It is also unclear why deaminated cccDNA is degraded rather than repaired. In addition, hepatocytes lacking an *APOBEC3B* allele associated with more frequent HBV persistence (*11*) did not show markedly diminished cccDNA degradation in response to LTβR agonists. However, these in vitro results were obtained with hepatocytes derived from a limited number of donors.

The findings of Lucifora *et al*. add to other studies showing that IFN-α acts on multiple levels of the HBV life cycle. Further defining the precise mechanisms of the anti-HBV effect of IFN-α and other cytokines on cccDNA degradation may open up potential new avenues for more effective HBV elimination. LTβR agonists, if proven safe, could be an alternative to IFN-α treatment, with enhanced cure rates. Human studies are needed, but one hopes that we may be getting closer to making the notion of "once HBV, always HBV" a vanishing memory.

References

1. G. Dusheiko, *Liver Int.* **33** (suppl. 1), 137 (2013).
2. J. Lucifora *et al*., *Science* **343**, 1221 (2014); 10.1126/science.1243462.
3. L. G. Guidotti *et al*., *Science* **284**, 825 (1999).
4. P. Turelli, B. Mangeat, S. Jost, S. Vianin, D. Trono, *Science* **303**, 1829 (2004).
5. R. Suspène *et al*., *Proc. Natl. Acad. Sci. U.S.A.* **102**, 8321 (2005).
6. M. Bonvin *et al*., *Hepatology* **43**, 1364 (2006).
7. J. Liu *et al.*, *Gastroenterology* **139**, 474 (2010).
8. Z. Makowska, F. H. Duong, G. Trincucci, D. F. Tough, M. H. Heim, *Hepatology* **53**, 1154 (2011).
9. L. Belloni *et al*., *J. Clin. Invest.* **122**, 529 (2012).
10. H. L. A. Janssen *et al.*, *Lancet* **365**, 123 (2005).
11. T. Zhang *et al*., *Hum. Mol. Genet.* **22**, 1262 (2013).

10.1126/science.1252186

ECOLOGY

Society, Where None Intrudes

A field study reveals an intricate tropical community of plants, herbivores, and parasitoids.

H. Charles J. Godfray

Explaining the diversity and structure of networks of interacting species is one of the main challenges in modern ecology. Even building the food webs needed to understand how these networks are structured can be a massive undertaking, especially in the tropics, where diversity is highest and understanding of the taxonomy of the species involved is often poor. However, progress has been made with communities of plant-eating insects and the specialized insects that feed on them, in particular parasitic wasps. On page 1240 of this issue, Condon *et al*. (*1*) combine field ecology and molecular biology to describe the structure of a self-contained community of tropical plant-eating flies and the wasps that attack them. The results reveal an unexpectedly intricate community structure.

The number of insect herbivore species on Earth is not known, but conservative estimates are in the millions, with peak diversity in the tropics (*2*). Lepidoptera (butterflies and moths) and beetles are the most common types of plant-eating insects; several groups of true flies have also evolved herbivory. Nearly all of these species are attacked by parasitic wasps, which typically lay their eggs in or on their host's body. The developing wasp larva requires just a single host (which it invariably kills) for its full development. Parasitic wasps and ecologically similar insects are often called parasitoids, because their life history is intermediate between predators and true parasites. Because parasitoids take some time to kill their hosts, it is much easier to construct plant-host-parasitoid food webs than is the case for predators, which must be observed in the act of killing and eating the prey to establish a trophic link. Thus, some of the best examples of large tropical food webs resolved at the species level involve this type of interaction (*3*–*5*).

One of the major structuring forces in community ecology is competition for resources: The more distinct resources—such as host-plant species—exist, the more species of consumers can coexist. But very often, a single host-plant species supports

Department of Zoology, University of Oxford, South Parks Road, Oxford OX1 3PS, UK. E-mail: charles.godfray@zoo.ox.ac.uk

Published by AAAS

many species of specialist insect herbivores. Of course, different species may specialize by feeding on different plant organs, or the different species may feed on the plants at nonoverlapping times of year, but even taking this into account, there appear to be more consumers than distinct resource niches (*6*).

But communities can also be structured by the actions of higher trophic levels—for example, the diseases, parasitoids, and predators that afflict plant-eating insects. Just as two consumer species cannot coexist in the long term on the same resource, with the less efficient competitor going extinct, so a natural enemy that attacks two species will drive the less resilient to extinction. Similarly, just as species are predicted to evolve to use unexploited resources, they are also expected to evolve into "enemy-free space"—ecological niches with few predators and parasitoids (*7*). This type of interaction between species mediated by shared natural enemies has been termed "apparent competition" (*8*) because its effects on community structure are similar to those of traditional resource competition. Experiments have shown that apparent competition occurs in insect food webs, including in the tropics (*9*).

Condon *et al*. studied a type of fly (belonging to the family Tephritidae) whose larvae feed on the succulent parts of the flowers of climbing squashes (cucurbits). At their study site in Peru, two species of squash grew together; each had morphologically distinct male and female flowers. The fly larvae are attacked by tiny wasps, a few millimeters in length, that lay their eggs in young larvae. The eggs hatch and the wasp larvae remain in a state of suspended development until their hosts become full grown, when they resume growth and kill them. During the developmental hiatus, the host can fight back by mounting an immunological defense that, if successful, kills the internal parasitoid.

The first surprise about this community was how many species were involved and how specialized they were. The authors reared 14 fly species, all in the same genus. Most species of fly specialized on only one of the four resource types—either a male or female flower of the two species. Up to 11 species shared a single resource type. A clue to how these species can coexist is provided by the 18 species of parasitoid wasps that were reared. They include two species that attack a broad range of hosts, but also a group of closely related species—all belonging to the same genus—that have very narrow host ranges. These wasps were each restricted to develop in a single fly species, even when several host types were present. Such patterns are exactly what one expects if resource competition and apparent competition are structuring the community.

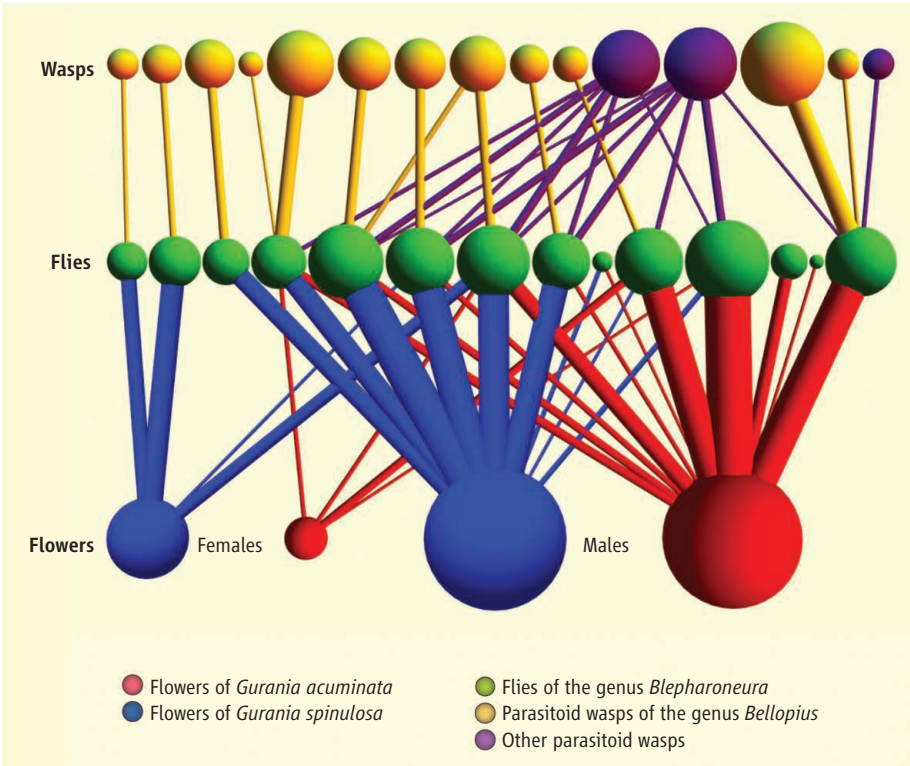

Intricate web. At their study site, Condon *et al*. collected 3636 flowers from two species of squash. A total of 1106 flies and 163 parasitoid wasps emerged from the flowers. In the resulting food web, the three trophic levels are represented by rows of balls. Within each trophic level, the size of the balls and thickness of the links are proportional to the abundance of species and the strength of feeding links, respectively. Most wasp species can only develop in a single fly host species.

Until recently, it has only been possible to record the parasitoids that have overcome host defenses, not those that have succumbed to, or have been outcompeted by, other parasitoid species. Using modern molecular techniques, it is now possible to detect the traces of unsuccessful parasitoid attacks, allowing interaction webs rather than trophic webs to be constructed (*10*). Condon *et al*. do this for the first time in a large tropical community. They find that although most parasitoid species only successfully develop in one host species, the searching females lay eggs in other species that feed on the same resource type but are able to successfully defend themselves against the parasitoid. This host specificity is again consistent with structuring by apparent competition, but it remains unclear why females lay eggs in the wrong host. Possibly, they cannot tell hosts apart; alternatively, laying eggs in the wrong host may be worthwhile because the opportunity cost of wasting an egg is low or because the offspring may survive in rare cases.

Condon *et al*. provide a wonderful example of a "society, where none intrudes." The web of interactions they reveal is complex and raises fascinating hypotheses about how different species influence each other's dynamics, both directly and indirectly. These ideas need to be tested experimentally, and this system, compared to most other tropical communities, may be relatively easy to manipulate in the field.

References

1. M. A. Condon *et al*, *Science* **343**, 1240 (2014).
2. A. J. Hamilton *et al*., *Am. Nat.* **176**, 90 (2010).
3. J. Memmott, H. C. J. Godfray, I. D. Gauld, *J. Anim. Ecol.* **63**, 521 (1994).
4. J. Hrcek, S. E. Miller, J. B. Whitfield, H. Shima, V. Novotny, *Oecologia* **173**, 521 (2013).
5. M. A. Smith *et al*., *Proc. Natl. Acad. Sci. U.S.A.* **105**, 12359 (2008).
6. P. D. Colley, T. A. Kursar, *Science* **343**, 35 (2014).
7. M. J. Jeffries, J. H. Lawton, *Biol. J. Linn. Soc. London* **23**, 269 (1984).
8. R. D. Holt, *Theor. Popul. Biol.* **12**, 197 (1977).
9. R. J. Morris, O. T. Lewis, H. C. J. Godfray, *Nature* **428**, 310 (2004).
10. R. Kaartinen, G. N. Stone, J. Hearn, K. Lohse, T. Roslin, *Ecol. Entomol.* **35**, 623 (2010).

10.1126/science.1251275

Published by AAAS

READ THE FULL ARTICLE ONLINE
http://dx.doi.org/10.1126/science.1247997

Structures of a family of genome-editing enzymes reveal how they target and cleave DNA.

Structures of Cas9 Endonucleases Reveal RNA-Mediated Conformational Activation

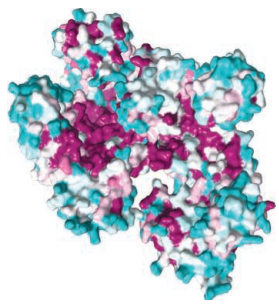

Martin Jinek,* Fuguo Jiang, David W. Taylor, Samuel H. Sternberg, Emine Kaya, Enbo Ma, Carolin Anders, Michael Hauer, Kaihong Zhou, Steven Lin, Matias Kaplan, Anthony T. Iavarone, Emmanuelle Charpentier, Eva Nogales,* Jennifer A. Doudna*

Introduction: Bacteria and archaea defend themselves against invasive DNA using adaptive immune systems comprising CRISPR (clustered regularly interspaced short palindromic repeats) loci and CRISPR-associated (Cas) genes. In association with Cas proteins, small CRISPR RNAs (crRNAs) guide the detection and cleavage of complementary DNA sequences. Type II CRISPR systems employ the RNA-guided endonuclease Cas9 to recognize and cleave double-stranded DNA (dsDNA) targets using conserved RuvC and HNH nuclease domains. Cas9-mediated cleavage is strictly dependent on the presence of a protospacer adjacent motif (PAM) in the target DNA. Recently, the biochemical properties of Cas9–guide RNA complexes have been harnessed for various genetic engineering applications and RNA-guided transcriptional control. Despite these ongoing successes, the structural basis for guide RNA recognition and DNA targeting by Cas9 is still unknown.

Rationale: To compare the architectures and domain organization of diverse Cas9 proteins, the atomic structures of Cas9 from *Streptococcus pyogenes* (SpyCas) and *Actinomyces naeslundii* (AnaCas9) were determined by x-ray crystallography. Crosslinking of target DNA containing 5-bromodeoxyuridines was conducted to identify PAM-interacting regions in SpyCas9. To test functional interactions with nucleic acid ligands, structure-based mutant SpyCas9 proteins were assayed for endonuclease activity with radiolabeled oligonucleotide dsDNA targets, and target DNA binding was monitored by electrophoretic mobility shift assays. To compare conformations of Cas9 in different states of nucleic acid binding, three-dimensional reconstructions of apo-SpyCas9, SpyCas9:RNA, and SpyCas9:RNA:DNA were obtained by negative-stain single-particle electron microscopy. Guide RNA and target DNA positions were determined with streptavidin labeling. Exonuclease protection assays were carried out to determine the extent of Cas9–target DNA interactions.

Results: The 2.6 Å–resolution structure of apo-SpyCas9 reveals a bilobed architecture comprising a nuclease domain lobe and an α-helical lobe. Both lobes contain conserved clefts that may function in nucleic acid binding. Photocrosslinking experiments show that the PAM in target DNA is engaged by two tryptophan-containing flexible loops, and mutations of both loops impair target DNA binding and cleavage. The 2.2 Å–resolution crystal structure of AnaCas9 reveals the conserved structural core shared by all Cas9 enzyme subtypes, and both SpyCas9 and AnaCas9 adopt autoinhibited conformations in their apo forms. The electron microscopic (EM) reconstructions of SpyCas9:RNA and SpyCas9:RNA:DNA complexes reveal that guide RNA binding results in a conformational rearrangement and formation of a central channel for target DNA binding. Site-specific labeling of guide RNA and target DNA define the orientations of nucleic acids in the target-bound complex.

Conclusion: The SpyCas9 and AnaCas9 structures define the molecular architecture of the Cas9 enzyme family in which a conserved structural core encompasses the two nuclease domains responsible for DNA cleavage, while structurally divergent regions, including the PAM recognition loops, are likely responsible for distinct guide RNA and PAM specificities. Cas9 enzymes adopt a catalytically inactive conformation in the apo state, necessitating structural activation for DNA recognition and cleavage. Our EM analysis shows that by triggering a conformational rearrangement in Cas9, the guide RNA acts as a critical determinant of target DNA binding.

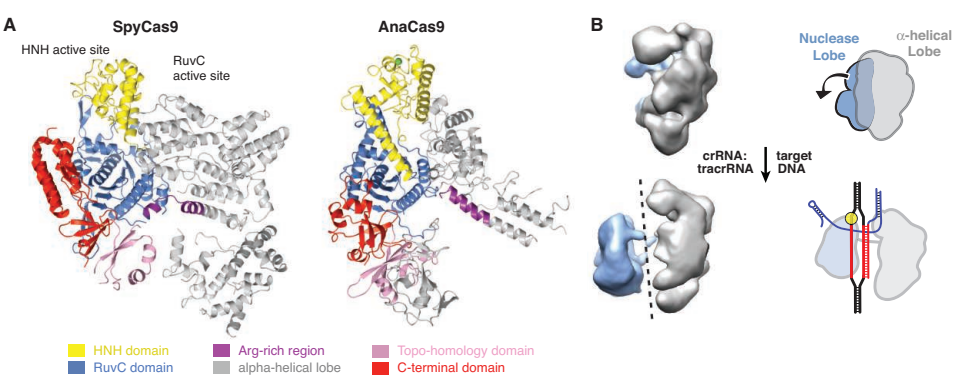

Structures of Cas9 endonucleases reveal RNA-mediated conformational activation. (**A**) Crystal structures of *S. pyogenes* (SpyCas9) and *A. naeslundii* (AnaCas9) Cas9 proteins. (**B**) Left: Negative-stain EM reconstructions of apo-SpyCas9 (top) and SpyCas9-RNA-target DNA complex (bottom) show that nucleic acid binding causes a reorientation of the nuclease (blue) and α-helical (gray) lobes in SpyCas9. Right: Cartoon representations of the structures. tracrRNA, trans-activating crRNA.

The list of author affiliations is available in the full article online.
*Corresponding author. E-mail: jinek@bioc.uzh.ch (M.J.); enogales@lbl.gov (E.N.); doudna@berkeley.edu (J.A.D.)
Cite this article as M. Jinek *et al.*, *Science* **343**, 1247997 (2014). DOI: 10.1126/science.1247997

Structures of Cas9 Endonucleases Reveal RNA-Mediated Conformational Activation

Martin Jinek,[1]*† Fuguo Jiang,[2]* David W. Taylor,[3,4]* Samuel H. Sternberg,[5]* Emine Kaya,[2] Enbo Ma,[2] Carolin Anders,[1] Michael Hauer,[2]‡ Kaihong Zhou,[3] Steven Lin,[2,3] Matias Kaplan,[3]§ Anthony T. Iavarone,[4] Emmanuelle Charpentier,[6,7,8] Eva Nogales,[2,3,4,9]† Jennifer A. Doudna[2,3,4,5,10]†

Type II CRISPR (clustered regularly interspaced short palindromic repeats)–Cas (CRISPR-associated) systems use an RNA-guided DNA endonuclease, Cas9, to generate double-strand breaks in invasive DNA during an adaptive bacterial immune response. Cas9 has been harnessed as a powerful tool for genome editing and gene regulation in many eukaryotic organisms. We report 2.6 and 2.2 angstrom resolution crystal structures of two major Cas9 enzyme subtypes, revealing the structural core shared by all Cas9 family members. The architectures of Cas9 enzymes define nucleic acid binding clefts, and single-particle electron microscopy reconstructions show that the two structural lobes harboring these clefts undergo guide RNA–induced reorientation to form a central channel where DNA substrates are bound. The observation that extensive structural rearrangements occur before target DNA duplex binding implicates guide RNA loading as a key step in Cas9 activation.

Bacteria and archaea target invasive DNA using RNA-guided adaptive immune systems encoded by CRISPR (clustered regularly interspaced short palindromic repeats)–Cas (CRISPR-associated) genomic loci (*1*–*4*). After integration of short fragments of invader-derived DNA into a CRISPR array within the host chromosome (*5*), enzymatic processing of CRISPR transcripts produces mature CRISPR RNAs (crRNAs) that direct Cas protein–mediated targeting of DNA bearing complementary sequences (protospacers) to foreign nucleic acids (*6*). Although type I and III CRISPR-Cas systems rely on multiprotein complexes for crRNA-guided DNA targeting (*1*, *4*, *7*), type II systems use a single RNA-guided endonuclease, Cas9, that requires both a mature crRNA and a trans-activating crRNA (tracrRNA) for target DNA recognition and cleavage (*8*, *9*). Both a seed sequence in the crRNA and conserved protospacer adjacent motif (PAM) sequence in the target are crucial for Cas9-mediated cleavage (*8*, *10*).

Cas9 proteins are abundant across the bacterial kingdom, but vary widely in both sequence and size. All known Cas9 enzymes contain an HNH domain that cleaves the DNA strand complementary to the guide RNA sequence (target strand), and a RuvC nuclease domain required for cleaving the noncomplementary strand (nontarget strand), yielding double-strand DNA breaks (DSBs) (*8*, *10*). In addition, Cas9 enzymes contain a highly conserved arginine-rich (Arg-rich) region previously suggested to mediate nucleic acid binding (*11*). On the basis of CRISPR-Cas locus architecture and protein sequence phylogeny, Cas9 genes cluster into three subfamilies: types II-A, II-B, and II-C (*12*, *13*). Cas9 proteins found in II-A and II-C subfamilies typically contain ~1400 and ~1100 amino acids, respectively.

The ability to program Cas9 for DNA cleavage at specific sites defined by guide RNAs has led to its adoption as a versatile platform for genome engineering (*14*). When directed to target loci in eukaryotes by either dual crRNA:tracrRNA guides or chimeric single-guide RNAs, Cas9 generates site-specific DSBs that are repaired either by nonhomologous end joining or by homologous recombination (*15*–*17*), which can be exploited to modify genomic sequences in the vicinity of the Cas9-generated DSBs. Furthermore, catalytically inactive Cas9 alone or fused to transcriptional activation or repression domains can be used to control transcription at sites defined by guide RNAs (*18*–*20*). Both type II-A and type II-C Cas9 proteins have been used in eukaryotic genome editing (*21*, *22*). Smaller Cas9 proteins, encoded by more compact genes, are potentially advantageous for cellular delivery using vectors that have limited size such as adeno-associated virus and lentivirus.

Here, we present the crystal structures of Cas9 enzymes from the two major enzyme subclasses (type II-A and type II-C). Both structures reveal the fundamental RNA-guided DNA endonuclease architecture, the locations of both active sites, and the likely nucleic acid binding clefts. Biochemical experiments show that PAM recognition occurs through a composite binding site that is disordered in the absence of guide RNA and substrate interactions. Single-particle electron microscopy (EM) structures show that guide RNA loading triggers a conformational change in Cas9 for productive DNA surveillance. Together, these data provide insights into the function, regulation, and evolution of the Cas9 enzyme family.

Streptococcus pyogenes Cas9 Structure Reveals a Two-Lobed Architecture with Adjacent Active Sites

Streptococcus pyogenes Cas9 (SpyCas9) is a prototypical type II-A Cas9 protein consisting of well-conserved RuvC and HNH domains, and flanking regions lacking apparent sequence similarity to known protein structures (Fig. 1A). As the first biochemically characterized Cas9, SpyCas9 is used in most of the current CRISPR-based genetic engineering methodologies (*14*). To obtain structural insights into the architecture of SpyCas9, we determined the 2.6-Å resolution crystal structure of the enzyme (Table 1). The structure reveals that SpyCas9 is a crescent-shaped molecule with approximate dimensions of 100 Å × 100 Å × 50 Å (Fig. 1B and fig. S1). The enzyme adopts a distinct bilobed architecture comprising the nuclease domains and the C-terminal domain in one lobe (the nuclease lobe), and a large α-helical domain in the other. The RuvC domain forms the structural core of the nuclease lobe, a six-stranded β sheet surrounded by four α helices, with all three conserved motifs contributing catalytic residues to the active site (fig. S1). The HNH and RuvC domains are juxtaposed in the SpyCas9 structure, with their active sites located ~25 Å apart. The HNH domain active site is poorly ordered in apo-SpyCas9 crystals, suggesting that the active site may undergo conformational ordering upon nucleic acid binding. The C-terminal region of SpyCas9 contains a β-β-α-β Greek key domain that bears structural similarity to a domain found in topoisomerase II (*23*) (hereafter referred to as the Topo-homology domain, residues 1136^{Spy} to 1200^{Spy}). A mixed α/β region (C-terminal domain, residues 1201^{Spy} to 1363^{Spy}) forms a protrusion on the nuclease domain lobe. The structural halves of SpyCas9 are connected by two linking segments, one formed by the Arg-rich region (residues 59^{Spy} to 76^{Spy}) and the other by a disordered linker comprising

[1]Department of Biochemistry, University of Zurich, CH-8057 Zurich, Switzerland. [2]Department of Molecular and Cell Biology, University of California, Berkeley, CA 94720, USA. [3]Howard Hughes Medical Institute (HHMI), University of California, Berkeley, CA 94720, USA. [4]California Institute for Quantitative Biosciences, University of California, Berkeley, CA 94720, USA. [5]Department of Chemistry, University of California, Berkeley, CA 94720, USA. [6]Laboratory for Molecular Infection Medicine Sweden (MIMS), Umeå University, Umeå S-90187, Sweden. [7]Department of Regulation in Infection Biology, Helmholtz Centre for Infection Research, D-38124 Braunschweig, Germany. [8]Hannover Medical School, D-30625 Hannover, Germany. [9]Life Sciences Division, Lawrence Berkeley National Laboratory, Berkeley, CA 94720, USA. [10]Physical Biosciences Division, Lawrence Berkeley National Laboratory, Berkeley, CA 94720, USA.

*These authors contributed equally to this work.
†Corresponding author. E-mail: jinek@bioc.uzh.ch (M.J.); enogales@lbl.gov (E.N.); doudna@berkeley.edu (J.A.D.)
‡Present address: Friedrich Miescher Institute for Biomedical Research, CH-4058 Basel, Switzerland.
§Present address: Department of Agricultural and Biological Engineering, University of Florida, Gainesville, FL 32611, USA.

residues 714^{Spy} to 717^{Spy} (Fig. 1B). The total surface area buried between the two structural lobes in SpyCas9 is 1034 Å^2.

SpyCas9 Contains Two Putative Nucleic Acid Binding Grooves

SpyCas9 contains two prominent clefts on one face of the molecule: a deep and narrow groove located within the nuclease lobe and a somewhat wider groove within the α-helical lobe (Fig. 1C). The nuclease lobe cleft is about 40 Å long, 15 to 20 Å wide, and 15 Å deep, with the RuvC active site located at its bottom. The C-terminal domain forms one side of the cleft, whereas the HNH domain and a protrusion of the α-helical lobe form the other. The concave surface of the α-helical lobe creates a wider, shallower groove that extends over almost its entire length (Fig. 1C). The groove is more than 25 Å across at its widest point, which would be sufficient to accommodate an RNA-RNA or DNA-RNA duplex. Its surface is highly positively charged (Fig. 1D), especially at the Arg-rich segment comprising R69^{Spy}, R70^{Spy}, R71^{Spy}, R75^{Spy}, and K76^{Spy}. Multiple sulfate or tungstate ions are bound to the α-helical lobe in the SpyCas9 crystals (fig. S2), hinting at a possible role in nucleic acid binding. Amino acid residues located in both the nuclease and α-helical lobe clefts are highly conserved within type II-A Cas9 proteins (Fig. 1E), suggesting that both clefts play important functional roles. Because the RuvC domain mediates cleavage of the nontarget DNA strand (*8*, *10*), the nuclease domain cleft likely binds the displaced nontarget strand. Conversely, the α-helical lobe, which contains the Arg-rich segment, might be involved in binding the crRNA:tracrRNA guide RNA and/or the crRNA–target DNA heteroduplex. This would be consistent with the observation that a mutation in the Arg-rich region in *Francisella novicida* Cas9 leads to loss of RNA-guided targeting in vivo (*11*).

PAM Recognition by SpyCas9 Involves Two Tryptophan-Containing Flexible Loops

SpyCas9 recognizes a 5′-NGG-3′ PAM sequence located 3 base pairs (bp) to the 3′ side of the cleavage site on the noncomplementary DNA strand, whereas other Cas9 orthologs have different PAM requirements (*8*, *10*, *22*, *24*–*27*). To gain insight into PAM binding by SpyCas9, we superimposed the SpyCas9 RuvC nuclease domain structure with that of the RuvC Holliday junction resolvase–substrate complex (*28*) (fig. S3A), which enabled us to model the likely trajectory of the nontarget DNA strand in the SpyCas9 holoenzyme (Fig. 2A and fig. S3, B and C). The DNA strand is located along the length of the nuclease lobe cleft in an orientation that would position the 3′ end of the DNA, and hence the PAM, at the junction of the two lobes, in the vicinity of the Arg-rich segment and the Topo-homology domain (Fig. 2B).

To directly identify regions of Cas9 involved in PAM binding, we reconstituted catalytically inactive SpyCas9 (D10A/H840A) with a crRNA:tracrRNA guide RNA and bound it to DNA targets carrying a photoactivatable 5-bromo-2′-deoxyuridine (BrdU) nucleotide adjacent to either end of the GG PAM motif on the nontarget strand (Fig. 2C). After ultraviolet (UV) irradiation and trypsin digestion, covalent peptide-DNA cross-links were detected (Fig. 2C and fig. S4). A

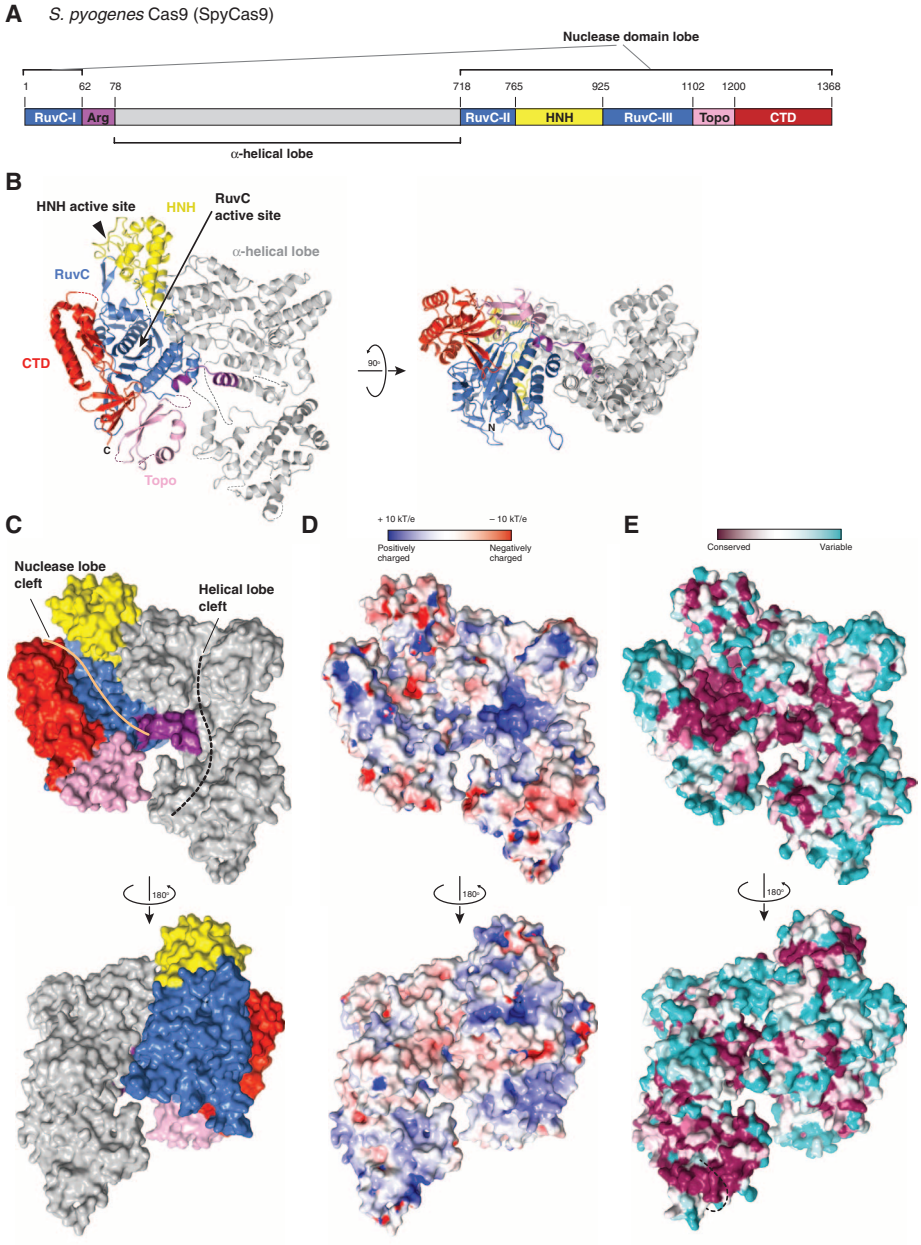

Fig. 1. Crystal structure of SpyCas9 reveals an open bilobed architecture and nucleic acid binding clefts. (**A**) Cartoon schematic of the polypeptide sequence and domain organization for the type II-A Cas9 protein from *S. pyogenes* (SpyCas9). Cas9 is predicted to contain a single HNH nuclease domain and a single RuvC nuclease domain. The RuvC domain is made up of three discontinuous segments (RuvC-I to RuvC-III), with the α-helical lobe inserted between the first and the second segments, and the HNH domain inserted between the second and the third segments. Arg, arginine-rich region; Topo, Topo-homology domain; CTD, C-terminal domain. (**B**) Orthogonal views of the overall structure of SpyCas9 shown in ribbon representation. Individual Cas9 domains are colored according to the scheme in (A). SpyCas9 consists of a nuclease domain lobe and an α-helical lobe. Disordered segments of the polypeptide chain are denoted with dotted lines. (**C**) Surface representation of SpyCas9 depicting the two nucleic acid binding clefts on the molecular surface. (**D**) Surface electrostatic potential map of SpyCas9 colored from −10 kT/e (red) to +10 kT/e (blue) (*61*). (**E**) Surface representation of SpyCas9 colored according to evolutionary conservation. The representation was generated using the ConSurf server (*62*) based on the multiple sequence alignment of type II-A Cas9 proteins shown in fig. S1. A disordered segment (residues 571^{Spy} to 586^{Spy}, indicated with a black dashed line) covers the apparently conserved patch on the reverse convex surface of SpyCas9.

DNA substrate containing BrdU on the target strand opposite the PAM failed to produce a cross-link (fig. S4). After nuclease and phosphatase digestion of cross-linked DNA, nano–high-performance liquid chromatography (HPLC) tandem mass spectrometry (MS/MS) was performed to identify tryptic peptides containing covalent dU or p-dU adducts (Fig. 2C and figs. S5 and S6). The nucleotide immediately 5′ to the GG motif cross-linked to residue $W476^{Spy}$, whereas the residue immediately 3′ to the motif cross-linked to residue $W1126^{Spy}$ (figs. S5 and S6). Both tryptophans are located in disordered regions of SpyCas9 located ~30 Å apart. $W476^{Spy}$ resides in a 53–amino acid loop at the edge of the α-helical lobe underneath the Arg-rich region, whereas $W1126^{Spy}$ is located in a 33–amino acid loop connecting the RuvC and Topo-homology domains (Fig. 2B). These tryptophan residues are conserved among type II-A Cas9 proteins that use the same NGG PAM to cleave target DNA in vitro (*8*, *27*), but are absent from type II-C Cas9 proteins, which are known to recognize different PAMs (*22*, *25*–*27*) (figs. S1 and S7). The type II-B Cas9 protein from *F. novicida*, whose PAM was recently shown to be 5′-NG-3′, contains a tryptophan ($W501^{Fno}$) at the position corresponding to $W476^{Spy}$, but lacks an aromatic residue equivalent to $W1126^{Spy}$ (*27*).

To test the roles of both loops in DNA target recognition and cleavage, we made triple alanine substitutions of residues 475^{Spy} to 477^{Spy} (P-W-N) and 1125^{Spy} to 1127^{Spy} (D-W-D) and performed cleavage assays with double-stranded DNA (dsDNA) targets (Fig. 2D and fig. S8). SpyCas9 mutated in residues 1125^{Spy} to 1127^{Spy} showed wild-type cleavage activity, whereas mutations in residues 475^{Spy} to 477^{Spy} caused a subtle, but reproducible, decrease in activity (fig. S9). Remarkably, mutating both loops simultaneously almost completely abolished SpyCas9 activity, indicating that at least one tryptophan-containing segment is necessary to promote DNA cleavage (Fig. 2D and fig. S10). The distance of both tryptophan residues from either nuclease domain argues against their direct catalytic role in DNA cleavage, instead suggesting that the residues are involved in PAM recognition. Consistent with this, DNA binding assays showed that each triple-mutant protein is moderately defective in DNA binding, whereas the dual triple-mutant protein has markedly reduced DNA binding affinity (fig. S11).

Actinomyces naeslundii Cas9 Structure Reveals the Architecture of a Smaller Cas9 Variant

Although most genome engineering methodologies currently use SpyCas9, there is considerable interest in exploiting more compact Cas9 enzymes for such applications (*21*, *22*). To understand how the large and small Cas9 variants are related and how they carry out similar catalytic functions, we determined the 2.2-Å resolution crystal structure of the type II-C Cas9 enzyme from *Actinomyces naeslundii* (AnaCas9) (Table 2). AnaCas9 also folds into a bilobed structure with approximate dimensions of 105 Å × 80 Å × 55 Å. The RuvC and HNH nuclease domains, a Topo-homology domain, and the C-terminal domain form an extended nuclease lobe with the RuvC domain

Table 1. X-ray data collection, refinement, and model statistics for SpyCas9.

Data set	Native	$MnCl_2$ soak	SeMet	Sodium tungstate	$CoCl_2$ soak	Er(III) acetate soak	Thimerosal soak
X-ray source	SLS PXI	SLS PXIII	ALS 8.2.2	SLS PXI	SLS PXIII	ALS 8.2.2	SLS PXIII
Space group	$P2_12_12$	$P2_12_12$	$P2_12_12$	$P2_12_12$	$P2_12_12$	$P2_12_12$	$P2_12_12$
Cell dimensions							
a, *b*, *c* (Å)	159.8, 209.6, 91.3	159.8, 209.3, 91.0	158.9, 201.1, 89.7	160.0, 209.5, 90.5	161.3, 210.9, 91.0	159.5, 209.2, 90.9	159.5, 209.1, 90.5
α, β, γ (°)	90.0, 90.0, 90.0	90.0, 90.0, 90.0	90.0, 90.0, 90.0	90.0, 90.0, 90.0	90.0, 90.0, 90.0	90.0, 90.0, 90.0	90.0, 90.0, 90.0
Wavelength (Å)	1.00000	1.00000	0.979168	1.2149	1.58955	1.475991	1.00392
Resolution (Å)*	127.07–2.62 (2.69–2.62)	47.48–3.10 (3.18–3.10)	87.64–4.20 (4.31–4.20)	49.77–3.90 (4.00–3.90)	47.9–3.60 (3.69–3.60)	87.45–3.30 (3.39–3.30)	47.38–3.59 (3.69–3.59)
R_{sym} (%)*	4.7 (63.6)	9.6 (94.0)	15.2 (71.4)	12.2 (87.0)	8.6 (76.3)	6.7 (39.7)	19.4 (78.8)
$I/\sigma I$*	13.02 (1.94)	19.1 (2.3)	9.7 (2.9)	17.3 (4.1)	14.2 (3.0)	10.4 (2.1)	10.4 (2.5)
Completeness (%)*	98.2 (98.5)	100.0 (100.0)	99.9 (99.8)	99.9 (99.9)	100.0 (100.0)	98.4 (99.4)	99.4 (92.8)
Redundancy*	2.3 (2.3)	7.1 (7.3)	6.0 (6.0)	14.0 (14.1)	7.1 (7.0)	2.1 (2.1)	7.0 (5.9)
Refinement							
Resolution (Å)	47.52–2.62	47.53–3.09					
No. of reflections	92,408	56,200					
R_{work}/R_{free}	0.253/0.286	0.252/0.278					
No. of atoms							
Protein	18,892	18,862					
Ion	26	43					
Water	203	0					
B-factors							
Mean	62.6	62.3					
Protein	62.8	62.2					
Ion	68.8	79.1					
Water	45.8	91.8					
Root mean square deviation							
Bond lengths (Å)	0.005	0.004					
Bond angles (°)	0.95	0.74					
Ramachandran plot							
% Favored	96.2	97.6					
% Allowed	3.8	2.4					
% Outliers	0.0	0.0					
MolProbity							
Clashscore	10.3	8.2					

*Values in parentheses denote highest-resolution shell.

located at its center (Fig. 3, A and B). Similar to SpyCas9, the RuvC and HNH domains comprise a compact catalytic core, with the two active sites positioned ~30 Å apart. In contrast to SpyCas9, an additional domain (residues 822^{Ana} to 924^{Ana}, hereafter referred to as the β-hairpin domain) is found between the RuvC and Topo-homology domains, and adopts a novel fold composed primarily of three antiparallel β-hairpins. As in SpyCas9, the polypeptide sequence found between the RuvC-I and RuvC-II motifs forms an α-helical lobe. However, the AnaCas9 α-helical lobe is much smaller, and its orientation relative to the nuclease lobe is different (Fig. 3C and fig. S12, A to C). Comparison of the helical lobes in AnaCas9 and SpyCas9 reveals that regions 95^{Ana} to 251^{Ana} and 77^{Spy} to 447^{Spy} are highly divergent and do not align in sequence and structure (fig. S7). Moreover, the 95^{Ana} to 251^{Ana} region is poorly ordered (fig. S13A), and only parts of it could be modeled. By contrast, residues 252^{Ana} to 468^{Ana} and 502^{Spy} to 713^{Spy}, which share ~32% sequence identity, superimpose well with a root mean square deviation of ~3.6 Å over 149 Cα atoms (Fig. 3C and fig. S12, A to H). Intriguingly, the position and orientation of this portion of the α-helical domain with respect to the RuvC domain in the AnaCas9 and SpyCas9 structures are substantially different, with a large displacement of ~70 Å toward the RuvC domain and an about 35° rotation about the junction between two domains in AnaCas9 (fig. S12C).

The higher resolution of the AnaCas9 structure provides insights into active-site chemistries for both nuclease domains. The well-defined AnaCas9 HNH domain contains a two-stranded antiparallel β sheet flanked by two α helices on each side, as well as a nonconserved noncatalytic zinc binding site (Fig. 3C and fig. S13B). The HNH active site reveals D581^{Ana} and N606^{Ana} coordinating a hydrated magnesium ion that would be involved in binding the scissile phosphate in the target DNA strand (Fig. 3D), and the general base residue H582^{Ana} (corresponding to H840^{Spy}) involved in deprotonating the attacking water nucleophile, in agreement with a one–metal ion catalytic mechanism for the endonucleases containing the ββα metal motif (*29*). In the RuvC domain, two Mn^{2+} ions, spaced 3.8 Å apart and coordinated by the invariant residues D17^{Ana}, E505^{Ana}, H736^{Ana}, and D739^{Ana}, are consistent

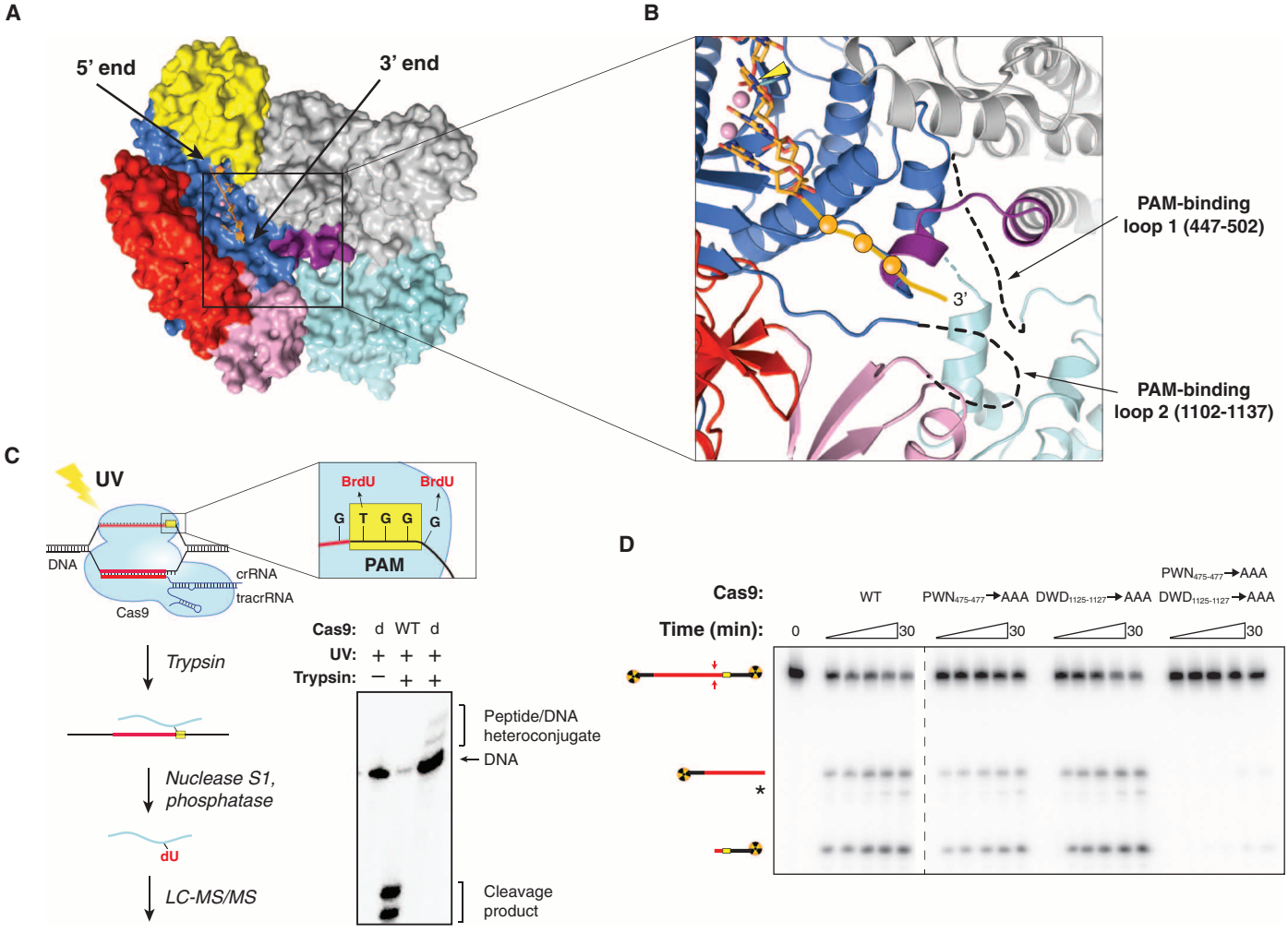

Fig. 2. Cross-linking identifies a PAM binding region adjacent to the active-site cleft. (**A**) Model of noncomplementary DNA strand bound to the RuvC domain based on a superposition with the DNA-bound complex of *Thermus thermophilus* RuvC Holliday junction resolvase [Protein Data Bank (PDB) entry 4LD0]. The modeled DNA strand contains three nucleotides upstream and three nucleotides downstream of the scissile phosphate. Divalent ions in the RuvC active site are depicted as pink spheres. (**B**) Zoomed-in view of the RuvC cleft showing the modeled nontarget DNA strand (stick format, scissile phosphate indicated with yellow arrowhead) and the predicted path of the downstream (3′) sequence containing the PAM (orange ball and string). Disordered loops identified by cross-linking are denoted with dashed lines. (**C**) Cartoon (left) showing the design and workflow of cross-linking experiments with DNA substrates containing BrdU nucleotides for LC-MS/MS analysis. The guide/target sequence is depicted in red, and the PAM is highlighted in yellow. The denaturing polyacrylamide gel (right) demonstrates the generation of covalent peptide-DNA adducts with catalytically inactive SpyCas9 (dCas9) after UV irradiation and trypsin digestion. (**D**) DNA cleavage activity assays with SpyCas9 constructs containing mutations in residues identified by cross-linking and LC-MS/MS experiments. The asterisk denotes trimming of the nontarget strand.

with a two–metal ion mechanism, as observed in other nucleases containing the ribonuclease (RNase) H fold (Fig. 3E) (*30*, *31*).

A Common Cas9 Functional Core Suggests Structural Plasticity that Supports RNA-Guided DNA Cleavage

Comparison of the SpyCas9 and AnaCas9 structures reveals a conserved functional core consisting of the RuvC and HNH domains, the Arg-rich region, and the Topo-homology domain, with divergent C-terminal and α-helical domains (Fig. 3F). In both SpyCas9 and AnaCas9, the Arg-rich region connects the nuclease and helical lobes of the proteins. The central position of the Arg-rich segment and its proximity to the PAM binding loops in SpyCas9 suggest that this region may be involved in guide RNA and/or target DNA binding and could function as a hinge to enable conformational rearrangements in the enzyme.

Although the helical lobes of SpyCas9 and AnaCas9 share a common region (residues 252^{Ana} to 468^{Ana} versus 502^{Spy} to 713^{Spy}), the orientation of this region relative to the nuclease lobe varies in the two structures (Fig. 3F). Differences between SpyCas9 and AnaCas9 thus illustrate the structural divergence likely responsible for the diversity of guide RNA structures and PAM specificities within the Cas9 superfamily. The PAM-interacting regions identified in SpyCas9 are located in loops that are highly variable within Cas9 enzymes (*12*, *13*). In AnaCas9, the β-hairpin domain (residues 822^{Ana} to 924^{Ana}) is inserted at a position corresponding to one of the SpyCas9 PAM loops (1102^{Spy} to 1136^{Spy}), suggesting that AnaCas9 uses a distinct mechanism of PAM recognition (Fig. 3C and fig. S7). The β-hairpin domain is not conserved in all type II-C Cas9 proteins (figs. S7 and S14), further underscoring the notion that the sequence- and structure-divergent regions of Cas9 proteins may have coevolved with specific guide RNA structures and PAM sequences (*13*, *27*).

SpyCas9 and AnaCas9 Adopt Autoinhibited Conformations in the Apo State

Target DNA cleavage by Cas9 RuvC and HNH domains is thought to occur upon base pairing between the crRNA guide and the target DNA (*8*, *10*, *32*). Although SpyCas9 and AnaCas9 adopt distinct conformations in their helical lobes, the relative orientations of the RuvC and HNH active sites within the nuclease lobes are very similar (Fig. 3C and fig. S12). In both structures, the HNH active site faces outwards, away from the putative nucleic acid binding clefts (Figs. 1B and 4B). Structural superpositions with the DNA-bound complex of the HNH homing endonuclease I-HmuI (*33*) suggest that this orientation is unlikely to be compatible with target DNA binding and cleavage (Fig. 4A). In SpyCas9, the HNH domain active site is blocked by a β-hairpin formed by residues 1049^{Spy} to 1059^{Spy} of the RuvC domain. The RNA-DNA heteroduplex would additionally clash sterically with the C-terminal domain (Fig. 4, A and B). In AnaCas9, the bound crRNA–target DNA heteroduplex would conversely make few contacts with the protein outside of the HNH domain in the absence of HNH domain reorientation (Fig. 4A, right panel). The finding that two highly divergent Cas9 orthologs exhibit similar inactive states suggests that this may be a general property of Cas9 enzymes and not a consequence of crystallization. It is also consistent with the observation that Cas9 enzymes are inactive as nucleases in the absence of bound guide RNAs (*8*, *9*). Together, these observations suggest that the enzymes undergo a conformational rearrangement upon guide RNA and/or target DNA binding.

RNA Loading Rearranges the Two Lobes of SpyCas9 to Form a Central Channel

To visualize conformational states adopted by Cas9 upon guide RNA and target DNA binding, we determined the molecular architectures of SpyCas9 without guide RNA (apo-SpyCas9), in complex with crRNA:tracrRNA (SpyCas9:RNA), and bound to target DNA (SpyCas9:RNA:DNA) using negative-stain EM. Raw micrographs of the ~160-kD apo-SpyCas9 enzyme show monodisperse, globular particles with approximate dimensions of 120 Å × 140 Å, and two-dimensional (2D) reference-free class averages reveal that the enzyme has a two-lobed morphology in agreement with the crystal structure (fig. S15). We used the random conical tilt (RCT) method (*34*) to obtain an initial, ab initio 3D model of the complex (fig. S15). Using multiple refinement procedures (see Materials and Methods), we arrived at a final reconstruction of apo-SpyCas9 at ~19-Å resolution [using the 0.5 Fourier shell correlation (FSC) criterion] that reveals a clam-shaped morphology with one large, globular lobe connected to a smaller lobe (Fig. 5A). Using Situs (*35*), we were able to computationally dock the α-helical and nuclease domain lobes of the SpyCas9 crystal structure as rigid bodies into the larger and smaller lobes, with cross-correlation coefficients (CCCs) of 0.74 and 0.66, respectively (fig. S16 and table S1). To further support our lobe assignment, we generated a 3D reconstruction of Cas9 containing an N-terminal maltose-binding protein (N-MBP) fusion directly upstream of the RuvC-I

Table 2. X-ray data collection, refinement, and model statistics for AnaCas9.

Data set	SeMet	Native	Mn soak
X-ray source	ALS 8.3.1	ALS 8.3.1	ALS 8.2.2
Space group	$P1\ 2_1\ 1$	$P1\ 2_1\ 1$	$P1\ 2_1\ 1$
Cell dimensions			
a, *b*, *c* (Å)	74.58, 133.09, 80.17	75.415, 133.025, 80.69	74.61, 132.56, 80.04
α, β, γ (°)	90.00, 95.79, 90.00	90, 96.22, 90	90, 95.38, 90
Wavelength (Å)	0.978	1.116	1.000
Resolution (Å)*	79.76–3.19 (3.37–3.19)	80.2–2.2 (2.32–2.2)	79.69–2.80 (2.95–2.80)
R_{merge} (%)*	0.124 (0.428)	0.096 (0.795)	0.090 (0.628)
R_{pim}†	0.05 (0.176)	0.029 (0.322)	0.05 (0.358)
$I/\sigma I$*	11.9 (4.6)	14.89 (2.24)	10.86 (2.27)
Completeness (%)*	99.9 (99.7)	98.0 (86.8)	99.98 (100.00)
Redundancy*	7.9 (7.8)	8.6 (5.8)	4.0 (4.0)
Refinement			
Resolution (Å)		68.0–2.2	68.3–2.8 (2.9–2.8)
No. of reflections		78,398	38,217
R_{work}/R_{free}		0.1867/0.2281	0.1941/0.2310
No. of atoms			
Protein		7693	6888
Ligands		24	27
Water		348	4
B-factors			
Mean		57.9	67.3
Protein		58.6	67.3
Ion		52.2	64.9
Water		42.01	42.7
Root mean square deviations			
Bond lengths (Å)		0.009	0.005
Bond angles (°)		1.22	0.84
Ramachandran plot			
% Favored		94.00	95.00
% Allowed		5.80	4.77
% Outliers		0.20	0.23
MolProbity			
Clashscore		9.8	6.2

*Values in parentheses denote highest-resolution shell. †R_{pim} = precision-indicating (multiplicity-weighted) R_{merge}.

motif; N-MBP–Cas9 retains full DNA cleavage activity (fig. S16). By 3D difference mapping, the additional density observed in this reconstruction was found to localize to the smaller lobe containing the RuvC nuclease domain (fig. S16).

We next prepared ribonucleoprotein complexes containing catalytically inactive D10A/H840A-SpyCas9 mutant, full-length crRNA:tracrRNA (SpyCas9:RNA), and bound these complexes to a 55-bp dsDNA substrate at substrate concentrations expected to saturate Cas9, given an equilibrium dissociation constant of ~4 nM (fig. S17). Reference-free 2D class averages of the DNA-bound complex (SpyCas9:RNA:DNA) hinted at a large-scale conformational change, with both lobes separating from one another into discrete structural units (fig. S17). Using the apo-SpyCas9 structure low-pass filtered to 60 Å as a starting model, we obtained a 3D reconstruction of SpyCas9:RNA:DNA at ~19 Å resolution (using the 0.5 FSC criterion) that further revealed a substantial reorganization of the major lobes (Fig. 5B). An independently determined ab initio 3D structure using the RCT method (*34*) yielded similar results (fig. S17). The shape of the larger lobe remains relatively unchanged from that in apo-Cas9 (CCC of 0.78), but the smaller lobe rotates by ~100° with respect to its position in the apo structure (Fig. 5B). An alternative model, assuming opposite handedness, also shows a large conformational change relative to the apo-Cas9 structure (fig. S18). A reconstruction of SpyCas9:RNA:DNA using the N-MBP fusion (fig. S17) confirmed that the nuclease domain–containing lobe is rearranged with respect to the α-helical lobe in this complex. In this rearrangement, the nuclease domain lobe closes over the putative nucleic acid binding cleft on the α-helical lobe, forming a central channel with a width of ~25 Å that spans the length of both lobes (fig. S16). Because nucleic acids cannot be visualized directly in EM structures of negatively stained complexes, this channel could be occupied by RNA and/or DNA.

We next wondered whether guide RNA alone induces the observed conformational rearrangements in SpyCas9, or whether both RNA and DNA are required for this structural change. To distinguish between these possibilities, we examined the architecture of SpyCas9:RNA in the absence of a bound target DNA molecule. Strikingly, reference-free 2D class averages of the SpyCas9:RNA showed a clear central channel similar to SpyCas9:RNA:DNA (fig. S19). Using the 3D reconstruction of SpyCas9:RNA:DNA low-pass filtered to 60 Å as a starting model, we obtained a reconstruction of SpyCas9:RNA at ~21-Å resolution (using the 0.5 FSC criterion), which reveals a conformation similar to that of the DNA-bound complex (CCC of 0.89 with DNA-bound versus 0.81 with apo), with a central channel extending between the two lobes (Fig. 5C and fig. S19). Both the SpyCas9:RNA and SpyCas9:RNA:DNA complexes were more resistant to limited proteolysis by trypsin than apo-SpyCas9 and displayed similar digestion patterns,

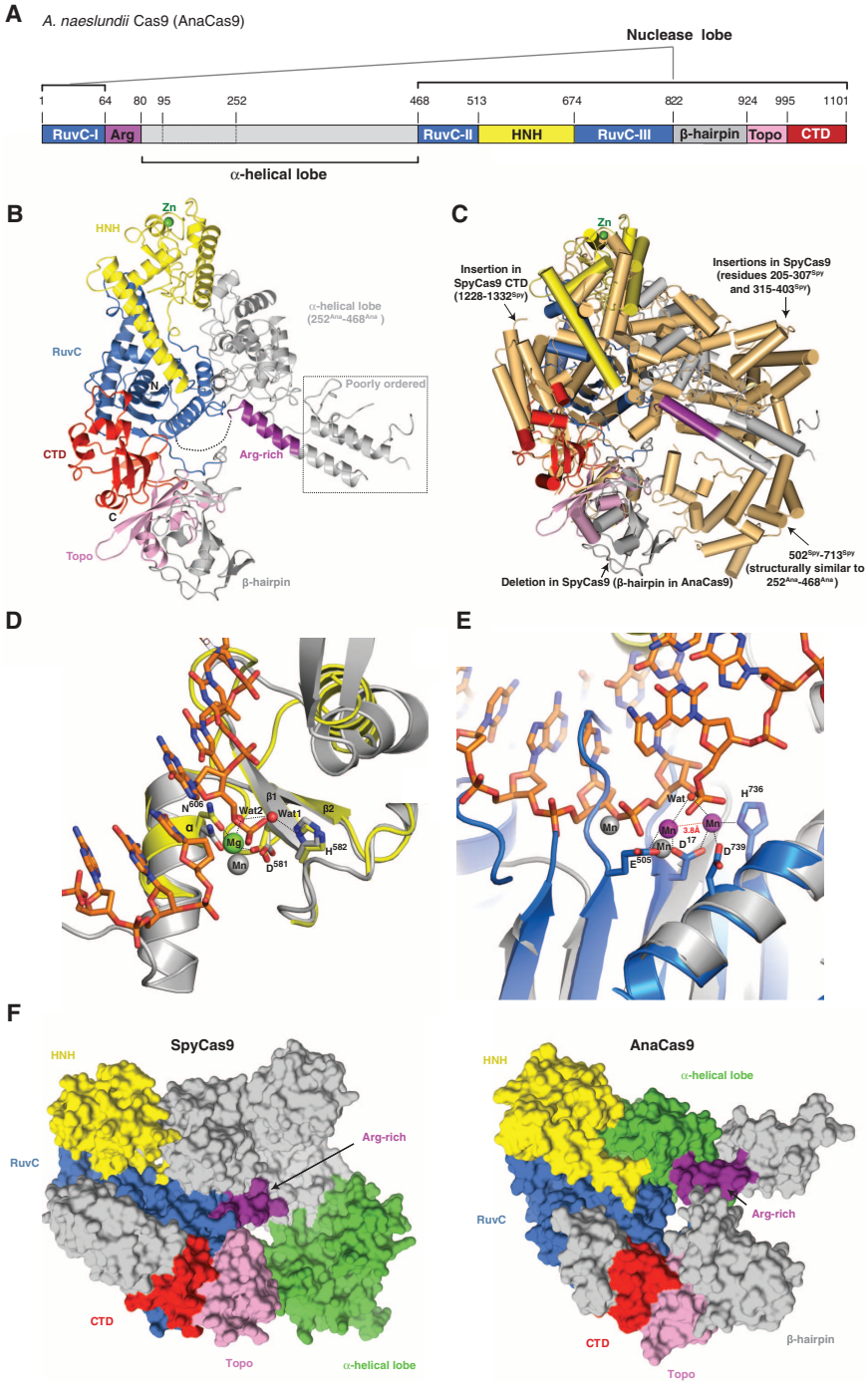

Fig. 3. Crystal structure of AnaCas9 defines the conserved structural core of Cas9 enzymes. (**A**) Cartoon schematic of the polypeptide sequence and domain organization for the type II-C Cas9 protein from *A. naeslundii* (AnaCas9). (**B**) Overall structure of AnaCas9 shown in ribbon representation. Individual Cas9 domains are colored according to the scheme in (A). A disordered segment connecting a RuvC motif and Arg-rich region is denoted with a dashed line. The disordered region in the helical lobe is denoted with a dotted line box. A green sphere denotes a bound zinc ion in the HNH domain. (**C**) Superposition of AnaCas9 [colored as in (A)] with SpyCas9 (colored light orange). (**D**) Close-up view of the active site of AnaCas9 HNH domain (yellow) superimposed with the structure of I-HmuI–DNA complex (PDB entry 1U3E). The DNA cleavage product in the I-HmuI–DNA complex is colored orange, and I-HmuI and its bound Mn^{2+} ion are colored gray. (**E**) Close-up view of the AnaCas9 RuvC active site (marine, bound Mn^{2+} ions shown as purple spheres) overlaid with the structure of RNase H and its bound Mn^{2+} ions (gray) complexed with a DNA-RNA duplex (orange) (PDB entry 3O3H). (**F**) Surface representations of SpyCas9 (left panel) and AnaCas9 (right panel) with conserved RuvC, HNH, Arg-rich, Topo-homology, and the conserved cores of the C-terminal domains, colored as in Fig. 1A. The structurally preserved portion of the α-helical lobe is colored green. The nonconserved regions of each protein are colored in gray.

in agreement with these nucleic acid–bound complexes occupying a similar structural state (fig. S20). Although the smaller lobe appears to undergo an additional ~50° rotation along an axis perpendicular to the channel in the DNA-bound complex compared to SpyCas9:RNA, the same ~100° rotation around the channel is observed in both structures. Thus, loading of crRNA and tracrRNA alone is sufficient to convert the endonuclease into an active conformation for target surveillance.

The Central Channel in SpyCas9 Accommodates Bound Target DNA and Guide RNAs

On the basis of the dimensions of the channel and the requirement for SpyCas9:RNA to recognize ~23 bp of its DNA substrate, we hypothesized that target DNA spans the central channel. To test this, we reconstituted SpyCas9:RNA:DNA complexes using DNA substrates containing 3′-biotin modifications (table S2) to visualize the duplex ends via streptavidin labeling. Negative-stain EM analysis of samples labeled at either the PAM-distal (non-PAM) end or both ends showed additional circular density below, or both above and below the complex, respectively, along the central channel positioned between the two structural lobes (Fig. 6, A and B). These data support the conclusion that the major lobes of SpyCas9 enclose the target DNA, positioning the RNA-DNA heteroduplex along the central channel with the PAM oriented near the top. The additional streptavidin densities in the double-end labeled class averages are not completely parallel with the channel and instead wrap around the nuclease lobe (Fig. 6B), consistent with some degree of bending of the target DNA. Finally, we determined the orientation of RNA within SpyCas9:RNA complexes using streptavidin labeling of crRNA and tracrRNA containing biotin at their 3′ termini, after ensuring that SpyCas9 retains full activity with these modified RNAs (fig. S21). Using the same 2D and 3D difference mapping approach, we pinpointed the 3′ end of the crRNA to the top of the channel (Fig. 6C), whereas the 3′ end of the tracrRNA is extended roughly perpendicular to the central channel from the side of the nuclease domain lobe (Fig. 6D). The finding that the 3′ end of the crRNA localizes to a similar position above the channel as the PAM-proximal side of the target suggests that the crRNA-DNA heteroduplex may be oriented roughly in parallel with the crRNA:tracrRNA duplex.

The channel between the lobes of SpyCas9:RNA:DNA can easily accommodate ~25 bp of a modeled A-form helix (Fig. 7A). Corroborating this, exonuclease III footprinting experiments indicated that Cas9 protects a ~26-bp segment of the target DNA (Fig. 7B). Additionally, P1 nuclease mapping experiments reveal that the displaced nontarget strand is susceptible to hydrolysis toward the 5′ end of the protospacer, whereas the target strand that hybridizes to crRNA is protected along nearly its entire length. These results are consistent with the formation of an R-loop structure (Fig. 7B), as observed for other CRISPR-Cas targeting complexes (*36*).

Discussion

The crystal structures of type II-A and II-C Cas9 proteins described here highlight the features in Cas9 enzymes that support their function as RNA-guided endonucleases. Cas9 enzymes adopt a bilobed architecture composed of a nuclease lobe containing juxtaposed RuvC and HNH nuclease domains and a variable α-helical lobe likely to be involved in nucleic acid binding. The identification of variable regions appended to a conserved Cas9 structural core provides a rationale for the diversity of crRNA:tracrRNA guide structures recognized by Cas9 enzymes and outlines a framework for protein engineering approaches aimed at altering catalytic function, guide RNA specificity, or PAM requirements.

Cross-linking experiments conducted in this study suggest that two unstructured tryptophan-containing loops in SpyCas9 contact the PAM in the target-bound complex. The location of the PAM binding loops suggests that Cas9 interrogates DNA using flexible regions that may form an ordered binding site upon engaging target DNA. It is tempting to speculate that the two tryptophan residues in SpyCas9 mediate base-stacking interactions with the GG dinucleotide PAM. Alternatively, the tryptophan residues could be involved in extrahelical base extrusion of the PAM motif, in a manner similar to the mechanisms of numerous DNA modification and repair enzymes (*37*–*40*). It is also possible that the tryptophan residues are not directly involved in PAM binding, but instead reside near the PAM binding pocket in the enzyme. We note, however, that the involvement of aromatic loop regions in SpyCas9 is highly reminiscent of the mechanism used by the Cascade complex in type I CRISPR-Cas systems (*41*). The lack of conservation of the PAM binding region in type II-C Cas9 enzymes is consistent with different PAM specificities observed for these endonucleases and points to distinct mechanisms of PAM recognition across the Cas9 enzyme family.

Single-molecule and biochemical experiments underscore the singular importance of PAM binding in both DNA interrogation and cleavage by Cas9 (*42*). The observed prevalence of PAM mutation as a mechanism of viral escape from CRISPR/Cas9 targeting (*43*, *44*) has presumably spurred the evolution of Cas9 proteins with a variety of PAM specificities. It will be interesting to elucidate how PAM binding couples to Cas9 activation across the Cas9 superfamily, which has important implications for the use of these enzymes in genome engineering applications.

Both SpyCas9 and AnaCas9 structures support the conclusion that Cas9 enzymes maintain an autoinhibited conformation in the absence of nucleic acid ligands that requires restructuring upon guide RNA and target DNA binding. Consistent with this finding, EM reconstructions of SpyCas9–nucleic acid complexes show that the two lobes of the protein reorient substantially upon guide RNA association. On the basis of these observations, we propose a model for Cas9 function in which RNA loading drives structural rearrangements of the enzyme to enable productive encounters with target DNA (Fig. 8). Binding of crRNA:tracrRNA

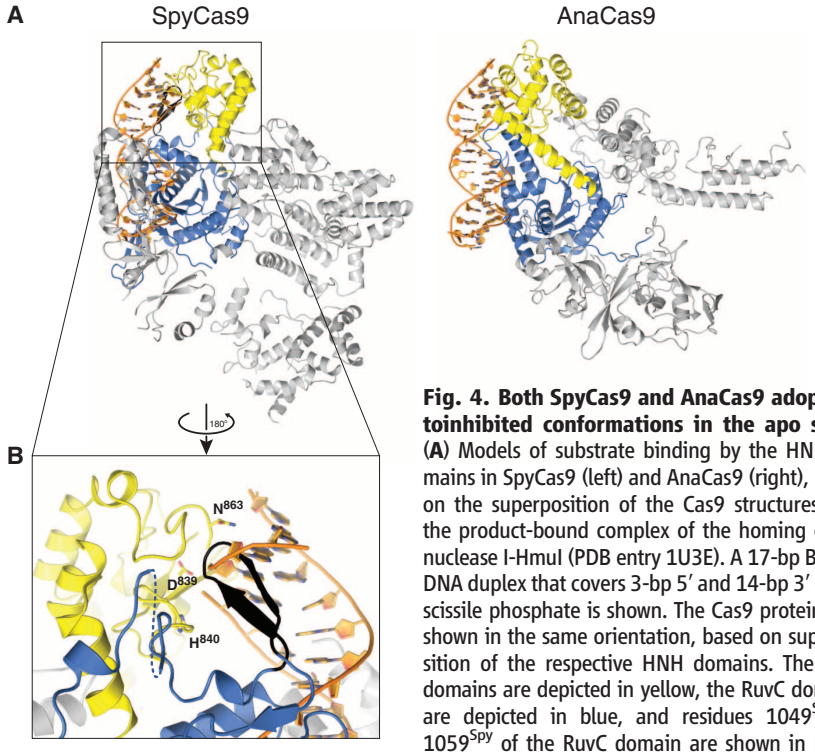

Fig. 4. Both SpyCas9 and AnaCas9 adopt autoinhibited conformations in the apo state. (**A**) Models of substrate binding by the HNH domains in SpyCas9 (left) and AnaCas9 (right), based on the superposition of the Cas9 structures with the product-bound complex of the homing endonuclease I-HmuI (PDB entry 1U3E). A 17-bp B-form DNA duplex that covers 3-bp 5′ and 14-bp 3′ of the scissile phosphate is shown. The Cas9 proteins are shown in the same orientation, based on superposition of the respective HNH domains. The HNH domains are depicted in yellow, the RuvC domains are depicted in blue, and residues 1049^{Spy} to 1059^{Spy} of the RuvC domain are shown in black. (**B**) Zoomed-in view of the HNH domain (yellow) active site in SpyCas9 occluded by the 1049^{Spy} to 1059^{Spy} β-hairpin (black).

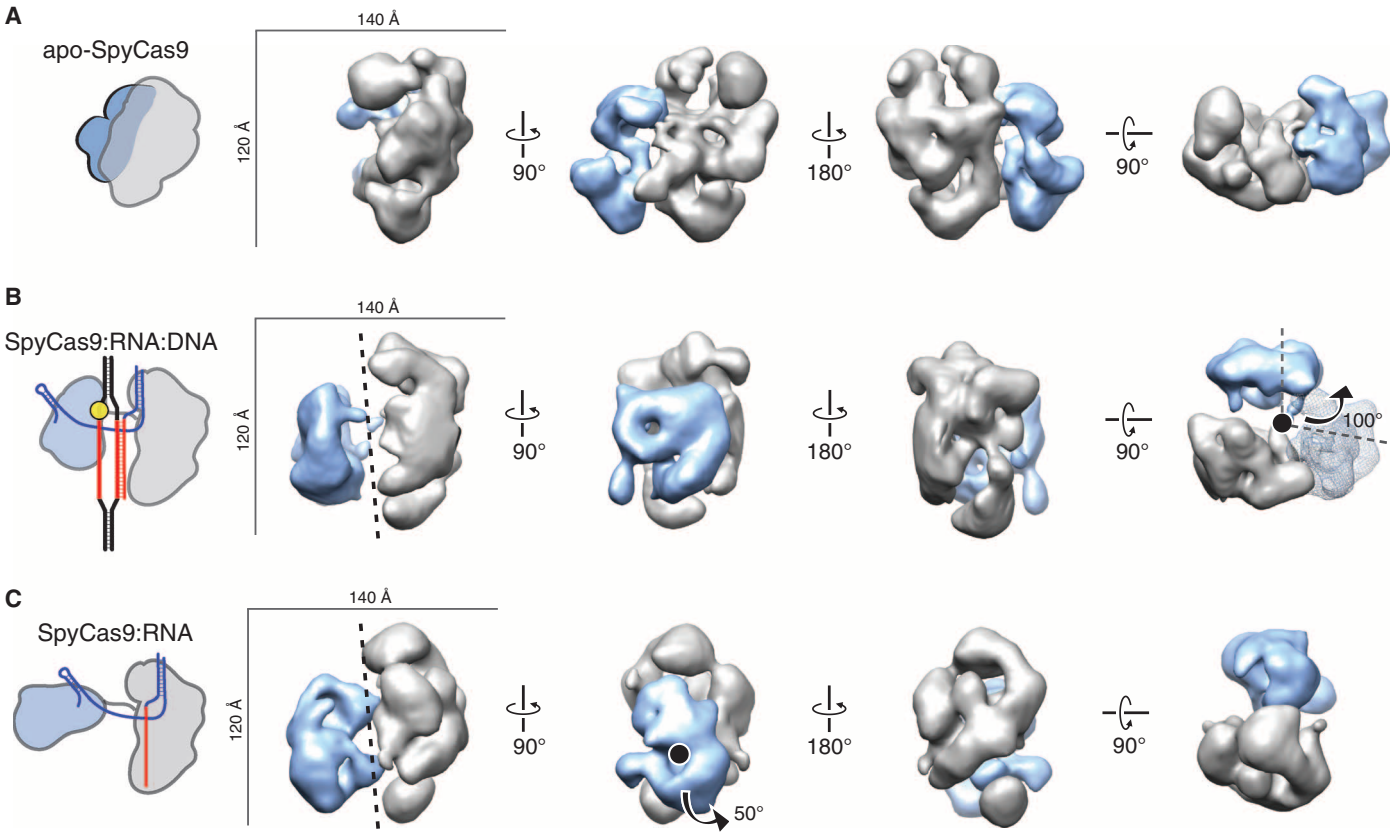

Fig. 5. RNA loading positions the two major lobes of SpyCas9 around a central channel. (**A** to **C**) Single-particle EM reconstructions of negatively stained apo-SpyCas9 (A), SpyCas9:RNA:DNA (B), and SpyCas9:RNA (C) at 19-, 19-, and 21-Å resolution (using the 0.5 FSC criterion), respectively. Cartoon representations of the structures are shown (left). The structures are aligned on the basis of the optimal CCCs between the independent α-helical lobes (gray). The smaller RuvC lobe (blue) in SpyCas9:RNA:DNA and SpyCas9:RNA rotates by ~100° [arrow in (B)] with respect to this lobe in the apo-Cas9 structure (transparent mesh) to form a central channel (black dashed line). There is a ~50° rotation [arrow in (C)] of the smaller lobe of SpyCas9:RNA along an axis perpendicular to this channel relative to SpyCas9:RNA:DNA.

to Cas9 causes a substantial rotation of the small nuclease lobe relative to the larger lobe. This RNA-induced conformational change could occur either through direct interactions between the RNA and both lobes, or indirectly through allosteric effects. This reorganization may position the two major catalytic centers of the enzyme on opposite sides of the central channel, where the two separated strands are threaded into either active site.

Although types I and III CRISPR-Cas RNA-guided surveillance complexes form helical architectures that wrap around the crRNA (*45*–*48*), Cas9 instead forms a central channel. The helical morphology in these other systems may have evolved to accommodate the topological requirements of a longer crRNA-DNA heteroduplex, and the open helical arrangement exhibited by the type I multisubunit Cascade complex likely facilitates recruitment of the trans-acting Cas3 nuclease for target cleavage (*49*). In contrast, Cas9 functions alone to both bind and cleave the DNA target, which could be facilitated by sequestering the substrate within the interior surface of the channel formed by both lobes. Although we do not observe extensive connecting density between the two lobes, we hypothesize that only one face will enable dsDNA to enter the central channel during 3D target search. Although further experiments will be necessary to elucidate the precise search and recognition mechanisms used by Cas9, our structural analysis shows that RNA loading serves as a key conformational switch in the activation and regulation of Cas9 enzymes.

Materials and Methods

Full details of experimental procedures are provided in the supplementary materials. SpyCas9 and its point mutants were expressed in *Escherichia coli* Rosetta 2 strain and purified essentially as described (*8*). SpyCas9 crystals were grown using the hanging drop vapor diffusion method from 0.1 M tris-Cl (pH 8.5), 0.2 to 0.3 M Li_2SO_4, and 14 to 15% (w/v) PEG 3350 (polyethylene glycol, molecular weight 3350) at 20°C. Diffraction data were measured at beamlines 8.2.1 and 8.2.2 of the Advanced Light Source (Lawrence Berkeley National Laboratory), and at beamlines PXI and PXIII of the Swiss Light Source (Paul Scherrer Institut) and processed using XDS (*50*). Phasing was performed with crystals of selenomethionine (SeMet)–substituted SpyCas9 and native Cas9 crystals soaked individually with 10 mM Na_2WO_4, 10 mM $CoCl_2$, 1 mM thimerosal, and 1 mM Er(III) acetate. Phases were calculated using autoSHARP (*51*) and improved by density modification using Resolve (*52*). The atomic model was built in Coot (*53*) and refined using phenix.refine (*54*).

A. naeslundii Cas9 (AnaCas9) was expressed in *E. coli* Rosetta 2 (DE3) as a fusion protein containing an N-terminal His_{10} tag followed by MBP and a TEV (tobacco etch virus) protease cleavage site. The protein was purified by Ni-NTA (nickel–nitrilotriacetic acid) and heparin affinity chromatography, followed by a gel filtration step. Crystals of native and SeMet-substituted AnaCas9 were grown from 10% (w/v) PEG 8000, 0.25 M calcium acetate, 50 mM magnesium acetate, and 5 mM spermidine. Native and SeMet single-wavelength anomalous diffraction (SAD) data sets were collected at beamline 8.3.1 of the Advanced Light Source, processed using Mosflm (*55*), and scaled in Scala (*56*). Phases were calculated in Solve/Resolve (*52*), and the atomic model was built in Coot and refined in Refmac (*57*) and phenix.refine (*54*).

For biochemical assays, crRNAs were synthesized by Integrated DNA Technologies, and tracrRNA was prepared by in vitro transcription

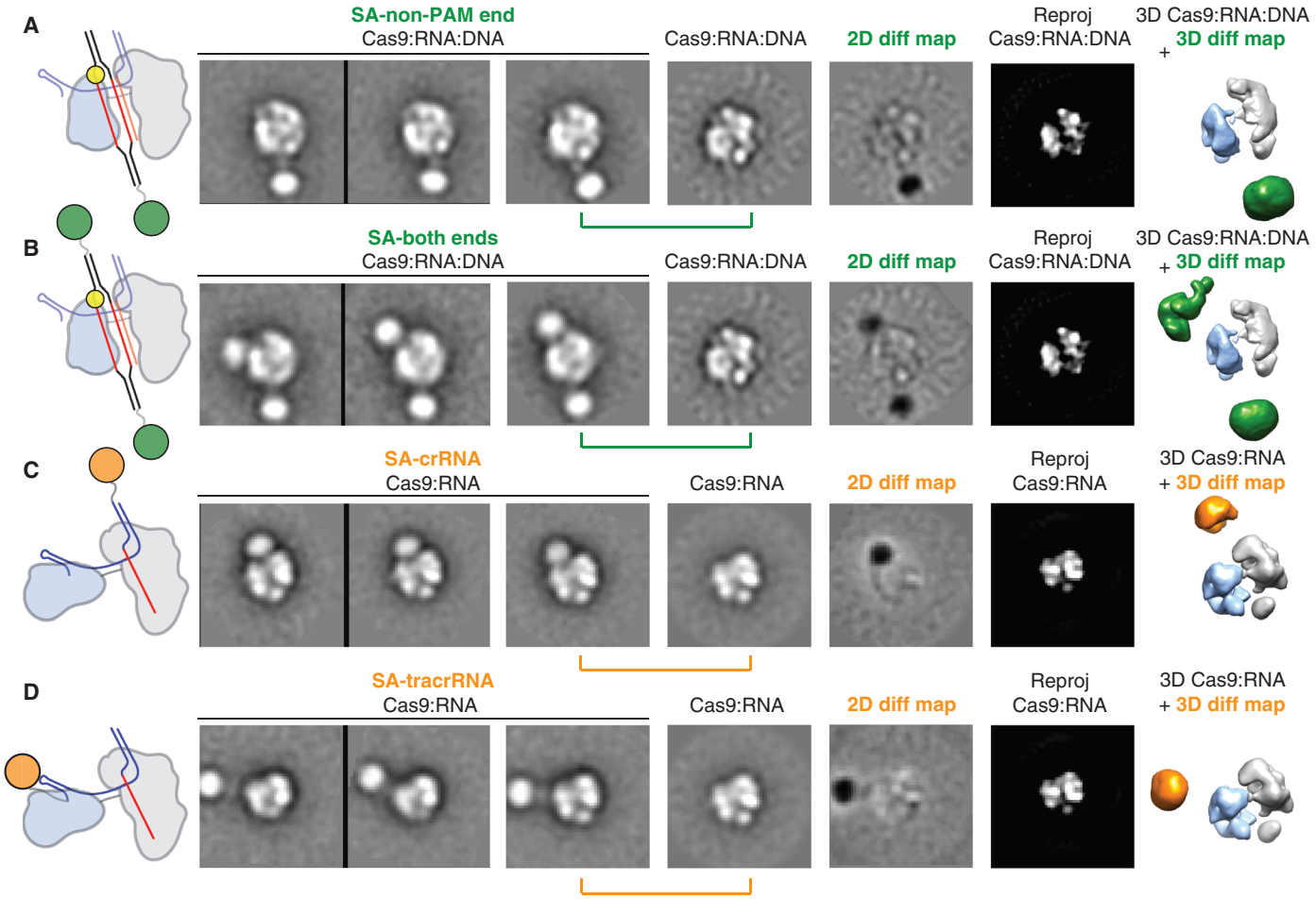

Fig. 6. Bound target DNA and guide RNAs span the central channel. (**A** and **B**) Biotinylated DNA duplexes were labeled with streptavidin (SA) at either the end distal to the PAM (A, non-PAM) or both ends (B). From left to right: schematic of structures and labels, three representative reference-free 2D class averages, the corresponding reference-free 2D class average of unlabeled SpyCas9:RNA:DNA, a 2D difference map between the unlabeled and labeled structures, and the corresponding reprojection of the SpyCas9:RNA:DNA structure. The SpyCas9:RNA:DNA reconstruction is shown on the right with superimposed 3D difference density at ≥5σ (green) between the SpyCas9:RNA:DNA reconstruction and the SA-labeled reconstruction. (**C** and **D**) Single-particle EM analyses of SpyCas9:RNA labeled with SA at the 3′ end of the crRNA (C) or tracrRNA (D). Data are shown as in (A), with the 3D difference density at ≥6σ depicted in orange. The width of the boxes is ~316 Å.

as described (*8*). The sequences of RNA and DNA reagents used in this study are listed in table S2. Cleavage reactions were performed at room temperature in reaction buffer [20 mM tris-Cl (pH 7.5), 100 mM KCl, 5 mM $MgCl_2$, 5% glycerol, 1 mM dithiothreitol] using 1 nM radiolabeled dsDNA substrates and 1 nM or 10 nM Cas9:crRNA:tracrRNA. Cleavage products were resolved by 10% denaturing (7 M urea) PAGE and visualized by phosphorimaging. Cross-linked peptide-DNA heteroconjugates were obtained by incubating 200 pmol of catalytically inactive (D10A/H840A) Cas9 with crRNA:tracrRNA guide and 10-fold molar excess of BrdU containing dsDNA substrate for 30 min at room temperature, followed by irradiation with UV light (308 nm) for 30 min. S1 nuclease and phosphatase–treated tryptic digests were analyzed using a Dionex UltiMate3000 RSLCnano liquid chromatograph connected in-line with an LTQ Orbitrap XL mass spectrometer equipped with a nanoelectrospray ionization source (Thermo Fisher Scientific).

For negative-stain EM, apo-SpyCas9, SpyCas9:RNA, and SpyCas9:RNA:DNA complexes were reconstituted in reaction buffer, diluted to a concentration of ~25 to 60 nM, applied to glow-discharged 400-mesh continuous carbon grids, and stained with 2% (w/v) uranyl acetate solution. Data were acquired using a Tecnai F20 Twin transmission electron microscope operated at 120 keV at a nominal magnification of either ×80,000 (1.45 Å at the specimen level) or ×100,000 (1.08 Å at the specimen level) using low-dose exposures (~20 e^{-} $Å^{-2}$) with a randomly set defocus ranging from −0.5 to −1.3 μm. A total of 300 to 400 images of each Cas9 sample were automatically recorded on a Gatan 4k × 4k CCD (charge-coupled device) camera using the MSI-Raster application within the automated macromolecular microscopy software Leginon (*58*). Particles were preprocessed in Appion (*45*) before projection matching refinement with libraries from EMAN2 and SPARX (*59*, *60*) using RCT reconstructions (*34*) as initial models.

References and Notes

1. B. Wiedenheft, S. H. Sternberg, J. A. Doudna, RNA-guided genetic silencing systems in bacteria and archaea. *Nature* **482**, 331–338 (2012). doi: 10.1038/nature10886; pmid: 22337052
2. S. Al-Attar, E. R. Westra, J. van der Oost, S. J. J. Brouns, Clustered regularly interspaced short palindromic repeats (CRISPRs): The hallmark of an ingenious antiviral defense mechanism in prokaryotes. *Biol. Chem.* **392**, 277–289 (2011). doi: 10.1515/bc.2011.042; pmid: 21294681
3. M. P. Terns, R. M. Terns, CRISPR-based adaptive immune systems. *Curr. Opin. Microbiol.* **14**, 321–327 (2011). doi: 10.1016/j.mib.2011.03.005; pmid: 21531607
4. R. Sorek, C. M. Lawrence, B. Wiedenheft, CRISPR-mediated adaptive immune systems in bacteria and archaea. *Annu. Rev. Biochem.* **82**, 237–266 (2013). doi: 10.1146/annurev-biochem-072911-172315; pmid: 23495939
5. R. Barrangou *et al.*, CRISPR provides acquired resistance against viruses in prokaryotes. *Science* **315**, 1709–1712 (2007). doi: 10.1126/science.1138140; pmid: 17379808
6. S. J. J. Brouns *et al.*, Small CRISPR RNAs guide antiviral defense in prokaryotes. *Science* **321**, 960–964 (2008). doi: 10.1126/science.1159689; pmid: 18703739
7. K. S. Makarova *et al.*, Evolution and classification of the CRISPR–Cas systems. *Nat. Rev. Microbiol.* **9**, 467–477 (2011). doi: 10.1038/nrmicro2577; pmid: 21552286

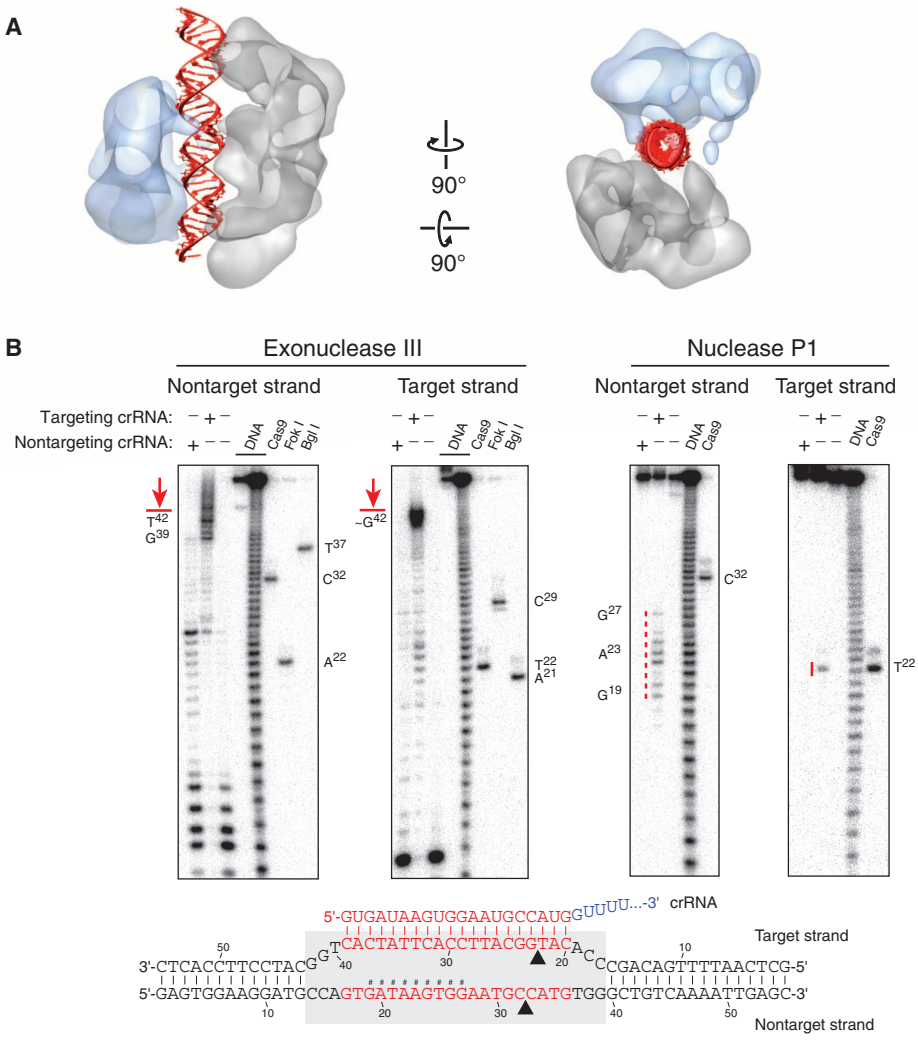

Fig. 7. SpyCas9 wraps around target DNA. (**A**) The central channel of the SpyCas9:RNA:DNA reconstruction (transparent surface) can easily accommodate ~25 bp of an A-form duplex (red). (**B**) Footprinting experiment with target DNA bound by SpyCas9:RNA. A 55-bp DNA substrate was 5′-radiolabeled on either the target or the nontarget strand and incubated with catalytically inactive SpyCas9:RNA programmed with a complementary crRNA (targeting) or a mismatched control crRNA (nontargeting), before being subjected to exonuclease III (left) or nuclease P1 (right) treatment. Reaction products were resolved by denaturing polyacrylamide gel electrophoresis; markers generated via digestion with Bgl I and Fok I restriction enzymes and wild-type SpyCas9:RNA are labeled. The borders of the DNA target protected by SpyCas9:RNA are indicated in red next to the gel and with a gray box (bottom), and nucleotides susceptible to P1 digestion are indicated in red next to the gel and with hashtags in the schematic at the bottom.

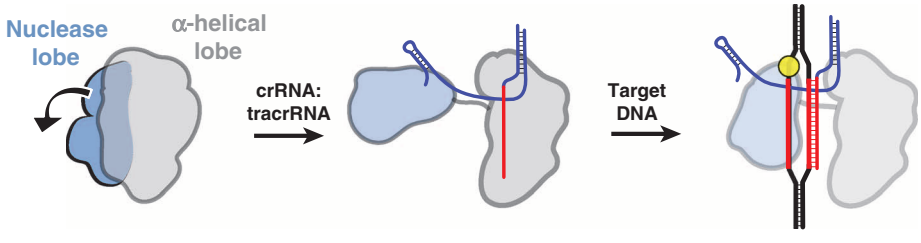

Fig. 8. Model for RNA-induced conversion of Cas9 into a structurally activated DNA surveillance complex. Upon binding the crRNA:tracrRNA guide, the two structural lobes of Cas9 reorient such that the two nucleic acid binding clefts face each other. This generates a central DNA binding channel, which allows access to dsDNA. Target DNA binding in the central channel and PAM-dependent R-loop formation result in a further structural rearrangement. Here, the nuclease domain lobe undergoes further rotation relative to the α-helical lobe, fully enclosing the DNA target, and the two nuclease domains engage both DNA strands for cleavage.

8. M. Jinek *et al.*, A programmable dual-RNA–guided DNA endonuclease in adaptive bacterial immunity. *Science* **337**, 816–821 (2012). doi: 10.1126/science.1225829; pmid: 22745249
9. T. Karvelis *et al.*, crRNA and tracrRNA guide Cas9-mediated DNA interference in *Streptococcus thermophilus*. *RNA Biol.* **10**, 841–851 (2013). doi: 10.4161/rna.24203; pmid: 23535272
10. G. Gasiunas, R. Barrangou, P. Horvath, V. Siksnys, Cas9–crRNA ribonucleoprotein complex mediates specific DNA cleavage for adaptive immunity in bacteria. *Proc. Natl. Acad. Sci. U.S.A.* **109**, E2579–E2586 (2012). doi: 10.1073/pnas.1208507109; pmid: 22949671
11. T. R. Sampson, S. D. Saroj, A. C. Llewellyn, Y.-L. Tzeng, D. S. Weiss, A CRISPR/Cas system mediates bacterial innate immune evasion and virulence. *Nature* **497**, 254–257 (2013). doi: 10.1038/nature12048; pmid: 23584588
12. K. S. Makarova, L. Aravind, Y. I. Wolf, E. V. Koonin, Unification of Cas protein families and a simple scenario for the origin and evolution of CRISPR-Cas systems. *Biol. Direct* **6**, 38 (2011). doi: 10.1186/1745-6150-6-38; pmid: 21756346
13. K. Chylinski, A. Le Rhun, E. Charpentier, The tracrRNA and Cas9 families of type II CRISPR-Cas immunity systems. *RNA Biol.* **10**, 726–737 (2013). doi: 10.4161/rna.24321; pmid: 23563642
14. P. Mali, K. M. Esvelt, G. M. Church, Cas9 as a versatile tool for engineering biology. *Nat. Methods* **10**, 957–963 (2013). doi: 10.1038/nmeth.2649; pmid: 24076990
15. P. Mali *et al.*, RNA-guided human genome engineering via Cas9. *Science* **339**, 823–826 (2013). doi: 10.1126/science.1232033; pmid: 23287722
16. L. Cong *et al.*, Multiplex genome engineering using CRISPR/Cas systems. *Science* **339**, 819–823 (2013). doi: 10.1126/science.1231143; pmid: 23287718
17. M. Jinek *et al.*, RNA-programmed genome editing in human cells. *ELife* **2**, e00471 (2013). doi: 10.7554/eLife.00471; pmid: 23386978
18. L. S. Qi *et al.*, Repurposing CRISPR as an RNA-guided platform for sequence-specific control of gene expression. *Cell* **152**, 1173–1183 (2013). doi: 10.1016/j.cell.2013.02.022; pmid: 23452860
19. L. A. Gilbert *et al.*, CRISPR-mediated modular RNA-guided regulation of transcription in eukaryotes. *Cell* **154**, 442–451 (2013). doi: 10.1016/j.cell.2013.06.044; pmid: 23849981
20. P. Mali *et al.*, CAS9 transcriptional activators for target specificity screening and paired nickases for cooperative genome engineering. *Nat. Biotechnol.* **31**, 833–838 (2013). doi: 10.1038/nbt.2675; pmid: 23907171
21. Z. Hou *et al.*, Efficient genome engineering in human pluripotent stem cells using Cas9 from *Neisseria meningitidis*. *Proc. Natl. Acad. Sci. U.S.A.* **110**, 15644–15649 (2013). doi: 10.1073/pnas.1313587110; pmid: 23940360
22. K. M. Esvelt *et al.*, Orthogonal Cas9 proteins for RNA-guided gene regulation and editing. *Nat. Methods* **10**, 1116–1121 (2013). doi: 10.1038/nmeth.2681; pmid: 24076762
23. J. M. Berger, S. J. Gamblin, S. C. Harrison, J. C. Wang, Structure and mechanism of DNA topoisomerase II. *Nature* **379**, 225–232 (1996). doi: 10.1038/379225a0; pmid: 8538787
24. R. Sapranauskas *et al.*, The *Streptococcus thermophilus* CRISPR/Cas system provides immunity in *Escherichia coli*. *Nucleic Acids Res.* **39**, 9275–9282 (2011). doi: 10.1093/nar/gkr606; pmid: 21813460
25. J. E. Garneau *et al.*, The CRISPR/Cas bacterial immune system cleaves bacteriophage and plasmid DNA. *Nature* **468**, 67–71 (2010). doi: 10.1038/nature09523; pmid: 21048762
26. Y. Zhang *et al.*, Processing-independent CRISPR RNAs limit natural transformation in *Neisseria meningitidis*. *Mol. Cell* **50**, 488–503 (2013). doi: 10.1016/j.molcel.2013.05.001; pmid: 23706818
27. I. Fonfara *et al.*, Phylogeny of Cas9 determines functional exchangeability of dual-RNA and Cas9 among orthologous type II CRISPR-Cas systems. *Nucleic Acids Res.* (2013). doi: 10.1093/nar/gkt1074; pmid: 24270795

28. K. M. Górecka, W. Komorowska, M. Nowotny, Crystal structure of RuvC resolvase in complex with Holliday junction substrate. *Nucleic Acids Res.* **41**, 9945–9955 (2013). doi: 10.1093/nar/gkt769; pmid: 23980027
29. W. Yang, An equivalent metal ion in one- and two-metal-ion catalysis. *Nat. Struct. Mol. Biol.* **15**, 1228–1231 (2008). doi: 10.1038/nsmb.1502; pmid: 18953336
30. W. Yang, Nucleases: Diversity of structure, function and mechanism. *Q. Rev. Biophys.* **44**, 1–93 (2011). doi: 10.1017/S0033583510000181; pmid: 20854710
31. W. Yang, J. Y. Lee, M. Nowotny, Making and breaking nucleic acids: Two-Mg^{2+}-ion catalysis and substrate specificity. *Mol. Cell* **22**, 5–13 (2006). doi: 10.1016/j.molcel.2006.03.013; pmid: 16600865
32. I. Ivančić-Baće, J. A. Howard, E. L. Bolt, Tuning in to interference: R-loops and Cascade complexes in CRISPR immunity. *J. Mol. Biol.* **422**, 607–616 (2012). doi: 10.1016/j.jmb.2012.06.024; pmid: 22743103
33. B. W. Shen, M. Landthaler, D. A. Shub, B. L. Stoddard, DNA binding and cleavage by the HNH homing endonuclease I-HmuI. *J. Mol. Biol.* **342**, 43–56 (2004). doi: 10.1016/j.jmb.2004.07.032; pmid: 15313606
34. M. Radermacher, T. Wagenknecht, A. Verschoor, J. Frank, Three-dimensional reconstruction from a single-exposure, random conical tilt series applied to the 50S ribosomal subunit of Escherichia coli. *J. Microsc.* **146**, 113–136 (1987). doi: 10.1111/j.1365-2818.1987.tb01333.x; pmid: 3302267
35. P. Chacón, W. Wriggers, Multi-resolution contour-based fitting of macromolecular structures. *J. Mol. Biol.* **317**, 375–384 (2002). doi: 10.1006/jmbi.2002.5438; pmid: 11922671
36. M. M. Jore *et al*., Structural basis for CRISPR RNA-guided DNA recognition by Cascade. *Nat. Struct. Mol. Biol.* **18**, 529–536 (2011). doi: 10.1038/nsmb.2019; pmid: 21460843
37. C.-G. Yang *et al*., Crystal structures of DNA/RNA repair enzymes AlkB and ABH2 bound to dsDNA. *Nature* **452**, 961–965 (2008). doi: 10.1038/nature06889; pmid: 18432238
38. Y. Qi *et al*., Encounter and extrusion of an intrahelical lesion by a DNA repair enzyme. *Nature* **462**, 762–766 (2009). doi: 10.1038/nature08561; pmid: 20010681
39. C. M. Crenshaw *et al*., Enforced presentation of an extrahelical guanine to the lesion recognition pocket of human 8-oxoguanine glycosylase, hOGG1. *J. Biol. Chem.* **287**, 24916–24928 (2012). doi: 10.1074/jbc.M111.316497; pmid: 22511791
40. J. Song, O. Rechkoblit, T. H. Bestor, D. J. Patel, Structure of DNMT1-DNA complex reveals a role for autoinhibition in maintenance DNA methylation. *Science* **331**, 1036–1040 (2011). doi: 10.1126/science.1195380; pmid: 21163962
41. D. G. Sashital, B. Wiedenheft, J. A. Doudna, Mechanism of foreign DNA selection in a bacterial adaptive immune system. *Mol. Cell* **46**, 606–615 (2012). doi: 10.1016/j.molcel.2012.03.020; pmid: 22521690
42. S. H. Sternberg, S. Redding, M. Jinek, E. C. Greene, J. A. Doudna, DNA interrogation by the CRISPR RNA-guided endonuclease Cas9. *Nature* (2014). doi: 10.1038/nature13011; pmid: 24476820
43. E. Semenova, M. Nagornykh, M. Pyatnitskiy, I. I. Artamonova, K. Severinov, Analysis of CRISPR system function in plant pathogen *Xanthomonas oryzae*. *FEMS Microbiol. Lett.* **296**, 110–116 (2009). doi: 10.1111/j.1574-6968.2009.01626.x; pmid: 19459963
44. E. Semenova *et al*., Interference by clustered regularly interspaced short palindromic repeat (CRISPR) RNA is governed by a seed sequence. *Proc. Natl. Acad. Sci. U.S.A.* **108**, 10098–10103 (2011). doi: 10.1073/pnas.1104144108; pmid: 21646539
45. B. Wiedenheft *et al*., Structures of the RNA-guided surveillance complex from a bacterial immune system. *Nature* **477**, 486–489 (2011). doi: 10.1038/nature10402; pmid: 21938068
46. R. H. J. Staals *et al*., Structure and activity of the RNA-targeting Type III-B CRISPR-Cas complex of *Thermus thermophilus*. *Mol. Cell* **52**, 135–145 (2013). doi: 10.1016/j.molcel.2013.09.013; pmid: 24119403
47. C. Rouillon *et al*., Structure of the CRISPR interference complex CSM reveals key similarities with Cascade. *Mol. Cell* **52**, 124–134 (2013). doi: 10.1016/j.molcel.2013.08.020; pmid: 24119402
48. M. Spilman *et al*., Structure of an RNA silencing complex of the CRISPR-Cas immune system. *Mol. Cell* **52**, 146–152 (2013). doi: 10.1016/j.molcel.2013.09.008; pmid: 24119404
49. T. Sinkunas *et al*., In vitro reconstitution of Cascade-mediated CRISPR immunity in *Streptococcus thermophilus*. *EMBO J.* **32**, 385–394 (2013). doi: 10.1038/emboj.2012.352; pmid: 23334296
50. W. Kabsch, XDS. *Acta Crystallogr. D Biol. Crystallogr.* **66**, 125–132 (2010). doi: 10.1107/S0907444909047337; pmid: 20124692
51. C. Vonrhein, E. Blanc, P. Roversi, G. Bricogne, Automated structure solution with autoSHARP. *Methods Mol. Biol.* **364**, 215–230 (2007). pmid: 17172768
52. T. Terwilliger, SOLVE and RESOLVE: Automated structure solution, density modification and model building. *J. Synchrotron Radiat.* **11**, 49–52 (2004). doi: 10.1107/S0909049503023938; pmid: 14646132
53. P. Emsley, K. Cowtan, *Coot*: Model-building tools for molecular graphics. *Acta Crystallogr. D Biol. Crystallogr.* **60**, 2126–2132 (2004). doi: 10.1107/S0907444904019158; pmid: 15572765
54. P. V. Afonine *et al*., Towards automated crystallographic structure refinement with *phenix.refine*. *Acta Crystallogr. D Biol. Crystallogr.* **68**, 352–367 (2012). doi: 10.1107/S0907444912001308; pmid: 22505256
55. H. R. Powell, O. Johnson, A. G. W. Leslie, Autoindexing diffraction images with *iMosflm*. *Acta Crystallogr. D Biol. Crystallogr.* **69**, 1195–1203 (2013). doi: 10.1107/S0907444912048524; pmid: 23793145
56. P. Evans, Scaling and assessment of data quality. *Acta Crystallogr. D Biol. Crystallogr.* **62**, 72–82 (2006). doi: 10.1107/S0907444905036693; pmid: 16369096
57. G. N. Murshudov, A. A. Vagin, E. J. Dodson, Refinement of macromolecular structures by the maximum-likelihood method. *Acta Crystallogr. D Biol. Crystallogr.* **53**, 240–255 (1997). doi: 10.1107/S0907444996012255; pmid: 15299926
58. C. Suloway *et al*., Automated molecular microscopy: The new Leginon system. *J. Struct. Biol.* **151**, 41–60 (2005). doi: 10.1016/j.jsb.2005.03.010; pmid: 15890530
59. M. Hohn *et al*., SPARX, a new environment for Cryo-EM image processing. *J. Struct. Biol.* **157**, 47–55 (2007). doi: 10.1016/j.jsb.2006.07.003; pmid: 16931051
60. G. Tang *et al*., EMAN2: An extensible image processing suite for electron microscopy. *J. Struct. Biol.* **157**, 38–46 (2007). doi: 10.1016/j.jsb.2006.05.009; pmid: 16859925
61. N. A. Baker, D. Sept, S. Joseph, M. J. Holst, J. A. McCammon, Electrostatics of nanosystems: Application to microtubules and the ribosome. *Proc. Natl. Acad. Sci. U.S.A.* **98**, 10037–10041 (2001). doi: 10.1073/pnas.181342398; pmid: 11517324
62. H. Ashkenazy, E. Erez, E. Martz, T. Pupko, N. Ben-Tal, ConSurf 2010: Calculating evolutionary conservation in sequence and structure of proteins and nucleic acids. *Nucleic Acids Res.* **38** (Web Server), W529–W533 (2010). doi: 10.1093/nar/gkq399; pmid: 20478830

Acknowledgments: We are grateful to T. Tomizaki and V. Olieric (beamlines PXI and PXIII of the Swiss Light Source, Paul Scherrer Institut), and to G. Meigs, J. Holton, and C. Ralston (beamlines 8.2.2 and 8.3.1 of the Advanced Light Source, Lawrence Berkeley National Laboratory). We thank P. Kranzusch, S. Floor, R. Wilson, J. Noeske, Z. Kasahara, A. May, R. Haurwitz, P. Grob, Y. He, T. Houweling, D. Black, H.-W. Wang, J. Cate, and J. Berger for technical support and/or helpful discussions. This work was funded by HHMI (E.N. and J.A.D.), the Bill and Melinda Gates Foundation (J.A.D.), and the National Science Foundation (J.A.D.) and by start-up funds from the University of Zurich and the European Research Council (ERC) Starting Grant ANTIVIRNA (M.J.). F.J. acknowledges support for study abroad from the China Scholarship Council. E.K. was funded by the German Academic Exchange Program (DAAD). S.H.S. acknowledges support from the National Science Foundation and National Defense Science and Engineering Graduate Research Fellowship programs. E.C. and J.A.D. acknowledge support from the Swedish Foundation for International Cooperation in Research and Education. E.N. and J.A.D. are HHMI Investigators. The atomic coordinates have been deposited into the PDB with accession codes 4CMP (SpyCas9), 4CMQ (Mn^{2+}-bound SpyCas9), 4OGE (AnaCas9), and 4OGC (Mn^{2+}-bound AnaCas9), respectively. The EM structures of apo-SpyCas9, SpyCas9:RNA, and SpyCas9:RNA:DNA have been deposited into the EMDataBank with accession codes EMD-5858, EMD-5859, and EMD-5860, respectively.

Supplementary Materials

www.sciencemag.org/content/343/6176/1247997/suppl/DC1
Materials and Methods
Figs. S1 to S21
Tables S1 and S2
References (*62*–*86*)

4 November 2013; accepted 21 January 2014
Published online 6 February 2014;
10.1126/science.1247997

Ligand-Controlled C(sp^3)–H Arylation and Olefination in Synthesis of Unnatural Chiral α–Amino Acids

Jian He,* Suhua Li,* Youqian Deng, Haiyan Fu, Brian N. Laforteza, Jillian E. Spangler, Anna Homs, Jin-Quan Yu†

The use of ligands to tune the reactivity and selectivity of transition metal catalysts for C(sp^3)–H bond functionalization is a central challenge in synthetic organic chemistry. Herein, we report a rare example of catalyst-controlled C(sp^3)–H arylation using pyridine and quinoline derivatives: The former promotes exclusive monoarylation, whereas the latter activates the catalyst further to achieve diarylation. Successive application of these ligands enables the sequential diarylation of a methyl group in an alanine derivative with two different aryl iodides, affording a wide range of β-Ar-β-Ar′-α–amino acids with excellent levels of diastereoselectivity (diastereomeric ratio > 20:1). Both configurations of the β-chiral center can be accessed by choosing the order in which the aryl groups are installed. The use of a quinoline derivative as a ligand also enables C(sp^3)–H olefination of a protected alanine.

Over the past decade, substantial progress has been achieved in the palladium-catalyzed activation of the inert β-C(sp^3)–H bonds of aliphatic carboxylic acid derivatives using chiral oxazolines (*1*), the 8-aminoquinoline auxiliary (*2*, *3*), and a variety of weakly coordinating amide directing groups (*4*, *5*). In particular, the synthesis of unnatural amino acids via the direct β-functionalization of α–amino acids has been an area of extensive research since a seminal report by Reddy *et al*. (*6*). We envisioned that a sequential diarylation of alanine with two different aryl iodides could potentially provide an efficient route for the preparation of β-Ar-β-Ar′-α–amino acids containing a β-chiral center (Fig. 1). Although the more strongly coordinating 8-aminoquinoline auxiliary developed by Zaitsev *et al*. (*2*) is a powerful directing group for the β-arylation of alanine, this auxiliary provides predominantly β,β-homo-diarylated products, which prevents the sequential installation of two different aryl groups. It is possible to use a specifically designed 2-methylthioaniline auxiliary to achieve monoarylation of alanine in moderate yield and then use a different auxiliary to perform the secondary C(sp^3)–H arylation with a distinct aryl iodide (Fig. 1A) (*7*). However, this hypothetical route has not yet been used for preparing β-Ar-β-Ar′-α–amino acids because the removal and installation of the second auxiliary would add three synthetic steps to the sequence. In addition, the basic reaction conditions used in the first arylation step partially racemize the amino acid to 90% enantiomeric excess (*7*).

We reasoned that a ligand-controlled strategy could provide an ideal solution for the synthesis of β-Ar-β-Ar′-α–amino acids. Specifically, we envisioned the application of two different ligands: one that would selectively promote primary β-C(sp^3)–H arylation [without further arylating the remaining, now secondary, β-C(sp^3)–H bonds] and another that would enable further secondary β-C(sp^3)–H arylation, thereby introducing both aryl substituents successively onto a single substrate in one pot (Fig. 1B). This reaction sequence provides an alternative synthetic disconnection to the existing asymmetric hydrogenation method for the synthesis of chiral β-Ar-β-Ar′-α–amino acids (Fig. 1C) (*8*–*11*). Fundamentally, the development of appropriate ligands to confer selectivity for primary or secondary β-C(sp^3)–H bonds on a weakly coordinating substrate can greatly improve C(sp^3)–H activation reactions (*12*–*20*).

Herein, we report the discovery that a pyridine-based ligand promotes monoarylation of primary β-C(sp^3)–H bonds exclusively and that a second, quinoline-based ligand enables introduction of a distinct aryl group via subsequent secondary β-C(sp^3)–H activation in one pot. The reactions proceed with excellent levels of diastereoselectivity with respect to the starting configuration at the α carbon (Fig. 1B). As such, both configurations at the new β-stereogenic center can be constructed by simply choosing the order of aryl group installation. We further demonstrate that the use of the quinoline-based ligand enables the C(sp^3)–H olefination of an alanine-derived substrate to afford olefin-substituted chiral α–amino acids.

A Ligand for Monoarylation

Our first challenge in the development of a versatile method for the preparation of stereo-defined β-Ar-β-Ar′-α–amino acids from alanine (Fig. 1B) was to achieve selective monoarylation of primary C(sp^3)–H bonds without further arylating the secondary C(sp^3)–H bonds. Our group has recently focused on the development of simple auxiliaries, such as *N*-methoxyamides and

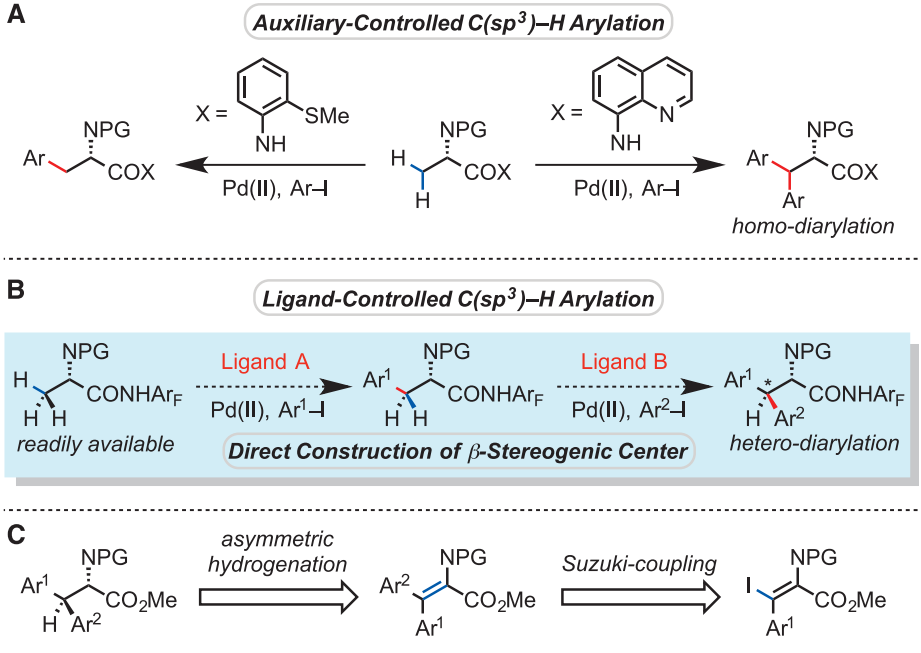

Fig. 1. Methods for synthesizing chiral β-Ar-β-Ar′-α–amino acids. (**A**) C(sp^3)–H activation using substrate-bound auxiliaries to govern selectivity. NPG, protected amino groups; COX, amides; Me, methyl. (**B**) C(sp^3)–H activation using catalyst-bound ligands to govern selectivity. (**C**) Asymmetric hydrogenation.

The Scripps Research Institute, 10550 North Torrey Pines Road, La Jolla, CA 92037, USA.

*These authors contributed equally to this work.
†Corresponding author. E-mail: yu200@scripps.edu

perfluorinated arylamides, to direct a wide range of C(sp^3)–H activation reactions by weak coordination to palladium catalysts (*4*, *5*). However, to date we have found that these auxiliaries are incompatible with the functionalization of the C(sp^3)–H bonds of α–amino acids (*4*, *5*). We recently demonstrated that the use of an alkoxypyridine ligand can match the weak coordination of the amide auxiliary (CONHAr$_F$) and facilitate secondary C(sp^3)–H activation (albeit, with only simple aliphatic amides) (*21*), indicating that pyridine-based ligands are capable of lowering the transition state energy of C(sp^3)–H activation. This finding prompted us to test a diverse array of monodentate pyridine-derived ligands for their ability to selectively promote primary C(sp^3)–H activation, thereby allowing for highly monoselective arylation of alanine-derived amide **1**.

To obtain preliminary information regarding the reactivity of the CONHAr$_F$ amide auxiliary with amino acid substrates, we initiated our experimental efforts by studying C(sp^3)–H arylation of **1** under a variety of different reaction conditions in the absence of an ancillary ligand. Through extensive screening, we found that the use of 20 mol % trifluoroacetic acid (TFA) prevented substrate decomposition, which had been observed with **1** under previously developed basic conditions (*21*). Under the best conditions from this initial screen, monoarylated product **2** could be obtained in 47% yield, along with full recovery of the remaining starting material (Fig. 2A). Additional attempts to fine-tune various reaction parameters, including increasing the catalyst loading to 30 mol %, failed to improve the reaction conversion. The low conversion was found to result primarily from product inhibition (see supplementary materials: table S2, entry 16). Alternative aryl iodide coupling partners reacted in even lower yields (Fig. 2A, **2m** to **2p**). These findings point to the need for the identification of a ligand that will promote the activation of primary β-C(sp^3)–H bonds exclusively but not the secondary β-C(sp^3)–H bonds in the product. Hence, a library of pyridine ligands was tested for their efficiency of promoting monoarylation in the presence of TFA. Pyridine and 4-dimethylaminopyridine (**L1** and **L2**) are highly selective for monoarylation, but neither enhances conversion substantially relative to the ligand-free catalyst. In contrast, we found that 2,6-dimethoxypyridine, acridine, 2,6-lutidine, and 2-picoline (**L4** to **L7**) promote substantially higher conversion, though the use of **L4** to **L6** leads to appreciable quantities of the undesired diarylated product **3** as well. The 2-picoline ligand (**L7**) seems to possess an optimal balance of steric and electronic properties to provide **2** in high yield with an excellent level of selectivity for monoarylation [nuclear magnetic resonance (NMR) yield of 94%]. The monoarylation reaction also proceeded in the presence of 5 mol % of Pd(TFA)$_2$ and 10 mol % of **L7** to give the desired product **2** in 79% yield (table S2, entry 4).

The applicability of this ligand-controlled monoarylation protocol in the preparation of diverse chiral β-Ar-β-Ar′-α–amino acids is shown in Fig. 2A: Phenylalanine derivatives with electron-rich or electron-poor groups in the ortho, meta, or para positions can be synthesized in high yields. This reaction is tolerant of halide substituents and a wide range of polar functional groups. Arylation with 4-methylthiophenyl iodide also proceeds to give the arylated product (**2p**) in a synthetically useful yield, indicating that the pyridine ligand is able to out-compete the methylthio group for coordination at Pd(II). The reaction of **1** with 2-iodonaphthalene to give **2q** is particularly useful, as the resulting product could be applied to synthesis of bioactive peptides that block cell cycle progression in HeLa cells (*22*). Arylation with disubstituted aryl iodides is also efficient, giving **2r** to **2t** in >85% yields.

When conducted at 100°C, these reactions are typically complete within 20 hours, and no racemization of the α-chiral center is observed. Subsequent removal of the auxiliary can be accomplished under mild conditions without loss of enantiomeric purity (Fig. 2B), and the monoarylated products are readily converted to the corresponding *N*-fluorenylmethyloxycarbonyl–protected unnatural amino acids following literature procedures (see supplementary materials). The auxiliary 2,3,5,6-tetrafluoro-4-(trifluoromethyl)aniline is readily prepared from octafluorotoluene ($0.47/g) on a 100-g scale or purchased directly from Aldrich.

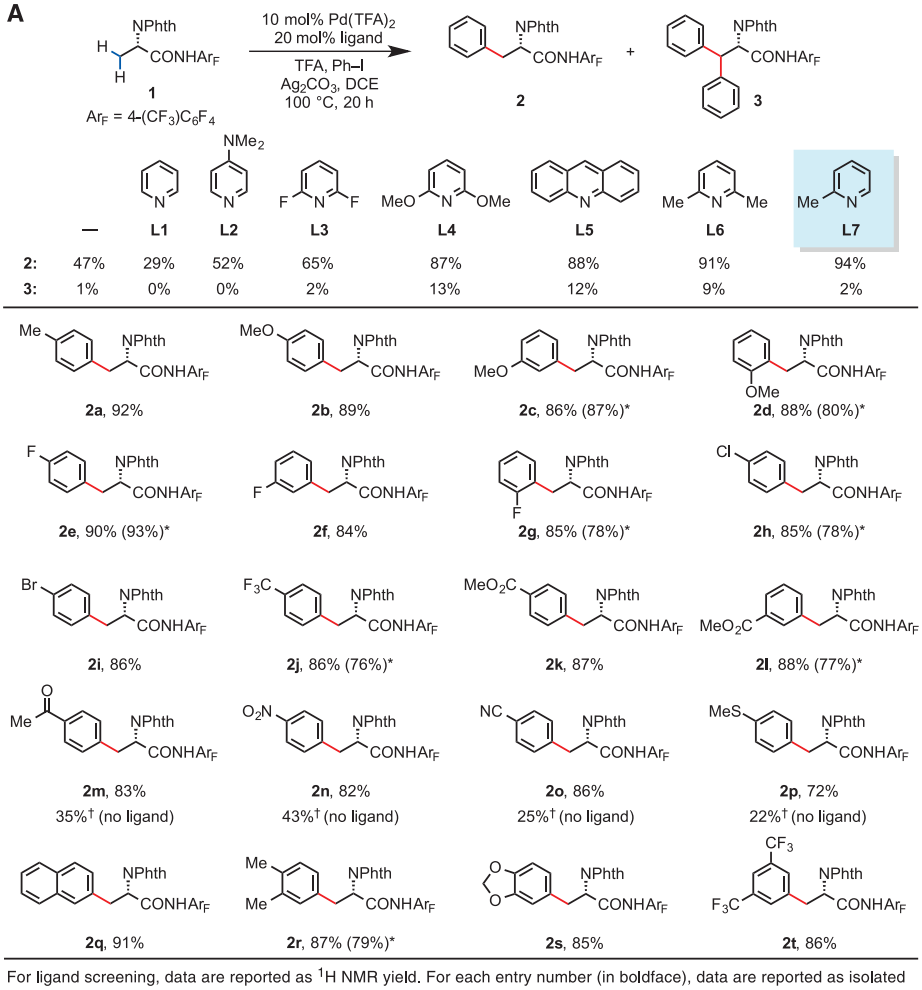

For ligand screening, data are reported as ^{1}H NMR yield. For each entry number (in boldface), data are reported as isolated yield. See supplementary materials for experimental details. *Isolated yield of gram-scale reactions (10–15 mmol) in parentheses. †Data are reported as ^{1}H NMR yield.

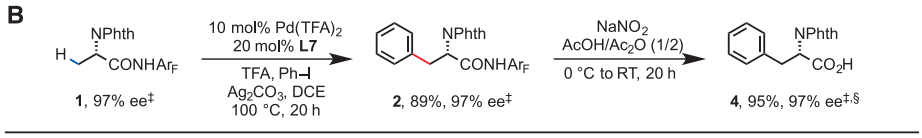

‡The ee values were determined by chiral HPLC. §The ee value was determined from the corresponding methyl ester.

Fig. 2. Palladium-catalyzed arylation of primary C(sp^3)–H bonds. (**A**) Ligand-promoted monoarylation of auxiliary-substituted alanine. Phth, phthalimido; DCE, 1,2-dichloroethane (**B**) Removal of amide auxiliary and determination of enantiomeric purity of *N*-Phth–protected chiral α–amino acid. Ac, acetyl; RT, room temperature; ee, enantiomeric excess; HPLC, high-performance liquid chromatography.

Due to these practical advantages, we have prepared a variety of monoarylated alanines on a 10-mmol scale to facilitate peptide drug discovery in collaboration with Bristol-Myers Squibb (**2c** to **2e**, **2g**, **2h**, **2j**, **2l**, and **2r**).

A Ligand for Diarylation

We next sought to identify a second ligand that could promote the subsequent arylation of the secondary β-C(sp^3)–H bonds. As previously mentioned, our recently disclosed procedure for the ligand-promoted arylation of secondary C(sp^3)–H bonds under basic reaction conditions (*21*) is not compatible with amino acid substrates. However, the formation of minor amounts of the diarylated product **3** from amide **1** with ligand **L4** (13% yield, Fig. 2A) suggested that these new conditions could be effective for secondary β-C(sp^3)–H bond arylation with an appropriate ligand. We were pleased to find that the arylation of phenylalanine-derived amide **2**, in the presence of ligand **L4**, afforded the desired product **3** in 47% yield. The modest success of this ligand and our previously reported 2-alkoxylquinoline ligand **L9** (*21*) led us to explore a variety of electron-rich 2-alkoxylpyridine and 2-alkoxylquinoline ligands for this secondary C(sp^3)–H bond arylation.

A substantial improvement in reaction efficiency using ligand **L8** or **L9** suggested that the 2-substituted quinoline motif possesses favorable steric and electronic properties that promote C(sp^3)–H activation. Next, we examined the impact of further increasing the electron-donating ability of the alkoxyl group by synthesizing the tricyclic ligand **L10**, in which the conformation of the lone pairs on the oxygen atom is rigidified to favor π-conjugation with the pyridine ring. The use of this new ligand led to a dramatic improvement in reaction efficiency, affording product **3** in 92% yield (90% isolated yield). Further modifications of **L10** to weaken or strengthen the coordinating ability of the quinoline led to a decrease in product yield (**L11** and **L12**).

Under these optimized reaction conditions, phenylalanine-derived amide **2** can be arylated with a broad range of electron-rich and electron-poor aryl iodides in high yields (Fig. 3A). Despite the known steric hindrance associated with the arylation of secondary C(sp^3)–H bonds (**3j**), ortho-substituted aryl iodides are also compatible with this reaction. To demonstrate the generality of this ligand effect for secondary C(sp^3)–H activation, we also performed the arylation of four representative open-chain and cyclic alkyl amino acids. Amide substrates derived from lysine, L-2-aminobutyric acid, 1-aminocyclobutane-1-carboxylic acid, and 1-aminocyclopropane-1-carboxylic acid were successfully arylated using ligand **L10** to give the corresponding β-alkyl-β-aryl-α–amino acid derivatives in good to excellent yields (Fig. 3B). These arylation reactions all proceeded with high levels of diastereoselectivity. These aliphatic secondary C(sp^3)–H bonds are less reactive than benzylic C(sp^3)–H bonds, and the use of ligand **L10** is crucial to achieve this reactivity.

One-Pot Diarylation

Ligands **L7** and **L10**, which enable the arylation of primary and secondary β-C(sp^3)–H bonds, respectively, can be employed for the sequential one-pot incorporation of two distinct aryl groups onto the β carbon of alanine-derivative **1** (Fig. 4). Thus, after the completion of the monoarylation of **1** with an aryl iodide using **L7**, we can add **L10** and a second aryl iodide to provide a β-Ar-β-Ar′-α–amino acid. The aryl iodide (1.5 equivalents) used in the first step is mostly incorporated into the product, with small amount being converted to the biaryl (*23*). The remaining aryl iodide is outcompeted by a large excess of the second aryl iodide (3 equivalents), thus avoiding participation in a second arylation event. This one-pot procedure is successfully applied with both electron-rich and electron-deficient aryl iodides to prepare a variety of diarylated amino acids (**7a** to **7f**) in good yields with excellent levels of diastereoselectivity (*24*). By simply switching the order of the addition of the two different aryl iodides, the inverse configuration at the β-stereogenic center can be obtained, as shown with **7e** and **7f** (absolute configuration of **7f** was confirmed by x-ray crystallography). When the sequential hetero-diarylation of **1** was conducted

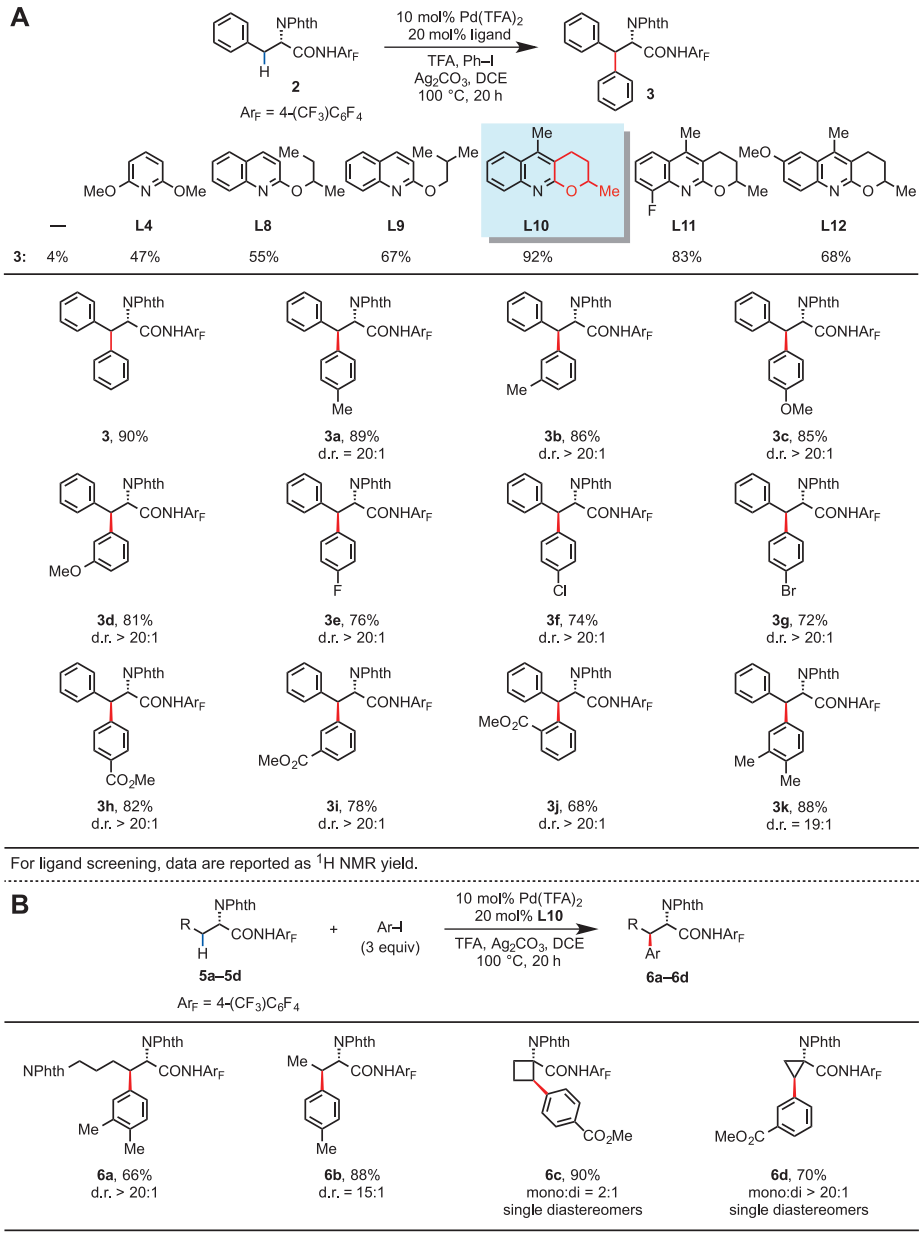

Fig. 3. Palladium-catalyzed arylation of secondary C(sp^3)–H bonds. (**A**) Ligand-promoted arylation of phenylalanine-derived substrate. d.r., diastereomeric ratio. (**B**) Arylation of alkyl amino acid derivatives. R, alkyl.

in one pot on a 5-mmol scale (2.2 g), the desired product **7b** was isolated in 60% yield.

The superior reactivity of ligand **L10** prompted us to revisit previously unsuccessful arylation with heteroaryl iodides. Although secondary C(sp^3)–H arylation of **2** with heteroaryl iodides proved inefficient, primary C(sp^3)–H arylation of **1** with pyridyl, indolyl, and thiophenyl iodides afforded synthetically useful yields (Fig. 5A). These heteroaryl-containing unnatural amino acids are especially desirable for developing peptide drug molecules.

Olefination with Ligand L10

We also examined the feasibility of using ligand **L10** to effect the olefination of alanine-derived substrate **1**, and we observed efficient reactivity under slightly modified reaction conditions. The subsequent lactamization in situ also ensured the monoselectivity of the reaction. With the use of established procedures, lactam **8** is converted to *N*-Boc–protected product **10** (Fig. 5B). Further improvement of this olefination reaction could lead to a useful method for the preparation of β-olefinated α–amino acids that is complementary to the asymmetric hydrogenation route (*25*). The olefinated product **10** can be subjected to cross metathesis to afford olefinated products **11** and **12** with high levels of *E*/*Z* selectivity or hydrogenated to provide the corresponding alkylated product **13** (Fig. 5C).

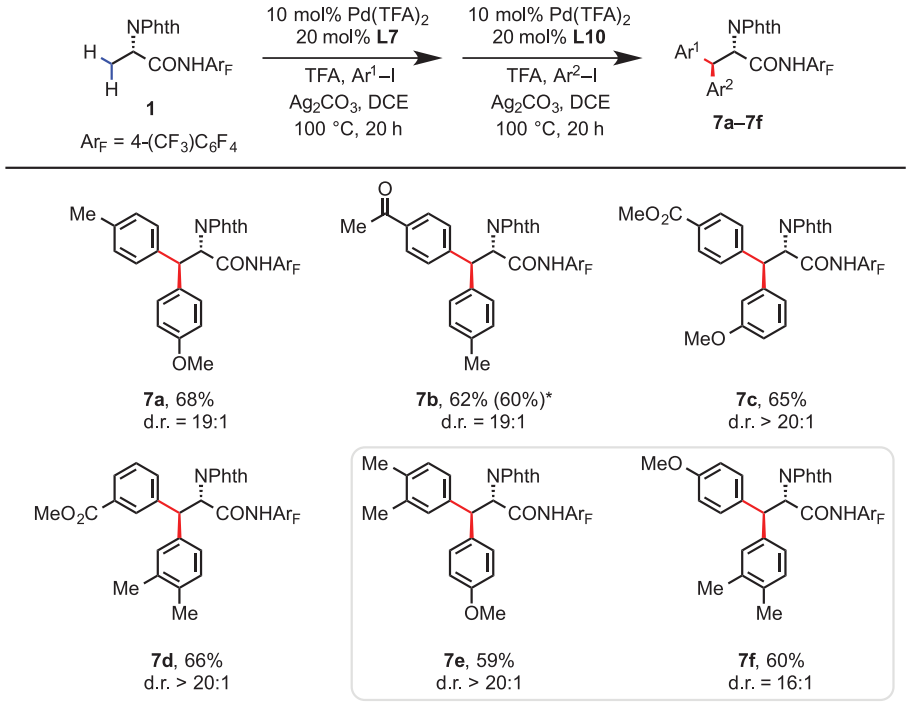

For each entry number (in boldface), data are reported as isolated yield. See supplementary materials for experimental details. Diastereomer ratios were determined by ^{1}H NMR analysis of the crude reaction mixture.*Isolated yield of a 5 mmol scale reaction in the parenthesis.

Fig. 4. Synthesis of β-Ar-β-Ar′-α–amino acids via sequential C(sp^3)–H arylations in one pot.

Mechanistic Studies

Whereas C(sp^3)–H arylation with aryl iodides likely proceeds via a Pd(II)/Pd(IV) catalytic cycle, olefination probably proceeds via a Pd(II)/Pd(0) redox manifold. The considerable ligand effect observed in these distinct reaction pathways implicates the intimate involvement of the ligand in the C(sp^3)–H cleavage step as the common step. This is further substantiated by the intramolecular kinetic isotope effect observed in the arylation reaction, which showed a noticeable and consistent dependence on the ligand (without ligand, intramolecular isotope effect value k_H/k_D = 6.0; with **L7**, k_H/k_D = 8.1; with **L10**, k_H/k_D = 10.7; see supplementary materials).

To obtain further insights into the coordination of the substrate and ligands at the Pd(II) centers, we have successfully characterized the C–H insertion intermediates (intermediate **A** and intermediate **B**), formed via primary and secondary C(sp^3)–H activation, respectively (Fig. 6A). The formation of these C(sp^3)–H insertion intermediates

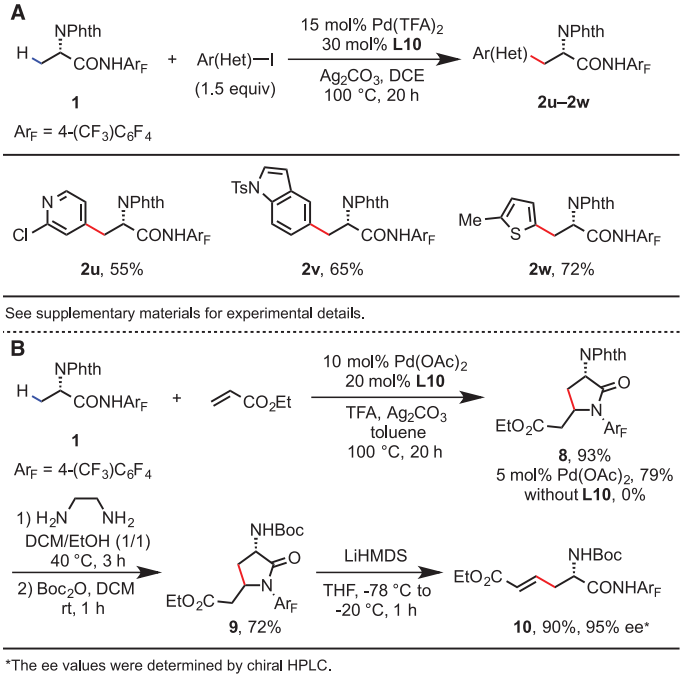

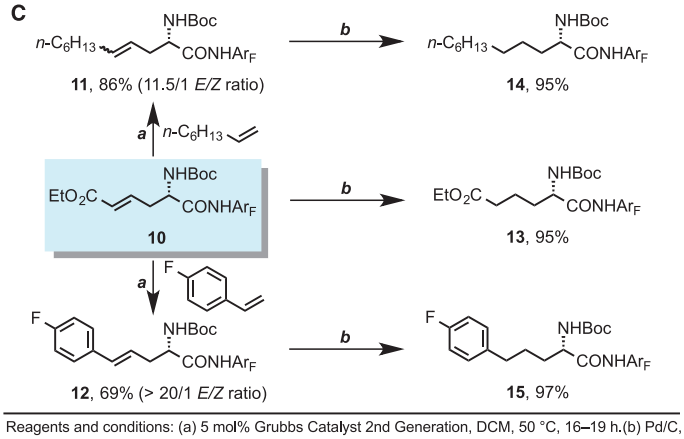

Fig. 5. Further applications of Pd catalysis with L10. (A) Ligand-enabled C(sp^3)–H arylation with heteroaryl iodides. **(B)** C(sp^3)–H olefination of alanine derivatives. DCM, dichloromethane; Et, ethyl; Boc, *tert*-butoxycarbonyl; HMDS, hexamethyldisilazide. **(C)** Unnatural α–amino acid elaboration.

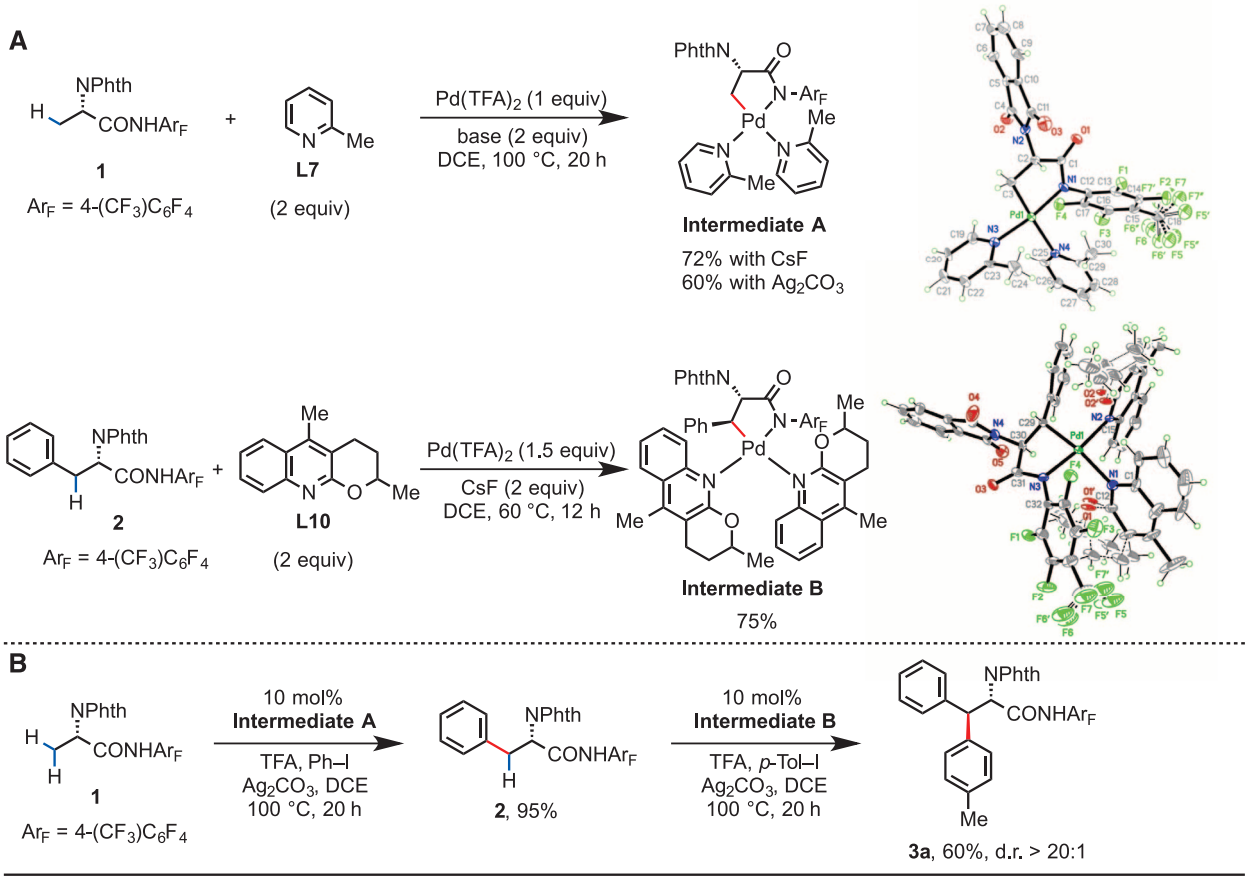

For each entry number (in boldface), data are reported as isolated yield. See supplementary materials for experimental details.

Fig. 6. Mechanistic studies. (**A**) Synthesis and crystallography of primary and secondary C(sp^3)–H activation intermediates. Oak Ridge thermal ellipsoid plots (30% probability ellipsoids) of intermediate **A** and intermediate **B** are shown. (**B**) Catalytic reactivity of intermediates in C(sp^3)–H arylation reactions.

in the absence of aryl iodides is consistent with the Pd(II)/Pd(IV) pathway in which Pd(II) cleaves the C–H bond first and subsequently undergoes oxidative addition with an aryl iodide (*26*). We have found that intermediate **A** reacts with iodobenzene stoichiometrically to provide **2** (see supplementary materials). However, the addition of TFA is required for this transformation, presumably to facilitate the dissociation of one of the pyridine ligands. These intermediates are viable precatalysts for primary and secondary C(sp^3)–H arylation, respectively (Fig. 6B). These rare and valuable C(sp^3)–H insertion intermediates provide a promising platform for further kinetic and computational study of elementary steps in a well-defined manner.

References and Notes

1. R. Giri, X. Chen, J.-Q. Yu, *Angew. Chem. Int. Ed.* **44**, 2112–2115 (2005).
2. V. G. Zaitsev, D. Shabashov, O. Daugulis, *J. Am. Chem. Soc.* **127**, 13154–13155 (2005).
3. S.-Y. Zhang, Q. Li, G. He, W. A. Nack, G. Chen, *J. Am. Chem. Soc.* **135**, 12135–12141 (2013).
4. D.-H. Wang, M. Wasa, R. Giri, J.-Q. Yu, *J. Am. Chem. Soc.* **130**, 7190–7191 (2008).
5. M. Wasa, K. M. Engle, J.-Q. Yu, *J. Am. Chem. Soc.* **131**, 9886–9887 (2009).
6. B. V. S. Reddy, L. R. Reddy, E. J. Corey, *Org. Lett.* **8**, 3391–3394 (2006).
7. L. D. Tran, O. Daugulis, *Angew. Chem. Int. Ed.* **51**, 5188–5191 (2012).
8. P. M. T. Ferreira, L. S. Monteiro, G. Pereira, *Eur. J. Org. Chem.* **2008**, 4676–4683 (2008).
9. R. Noyori, H. Takaya, *Acc. Chem. Res.* **23**, 345–350 (1990).
10. W. Tang, X. Zhang, *Chem. Rev.* **103**, 3029–3070 (2003).
11. S. J. Roseblade, A. Pfaltz, *Acc. Chem. Res.* **40**, 1402–1411 (2007).
12. N. Rodríguez, J. A. Romero-Revilla, M. Á. Fernández-Ibáñez, J. C. Carretero, *Chem. Sci.* **4**, 175–179 (2013).
13. R. Shang, L. Ilies, A. Matsumoto, E. Nakamura, *J. Am. Chem. Soc.* **135**, 6030–6032 (2013).
14. E. M. Simmons, J. F. Hartwig, *Nature* **483**, 70–73 (2012).
15. W. R. Gutekunst, P. S. Baran, *J. Am. Chem. Soc.* **133**, 19076–19079 (2011).
16. N. Hasegawa, V. Charra, S. Inoue, Y. Fukumoto, N. Chatani, *J. Am. Chem. Soc.* **133**, 8070–8073 (2011).
17. O. Baudoin, *Chem. Soc. Rev.* **40**, 4902–4911 (2011).
18. T. W. Lyons, M. S. Sanford, *Chem. Rev.* **110**, 1147–1169 (2010).
19. R. Jazzar, J. Hitce, A. Renaudat, J. Sofack-Kreutzer, O. Baudoin, *Chemistry* **16**, 2654–2672 (2010).
20. M. Wasa, K. M. Engle, J.-Q. Yu, *Isr. J. Chem.* **50**, 605–616 (2010).
21. M. Wasa *et al.*, *J. Am. Chem. Soc.* **134**, 18570–18572 (2012).
22. D. Wildemann *et al.*, *J. Med. Chem.* **49**, 2147–2150 (2006).
23. L. Wang, W. Lu, *Org. Lett.* **11**, 1079–1082 (2009).
24. Small amounts of unreacted monoarylated products (15 to 25%) from the first step are also isolated as a by-product of this transformation.
25. M. J. Burk, J. G. Allen, W. F. Kiesman, *J. Am. Chem. Soc.* **120**, 657–663 (1998).
26. X. Chen, K. M. Engle, D.-H. Wang, J.-Q. Yu, *Angew. Chem. Int. Ed.* **48**, 5094–5115 (2009).

Acknowledgments: We gratefully acknowledge The Scripps Research Institute, the NIH (National Institute of General Medical Sciences, grant 2R01GM084019), and Bristol-Myers Squibb for financial support. H.F. is a visiting scholar sponsored by Sichuan University. J.H. developed C(sp^3)–H arylation and olefination and conducted most of the experiments; S.L. synthesized quinoline ligands; Y.D., H.F., B.N.L., and J.E.S. performed large-scale reactions; A.H. obtained the crystal structures shown in Fig. 6; and J.-Q.Y. directed the project. Metrical parameters for the structures of **7f**, intermediate **A**, and intermediate **B** are available free of charge from the Cambridge Crystallographic Data Centre under reference numbers CCDC-985675, -985676, and -985677, respectively. A provisional patent application has been filed and is available under patent application no. U.S. 61/946165.

Supplementary Materials

www.sciencemag.org/content/343/6176/1216/suppl/DC1
Supplementary Text
Figs. S1 to S3
Tables S1 to S6
NMR Spectra
References (*27*–*31*)

2 December 2013; accepted 19 February 2014
10.1126/science.1249198

Specific and Nonhepatotoxic Degradation of Nuclear Hepatitis B Virus cccDNA

Julie Lucifora,[1,2]* Yuchen Xia,[1]* Florian Reisinger,[1] Ke Zhang,[1] Daniela Stadler,[1] Xiaoming Cheng,[1] Martin F. Sprinzl,[1,3] Herwig Koppensteiner,[1] Zuzanna Makowska,[4] Tassilo Volz,[5] Caroline Remouchamps,[6] Wen-Min Chou,[1] Wolfgang E. Thasler,[7] Norbert Hüser,[8] David Durantel,[9] T. Jake Liang,[10] Carsten Münk,[11] Markus H. Heim,[4] Jeffrey L. Browning,[12] Emmanuel Dejardin,[6] Maura Dandri,[2,5] Michael Schindler,[1] Mathias Heikenwalder,[1]†‡ Ulrike Protzer[1,2]†‡

Current antiviral agents can control but not eliminate hepatitis B virus (HBV), because HBV establishes a stable nuclear covalently closed circular DNA (cccDNA). Interferon-α treatment can clear HBV but is limited by systemic side effects. We describe how interferon-α can induce specific degradation of the nuclear viral DNA without hepatotoxicity and propose lymphotoxin-β receptor activation as a therapeutic alternative. Interferon-α and lymphotoxin-β receptor activation up-regulated APOBEC3A and APOBEC3B cytidine deaminases, respectively, in HBV-infected cells, primary hepatocytes, and human liver needle biopsies. HBV core protein mediated the interaction with nuclear cccDNA, resulting in cytidine deamination, apurinic/apyrimidinic site formation, and finally cccDNA degradation that prevented HBV reactivation. Genomic DNA was not affected. Thus, inducing nuclear deaminases—for example, by lymphotoxin-β receptor activation—allows the development of new therapeutics that, in combination with existing antivirals, may cure hepatitis B.

Hepatitis B virus (HBV) infection remains a major public health threat, with more than 350 million humans chronically infected worldwide at risk of developing end-stage liver disease and hepatocellular carcinoma. Each year, more than 600,000 people die from the consequences of chronic HBV infection. A prophylactic vaccine has been available for hepatitis B for almost 30 years, but the overall number of chronic infections remains high.

HBV is a small, enveloped DNA virus replicating via an RNA intermediate. The encapsidated viral genome consists of a 3.2-kb partially double-stranded relaxed circular DNA (rcDNA) molecule. The virus has optimized its life cycle for long-term persistence in the liver (*1*). Upon translocation to the nucleus, the rcDNA genome is converted into a covalently closed circular DNA (cccDNA), which serves as the template for viral transcription and secures HBV persistence. Nucleoside or nucleotide analogs are efficient antivirals but only control and do not cure HBV infection owing to the persistence of HBV cccDNA. Therefore, long-term treatment is required, which is expensive and may lead to concomitant resistance (*2*). Interferon (IFN)–α is licensed for hepatitis B therapy, and treatment with this cytokine can result in virus clearance in a proportion of patients; however, its efficacy is limited and high doses are not tolerated (*3*). Thus, efficient and nontoxic elimination of cccDNA in hepatocytes is a major goal of HBV research.

Using animal models, it has been shown that HBV replication—in particular, the cccDNA content of the liver—can be affected by noncytopathic mechanisms involving cytokines such as interferons and tumor necrosis factor (TNF), which influence RNA and capsid stability (*4*–*7*). Here, we describe an antiviral mechanism that interferes with cccDNA stability and is distinct from influences of antiviral cytokines on cccDNA activity (*8*).

High-Dose IFN-α Leads to cccDNA Degradation in HBV-Infected Hepatocytes

IFN-α is known to exert transcriptional, post-transcriptional, and epigenetic antiviral effects on HBV (*8*–*12*). To study the effect of IFN-α on HBV cccDNA, we used HBV-infected, differentiated HepaRG (dHepaRG) cells and primary human hepatocytes (PHHs). These are human cell types susceptible to HBV infection (*13*, *14*) and responsive to IFN-α treatment in vitro (fig. S1A). IFN-α treatment did not lead to detectable hepatotoxicity, even at very high doses (fig. S1B). Treating dHepaRG cells with IFN-α (500 or 1000 IU/ml) controlled HBV-DNA synthesis as efficiently as the nucleoside analog lamivudine (LAM) at 0.5 μM (5 times the median effective concentration, EC_{50}). IFN-α, however, unlike LAM, also significantly reduced expression of HBV-RNA and hepatitis B surface (HBsAg) and e (HBeAg) antigens (Fig. 1A and fig. S1C).

In patients, interruption of LAM treatment results in a rebound of HBV replication (*2*). Using IFN-α, we observed only a partial rebound, or none at all, in HBV-infected dHepaRG cells after treatment cessation (Fig. 1A). Because dHepaRG cells do not allow virus spread, reduction of HBeAg and the lack of rebound indicated an effect of IFN-α on the established HBV cccDNA transcription template separate from the known antiviral effects on viral replication (*14*). By cccDNA-specific quantitative polymerase chain reaction (qPCR), we determined an 80% reduction of cccDNA after 10 days of treatment (Fig. 1B). Reduction of cccDNA was confirmed by Southern blot analysis (fig. S1D) and was dose-dependent (fig. S1E). cccDNA reduction could be induced at any time point (Fig. 1C) and persisted over time (Fig. 1, A and C). The effect was corroborated in HBV-infected PHHs (Fig. 1D). In contrast to IFN-α, LAM and the even more potent nucleoside analog entecavir (ETV) at very high doses (0.5 μM; 1000 times EC_{50}) only inhibited reverse transcription, and thus HBV replication, but not viral persistence (Fig. 1E). Pretreatment with ETV did not enhance the effect of IFN-α (Fig. 1F), indicating that IFN-α induces the decay of established HBV cccDNA. Because the doses of IFN-α used to achieve this effect were high, we screened for other cytokines showing similar antiviral effects at moderate doses.

LTβR Activation Controls HBV and Leads to cccDNA Degradation in HBV-Infected Cells

IFN-γ and TNF-α are known to control HBV in a noncytopathic fashion (*4*, *7*) but cannot be used as therapeutics because they cause severe side effects. We tested the effect of lymphotoxin (LT) β receptor (LTβR) activation as an alternative therapeutic option. The TNF superfamily members LTα, LTβ, and CD258 are the physiological ligands for LTβR and activate either inflammatory or anti-inflammatory pathways or induce apoptosis (*15*). Like hepatocytes (*16*), dHepaRG (*14*) and HepG2-H1.3 cells permit HBV replication (*17*) and express LTβR (fig. S2, A and B). To activate LTβR, we used a superagonistic tetravalent bispecific antibody (BS1) and a bivalent anti-LTβR monoclonal antibody (CBE11) (*18*, *19*). As expected, LTβR agonists activated canonical (*20*) and noncanonical nuclear factor κB (NF-κB) pathways to trigger p100 cleavage (fig. S2C), RelA phosphorylation (fig. S2D), nuclear RelB and RelA translocation (fig. S2, E and F), and up-regulation of known target genes (fig. S2G) without causing any detectable hepatocytotoxicity (fig. S2H).

[1]Institute of Virology, Technische Universität München–Helmholtz Zentrum München, 81675 Munich, Germany. [2]German Center for Infection Research (DZIF), Munich and Hamburg sites, Germany. [3]1st Medical Department, University Hospital Mainz, 55131 Mainz, Germany. [4]Department of Biomedicine, University Hospital Basel, 4031 Basel, Switzerland. [5]Department of Internal Medicine, University Medical Center Hamburg-Eppendorf, 20246 Hamburg, Germany. [6]GIGA-Research Laboratory of Molecular Immunology and Signal Transduction, University of Liège, 4000 Liège, Belgium. [7]Department of General, Visceral, Transplantation, Vascular and Thoracic Surgery, Grosshadern Hospital, Ludwig Maximilians University, 81377 Munich, Germany. [8]Department of Surgery, University Hospital Rechts der Isar, Technische Universität München, 85748 Munich, Germany. [9]INSERM U1052, CNRS UMR 5286, Cancer Research Center of Lyon, University of Lyon, LabEx DEVweCAN, 69007 Lyon, France. [10]Liver Diseases Branch, National Institute of Diabetes and Digestive and Kidney Diseases, Bethesda, MD 20892, USA. [11]Clinic for Gastroenterology, Hepatology and Infectiology, Medical Faculty, Heinrich-Heine University, 40225 Düsseldorf, Germany. [12]Department of Immunobiology, Biogen Idec, Cambridge, MA 02142, USA.

*These authors contributed equally to this work.
†Corresponding author. E-mail: protzer@tum.de (U.P.); heikenwaelder@helmholtz-muenchen.de (M.H.)
‡These authors contributed equally to this work.

To test the effect of LTβR activation on HBV infection, we treated dHepaRG cells with BS1 for 12 days starting 24 hours before HBV infection. LTβR activation decreased levels of all HBV markers, including cccDNA, by ~90% without toxicity (Fig. 2A). The antiviral effect was highly potent, with an EC_{50} of ~0.01 μg/ml (fig. S3A). Inhibition of apoptosis did not alter antiviral activity (fig. S4). Neither IFN-β nor representative IFN-stimulated genes were upregulated upon BS1 treatment (fig. S2G), and antiviral activity was independent of IFN induction (fig. S5).

In vivo, activation of the murine LTβR by systemic application of an agonistic antibody (ACH6) induced RelA and RelB nuclear translocation in hepatocytes of HBV-transgenic mice (fig. S6A) and reduced HBV viremia (fig. S6B), HBV RNA (fig. S6C), and HBV core (HBc) protein expression in the liver (fig. S6, D and E). Neither signs of hepatocyte apoptosis (fig. S6F) nor elevation of aminotransferases (ALT) (fig. S6G, right panel) were observed, indicating good in vivo tolerability of LTβR activation. Because HBV-transgenic mice do not establish HBV cccDNA, this indicated additional antiviral effects of LTβR activation on HBV RNA transcription or stability. Accordingly, discontinuation of LTβR activation induced an immediate, strong rebound of HBV replication (fig. S6G).

To investigate whether LTβR activation would affect established HBV cccDNA in the context of a persistent infection and prevent HBV reactivation, we treated dHepaRG cells with LTβR agonists BS1 or CBE11 when a stable, nuclear cccDNA pool had established. All HBV markers, including HBV cccDNA, were reduced upon LTβR activation in HBV-infected dHepaRG cells (Fig. 2, B and C, and fig. S3) as well as in stably transfected HepG2-H1.3 cells containing high levels of cccDNA (Fig. 2C). In HBV-infected PHHs, LTβR agonization reduced HBV cccDNA, HBeAg secretion, and—most effectively—HBV-DNA replication (Fig. 2D). cccDNA degradation was more effective (up to 95%) when treatment was prolonged (fig. S3, C and D). Treatment interruption for 10 days was almost as efficient as continuous treatment (fig. S3C), indicating that LTβR agonists

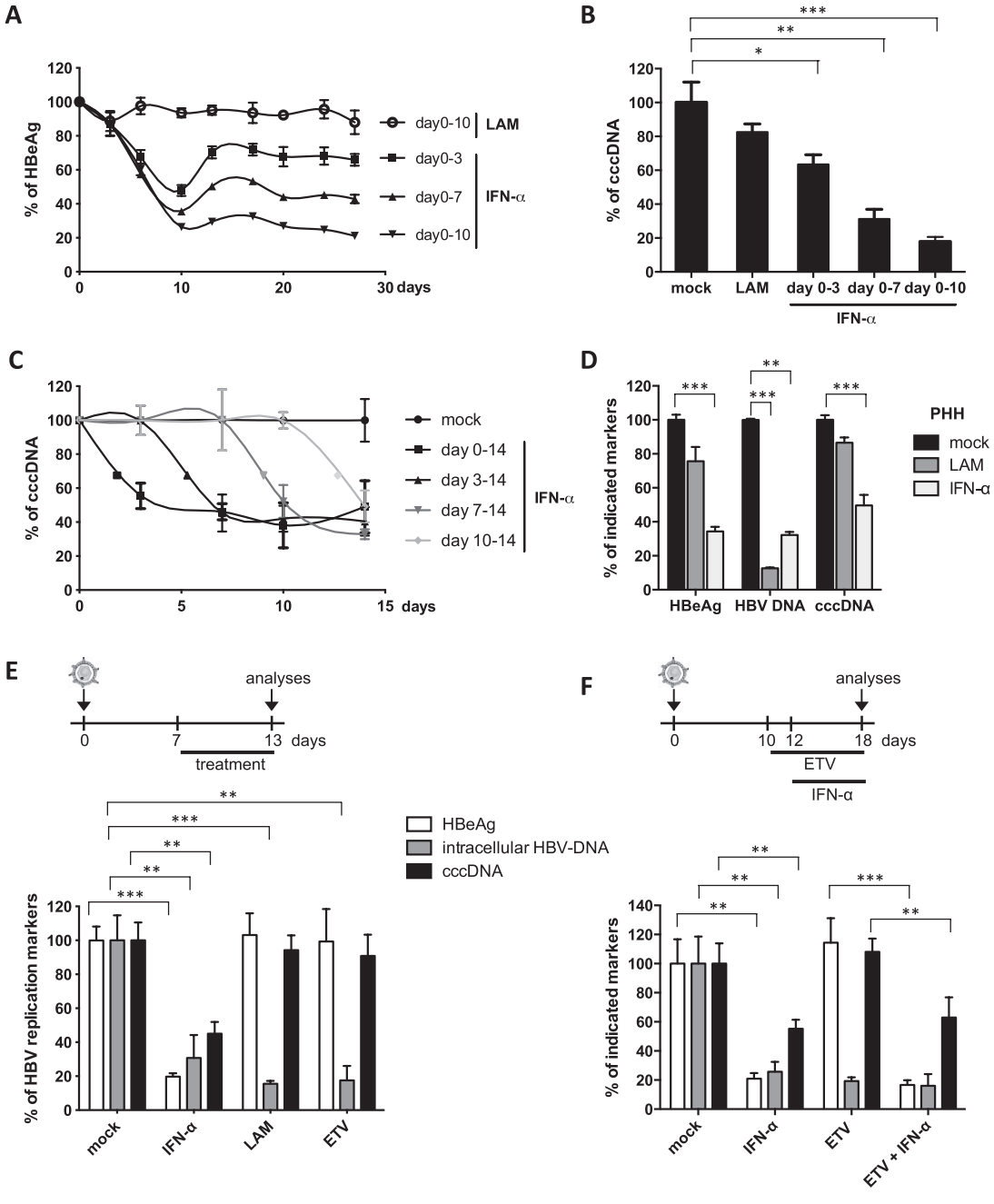

Fig. 1. Degradation of cccDNA in IFN-α–treated HepaRG cells and primary human hepatocytes. (**A**, **B**, **C**, **E**, and **F**) HBV-infected dHepaRG cells were treated with IFN-α at day 10 post-infection (dpi). Different regimens of treatment were applied as indicated. (**D**) HBV-infected PHHs were treated with IFN-α at dpi 3 for 13 days. Levels of HBeAg, total intracellular DNA, and cccDNA are given relative to mock-treated cells. LAM, lamivudine; ETV, entecavir. Data are means ± SD of replicates from independent experiments and were analyzed by *t* test. **P* < 0.05, ***P* < 0.01, ****P* < 0.001.

induce a persistent antiviral effect. In contrast to LAM treatment, no rebound of HBV replication was observed when BS1 treatment stopped (Fig. 2E). Hence, LTβR activation not only suppressed HBV replication but also caused nuclear cccDNA degradation, which is needed to achieve virus elimination.

LTβR Activation and IFN-α Treatment Induce Deamination and Apurinic/Apyrimidinic (AP) Site Formation in cccDNA

To investigate whether cccDNA degradation upon LTβR activation or IFN-α treatment was a result of DNA damage, we examined cccDNA deamination by differential DNA denaturation PCR (3D-PCR) (*21*). Lower denaturing temperatures were sufficient for cccDNA amplification from HBV-infected dHepaRG cells and for PHHs treated with IFN-α or BS1, compared with denaturing temperatures needed to amplify cccDNA from untreated, LAM-treated, or ETV-treated cells (Fig. 3A and fig. S7, C and D). Using a cocktail of recombinant proteins containing all enzymes necessary for DNA repair, we could reverse the denaturation of cccDNA (Fig. 3A, lower panels). The fact that the denaturation temperatures of mock-, LAM-, and ETV-treated cells also shifted indicated that this modification of HBV cccDNA existed even without exposure to exogenous drugs. Deamination of cccDNA (Fig. 3A, right panel) and a drop in cccDNA levels after treatment with CBE11 (table S1) were confirmed in vivo in human liver chimeric uPA-SCID mice infected with HBV. Sequencing analyses showed that G→A transitions occurred under treatment (Fig. 3B and fig. S7, A and B), indicating deamination of cytidines to uridine in the HBV cccDNA minus strand. At lower denaturation temperatures, G→A transitions became more obvious (Fig. 3C and fig. S7A). These data showed that both LTβR activation and IFN-α treatment led to cccDNA deamination in vitro and in vivo, and help to explain the G→A hypermutation observed in patient samples (*21*).

Neither deamination nor mutations of genomic DNA were observed by 3D-PCR (fig. S8A) or by deep sequencing of selected housekeeping genes or of IFN and LTβR target genes (fig. S8B). This finding indicated that DNA modifications were specifically targeted to viral cccDNA.

After cytidine deamination, DNA glycosylases recognize the damaged DNA and cleave N-glycosidic bonds to release the base and create an accessible apurinic/apyrimidinic site (AP site) that can then be cleaved by endonucleases (*22*). These AP sites can be repaired, can lead to mutations upon DNA replication, or can induce DNA degradation (*23*). We quantified AP sites created by LTβR activation or IFN-α treatment. However, no increase of AP sites in total DNA extracts from dHepaRG cells or PHHs treated with IFN-α or LTβR agonists (fig. S8C) was found, indicating again that our treatments did not lead to detectable damage in genomic DNA. Because AP sites in the small (3.2 kb) cccDNA are very likely to be missed by this analysis, we digested total DNA extracts with an AP endonuclease (APE1) and then amplified cccDNA by qPCR. APE digestion further decreased cccDNA extracted from dHepaRG cells and PHHs treated with IFN-α or LTβR agonists but not with LAM (Fig. 3D). Taken together, our data indicate that both LTβR activation and IFN-α treatment induced deamination and AP site formation in HBV cccDNA, leading to its degradation, but did not affect genomic DNA.

LTβR Activation and IFN-α Treatment Up-Regulate Expression of Nuclear APOBEC3 Deaminases

IFN-α is known to induce several cytidine deaminases (*23*, *24*). We performed genome-wide expression profiling of HBV-infected dHepaRG

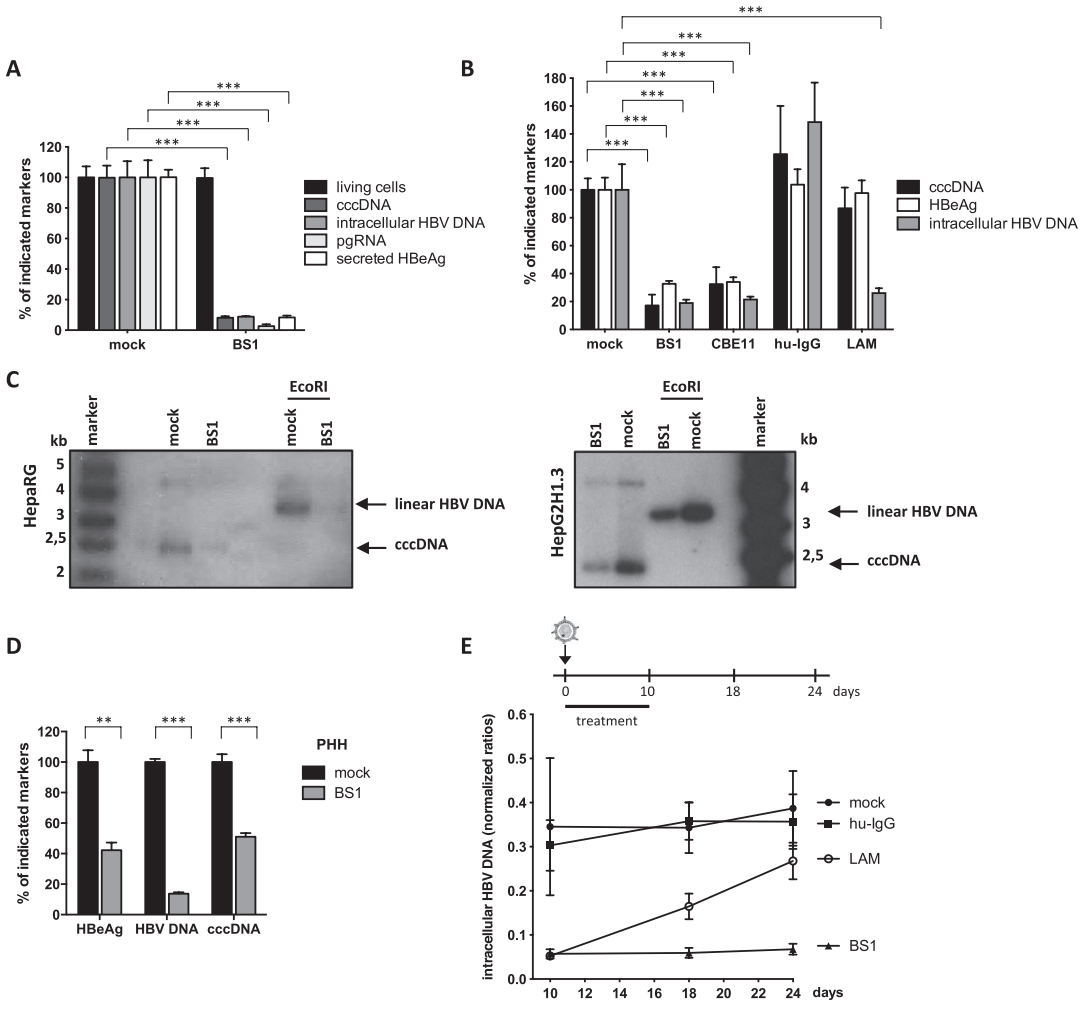

Fig. 2. LTβR activation inhibits HBV infection and leads to cccDNA degradation in HepaRG cells and PHHs. (**A** and **B**) HBV-infected dHepaRG cells were treated with BS1, CBE11, human immunoglobulin (hu-IgG) control, or lamivudine (LAM). Treatment started 24 hours before infection for 12 days (A) or at 18 dpi for 10 days (B). Levels of the indicated HBV markers as well as cell viability are given relative to untreated controls (mock). (**C**) cccDNA levels were analyzed after 14 days of BS1 treatment by Southern blot in HBV-infected dHepaRG and HBV-replicating HepG2-H1.3 cells. Supercoiled cccDNA bands were identified by their expected size and linearization upon Eco RI digestion (3.2 kb). (**D**) PHHs were infected with HBV and treated with BS1 at 7 dpi for 10 days. Levels of the indicated HBV markers were compared to untreated PHHs of the same donor (donor 3) (mock). (**E**) HBV-infected dHepaRG cells were treated with BS1, hu-IgG control, or LAM. Intracellular HBV-DNA was analyzed 8 and 14 days after treatment cessation. Data are means ± SD of replicates from independent experiments and were analyzed by *t* test. $^{*}P < 0.05$, $^{**}P < 0.01$, $^{***}P < 0.001$.

cells after LTβR activation (fig. S9A) and classified regulated genes according to their activity and properties (fig. S9B). The gene encoding APOBEC3B (A3B) was identified as the most up-regulated gene with nucleic acid–binding properties (fig. S9C).

Analysis of all APOBEC3 family members showed that LTβR activation leads to strong up-regulation of A3B, and to a lesser extent A3G, in HBV-infected dHepaRG cells and PHHs and after systemic application in human liver chimeric uPA-SCID mice (fig. S10A). A3B expression was induced by LTβR activation in a dose-dependent manner, and expression levels steadily increased during continuous treatment (fig. S11), correlating with a concomitant increase in treatment efficacy over time (fig. S3C). Treatment of PHHs isolated from different donors with the LTβR agonist BS1 resulted in cccDNA degradation at different levels (Fig. 3E and fig. S10B), which could be explained neither by the difference in the level of A3B up-regulation (Fig. 3E) nor by detection of a previously described (*25*) genomic deletion of the A3B allele, which seems to correlate with

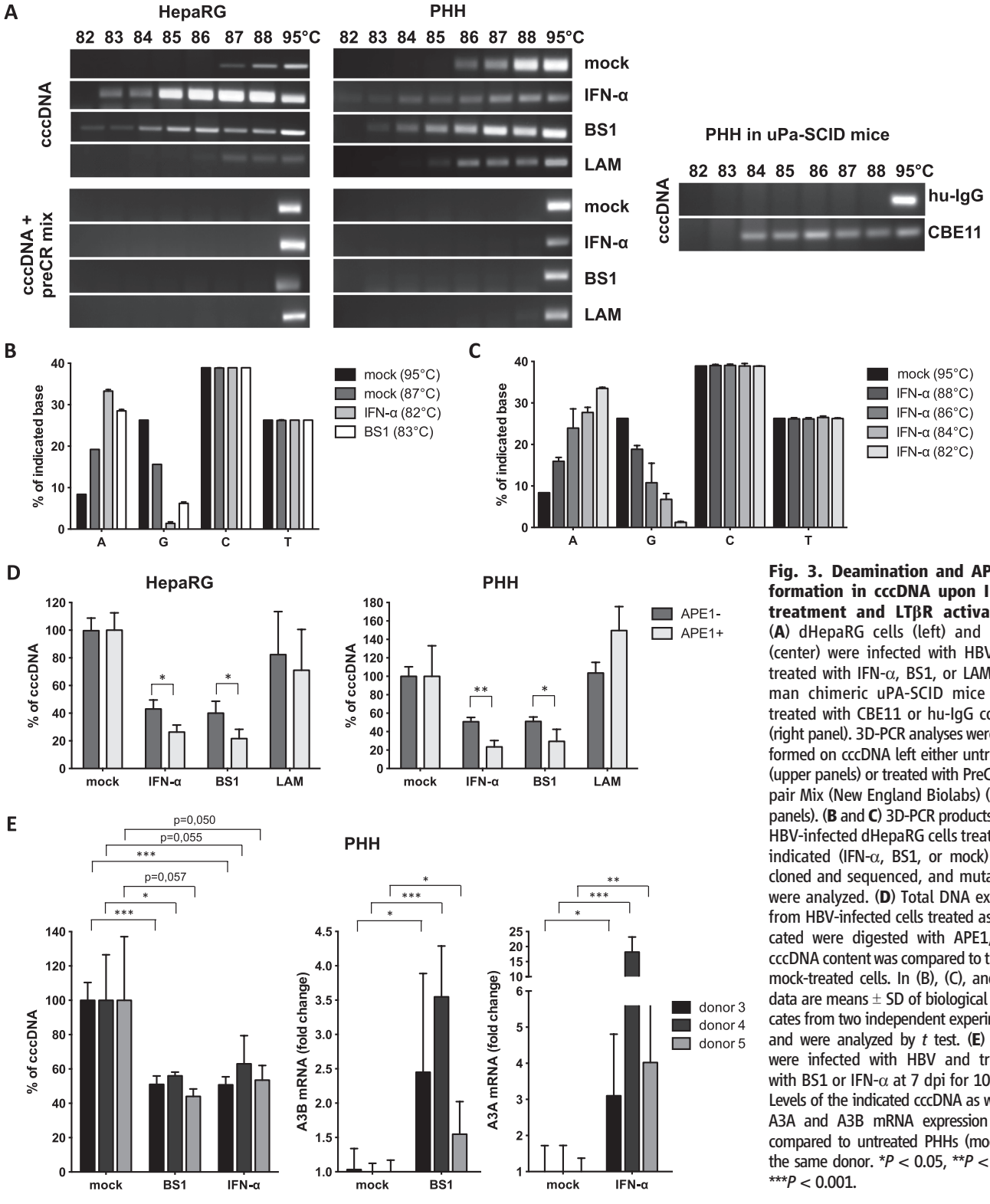

Fig. 3. Deamination and AP site formation in cccDNA upon IFN-α treatment and LTβR activation. (**A**) dHepaRG cells (left) and PHHs (center) were infected with HBV and treated with IFN-α, BS1, or LAM. Human chimeric uPA-SCID mice were treated with CBE11 or hu-IgG control (right panel). 3D-PCR analyses were performed on cccDNA left either untreated (upper panels) or treated with PreCR Repair Mix (New England Biolabs) (lower panels). (**B** and **C**) 3D-PCR products from HBV-infected dHepaRG cells treated as indicated (IFN-α, BS1, or mock) were cloned and sequenced, and mutations were analyzed. (**D**) Total DNA extracts from HBV-infected cells treated as indicated were digested with APE1, and cccDNA content was compared to that of mock-treated cells. In (B), (C), and (D), data are means ± SD of biological triplicates from two independent experiments and were analyzed by *t* test. (**E**) PHHs were infected with HBV and treated with BS1 or IFN-α at 7 dpi for 10 days. Levels of the indicated cccDNA as well as A3A and A3B mRNA expression were compared to untreated PHHs (mock) of the same donor. $*P < 0.05$, $**P < 0.01$, $***P < 0.001$.

HBV persistence in infected patients (fig. S10, B and C).

In contrast to LTβR activation, IFN-α treatment induced mainly A3A expression, as well as A3F and A3G expression, in HBV-infected dHepaRG cells and PHHs (fig. S12A) and A3D expression in isolated PHHs. By systemic IFN treatment of chimpanzees (*26*), A3A was strongly up-regulated in liver needle biopsies (fig. S12B). Activation of A3A, A3F, and A3G after IFN-α treatment was dose- and time-dependent and decreased after an initial peak despite continuous treatment, indicating that cells become refractory to IFN-α (fig. S13). In patients treated with subcutaneous pegylated IFN-α, needle biopsies obtained at different time points confirmed a rapid, strong up-regulation of A3A (and, to a lesser extent, A3G) in the liver, peaking at 16 hours after treatment (fig. S12C). Expression levels declined after this time point and remained low until day 6 after treatment, confirming a fast but transient induction of A3A by IFN-α treatment. The findings that IFN-α induced a transient A3A induction and that cells rapidly became refractory to IFN-α may account for the limited effect of IFN-α treatment in HBV-infected patients (*3*).

APOBEC3A or APOBEC3B Activity Is Essential to Induce cccDNA Degradation

Among the APOBEC3 family members up-regulated in our experiments, only A3A and A3B located to the nucleus (fig. S14), where they can gain access to cccDNA. To verify that they are indeed responsible for the induction of cccDNA degradation, we overexpressed the HIV-Vif protein [known to promote the degradation of all APOBEC3 proteins except A3B (*27*, *28*)] in dHepaRG cells in a tetracycline-regulated fashion. Expression of HIV-Vif reduced A3A, A3F, and A3G expression (fig. S15A), reverted IFN-α–induced cccDNA deamination, and prevented cccDNA degradation induced by IFN-α treatment (Fig. 4A). However, expression of HIV-Vif did not alter A3B levels (fig. S15B) and had no impact on cccDNA degradation by LTβR activation (fig. S15C). To specifically address the role of A3A or A3B in cccDNA degradation, we further knocked down A3A and A3B in dHepaRG cells under IFN-α or LTβR agonist treatment, respectively, and observed reduced cccDNA deamination (Fig. 4, B and C, left panels). Both A3A and A3B knockdown completely reverted cccDNA degradation but could not rescue the additional effect of IFN-α or LTβR activation on HBV replication (Fig. 4, B and C, right panels).

To confirm the impact of A3A and A3B on cccDNA deamination, we overexpressed A3A and A3B, respectively, in HBV-replicating HepG2-H1.3 cells (Fig. 4, D and E). Cytidine deamination of nuclear cccDNA by A3A and A3B is in accordance with other studies showing that both localize to the nucleus (*29*) and may be involved in the elimination of foreign DNA (*23*).

APOBEC3A Interacts with HBV Core Protein and Binds to cccDNA

APOBECs have evolved to restrict retroviral replication (*30*) as well as DNA transfer into cells. They are able to clear foreign nuclear DNA (*23*, *31*),

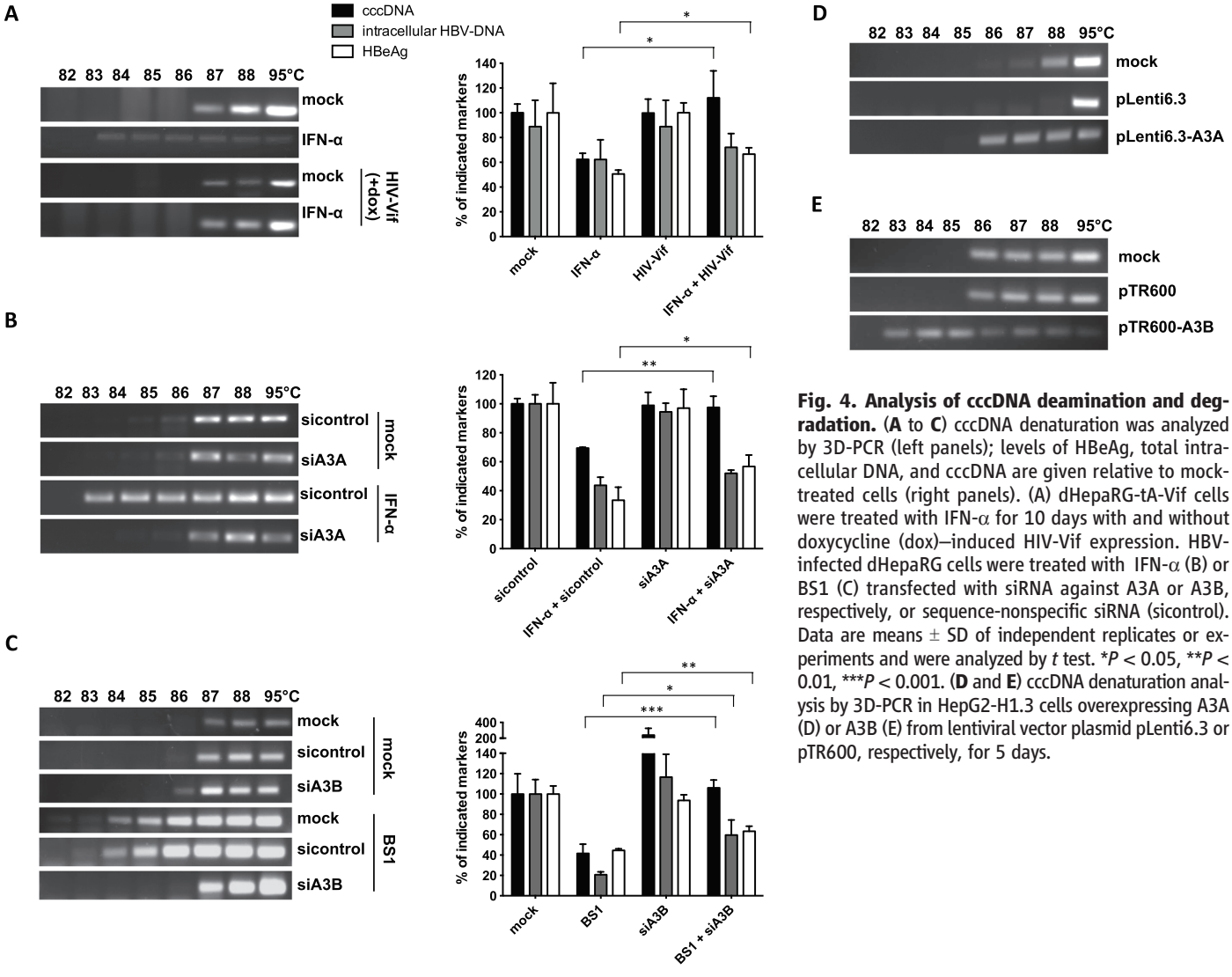

Fig. 4. Analysis of cccDNA deamination and degradation. (**A** to **C**) cccDNA denaturation was analyzed by 3D-PCR (left panels); levels of HBeAg, total intracellular DNA, and cccDNA are given relative to mock-treated cells (right panels). (A) dHepaRG-tA-Vif cells were treated with IFN-α for 10 days with and without doxycycline (dox)–induced HIV-Vif expression. HBV-infected dHepaRG cells were treated with IFN-α (B) or BS1 (C) transfected with siRNA against A3A or A3B, respectively, or sequence-nonspecific siRNA (sicontrol). Data are means ± SD of independent replicates or experiments and were analyzed by *t* test. $*P < 0.05$, $**P < 0.01$, $***P < 0.001$. (**D** and **E**) cccDNA denaturation analysis by 3D-PCR in HepG2-H1.3 cells overexpressing A3A (D) or A3B (E) from lentiviral vector plasmid pLenti6.3 or pTR600, respectively, for 5 days.

but it remains unclear how HBV cccDNA was recognized and whether it was specifically targeted in our experiments. To assess specificity, we generated cell lines replicating a mammalian replicon plasmid pEpi containing a linear HBV 1.3× overlength sequence. From the linear HBV genome, HBV replication was initiated and, in addition to the pEpi-H1.3 replicon, HBV cccDNA was established in the nucleus. Treatment with either IFN-α or the LTβR agonist BS1 inhibited HBV replication and resulted in deamination and degradation of HBV cccDNA, but not of the HBV sequence–containing replicon (fig. S16). This result indicated that the deamination and subsequent degradation induced by both treatments is HBV cccDNA–specific.

HBV core protein associates with A3G (*32*) and HBV cccDNA (*33*) and was thus a candidate to mediate the targeting of A3 deaminases to HBV cccDNA. Confocal microscopy indicated a colocalization of A3A and A3B with the HBV core in different cell lines and PHHs (Fig. 5 and fig. S17). Chromatin immunoprecipitation (ChIP) experiments using stably (fig. S18A) or transiently transfected HepG2-H1.3 cells or HBV-infected and IFN-α treated dHepaRG cells showed that HBV core protein and A3A both bind to the cccDNA minichromosome (Fig. 6A). Supporting the possibility that a guardian protein prevents A3A direct binding to DNA (*34*), we could not detect A3A binding to genomic DNA (fig. S18B) even in the presence of the HBV core, which has been reported to also bind to cellular DNA (*35*).

HBV core protein coimmunoprecipitated A3A in HepG2-H1.3 cells and transfected HuH7 cells, indicating physical interaction with A3A (fig. S19). Proximity ligation assay (PLA) (Fig. 6B and fig. S20) and fluorescence resonance energy transfer (FRET) analysis (Fig. 6C) confirmed that the HBV core expressed after HBV infection directly interacted with A3A induced by IFN-α. By deletion analysis, we determined that the central region of HBc (amino acids 77 to 149) is involved in the interaction with A3A (Fig. 6C and fig. S21).

These data suggest that A3A may be targeted to cccDNA by interaction with the HBV core. No such targeting to genomic DNA has been described so far. Because APOBEC3 deaminases are thought to act on single-stranded DNA (*36*), one possibility is that A3A and A3B act on cccDNA when it is transiently rendered into single-stranded form by RNA polymerase II before transcription initiation.

We therefore suggest the following mechanism of APOBEC-dependent degradation of HBV cccDNA (Fig. 6D). High-dose IFN-α treatment or LTβR activation up-regulate the expression of A3A and A3B, respectively, which subsequently colocalize or directly interact with HBV core in infected hepatocytes and then translocate to the nucleus, where they are brought into close contact with cccDNA by the HBV core. The APOBECs can now deaminate cccDNA that is transiently rendered single-stranded during transcription. Uracils in HBV cccDNA are recognized and excised by cellular DNA glycosylases, leading to the formation of AP sites, which are then recognized by cellular AP endonucleases (*23*), leading in turn to cccDNA digestion. Why cccDNA is degraded instead of being repaired by the cellular DNA repair machinery has remained elusive. Using a mixture of various enzymes, we were able to repair deaminated cccDNA in tubo (Fig. 3A); this suggests the induction of an additional factor promoting DNA degradation or an impaired function of the repair machinery, rather than a lack of recognition by the repair machinery. Thus, we can only speculate that either (i) the number of AP sites introduced after treatment is too high and exceeds the capacity of the cellular repair machinery, or (ii) IFN-α treatment or LTβR activation [or even HBV itself (*37*)] modulates the repair machinery. This may shift the equilibrium from cccDNA repair (*38*) to degradation.

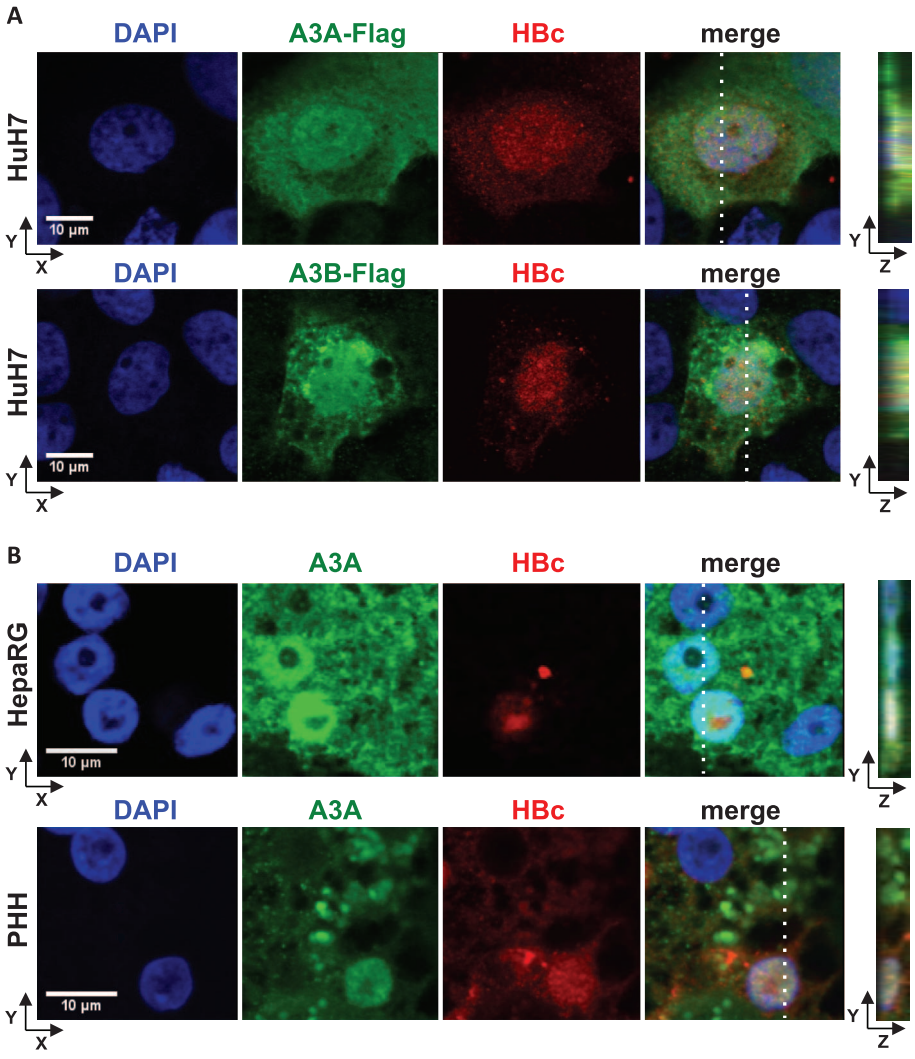

Fig. 5. Colocalization of A3A and A3B with HBV core protein (HBc). (**A**) HuH7 cells were cotransfected with an HBV 1.1× overlength genome and A3A-Flag– or A3B-Flag–expressing plasmids and stained using 4′,6-diamidino-2-phenylindole (DAPI) and antibodies to HBc and Flag. (**B**) HBV-infected dHepaRG cells and PHHs were treated with IFN-α at 7 dpi for 3 days. A3A and HBc were analyzed by immunofluorescence staining. Right panels indicate Z stacks taken at the dotted lines.

Ideally, a cure for HBV infection needs to eliminate cccDNA. Therefore, cytokines or cytokine receptor agonists that can trigger HBV cccDNA deamination and its degradation are interesting antiviral candidates. Antivirals that induce A3A and/or A3B activity should be combined with nucleoside or nucleotide analogs to avoid the replenishment of nuclear cccDNA after degradation. LTβR agonists were active at low doses, and we did not observe any toxicity in vitro or in vivo, nor did we detect any modification of genomic DNA. Constitutive overexpression of LTα/β for more than 1 year has been associated with inflammatory liver disease and hepatocellular carcinoma (*16*). As antivirals, however, LTβR agonists would be used for only a limited period of time, minimizing the risk of side effects. Moreover, LTβR activation has already been explored as a cancer treatment (*18*).

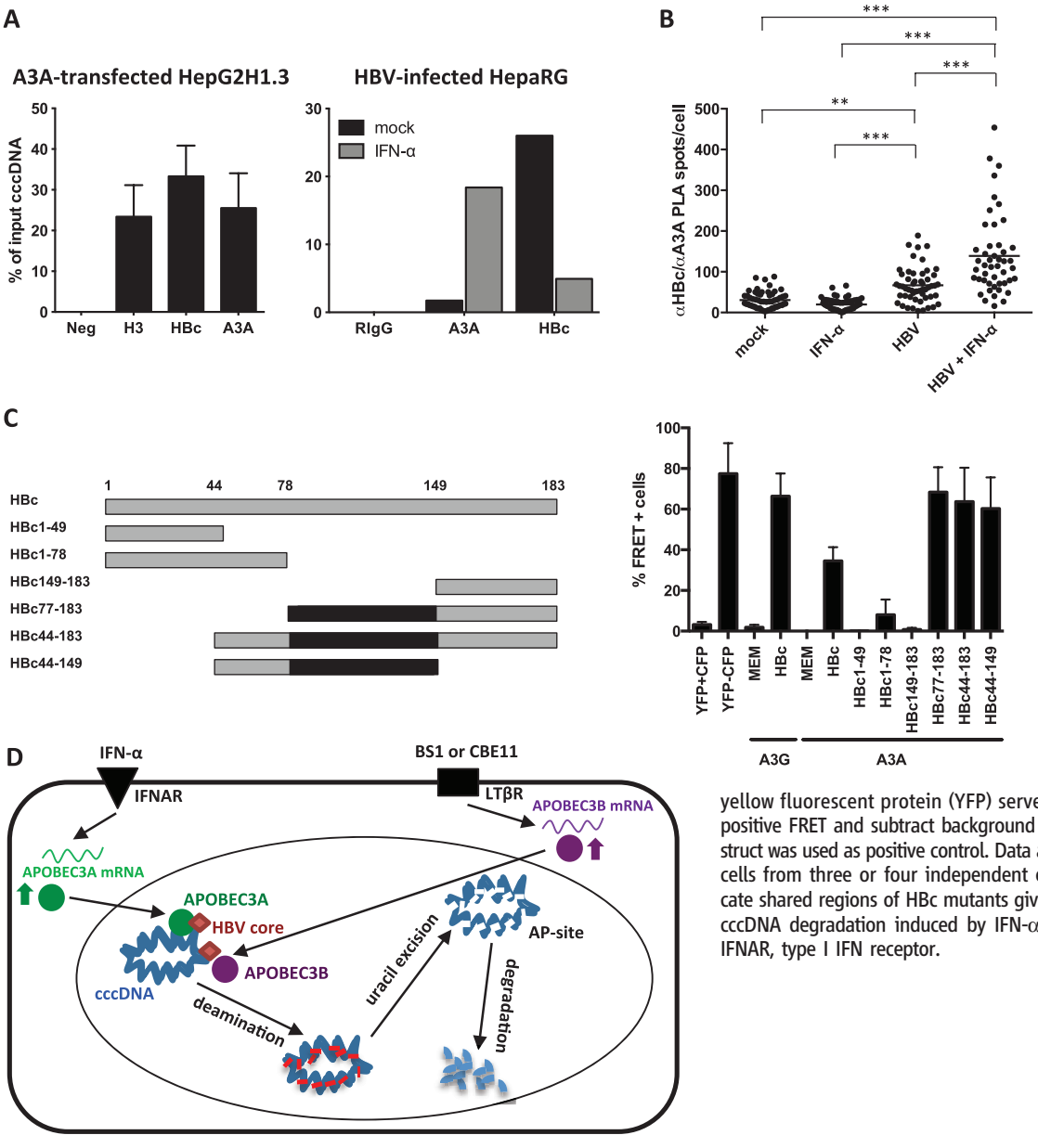

Fig. 6. Interaction of A3A, HBV core protein (HBc), and cccDNA. (**A**) Chromatin immunoprecipitation (ChIP) was performed using lysates of HepG2-H1.3 cells transfected with A3A-expressing plasmid or HBV-infected dHepaRG cells treated with IFN-α for 3 days. IPs using antibodies against histone H3, A3A, HBc, and control rabbit IgG (RIgG) were analyzed by qPCR for cccDNA. (**B**) Interaction between HBc and A3A was assessed by proximity ligation assay (PLA) in HBV-infected, IFN-α–treated dHepaRG cells. PLA spots were quantified in single cells by software-based spot counting. Data were analyzed by one-way analysis of variance. $^{**}P < 0.01$, $^{***}P < 0.001$. (**C**) Serial HBV core deletion mutants (left) were fused to cyan fluorescent protein (CFP), and interaction with A3A-YFP was assessed by fluorescence-activated cell sorting and FRET in HuH7.5 hepatoma cells (right). Cells cotransfected with CFP and yellow fluorescent protein (YFP) served as controls to exclude false positive FRET and subtract background signals. A CFP-YFP fusion construct was used as positive control. Data are means ± SD of FRET-positive cells from three or four independent experiments. Black boxes indicate shared regions of HBc mutants giving a FRET signal. (**D**) Model of cccDNA degradation induced by IFN-α treatment or LTβR activation. IFNAR, type I IFN receptor.

A recent study has shown a higher frequency of an A3B deletion allele in persistent HBV carriers and hepatocellular carcinoma patients relative to healthy controls (*25*). This finding was further supported by the moderate deamination of cccDNA even in the absence of treatment, and by the observation that knockdown of A3B in the absence of any treatment increased cccDNA levels. Although deregulated expression of A3A and A3B has been shown to correlate with genomic DNA mutations (*39*, *40*), we did not detect any alterations of genomic DNA using analyses of AP sites, 3D-PCR analysis, and deep sequencing of a set of human genes.

Our data indicate that cccDNA degradation is possible and can be induced without side effects on the infected host cell. An important task will be the testing of combinations of nucleoside or nucleotide analogs with novel antiviral strategies [e.g., LTβR agonists or adoptive T cell therapy (*41*)] to activate A3A or A3B to cure hepatitis B.

References and Notes

1. U. Protzer, M. K. Maini, P. A. Knolle, *Nat. Rev. Immunol.* **12**, 201–213 (2012).
2. F. Zoulim, *Liver Int.* **31** (suppl. 1), 111–116 (2011).
3. K. Wursthorn *et al.*, *Hepatology* **44**, 675–684 (2006).
4. L. G. Guidotti *et al.*, *Proc. Natl. Acad. Sci. U.S.A.* **91**, 3764–3768 (1994).
5. L. G. Guidotti *et al.*, *Science* **284**, 825–829 (1999).
6. S. F. Wieland, H. C. Spangenberg, R. Thimme, R. H. Purcell, F. V. Chisari, *Proc. Natl. Acad. Sci. U.S.A.* **101**, 2129–2134 (2004).
7. H. McClary, R. Koch, F. V. Chisari, L. G. Guidotti, *J. Virol.* **74**, 2255–2264 (2000).
8. L. Belloni *et al.*, *J. Clin. Invest.* **122**, 529–537 (2012).
9. A. Rang, S. Günther, H. Will, *J. Hepatol.* **31**, 791–799 (1999).
10. V. Pasquetto, S. F. Wieland, S. L. Uprichard, M. Tripodi, F. V. Chisari, *J. Virol.* **76**, 5646–5653 (2002).
11. S. F. Wieland, L. G. Guidotti, F. V. Chisari, *J. Virol.* **74**, 4165–4173 (2000).
12. S. L. Uprichard, S. F. Wieland, A. Althage, F. V. Chisari, *Proc. Natl. Acad. Sci. U.S.A.* **100**, 1310–1315 (2003).
13. P. Gripon *et al.*, *J. Virol.* **62**, 4136–4143 (1988).
14. P. Gripon *et al.*, *Proc. Natl. Acad. Sci. U.S.A.* **99**, 15655–15660 (2002).
15. M. J. Wolf, G. M. Seleznik, N. Zeller, M. Heikenwalder, *Oncogene* **29**, 5006–5018 (2010).
16. J. Haybaeck *et al.*, *Cancer Cell* **16**, 295–308 (2009).
17. S. Jost, P. Turelli, B. Mangeat, U. Protzer, D. Trono, *J. Virol.* **81**, 10588–10596 (2007).
18. M. Lukashev *et al.*, *Cancer Res.* **66**, 9617–9624 (2006).
19. X. Hu *et al.*, *Carcinogenesis* **34**, 1105–1114 (2013).
20. E. Dejardin *et al.*, *Immunity* **17**, 525–535 (2002).
21. R. Suspène *et al.*, *Proc. Natl. Acad. Sci. U.S.A.* **102**, 8321–8326 (2005).
22. J. I. Friedman, J. T. Stivers, *Biochemistry* **49**, 4957–4967 (2010).
23. M. D. Stenglein, M. B. Burns, M. Li, J. Lengyel, R. S. Harris, *Nat. Struct. Mol. Biol.* **17**, 222–229 (2010).
24. M. Bonvin *et al.*, *Hepatology* **43**, 1364–1374 (2006).

25. T. Zhang *et al.*, *Hum. Mol. Genet.* **22**, 1262–1269 (2013).
26. Y. Huang *et al.*, *Gastroenterology* **132**, 733–744 (2007).
27. B. P. Doehle, A. Schäfer, B. R. Cullen, *Virology* **339**, 281–288 (2005).
28. G. Berger *et al.*, *PLOS Pathog.* **7**, e1002221 (2011).
29. H. Muckenfuss *et al.*, *J. Biol. Chem.* **281**, 22161–22172 (2006).
30. C. Münk, A. Willemsen, I. G. Bravo, *BMC Evol. Biol.* **12**, 71 (2012).
31. M. A. Carpenter *et al.*, *J. Biol. Chem.* **287**, 34801–34808 (2012).
32. P. Turelli, B. Mangeat, S. Jost, S. Vianin, D. Trono, *Science* **303**, 1829 (2004).
33. C. T. Bock *et al.*, *J. Mol. Biol.* **307**, 183–196 (2001).
34. M. M. Aynaud *et al.*, *J. Biol. Chem.* **287**, 39182–39192 (2012).
35. Y. Guo *et al.*, *BMC Genomics* **13**, 563 (2012).
36. H. C. Smith, R. P. Bennett, A. Kizilyer, W. M. McDougall, K. M. Prohaska, *Semin. Cell Dev. Biol.* **23**, 258–268 (2012).
37. T. H. Lee, S. J. Elledge, J. S. Butel, *J. Virol.* **69**, 1107–1114 (1995).
38. K. Kitamura *et al.*, *PLOS Pathog.* **9**, e1003361 (2013).
39. S. Landry, I. Narvaiza, D. C. Linfesty, M. D. Weitzman, *EMBO Rep.* **12**, 444–450 (2011).
40. M. B. Burns *et al.*, *Nature* **494**, 366–370 (2013).
41. K. Krebs *et al.*, *Gastroenterology* **145**, 456–465 (2013).

Acknowledgments: We thank R. Bester, T. Asen, K. Ackermann, K. Kappes, M. Feuerherd, R. Baier, R. Hillermann, U. Finkel, A. Krikoni, and F. Zhang for technical support; L. Terracciano for analysis of acute hepatitis patients; F. Chisari for HBV transgenic mice (HBV 1.3.32); T. Buch and O. Prazeres da Costa for help with array analysis and data discussions; L. Allweiss and A. Groth for help in generating and treating humanized uPA-SCID mice; and Siemens Healthcare Diagnostics for reagents. Supported by grants from Fédération Belge Contre le Cancer (E.D.), a European Research Council starting grant (LiverCancerMechanism) (M.H.), the German Research Foundation (SFB 841 to M.D., SFB TR 36 to M.H., and SFB TR 22), the Peter-Hans Hofschneider Foundation and the Helmholtz Alliances HAIT (U.P.), and PCCC (M.H.). We acknowledge the support of the nonprofit foundation HTCR, which holds human tissue on trust, making it broadly available for research on an ethical and legal basis. Patent application EP12006XXX has been filed at the European patent office: "Lymphotoxin signaling activation and its downstream mediators eliminate HBV ccc DNA." Microarray data have been submitted to the GEO database (www.ncbi.nlm.nih.gov/geo/) with accession number GSE46667. Human liver chimeric uPA-SCID mice were handled in accordance with protocols approved by the ethical committee of the city and state of Hamburg (permission number G12/015). Experiments with HBV-transgenic mice were performed in accordance with German legislation governing animal studies and the Principles of Laboratory Animal Care guidelines, NIH (55.1-1-54-2531.3-27-08). The study protocol for the animal experiment in fig. S12B was approved at the Southwest Foundation for Biomedical Research, San Antonio, TX (IACUC 869 PT, approved in 2004).

Supplementary Materials
www.sciencemag.org/content/343/6176/1221/suppl/DC1
Materials and Methods
Figs. S1 to S21
Table S1
References (*42*–*62*)

18 July 2013; accepted 5 February 2014
Published online 20 February 2014;
10.1126/science.1243462

REPORTS

Free-Standing Single-Atom-Thick Iron Membranes Suspended in Graphene Pores

Jiong Zhao,[1,3] Qingming Deng,[2] Alicja Bachmatiuk,[1,3,4] Gorantla Sandeep,[1] Alexey Popov,[2] Jürgen Eckert,[1,5] Mark H. Rümmeli[3,6]*

The excess of surface dangling bonds makes the formation of free-standing two-dimensional (2D) metals unstable and hence difficult to achieve. To date, only a few reports have demonstrated 2D metal formation over substrates. Here, we show a free-standing crystalline single-atom-thick layer of iron (Fe) using in situ low-voltage aberration-corrected transmission electron microscopy and supporting image simulations. First-principles calculations confirm enhanced magnetic properties for single-atom-thick 2D Fe membranes. This work could pave the way for new 2D structures to be formed in graphene membranes.

The success and promise of atomically thin carbon–namely, graphene (*1*)–has triggered enormous enthusiasm for the study of other two-dimensional (2D) materials such as hBN, MoS_2, and $MoSe_2$ (*2*, *3*). These 2D films are able to be reduced to atomically thin layers while still maintaining mechanical integrity, because they are layered structures where the bonding within a layer is covalent whereas the interlayer bonding occurs through weak van der Waals interactions, thus allowing individual layers to be easily separated. With bulk metals, at first glance, the nature of metallic bonding and their 3D structure prohibit them from existing as a monoatomic layer. The only reports for atomically thin metallic layers, thus far, are heteroepitaxial structures in which the metal atoms bond with the underlying substrates (*4*, *5*). On the other hand, because of nondirectional metallic bonding and the excellent plasticity of metals, at the nanoscale, one can build few-atom or even single-atom bridges (*6*, *7*). Many single atomic metallic layers (e.g., Fe, Co, and Mn) are attractive due to their inherent magnetic properties. For the case of 2D Fe monolayers, the magnetic moment is expected to be 3.1 μB, which is markedly higher than its bulk counterpart (2.2 μB), and, in addition, 2D Fe should have a large perpendicular magnetic anisotropy (*8*). Hence, 2D magnets could be promising for magnetic recording media. Most of what is known about 2D magnets is based on theoretical investigations. These studies point to their magnetic properties being highly sensitive to their structure (*9*). Face-centered cubic (FCC) Fe and body-centered cubic (BCC) Fe ultrathin films have been grown on Cu, W, SiC, MgO, and other surfaces (*9*–*13*). However, these structures interact with the underlying substrate. Free-standing 2D metal films do not suffer from substrate-based influences, thus preserving coordination and electron confinement.

Experimental and theoretical works have focused on the interactions between graphene and single metal atoms (including Fe atoms) (*14*–*16*) or clusters (*17*). We show that porous graphene under electron-beam irradiation can be extended to enable Fe atoms and clusters to entirely seal small perforations in graphene and form a single atomic crystalline Fe layer.

In our in situ investigation, a low-voltage spherical aberration-corrected transmission electron microscopy (LVACTEM) operating with an acceleration voltage of 80 kV was employed (*18*). The graphene samples were grown by chemical vapor deposition (CVD) over Ni/Mo substrates (*19*). The as-produced monolayer graphene was then transferred on to standard lacey carbon (TEM) grids using an $FeCl_3$ etching solution to detach the graphene (*20*). The transferred samples typically consist of large areas of monolayer graphene in which some regions contain remnant material from the transfer process, including remnant Fe species from decomposed $FeCl_3$ (*20*). Under close inspection, pure Fe can be found as small nanocrystals forming on the surface of the graphene, as single atoms or small clusters at the edge of pores in clean graphene, or as 2D crys-

[1]Leibniz-Institut für Festkörper- und Werkstoffforschung Dresden (IFW) Dresden, Institute of Complex Materials, P.O. Box 270116, D-01171 Dresden, Germany. [2]IFW Dresden, Institute of Solid State Research, P.O. Box 270116, D-01171 Dresden, Germany. [3]IBS Center for Integrated Nanostructure Physics, Institute for Basic Science (IBS), Daejon 305-701, Republic of Korea. [4]Centre of Polymer and Carbon Materials, Polish Academy of Sciences, M. Curie-Sklodowskiej 34, Zabrze 41-819, Poland. [5]Technische Universität Dresden, Institute of Materials Science, 01062 Dresden, Germany. [6]Department of Energy Science, Department of Physics, Sungkyunkwan University, Suwon 440-746, Republic of Korea.

*Corresponding author. E-mail: mark@rummeli.com

talline membranes suspended across perforations in the graphene. Typical examples are provided in Fig. 1. In the case of nanocrystalline structures forming on the surface of the graphene (Fig. 1, B and C), the measured lattice constants obtained from the Fourier domain from numerous micrographs indicates that they are either BCC or hexagonal close-packed (HCP) Fe structures. These structures match image simulations of BCC and HCP Fe nanocrystals as, for example, shown in the insets of Fig. 1, B and C, in which both the stick-and-ball models and image simulations are provided. In general, the Fe nanocrystals contain 200 to 1000 Fe atoms. Local electron energy-loss spectroscopy (EELS) spectra highlight the presence of pure Fe clusters (figs. S1 and S2). Detailed investigations at the local scale exclude other possible compounds—e.g., carbides and oxides—and confirm the presence of pure Fe nanostructures. Representative studies are provided in figs. S3 to S6.

In the case of individual Fe atoms or few-atom clusters, they tend to get trapped in small vacancies and pores in the graphene and are easily visible due to their high contrast relative to the graphene lattice. Typical examples are provided in Fig. 1D (Fe cluster in a pore) and Fig. 1E (individual atoms trapped at pore edges). Typically, these atoms are mobile around the edges when irradiated with electrons. These observations have been reported by others (*14*), so we do not elaborate further. What we do focus on here is the ability of larger numbers of Fe atoms to get trapped within a pore and form an ordered 2D crystalline lattice. Examples of such 2D Fe crystalline structures can easily be seen in Fig. 1, F and G, where the high-contrast Fe atoms fill a pore with the atoms arranging themselves, for the most part, in an ordered manner. The lattice constant for the observed nanocrystals is 2.65 ± 0.05 Å, which is appreciably larger than that for the (200) Miller-index plane distance for the FCC phase or the (110) plane distance for BCC Fe.

Figure 2A shows a higher-magnification TEM micrograph of one of these Fe membranes suspended in a graphene pore. Figure 2B shows the corresponding micrograph after Fourier transform filtering (to reduce noise), and Fig. 2C shows an image simulation of a 2D Fe membrane suspended in graphene. Initial visual inspection shows strong similarities. Figure 2D shows the

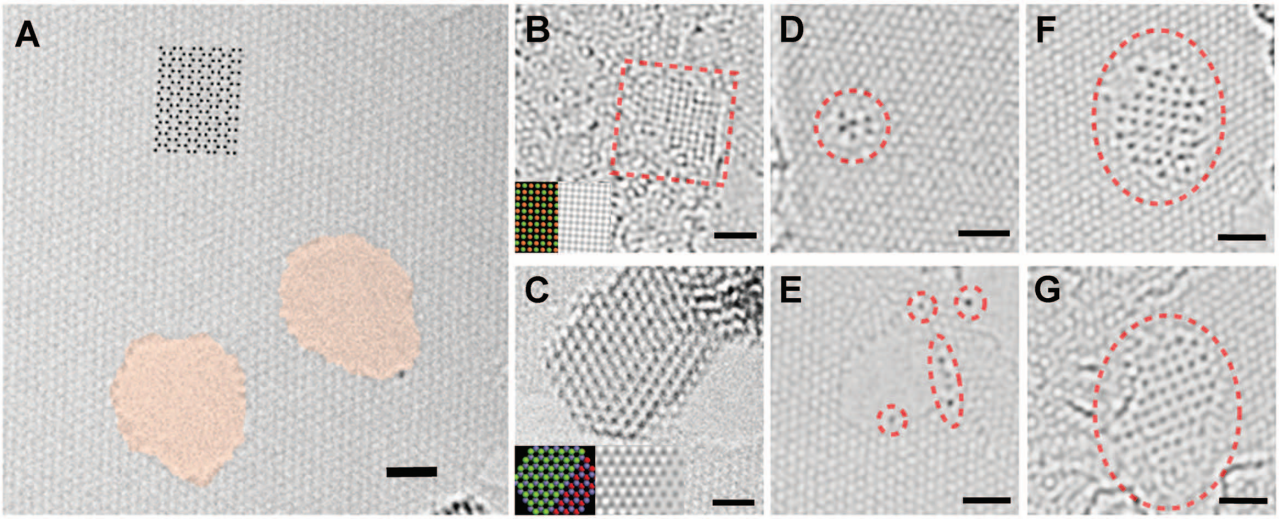

Fig. 1. LVACTEM images of graphene perforations and various Fe clusters. (**A**) Graphene perforations (highlighted). (**B**) BCC Fe nanocrystal, with atomic structure and image simulation as an inset. (**C**) HCP Fe nanocrystal, which has a step on it. The atomic structure and an image simulation are provided in the inset. (**D**) A several-atom cluster embedded in graphene. (**E**) Many individual Fe atoms residing on the edges of graphene. (**F** and **G**) Two typical monoatomic Fe layers suspended in a perforation in graphene. Scale bars, 1 nm.

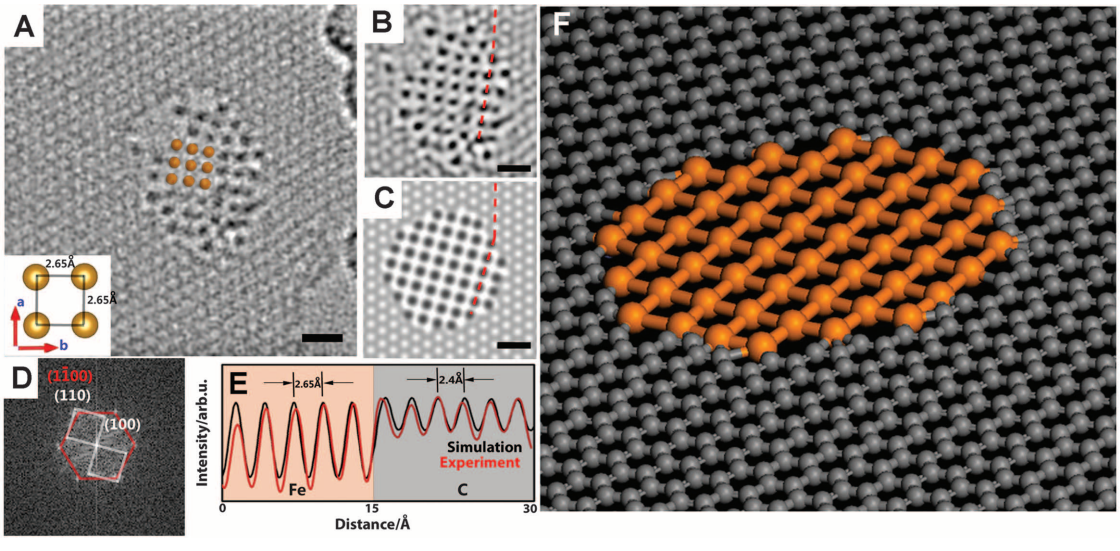

Fig. 2. Characterization of monoatomic Fe layer. (**A**) LVACTEM micrograph of a monoatomic Fe layer with the square unit cell. The inset highlights the interatomic spacing of the square unit cell. (**B**) Smoothed image of (A). (**C**) Image simulation of a monoatomic Fe layer. (**D**) Fast Fourier transform of the structure in (A) that shows the lattice relationship between the graphene (red) and the monoatomic Fe layer (white). (**E**) Normalized intensity profiles from the image simulation (black line) and experimental image (red line), corresponding to marked profiles in red dashed lines in (B) and (C). The intensity profiles match, confirming that the Fe membrane is a single atom thick. (**F**) Atomic structure of a suspended mono/atomic Fe layer in a graphene pore. All scale bars, 0.6 nm.

Fourier transform of Fig. 2A. The inner reflexes correspond to the (100) plane of Fe. The outer reflexes arise from the (1-100) plane of graphene. In addition, the (110) plane for Fe almost overlaps the (1-100) graphene planes. This indicates preferential alignment of the Fe(110) plane with the graphene (1-100) plane. This preferential alignment was observed for all the examined structures. We also compared the relative intensity variation between the graphene basal plane and the Fe structure filling the pore for both the experimentally obtained micrographs and the image simulations. An example is provided in Fig. 2E. The two profiles match each other extremely well. The image simulation is formed from a single atomic layer of Fe atoms (Fig. 2F) and so confirms that the suspended Fe structure we measure experimentally is a single-atom-thick Fe layer with a square lattice (see fig. S7 for more detail on thickness determination). EELS studies show only Fe peaks and no carbon or oxygen signatures, confirming that the monolayer membranes are made only of Fe.

To better comprehend these monolayer Fe structures, we conducted density functional theory (DFT) calculations based on the generalized gradient approximation with the Perdew-Burke-Ernzerhof function (*21*). The calculations show that the in-plane square lattice of monolayer Fe is energetically favored over the other possible 2D configurations, including tetragonal, hexagonal, and so forth. The calculations suggest the most stable lattice constant for monolayer Fe is ~2.35 Å, which is smaller than our experimental value of 2.65 ± 0.05 Å; however, the calculated energy difference between 2.35 Å and 2.65 Å is not large (0.2 eV per atom) (table S1). In addition, some physical aspects not considered in the calculations could lead to a larger lattice constant. For example, the effect of spin-orbit coupling and perpendicular magnetic anisotropy in atomically thin films will lead to energy variations. More important, strain due to lattice alignment and mismatch between graphene and 2D monolayer Fe cannot be ignored, particularly because our calculations show that the in-plane Young's modulus of monolayer iron is ~160 GPa, which is an order of magnitude smaller than that of graphene (1 TPa). Figures S8 to S11 and their accompanying discussion in the supplementary materials illustrate the effect of strain on the lattice spacing. Moreover, the phonons in monolayer Fe will differ from bulk 3D Fe (*22*) because the fraction of anharmonic vibrations increases with the reduction of thin-film thickness, which leads to a larger thermal expansion. To investigate this, an additional self-consistent lattice dynamics calculation or ab initio molecular dynamics calculation would be required (*23*).

One can get a sense of local strain effects by first looking at the interface between iron atoms attached to different graphene edges. Two possible binding configurations are possible between Fe atoms and graphene, namely, binding to the basal plane or at an open end or edge. In practice, binding at the basal plane is relatively common, whereas metallic atom binding at the open edges is rare even though such binding has been theoretically proposed (*24*). In our observations, the Fe atoms always bind at open graphene edges—for example, at the edges of a pore as shown in Fig. 3, A to C. We also study such Fe atom attachments using first-principle DFT calculations. Because the most stable edge terminations for graphene are the armchair and zigzag configurations (*25*), we investigated six possible configurations for single Fe atoms at armchair or zigzag edges, including an arrangement in which Fe atoms replace the first two rows of carbon atoms at an open edge (Fig. 3, D to I). The bonding energies of the Fe atoms for these config-

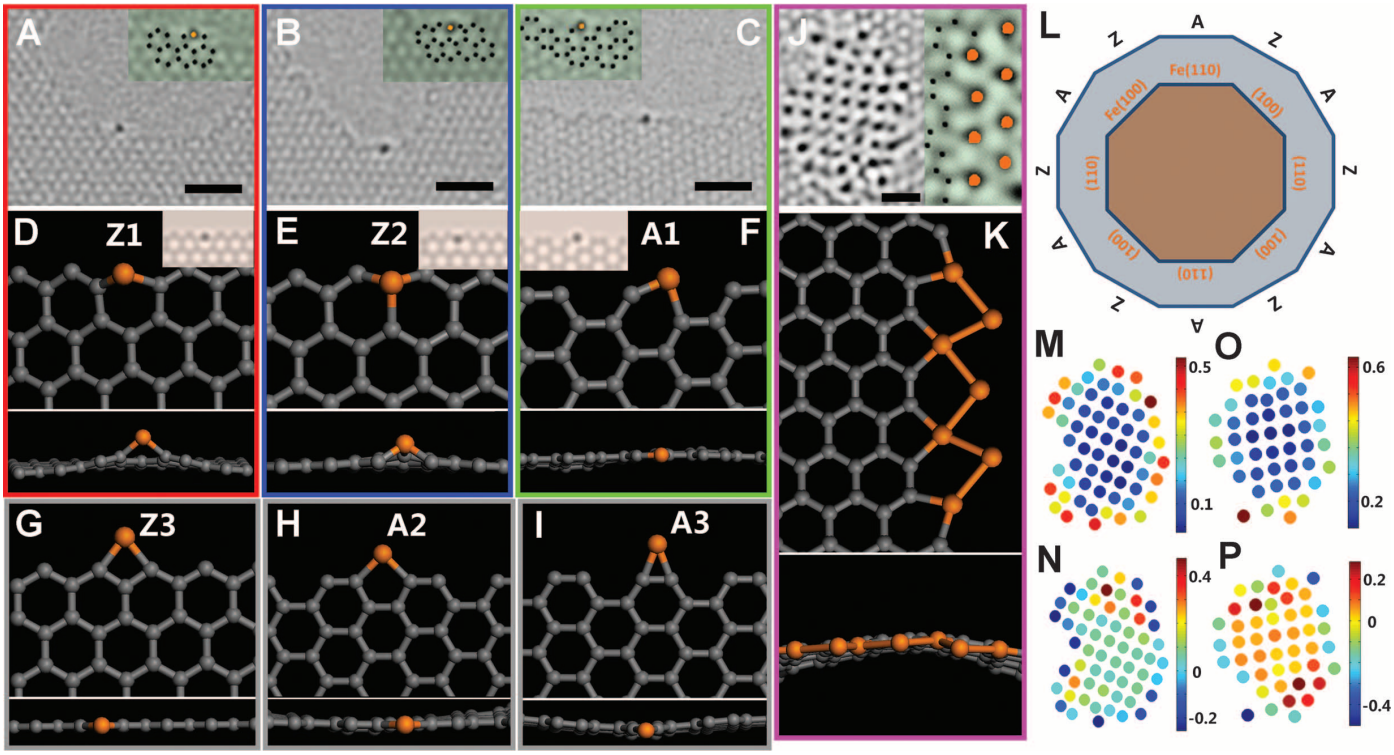

Fig. 3. The interface between a monoatomic Fe layer and graphene and local strain mapping. (**A**) LVACTEM image of the Z1 configuration as illustrated in (D). The insets show the highlighted edge structure, with carbon (black) atoms and Fe (orange) atoms highlighted. (**B** and **C**) LVACTEM images of the Z2 and A1 configurations [(E) and (F), respectively]. The insets show the highlighted edge structure with carbon (black) atoms and Fe (orange) atoms highlighted. Scale bars in (A) to (C), 1 nm. (**D** to **I**) First-principle calculation results showing top and cross-section views of different single-Fe atoms binding to different graphene-edge configurations. The insets for (D) to (F) show the corresponding image simulations from the stick-and-ball structure provided in the main panels. (**J** and **K**) The Fe(110) with armchair edge visible in a LVACTEM image and first-principle-calculated configuration, respectively. Scale bar in (J), 0.5 nm. (**L**) Schematic diagram showing the relationship between the (100) and (110) Fe edges and the zigzag (Z) and armchair (A) edges from graphene. (**M** to **P**) Calculated local von Mises-strain-invariant plots of two single-atom Fe layers. The atom positions are taken from the micrographs provided in Fig. 1, F and G; (M) and (O) provide the hydrostatic strain plots, and (N) and (P) show the shear strain plots. The color of each atom refers to the values in the vertical scale bar.

urations are provided in table S2. Despite the bonding energies not being at a minimum in the substitution configuration in which an Fe atom replaces a single carbon atom in a hexagonal ring (configurations Z1, Z2, and A1 in Fig. 3, D to F, respectively), as compared to configurations Z3, A2, and A3 (Fig. 3, G to I, respectively), they are favored because upon removal of an Fe atom, an incomplete hexagon structure is left, which is energetically unfavorable (as compared to zigzag or armchair terminations). Thus, the reaction barrier for the removal of substitution Fe atoms is high. Indeed, this is what we observe experimentally, where for the most part, Fe atoms are imaged as substituting a C atom in a benzene ring at the edge of graphene, as shown in Fig. 3, A to C. For comparison, image simulations based on the structures used for the first-principles calculations are provided as insets in Fig. 3, D to F.

Although substitution configurations are more stable, the formation of an Fe monoatomic layer occurs with a continuous placement of Fe atoms along the edges that are not always set in a substitution configuration. For example, linking configurations such as Z3 (Fig. 3G) and A2 (Fig. 3H) are also found, as can be seen in Fig. 3J. The linking formation shown in Fig. 3I is rarely observed; this is due to its reduced bonding energy. Linking formations are observed in monolayer Fe-graphene junctions, as illustrated in Fig. 3J; the corresponding calculated structure is also given (Fig. 3K).

Another aspect to consider at the Fe membrane-graphene interface is the preferential alignment of Fe atoms. For example, considering the graphene zigzag and armchair edges and the lattice constant for monolayer Fe, the best lattice match is twice the Fe(110) plane distance (1.9 Å) with an armchair edge (2.1 Å). This configuration provides the lowest mismatch strain and interfacial energy and is an alignment configuration that we observe in our experiments, as can be seen in the diffraction information shown in Fig. 2D. However, if an Fe(110) plane to armchair configuration exists, then the only other match is for the Fe(110) plane to align with a zigzag edge (Fig. 3L). In effect, in a membrane interface, mismatches lead to distortions at the interface (within 15°). The interfacial distortions can be seen more clearly on local strain maps, as illustrated in Fig. 3, M to P. The atomistic positions are obtained by the Gaussian fitting of atom locations taken from experimental micrographs. The local 2D atomistic strains are then calculated (*26*). The shear strain components and hydrostatic strain components are provided in Fig. 3, M and O, and Fig. 3, N and P, respectively, for two actual images (Fig. 1, G and F, respectively). Examination of the strain maps show lower shear at the center of an Fe membrane than at the edges. This is concomitant with the hydrostatic strain, which appears homogeneous at the center of the membrane. (See the supplementary materials for further discussion.)

We now turn to the formation and stability of single-atom-thick Fe membranes while under electron irradiation. Typically, Fe atoms on the surface of the graphene are mobile while exposed to electron irradiation. If they encounter a small hole (a few nm wide), the atoms collect and rearrange themselves within it to form a monolayer crystalline Fe membrane. The formation process usually occurs in a matter of seconds. Figure 4A shows a hole in the graphene with a number of Fe atoms perched by an edge. After 3 s of electron irradiation (1 pA/nm^2), the Fe atoms have moved into the hole and arranged themselves neatly into a crystalline 2D Fe membrane (Fig. 4B). (A more detailed set of images and the formation of a suspended Fe monolayer by etching the graphene beneath can be found in figs. S12 to S14.) Once a suspended Fe membrane has formed in a graphene pore, it is relatively stable in that it can sustain electron irradiation for several minutes, after which it starts to collapse (Fig. 4, C to J). Closer examination shows that the Fe monolayer edge disconnects first from a zigzag edge, whereas Fe (110) membrane-armchair interfaces tend to remain stable for far longer before forming an amorphous particle (see circled regions in Fig. 4, E and F). This is in agreement with our analysis above, in which armchair interfaces are shown to be the most stable configurations.

We also studied the diameter-stability dependence. By investigating the energy difference, ΔE, between a suspended Fe monolayer and a nanoparticle using the equivalent number of Fe atoms, one can estimate the largest stable Fe membrane that can form. ΔE is given by

$$\Delta E = E_{Fe\text{-}C} + E_{MLFe} - E_{Fe} \qquad (1)$$

where $E_{Fe\text{-}C}$ is the binding energy between the Fe membrane and graphene interface, E_{MLFe} is the total energy of the Fe monolayer, and E_{Fe} is the total energy of the Fe nanoparticle, including the surface energy. Neglecting the effects of lattice instabilities and using energy values determined in our previous DFT calculations, we find the largest stable membrane to be ~12 atoms wide (fig. S15) or 3 by 3 nm^2. This is in excellent agreement with our experimental observation, in which the largest observed diameters are ~10 atoms.

Finally, we examined the band structure of a freestanding monolayer Fe membrane through spin-polarized DFT calculations using the experimentally derived lattice constant (2.65 Å) and compare it to the (calculated) band structure of bulk BCC Fe. Some obvious differences between the two can be seen, as shown in fig. S16. By comparing the partial density of states, one can see that for the spin-up (majority) orbitals, the d_z^2 orbital for 2D Fe is appreciably smaller than for bulk BCC Fe. This is primarily due to the 2D nature of the Fe membrane, because the d_z^2

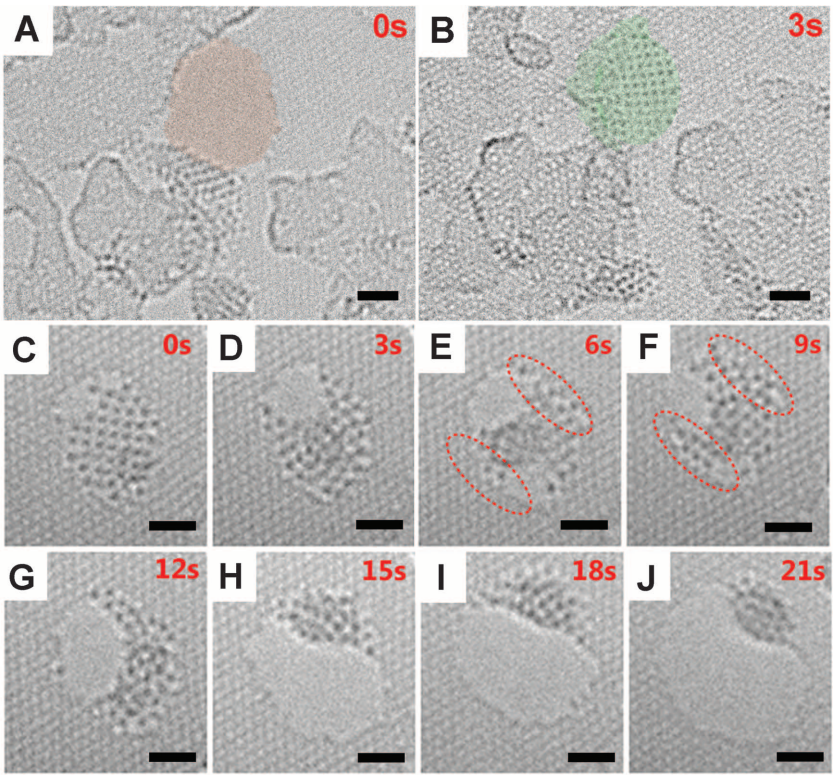

Fig. 4. The formation and collapse of a suspended single-atom Fe layer under electron irradiation. (**A**) An Fe cluster at the edge of a graphene pore (highlighted). (**B**) After 3 s, the Fe atoms move in to the perforation and form a single-atom Fe membrane sealing the entire graphene pore. (**C** to **J**) Continued electron irradiation leads to the collapse of the 2D Fe membrane. The Fe(110)–armchair graphene interfaces are the most stable and are highlighted in (E) and (F). All scale bars, 1 nm.

orbital is out of plane whereas the d_{xy} orbital is in plane. The first-principles calculations show a considerably enhanced magnetic moment for single-atom-thick Fe membranes (3.08 μB) as compared with bulk BCC Fe (2.1 μB), in good agreement with previously calculated values (*8*). The total magnetic moment is slightly decreased by the Fe-C boundary effect but is still much larger the bulk value (fig. S17).

In summary, the existence of free-standing monoatomic suspended Fe membranes is demonstrated. These 2D Fe nanomembranes are directly imaged and are shown to have a square lattice with a 2.65 Å lattice constant at room temperature. These studies provide valuable data for further more accurate and in-depth theoretical investigations. The potential of perforated graphene as a support for 2D membranes is shown, and one can anticipate new 2D structures from a variety of elements to emerge.

References and Notes

1. K. S. Novoselov *et al*., *Science* **306**, 666–669 (2004).
2. C. H. Jin, F. Lin, K. Suenaga, S. Iijima, *Phys. Rev. Lett.* **102**, 195505 (2009).
3. H. Komsa, A. V. Krasheninnikov, *J. Phys. Chem. Lett.* **3**, 3652–3656 (2012).
4. D. Qian, X. F. Jin, J. Barthel, M. Klaua, J. Kirschner, *Phys. Rev. Lett.* **87**, 227204 (2001).
5. G. Wedler, C. M. Schneider, A. Trampert, R. Koch, *Phys. Rev. Lett.* **93**, 236101 (2004).
6. H. Ohnishi, Y. Kondo, K. Takayanagi, *Nature* **395**, 780–783 (1998).
7. M. J. Lagos, F. Sato, D. S. Galvão, D. Ugarte, *Phys. Rev. Lett.* **106**, 055501 (2011).
8. J. Izquierdo *et al*., *Phys. Rev. B* **61**, 13639–13646 (2000).
9. R. Lorenz, J. Hafner, *Phys. Rev. B* **54**, 15937–15949 (1996).
10. W. Lu, K. Zhang, X. Xie, *Phys. Rev. B* **48**, 18159–18163 (1993).
11. J. G. Gay, R. Richter, *Phys. Rev. Lett.* **56**, 2728–2731 (1986).
12. M. Wuttig, J. Thomassen, *Surf. Sci.* **282**, 237–245 (1993).
13. A. Lehnert *et al*., *Phys. Rev. B* **82**, 094409 (2010).
14. A. W. Robertson *et al*., *Nano Lett.* **13**, 1468–1475 (2013).
15. O. Cretu *et al*., *Phys. Rev. Lett.* **105**, 196102 (2010).
16. A. V. Krasheninnikov, P. O. Lehtinen, A. S. Foster, P. Pyykkö, R. M. Nieminen, *Phys. Rev. Lett.* **102**, 126807 (2009).
17. H. Wang *et al*., *Sci. Rep.* **2**, 995 (2012).
18. F. Börrnert *et al*., *J. Microsc.* **249**, 87–92 (2013).
19. B. Dai *et al*., *Nat. Commun.* **2**, 522 (2011).
20. Y. C. Lin *et al*., *ACS Nano* **5**, 2362–2368 (2011).
21. J. P. Perdew, K. Burke, M. Ernzerhof, *Phys. Rev. Lett.* **77**, 3865–3868 (1996).
22. S. Stankov *et al*., *Phys. Rev. Lett.* **99**, 185501 (2007).
23. G. Grimvall, B. Magyari-Köpe, V. Ozolins, K. A. Persson, *Rev. Mod. Phys.* **84**, 945–986 (2012).
24. Y. Matsuda, W. Deng, W. A. Goddard III, *J. Phys. Chem. C* **114**, 17845–17850 (2010).
25. Ç. Ö. Girit *et al*., *Science* **323**, 1705–1708 (2009).
26. J. Li, I. S. Yip, *Handbook of Materials Modeling* (Kluwer Academic Publishers, Dordrecht, Netherlands, 2005).

Acknowledgments: J.Z. thanks the Deutscher Akademischer Austausch Dienst DAAD Foundation, and S.G. thanks the Deutsche Forschungsgemeinschaft (RU 1540/8-1). thanks the DFG (project PO 1602/1-1 to A.P.). This work was supported by the Institute of Basic Science (IBS) Korea. We also thank Y.-h. Luo (East China University of Science and Technology) for providing us with the Dmol3 code. We thank S. Melkhanova and J. Pang for the fabrication of the CVD-grown graphene. We thank the IFW Dresden for granting us use of their microscopy facilities.

Supplementary Materials

www.sciencemag.org/content/343/6176/1228/suppl/DC1
Materials and Methods
Supplementary Text
Figs. S1 to S17
Tables S1 and S2
References (*27*–*33*)

28 August 2013; accepted 19 February 2014
10.1126/science.1245273

Main-Group Compounds Selectively Oxidize Mixtures of Methane, Ethane, and Propane to Alcohol Esters

Brian G. Hashiguchi,[1]* Michael M. Konnick,[1] Steven M. Bischof,[1] Samantha J. Gustafson,[2] Deepa Devarajan,[2] Niles Gunsalus,[1] Daniel H. Ess,[2]* Roy A. Periana[1]*

Much of the recent research on homogeneous alkane oxidation has focused on the use of transition metal catalysts. Here, we report that the electrophilic main-group cations thallium(III) and lead(IV) stoichiometrically oxidize methane, ethane, and propane, separately or as a one-pot mixture, to corresponding alcohol esters in trifluoroacetic acid solvent. Esters of methanol, ethanol, ethylene glycol, isopropanol, and propylene glycol are obtained with greater than 95% selectivity in concentrations up to 1.48 molar within 3 hours at 180°C. Experiment and theory support a mechanism involving electrophilic carbon-hydrogen bond activation to generate metal alkyl intermediates. We posit that the comparatively high reactivity of these d^{10} main-group cations relative to transition metals stems from facile alkane coordination at vacant sites, enabled by the overall lability of the ligand sphere and the absence of ligand field stabilization energies in systems with filled d-orbitals.

The world is undergoing a revolution in raw hydrocarbon feedstock supply with the discovery of increasingly abundant sources of natural gas in shale and offshore gas fields (*1*). Although natural gas is primarily methane, natural gas—particularly from shale—also has substantial amounts of ethane and propane (*2*). The conversion of methane, as well as these higher alkanes in natural gas, into liquid fuels and commodity chemicals such as methanol, ethylene, ethanol, ethylene glycol, isopropanol, and propylene glycol at lower costs than the current multistep, capital-intensive processes could reduce emissions and our dependence on petroleum, as well as increase the value of natural gas.

An important approach that has emerged in the past few decades is the design of molecular (homogeneous) catalysts for the oxidative functionalization of alkanes based on the CH activation reaction. This involves selective reaction of an M-X catalyst with a hydrocarbon CH bond (R-H) under relatively mild conditions without the involvement of radicals in order to generate a M-R intermediate that is converted to the desired R-X product with regeneration of M-X (Eq. 1). There has been considerable effort in this area of research with homogeneous (*3*–*23*) as well as heterogeneous catalysts (*24*–*26*), and substantial progress has been made in recent years. Most of the work on the homogeneous systems have been primarily based on transition metals (with unfilled d-shells, $d^{<10}$) such as Pt (*3*, *4*, *16*), Pd (*14*, *17*–*19*, *23*), Rh (*20*–*22*), and Ir (*7*–*10*). In contrast, relatively few studies have been directed toward the classic main-group elements with a filled d-shell (d^{10}). In 1993, we reported an example of a main-group metal cation, Hg^{II}, in the superacid concentrated H_2SO_4 for direct conversion of methane to methanol esters (*15*). In spite of the simplicity of the Hg^{II} system, it was not further developed because of lack of reaction in more practical, weaker acid media such as CF_3CO_2H (TFAH), CH_3CO_2H (HOAc), or aqueous acids with which product separation could be practical. Another key issue was that the reactions of ethane and propane were unselective with the Hg^{II} system. We originally proposed an electrophilic CH activation mechanism for the Hg^{II} system. However, later work by Sen, based on the observation of products resulting from C-C cleavage reactions with higher alkanes, suggested that Hg(II) in superacid media was sufficiently oxidizing to initiate free-radical reactions (*5*)

$$\text{M-X} + \text{R-H} \rightarrow \text{M-R} \rightarrow \text{M-X} + \text{R-X} \qquad (1)$$

This possibility for unselective radical reactions with higher alkanes was also considered by Moiseev and co-workers in the early 1990s on the reaction of alkanes in TFAH with strongly oxidizing salts that were known to be effective for oxidizing hydrocarbons through free-radical mechanisms (*27*, *28*). The initial report showed high yield and selectivity for the stoichiometric reactions of Co^{III} with methane to Me-TFA (*27*). Carrying out

[1]The Scripps Energy and Materials Center, Department of Chemistry, The Scripps Research Institute, Jupiter, FL 33458, USA. [2]Department of Chemistry and Biochemistry, Brigham Young University (BYU), Provo, UT 84602, USA.

*Corresponding author. E-mail: rperiana@scripps.edu (R.A.P.); dhe@chem.byu.edu (D.H.E.); bhashigu@scripps.edu (B.G.H.)

the reaction with Co^{II} in the presence of O_2 showed a turn over number (TON) of ~4 for Me-TFA, along with comparable amounts of CO_2 generated through solvent decarboxylation. Along with Co^{IV} peroxo species, both radical and nonradical mechanisms were considered. In a later report that focused on the reactions of ethane and propane, the authors proposed a free-radical mechanism to account for the extensive C-C cleavage and overoxidation reactions with these higher alkanes. In addition to transition metal salts, there was one table entry in (*28*) on the reaction of methane with stoichiometric amounts of a main-group d^{10} cation, Pb^{IV}, that generated Me-TFA in ~10% yield. The higher alkanes were not examined in that initial work, and there are no follow-up reports by Moiseev, suggesting that Pb^{IV} operated by a different mechanism from the radical reactions proposed for Co^{III}. In our own work on Hg^{II}, the main-group d^{10} cation, Tl^{III}, was also found to be active for methane oxidation to the ester. However, this was only examined in superacid media and only with methane. We did not further examine on the Tl^{III} or Pb^{IV} systems in TFAH or with higher alkanes. The primary basis for this was the recognition that both Tl^{III} with a standard reduction potential (E^o) of 1.2 V and Pb^{IV} (E^o = 1.5 V) are stronger oxidants than is Hg^{II} (E^o = 0.9 V) (*29*). Consequently, on the basis of the general considerations at that time we considered that these main-group cations would be more likely than would Hg^{II} to initiate unselective radical reaction with the higher alkanes. To our knowledge, since those early publications in the 1990s there are no reported, deliberate studies of reactions of higher alkanes with those or other strongly oxidizing main-group electrophiles.

Our later work with Pt^{II} also led to models that directed our efforts away from these main-group systems. In 1998, we reported that the well-defined transition metal complex [η-2-(2,2′-bipyrimidyl)]platinum(II), $(bpym)Pt^{II}X_2$ when dissolved in superacid solvents such as concentrated H_2SO_4 (*16*) was an effective catalyst for the functionalization of methane to ~1 M protonated methanol and bisulfate ester. However—along with the high cost of Pt, as was the case for Hg^{II}—this system was inactive in more practical,

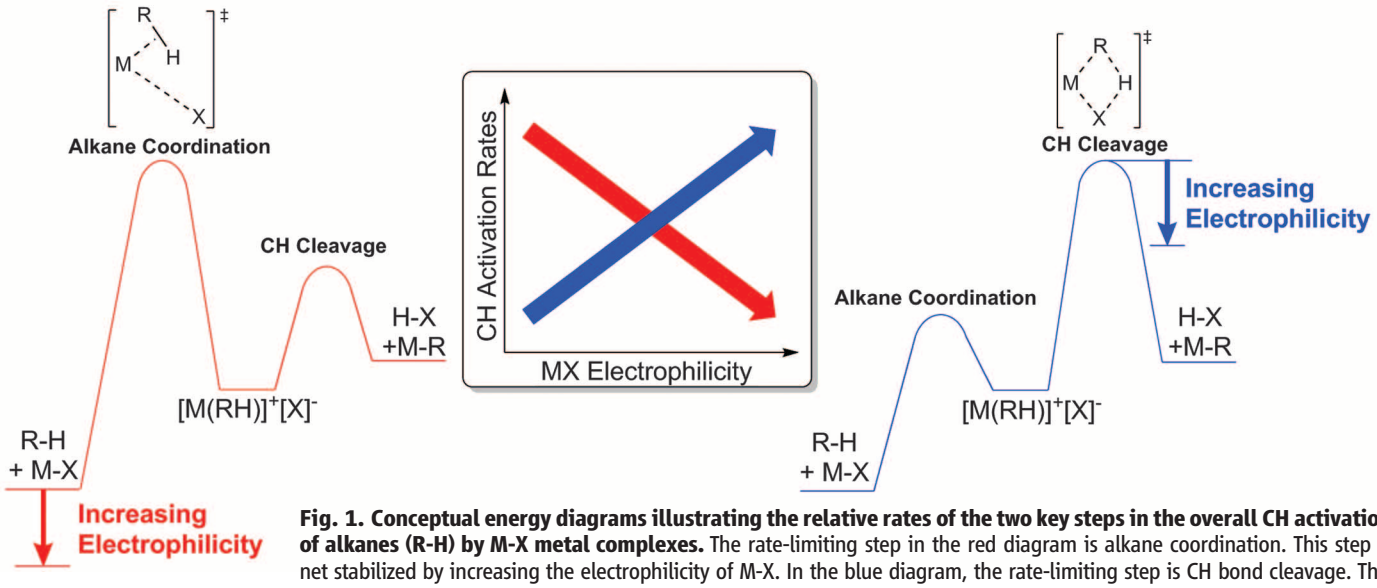

Fig. 1. Conceptual energy diagrams illustrating the relative rates of the two key steps in the overall CH activation of alkanes (R-H) by M-X metal complexes. The rate-limiting step in the red diagram is alkane coordination. This step is net stabilized by increasing the electrophilicity of M-X. In the blue diagram, the rate-limiting step is CH bond cleavage. This transition state is net stabilized by increasing the M-X electrophilicity. (Inset) The predicted trends in overall rate of CH activation with increasing electrophilicity of M-X for these cases are shown color-coordinated.

Table 1. Reaction of oxidants with methane, ethane, and/or propane. Standard conditions were 0.25 M $Tl(TFA)_3$ or $Pb(TFA)_4$ in 2 ml TFAH, gas pressure (MeH = 3.44 MPag, EtH = 3.44 MPag, or PrH = 0.861 MPag), 180°C for 3 hours. Conc (M), (moles oxidant)/(liters solvent added); product selectivity, [individual liquid product]/[total liquid products] × 100; yield based on ^{1}H-NMR, [oxidant]/[total liquid products] × 100; and [product], (moles product)/(liters solvent added).

Entry	Oxidant	Conc (M)	Solvent	Hydrocarbon	Products (% of total products)	Yield ([product])
1	$Tl(TFA)_3$	0.250	HTFA	MeH	MeTFA (100%)	74% (0.19 M)
2*	$Tl(TFA)_3$	2	HTFA	MeH	MeTFA (100%)	55% (1.1 M)
3	$Tl(TFA)_3$	0.250	HTFA	EtH	EtTFA (67%), $EG(TFA)_2$ (33%)	75% (0.16 M)
4	$Tl(TFA)_3$	3	HTFA	EtH	EtTFA (64%), $EG(TFA)_2$ (36%)	60% (1.48 M)
5	$Tl(TFA)_3$	0.250	HTFA	PrH	iPrTFA (77%), $PG(TFA)_2$ (23%)	>95% (>0.22 M)
6	$Tl(TFA)_3$	0.250	HTFA	100(MeH): 8(EtH):1(PrH)†	MeTFA (9%), EtTFA (21%), $EG(TFA)_2$ (11%), iPrTFA (10%), $PG(TFA)_2$ (19%)	82% (0.11 M)
7‡	$Tl(TFA)_3$	0.250	HTFA/H_2O	EtH	EtTFA (68%), $EG(TFA)_2$ (32%)	73% (0.16 M)
8§	$Tl(TFA)_3$	0.250	HTFA	EtH	EtTFA (66%), $EG(TFA)_2$ (34%)	76% (0.16 M)
9‖	$Tl(TFA)_3$	0.250	HTFA	EtH	EtTFA (65%), $EG(TFA)_2$ (35%)	30% (0.06 M)
10	$Tl(TFA)_3$	0.250	MSA	EtH	EtX (47%), $EG(X)_2$ (53%)¶	93% (0.18 M)
11	$Tl(OAc)_3$	0.250	HOAc	EtH	EtOAc (2%), $EG(OAc)_2$ (98%)	43% (0.06 M)
12	$Pb(TFA)_4$	0.250	HTFA	MeH	MeTFA (100%)	76% (0.19 M)
13	$Pb(TFA)_4$	0.250	HTFA	EtH	EtTFA (70%), $EG(TFA)_2$ (30%)	90% (0.2 M)
14‖	$Pb(TFA)_4$	0.250	HTFA	EtH	EtTFA (68%), $EG(TFA)_2$ (32%)	75% (0.18 M)
15	$Hg(TFA)_2$	0.250	HTFA	EtH	N/A	0% (0.0 M)

*Pressure, 5.52 MPag; and temperature (*T*) = 190°C. †Total pressure, 3.44 MPag. ‡Run with 2 M H_2O present. §Run with 100 kPa O_2 present. ‖Reactions were run at 150°C. ¶Products were a mixture of EtTFA, Et(MSA), $EG(TFA)_2$, and $EG(MSA)_2$.

weaker acids as well as unselective for reaction with higher alkanes. Studies suggested that this system operated by means of electrophilic CH activation and that the lack of reaction in weaker non-superacid solvents resulted from effectively complete inhibition of the CH activation step in these media (*30*). As shown conceptually in Fig. 1, electrophilic CH activation by M-X transition metal complexes are typically considered to proceed through two general steps, involving (i) alkane R-H coordination to M-X to generate $[M(R\text{-}H)]^+ + X^-$ followed by (ii) CH bond cleavage to generate M-R. Studies show that CH activation by the (bpym)Pt system operates as described with the red diagram in Fig. 1, in which R-H coordination is rate limiting, and inhibition in moving from superacid to weaker acid solvents results from stronger coordination of the more nucleophilic anions, X^-, present in weaker acid solvents to the electrophilic metal center. This results in net stabilization of the M-X resting state and increases the barrier to R-H coordination and CH activation.

At the time of these discoveries, we erroneously considered that all electrophilic CH activation systems would operate as in the model shown in red in Fig. 1. Consequently, we assumed that stabilization of the resting state also accounted for the inhibition of Hg^{II} in weaker, non-superacid media as well as the counterintuitive observations, in both the (bypm)Pt and Shilov PtCl systems, that the higher oxidation state Pt^{IV} is effectively inactive, whereas lower-oxidation-state Pt^{II} exhibits high rates of electrophilic CH activation. For systems operating as described with the red energy diagram in Fig. 1, it could be expected that the relative rate of CH activation would decrease with increasing electrophilicity (Fig. 1, inset, red arrow). Between this resting-state stabilization model and concerns of possible radical reactions, our studies were directed away from Tl^{III}, Pb^{IV}, and other main group cations that were more strongly oxidizing and electrophilic than are Pt^{II} (E^o = ~0.8 V) (*29*) and Hg^{II} for functionalization of higher alkanes in more practical, weaker acid media.

Contrary to those predictions, we now find that $Tl^{III}(TFA)_3$ and $Pb^{IV}(TFA)_4$ can rapidly functionalize methane, ethane, and propane separately or as mixtures, in high selectivity and concentrations to the corresponding trifluoroacetate esters of methanol (MeTFA), ethanol (EtTFA), ethylene glycol [$EG(TFA)_2$], isopropanol (iPrTFA), and 1,2-propylene glycol [$PG(TFA)_2$] (Table 1, entries 1 to 6, 8, 9, and 12 to 15). We focused primarily on TFAH as the reaction medium but also observed efficient reactivity in other non-superacidic solvents, such as methane sulfonic acid (MSA) (Table 1, entry 10), HOAc (Table 1, entry 11), and TFAH/H_2O mixtures (Table 1, entry 7). In contrast to the reported reactions with $(bpym)Pt^{II}$ or Hg^{II} in superacid media, no evidence for C-C cleavage or other side products were observed with the higher alkanes, ethane and propane. In spite of the original concerns of radical reactions and inhibition of CH activation in non-super acid media, we nonetheless believe it is plausible to rationalize the reactions of these nontransition metal, main-group d^{10} cations with alkanes by means of a general reaction mechanism involving electrophilic CH activation and M-R functionalization, which have primarily been associated with transition metals.

Some of the earliest studies on ligand interaction with metal cations show that the rates of ligand exchange for the third row, main-group, d^{10} strong electrophiles such as Hg^{II} and Tl^{III} are ~10^{19} faster than for the transition metal $d^{<10}$ cations such as Ir^{III} or Pt^{IV}. (*31*) These extraordinary differences in rate are conceptually attributed to lack of ligand field stabilization energies (LFSE) for cations with filled d-orbitals and strong LFSE for cations with unfilled d-orbitals. On the basis of these enormous differences in exchange rates, it is plausible that the rate of alkane coordination for main-group d^{10} electrophiles could be fast and that CH bond cleavage could be comparatively slow and rate limiting (Fig. 1, blue lines) for the overall CH activation process. It is also plausible that with this switch in the rate-limiting step, increasing electrophilicity could result in a net lowering of the transition state for CH bond cleavage. This can be explained by hard soft acid base (HSAB) theory, in which an increase in the M-C bond strength would be expected with increasing electrophilicity of these soft polarizable, third-row d^{10} electrophiles (*32*). As shown in Fig. 1, these considerations lead to the prediction that the rate of electrophilic CH activation (Fig. 1, inset, blue arrow) with these main-group d^{10} cations could increase with increasing electrophilicity (assuming that alkane coordination continues to be fast). This is opposite to the trend in our earlier model (Fig. 1, inset, red arrow). Counterintuitively, this new model suggests that the lack of reaction of Hg^{II} in weaker acid media was because its electrophilicity was too low rather than too high. These considerations led us to more closely examine the reaction mechanism of the Tl^{III}-mediated alkane oxidation.

The crude mixtures from the reactions of Tl^{III} with the alkane in TFAH are homogeneous and effectively colorless. The ^{1}H–nuclear magnetic resonance (NMR) spectra of the crude reaction mixtures in TFAH from separate reactions of 3.44 MPag of methane and ethane, and 0.861 MPag of propane with $Tl(TFA)_3$ in CF_3CO_2H solvent at 180°C for 3 hours are shown in Fig. 2, A to C. A coaxial insert was used as an external standard. The TFA-ester of methanol (MeTFA) and the corresponding esters of ethanol (EtTFA) and ethylene glycol [$EG(TFA)_2$] are the only products observed (within a 1% detection threshold) from methane and ethane, respectively. The reaction with propane (Table 1, entry 5) is also very efficient and only generates the corresponding esters of isopropanol (iPrTFA) and 1,2-propylene glycol [$PG(TFA)_2$]. Reactions conducted with 100% ^{13}C-labeled methane ($^{13}CH_4$) and ethane ($^{13}C_2H_6$) unambiguously confirmed that the esters are formed from the corresponding alkanes. Exclusively ^{13}C-labeled products were observed in the liquid phase, and only traces of $^{13}CO_2$ were detected in the gas phase. No products from C-C cleavage or other side reactions were observed in the liquid phases. Consistent with this high selectivity, control studies showed that the ester

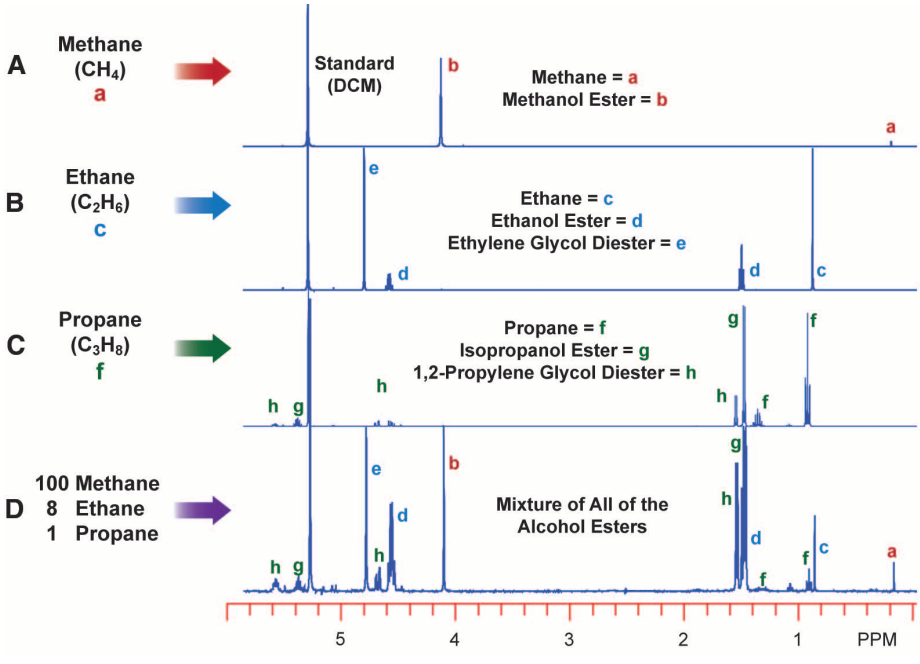

Fig. 2. Stacked ^{1}H-NMR (400 MHz) spectra of the crude reaction mixtures in TFAH after Tl^{III}–mediated oxidation of alkanes. The alkanes were, respectively, (**A**) methane, (**B**) ethane, (**C**) propane, and (**D**) a mixture of methane, ethane, and propane in a ratio typical in natural gas. The products are the alcohol esters of trifluoroacetic acid.

products are unreactive toward $Tl(TFA)_3$ when the hydrocarbon gas is replaced with argon under otherwise identical conditions. Assuming a detection limit of ~1% and a 5 mM methane concentration in the liquid phase, the parent alkanes appear to be at least 100 times more reactive than are the alcohol ester products. Because the TFA group is electron-withdrawing relative to a H atom, this is consistent with an electrophilic reaction with the CH bonds in which positive charge is developed on the carbon during CH cleavage.

Consistent with the 1:1 metal:alkane stoichiometry shown in Eq. 2, analysis of a crude reaction mixture with ethane by means of Tl-NMR before and after a reaction shows unreacted Tl^{III} as well as Tl^{I} (fig. S7). Increasingly abundant shale gas contains, in addition to methane, substantial amounts of ethane and propane. To examine whether these alkanes could be functionalized without separation in a one-pot procedure, we prepared and examined the reaction of a mixture of methane, ethane, and propane in a 100:8:1 ratio typical in natural gas. As can be seen from ^{1}H and ^{13}C-NMR analysis of the crude reaction mixture in TFAH (Fig. 2D), each alkane is converted to the corresponding alcohol esters, in high selectivity in a molar ratio of MeTFA:[EtTFA + $EG(TFA)_2$]:[iPrTFA + $PG(TFA)_2$] of ~1:3:3. When normalized for the number of hydrogens in each of the alkanes, the relative reactivity of the CH bonds in methane, ethane, and propane is ~1:25:150. This trend is also consistent with an electrophilic reaction with the CH bonds that would be expected to proceed in the order of $CH_4 < CH_3\text{-}CH_3 < CH_3CH_2CH_3$ as H-atoms on CH_4 are replaced by more electron-donating CH_3 groups

$$\text{R-H} + Tl^{III}(TFA)_3 \rightarrow Tl^{I}(TFA) + \text{TFAH} + \text{R-TFA} \quad (2)$$

As discussed above, a prediction of the blue reaction model in Fig. 1 is that in contrast to our earlier model for electrophilic CH activation, the rates of alkane functionalization should increase with increasing electrophilicity. Indeed, under identical conditions—in the absence of mass transfer limitations and at shorter reaction times so as to minimize conversion of the salts—the total yield of EtTFA and $EG(TFA)_2$ from $Hg(TFA)_2$, $Tl^{III}(TFA)_3$, and $Pb^{IV}(TFA)_4$ was 0, 30, and 75%, respectively (Table 1, entries 14, 9, and 13, respectively). In (*27*), the one data entry on the reaction of Pb^{IV} with methane in TFAH shows ~10% methanol ester yield. Compared with our result of 74% yield with $Tl^{III}(TFA)_3$ (Table 1, entry 1), this would conflict with our model because it would suggest that Tl^{III} is more reactive than Pb^{IV} is. However, we find that the yield from the reaction of methane with $Pb(TFA)_4$ is reproducibly, considerably higher (>70 versus 10%) (Table 1, entry 12). At this time, we do not understand the basis for this difference. Our results qualitatively show that the relative rates of reactivity of these electrophiles with ethane in TFAH is Hg^{II} (inactive) << $Tl^{III} < Pb^{IV}$. If the trend holds through this third-row d^{10} series, it is possible that Bi^{V} could be very reactive with alkanes. $Bi^{V}(TFA)_5$ as well as $Au^{I}(TFA)$ are unknown, and efforts are underway to synthesize and study these species.

These observations support a proposed electrophilic CH activation/M-R functionalization mechanism. However, given the general consideration that strongly oxidizing species can generate free-radical reactions with alkanes, we were prompted to carry out further mechanistic studies. Varying the alkane pressure shows a first-order rate dependence [observed rate constant (k_{obs}) = $2.6 \times 10^{-6} \pm 1.3 \times 10^{-7}$ s^{-1} MPa^{-1}] on alkane (fig. S7). Some key characteristics of free-radical reactions can be, but not always, poor reproducibility and changes in reaction rate and product selectivity in the presence of radical traps, such as O_2 (*28*). To examine these possibilities, we studied the kinetics for the reaction of $Tl(TFA)_3$ with a 33-fold excess of ethane in TFAH. The reaction exhibits highly reproducible, clean, first-order (in Tl^{III}) kinetics ($k_{obs} = 9.0 \times 10^{-5} \pm 4.5 \times 10^{-6}$ s^{-1} MPa^{-1}) for the generation of the TFA esters of EtTFA and $EG(TFA)_2$, with no induction period (fig. S9). The rate of formation of EtTFA is higher than $EG(TFA)_3$, but as can be seen in fig. S9, the ratio of [EtTFA] to [$EG(TFA)_2$] is constant as the reaction proceeds. This would suggest that these materials are generated in parallel rather than sequentially [EtH to EtTFA to $EG(TFA)_2$] as might be expected. Consistent with this control, experiments show that conversion of EtTFA to $EG(TFA)_2$ is slow in the presence of $Tl(TFA)_3$. In contrast, ethylene is found to rapidly convert to $EG(TFA)_2$ in the presence of $Tl(TFA)_3$. This could suggest that ethylene is the precursor to $EG(TFA)_2$ and is generated in parallel with EtTFA (scheme S2). These results would suggest a common intermediate—plausibly, a Tl^{III}-Et species—for the parallel formation of both products (Fig. 3, scheme S2, and fig. S9). Carrying out the reaction in the presence of added O_2 (a well-known radical trap that is stable under these reaction conditions) had no effect on the reaction rate or selectivity (Table 1, entry 8). These results—along with the high reaction selectivity and lack of any C-C cleavage products in the reaction of ethane and propane with $Tl(TFA)_3$—strongly argue against a free-radical mechanism.

To further investigate the possibility of a CH activation/M-R functionalization mechanism, we carried out the reaction of methane with $Tl(TFA)_3$ in deuterated trifluoroacetic acid (DTFA). Only CH_3TFA was generated in this reaction, and no CH_3D was observed. This result would be consistent with a reaction mechanism in which CH activation step is rate-limiting and irreversible, whereas functionalization of the putative Tl^{III}-CH_3 intermediate to the alcohol ester is fast. Consistent with assignment of CH bond cleavage as the rate-limiting step, the intramolecular kinetic isotope effect (KIE) based on reactions with H_3C-CD_3 was measured to be 3.4. A very small KIE or no KIE would be expected if alkane coordination or M-R functionalization were rate-limiting. The expected putative $(TFA)_2Tl^{III}$-Me intermediate is

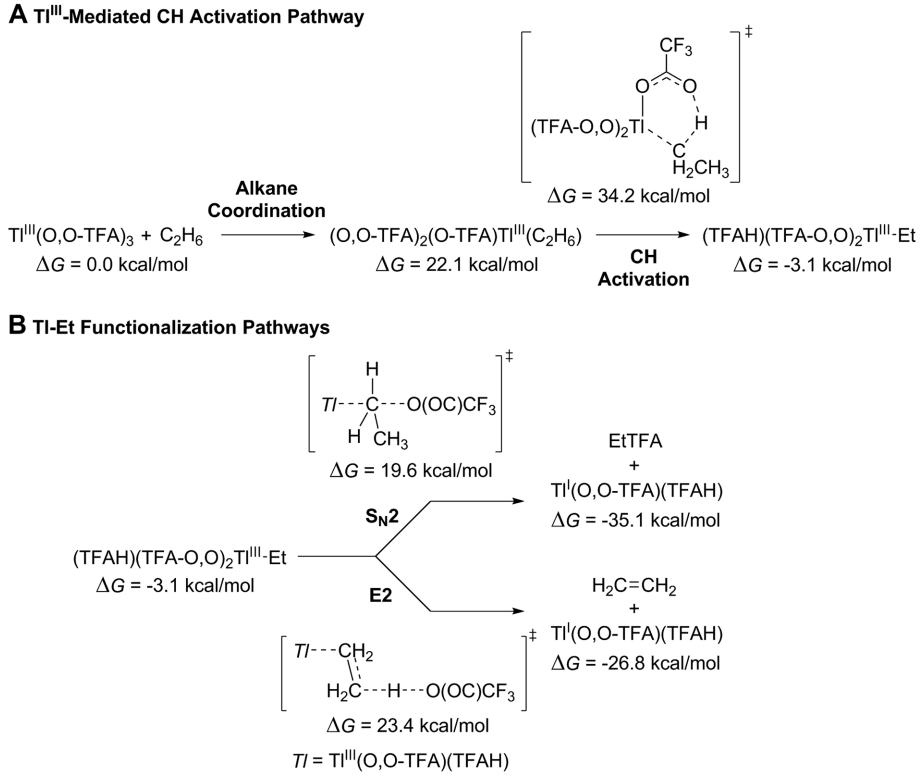

Fig. 3. M06/6-31+G(d,p)[LANL2DZ] DFT-calculated CH activation and M-R functionalization pathways in TFAH solvent.

unknown and likely unstable. However, the dimethyl species (TFA)Tl(CH_3)$_2$ is stable in TFAH at room temperature. Because this class of organometallic compounds are well known to undergo rapid alkyl transfer, we examined the reaction of (TFA)Tl(CH_3)$_2$ with Tl(TFA)$_3$ as a means of generating (TFA)$_2$Tl^{III}-Me in situ. Upon addition of Tl(TFA)$_3$ at room temperature to a solution of (TFA)Tl(CH_3)$_2$ in TFAH, within minutes two equivalents of MeTFA were cleanly generated in quantitative yield relative to (TFA)Tl(CH_3)$_2$ based on the stoichiometry shown in Eq. 3. Analysis of the crude reaction mixture by means of 1H-NMR immediately upon mixing showed a new, broad, transient Me-species that could be the (TFA)$_2$Tl(CH_3) intermediate. Consistent with the lack of H/D exchange in reactions of CH_4 with Tl(TFA)$_3$ in DTFA [which we attributed to irreversible formation of the putative (TFA)$_2$Tl^{III}-Me intermediate from CH activation], no CH_4 is generated from these functionalization reactions of (TFA)Tl(CH_3)$_2$ with Tl(TFA)$_3$ in TFAH. These results are also consistent with reports that treatment of (OAc)$_2$TlMe with HOAc generates MeOAc (*33*)

$$(\mathrm{TFA})\mathrm{Tl}^{\mathrm{III}}(\mathrm{CH_3})_2 + \mathrm{Tl}^{\mathrm{III}}(\mathrm{TFA})_3 \xrightarrow[\mathrm{TFAH}]{} 2\mathrm{MeTFA} + 2\mathrm{Tl}^{\mathrm{I}}(\mathrm{TFA}) \quad (3)$$

We have also used M06 density functional theory (DFT) calculations to examine possible mechanisms and the energy landscape for ethane CH functionalization, as well as to postulate a mechanism that accounts for the parallel formation of EtTFA and EG(TFA)$_2$. Calculation details can be found in the supplementary materials. To begin, we examined whether it is plausible that Tl(TFA)$_3$ can induce functionalization of ethane by a radical or one-electron oxidation pathway. Radical chain mechanisms beginning with a reactive (TFA)$_2$Tl•/CF_3COO•radical pair were ruled out because Tl-O bond homolysis requires 52.3 kcal mol^{-1} of free energy. Additionally, one-electron oxidation and Tl-mediated hydrogen atom abstraction were also ruled out because these pathways require greater than 75 kcal mol^{-1}. Instead, our calculations suggest that the most viable pathway for ethane CH functionalization is CH activation by means of electrophilic substitution (Fig. 3A). Calculations also suggest an identical mechanism for methane (supplementary materials).

In the ground state for Tl(O,O-TFA)$_3$, both oxygen atoms of the three TFA anions coordinate to the Tl center in an octahedral-like geometry, and one oxygen atom in each coordinated TFA is more tightly bound than the other. Ethane coordination requires dissociation of one oxygen atom in a O,O-TFA anion ligand to generate an open coordination site, to give (O,O-TFA)$_2$(O-TFA)Tl(C_2H_6). As anticipated from the conceptual model shown in Fig. 1 (blue energy diagram), ethane coordination requires a free energy change (ΔG) of 22.1 kcal mol^{-1}, in part because the d^{10} main group metal lacks LFSE. This ethane coordination energy in non-superacid solvent is much lower than the >35 kcal mol^{-1} value found for alkane coordination in superacid solvent with the d^8 (bpym)Pt^{II} system that has LFSE. Subsequent CH bond cleavage from (O,O-TFA)$_2$(O-TFA)Tl(C_2H_6) by means of an electrophilic substitution transition-state free energy change $\Delta G^{\ddagger}$ = 34.2 kcal mol^{-1} to generate (O,O-TFA)$_2$(TFAH)Tl-Et is consistent with the rates of reactions observed and with rate-limiting CH bond cleavage. Consistent with the experimentally measured KIE of 3.4, in this CH bond cleavage transition state there is considerable Tl-C bond formation and C-H bond stretching. Calculation of the KIE based on this transition state gave a value of 4.7. One prediction based on Fig. 1 is that Pb^{IV} should be more reactive than Tl^{III} is. Indeed, calculation of the electrophilic substitution transition state for Pb(O,O-TFA)$_4$ with ethane gave a lower $\Delta G^{\ddagger}$ of 29.2 kcal mol^{-1} (supplementary materials).

The thermodynamics for the CH activation step suggests that the Tl-Et species is more stable than are the Tl(TFA)$_3$ and ethane species (ΔG = –3.1 kcal mol^{-1}). Thus, a Tl-Et species such as (O,O-TFA)$_2$(TFAH)Tl-Et might be observable. However, calculations predict that Tl-Et functionalization has a much lower barrier than that of CH activation, and therefore, functionalization of the Tl-Et species is much more rapid than the CH activation reaction. This explains the lack of H/D exchange when the reactions are run in deuterated TFAD as well as the quantitative yield of MeTFA without any CH_4 formation from the reaction of (TFA)TlMe_2 with Tl(TFA)$_3$ in TFAH. Calculations suggest that there is parallel formation of EtTFA and EG(TFA)$_2$ from the Tl-Et intermediate. The two most plausible pathways for functionalization are shown in Fig. 3B. The S_N2 pathway forms EtTFA, whereas the E2 pathway forms ethylene. Control experiments show that although EtTFA conversion is slow, ethylene rapidly converts to EG(TFA)$_2$ in the presence of Tl(TFA)$_3$ (scheme S2). Thus, this E2 pathway leads to EG(TFA)$_2$. The calculations suggest that although the S_N2 and E2 pathways are competitive, there is a preference for the S_N2 pathway. This is consistent with experiments showing parallel but higher rates of formation of EtTFA relative to EG(TFA)$_2$.

Consistent with the proposed electrophilic CH activation mechanism and the experimental observations that MeTFA is less reactive than CH_4, the calculated $\Delta G^{\ddagger}$ for CH activation of MeTFA is ~9 kcal mol^{-1} higher than the $\Delta G^{\ddagger}$ for CH activation of CH_4 (supplementary materials). Calculations also reveal that the presence of the TFA electron-withdrawing group increases the activation barrier for CH activation of the methyl group of EtTFA to 40.4 kcal mol^{-1}. This suggests that the TFA group imparts a strong electron-withdrawing influence even two carbon atoms away. This result is consistent with the observed slow conversion of EtTFA to EG(TFA)$_2$. The electrophilic mechanism is also consistent with higher reactivity of ethane versus methane because methyl groups are electron-donating groups (calculations are available in the supplementary materials).

Experiment and theory taken together strongly support the proposed mechanism for alkane functionalization involving slow, irreversible electrophilic CH activation of alkanes with third-row, main-group cations, M^{n}X to generate M^n-R intermediates, followed by fast M-R functionalization to generate MeX and M^{n-2}. In the 1970 to 1980s, patented technologies were developed to reoxidize Tl^{I} to Tl^{III} by using O_2 in connection with Tl^{III}–mediated oxidation of olefins to glycols in HOAc (*34*–*36*). Applying this reoxidation technology to reactions of other main-group d^{10} cations, M^{n}X—with alkanes, either in two separate stoichiometric reactions or, ideally, with M^{n}X as a catalyst—could lead to practical processes for the selective hydroxylation of alkanes to alcohols by using air or other oxidants, such as H_2O_2. The absence of claims for reaction of ethane or other alkanes in these patented olefin oxidation technologies is most likely due to early beliefs that alkanes were inert to these main-group cations.

References and Notes

1. U. S. E. I. Administration, *U.S. Crude Oil and Natural Gas Proved Reserves* **2011**, 1–49 (2013).
2. D. L. George, E. B. Bowles Jr., *Pipeline Gas J.* **238**, 38–41 (2011).
3. N. F. Gol'dshleger, V. V. Es'kova, A. A. Shteinman, A. E. Shilov, *Russ. J. Phys. Ch. USSR* **46**, 785–786 (1972).
4. A. E. Shilov, A. A. Shteinman, *Coord. Chem. Rev.* **24**, 97–143 (1977).
5. A. Sen, *Acc. Chem. Res.* **31**, 550–557 (1998).
6. M. J. Burk, R. H. Crabtree, C. P. Parnell, R. J. Uriarte, *Organometallics* **3**, 816–817 (1984).
7. M. J. Burk, R. H. Crabtree, *J. Am. Chem. Soc.* **109**, 8025–8032 (1987).
8. M. C. Haibach, S. Kundu, M. Brookhart, A. S. Goldman, *Acc. Chem. Res.* **45**, 947–958 (2012).
9. J. Choi, A. H. R. MacArthur, M. Brookhart, A. S. Goldman, *Chem. Rev.* **111**, 1761–1779 (2011).
10. A. S. Goldman *et al.*, *Science* **312**, 257–261 (2006).
11. B. G. Hashiguchi, S. M. Bischof, M. M. Konnick, R. A. Periana, *Acc. Chem. Res.* **45**, 885–898 (2012).
12. C. J. Jones *et al.*, *Angew. Chem. Int. Ed.* **43**, 4626–4629 (2004).
13. R. A. Periana, O. Mironov, D. J. Taube, S. Gamble, *Chem. Commun. (Camb.)* **20**, 2376–2377 (2002).
14. R. A. Periana, O. Mironov, D. Taube, G. Bhalla, C. J. Jones, *Science* **301**, 814–818 (2003).
15. R. A. Periana *et al.*, *Science* **259**, 340–343 (1993).
16. R. A. Periana *et al.*, *Science* **280**, 560–564 (1998).
17. M. Muehlhofer, T. Strassner, W. A. Herrmann, *Angew. Chem. Int. Ed.* **41**, 1745–1747 (2002).
18. T. Strassner, M. Muehlhofer, A. Zeller, E. Herdtweck, W. A. Herrmann, *J. Organomet. Chem.* **689**, 1418–1424 (2004).
19. S. Ahrens, A. Zeller, M. Taige, T. Strassner, *Organometallics* **25**, 5409–5415 (2006).
20. J. F. Hartwig, *Acc. Chem. Res.* **45**, 864–873 (2012).
21. J. F. Hartwig *et al.*, *J. Am. Chem. Soc.* **127**, 2538–2552 (2005).
22. H. Chen, S. Schlecht, T. C. Semple, J. F. Hartwig, *Science* **287**, 1995–1997 (2000).
23. Z. An, X. Pan, X. Liu, X. Han, X. Bao, *J. Am. Chem. Soc.* **128**, 16028–16029 (2006).
24. G. J. Hutchings, M. S. Scurrell, J. R. Woodhouse, *Chem. Soc. Rev.* **18**, 251–283 (1989).
25. C. Hammond *et al.*, *Angew. Chem. Int. Ed.* **51**, 5129–5133 (2012).
26. P. Vanelderen, J. Vancauwenbergh, B. F. Sels, R. A. Schoonheydt, *Coord. Chem. Rev.* **257**, 483–494 (2013).
27. M. N. Vargaftik, I. P. Stolarov, I. I. Moiseev, *J. Chem. Soc. Chem. Commun.* **1990**, 1049–1050 (1990).

28. I. P. Stolarov, M. N. Vargaftik, D. I. Shishkin, I. I. Moiseev, *J. Chem. Soc. Chem. Commun.* **1991**, 938–939 (1991).
29. A. J. Bard, R. Parsons, J. Jordan, *Standard Potentials in Aqueous Solution* (International Union of Pure and Applied Chemistry, New York, 1985).
30. M. Ahlquist, R. A. Periana, W. A. Goddard Iii, *Chem. Commun. (Camb.)* **17**, 2373–2375 (2009).
31. F. Basolo, R. G. Pearson, *Mechanisms of Inorganic Reactions* (Wiley, New York, ed. 2, 1967).
32. R. G. Peterson, *Hard and Soft Acids and Bases* (Dowden, Hutchinson and Ross, Stroudsburg, PA, 1973).
33. H. Kurosawa, R. Okawara, *J. Organomet. Chem.* **10**, 211–217 (1967).
34. T. Fujii, K. Funahashi, I. Hirose, U.S. patent 3399956 (1968)
35. R. A. Johnson, U.S. patent 4113756 (1978)
36. R. A. Johnson, U.S. patent 4192814 (1980)

Acknowledgments: This work was supported as part of the Center for Catalytic Hydrocarbon Functionalization, an Energy Frontier Research Center Funded by the U.S. Department of Energy, Office of Science, Office of Basic Energy Sciences, under award DE-SC0001298 (to R.A.P. and D.H.E). D.H.E. thanks the BYU Fulton Supercomputing Lab. We also thank S. Burt (BYU) for assistance with Tl NMR. Several provisional and one nonprovisional patents have been filed (applications PCT/US2014/018175, 61/768,715, 61/862,715, 61/862,723, and 61/862,731).

Supplementary Materials
www.sciencemag.org/content/343/6176/1232/suppl/DC1
Materials and Methods
Figs. S1 to S9
Tables S1 to S3
Schemes S1 to S4
References (*37*–*47*)

5 December 2013; accepted 19 February 2014
10.1126/science.1249357

Changes in Seismic Anisotropy Shed Light on the Nature of the Gutenberg Discontinuity

Caroline Beghein,[1]* Kaiqing Yuan,[1] Nicholas Schmerr,[2] Zheng Xing[1]

The boundary between the lithosphere and asthenosphere is associated with a platewide high–seismic velocity "lid" overlying lowered velocities, consistent with thermal models. Seismic body waves also intermittently detect a sharp velocity reduction at similar depths, the Gutenberg (G) discontinuity, which cannot be explained by temperature alone. We compared an anisotropic tomography model with detections of the G to evaluate their context and relation to the lithosphere-asthenosphere boundary (LAB). We find that the G is primarily associated with vertical changes in azimuthal anisotropy and lies above a thermally controlled LAB, implying that the two are not equivalent interfaces. The origin of the G is a result of frozen-in lithospheric structures, regional compositional variations of the mantle, or dynamically perturbed LAB.

Plate tectonic theory describes a strong and rigid lithospheric "lid" that translates coherently atop a weaker and more deformable convecting asthenosphere. Determining the depth and pervasiveness of the interface between these two layers, known as the lithosphere-asthenosphere boundary (LAB), is key for understanding the formation, evolution, and thermochemical properties of plates and associated tectonics. The exact compositional and thermal mechanisms that control this rheological division remain enigmatic, but seismological imaging of anisotropy—the directional dependence of seismic wave velocity—across the upper mantle provides an essential tool for interrogating the transition in material properties across the LAB.

Seismological interrogations of the oceanic upper mantle beneath the Pacific Ocean find evidence for a sharp drop in seismic velocity, known as the Gutenberg (G) discontinuity (*1*), at 40- to 100-km depth. The depth of the G roughly coincides with the top of a low-velocity zone (LVZ) and may be the seismological expression of the LAB. However, correlating G depth with plate age and distance to mid-ocean ridges has not produced a unifying interpretation of the relationship between the G and the LAB (*2*–*6*). This has led to several alternative hypotheses for the origin of the G, including partial melt lenses in the asthenosphere (*3*), hydrogen depletion of olivine from decompression melting beneath mid-oceanic ridges (*7*, *8*), frequency-dependent attenuation effects reducing the shear modulus in the presence of mantle hydration (*9*), and dynamical melt-producing processes to explain the strong regional variations in G reflectivity from *SS* precursor data (*5*, *10*).

To improve our understanding of how isotropic and anisotropic velocity models relate to the observations of seismic discontinuities, we modeled the three-dimensional isotropic and anisotropic structure of the upper mantle beneath the Pacific Basin (Fig. 1) using a global data set of surface wave phase velocity maps (*11*, *12*). The dispersive properties of surface waves make them ideal to put depth constraints on seismic anisotropy and velocity, and the use of higher-mode surface waves to model azimuthal anisotropy provides sensitivity throughout the upper mantle (fig. S1). The detection of changes in seismic anisotropy has been successfully used to identify layering in the mantle, variations in LAB depth beneath continents and oceans (*13*, *14*), and chemical stratification within the lithosphere under the North American craton (*14*). Here we focus on anisotropy under the Pacific Plate, which is well sampled by surface waves and therefore constitutes a natural laboratory to constrain the evolution and cooling history of the oceanic lithosphere. The surface wave anisotropy results are compared to a large data set of high-frequency *SS* precursors that highlight the G (*5*).

Our models show a stratified upper mantle under the Pacific Ocean and a correlation between the boundaries of these layers and the location of observed seismic discontinuities (Fig. 2). The top layer (layer 1) is defined by a poor alignment between V_{SV} fast axes direction and the absolute plate motion (APM) (*15*), and the underlying layer (layer 2) by a better alignment with the APM. Layer 1 is also characterized by high seismic velocities away from ocean ridges [4 to 5% with respect to our reference model (*16*)], and its thickness increases with crustal age, similar to past surface wave studies (*13*, *17*–*19*). Furthermore, layer 1 is associated with 1 to 2% radial anisotropy with $V_{SV} > V_{SH}$, and azimuthal anisotropy amplitudes of 1 to 2%. This fast V_{SV} direction roughly follows the orientation of ocean floor fracture zones at 50-km depth near ridges, around 80-km depth for ocean ages between 80 and 120 million years ago (Ma), and at 100-km depth under old oceanic plates (Fig. 1). Ocean floor fracture zones are temporally stable features that record plate motion path and can thus be used as proxy for the paleospreading directions. Layer 2 has lower *S*-wave velocity (–5% relative perturbations), strong radial anisotropy (5%) with $V_{SH} > V_{SV}$, and 3% azimuthal anisotropy with, by definition, fast axes subparallel to the APM (<30° deviation from APM).

On the basis of the above seismological observations, we define the LAB in our models as the dipping interface between these two layers. The strong anisotropy of layer 2 suggests alignment of olivine fast axes with mantle flow direction associated with plate motion that can occur in the deformable asthenosphere by dislocation creep (*20*) or diffusion creep (*21*). Olivine lattice-preferred orientation (LPO) formed by mantle flow–induced shear strain in the dislocation creep regime is consistent with a low-viscosity asthenosphere (*22*) and a flow channel coincident with a low-velocity zone (*23*). The thickness of our tomographically defined layer 1 increases with plate age, following the 900° to 1100°C isotherms in a half-space cooling (HSC) model (black lines, Fig. 2). Combined with elevated seismic velocities, layer 1 is therefore consistent with cold lithosphere that has a thermally controlled thickness and implies that the LAB is a temperature-related phenomenon. Furthermore, the alignment of the V_{SV} fast axes with the fossil spreading direction in layer 1 is consistent with LPO and the frozen-in record

[1]Department of Earth, Planetary, and Space Sciences, University of California, Los Angeles, 595 Charles Young Drive East, Box 951567, Los Angeles, CA 90095–1567, USA. [2]Department of Geology, University of Maryland, College Park, MD 20742, USA.
*Corresponding author. E-mail: cbeghein@ucla.edu

of past deformation in that layer for ages up to 80 Ma (*13*, *19*, *21*). For older ages, the fast axes align with the sea-floor fracture zones below 50- to 80-km depth, but they do not align with either the APM or the fossil spreading directions at shallower depths, implying that another mechanism is required to explain the observations in this depth and age range. The depth of the change in radial anisotropy from $V_{SV} > V_{SH}$ to $V_{SH} > V_{SV}$ does not display any age dependence (Fig. 2E), similar to previous observations (*18*); however, synthetic tests and calculation of the resolution matrix revealed that the vertical resolution of radial anisotropy models is poor (figs. S3 and S5).

Of particular interest are the vertical changes in the fast direction of azimuthal anisotropy detected by surface waves beneath the Pacific that overlap with the location of *SS* precursor detections (*5*) of seismic discontinuities (Fig. 2). For younger crustal ages (<30 Ma), detections of the G reside at 50- to 55-km depth, falling above the weaker gradient in azimuthal anisotropy fast axes orientation arising from nearly parallel APM and fossil spreading directions. We caution that resolving the details of the G at depths of <50 km is challenging for the *SS* precursor technique, owing to the masking of shallower complexities by the large negative sidelobe of *SS* (*4*). In addition, ridges are relatively narrow structures compared to the long-wavelength *SS* Fresnel zone (>1000 km) and aliasing of small-scale structure may occur across the ridge axis. Nonetheless, G detections near the ridges fall within layer 2. For crustal ages between 30 and 100 Ma, G detections coincide with both the depth of a strong change in azimuthal anisotropy and fast axes directions (Fig. 2, A and C), and lying near the base of layer 1 (55 to 70 km). Beneath 100- to 130-Ma crust, the G detections are still associated with the strong gradient in azimuthal anisotropy fast axes direction, primarily falling beneath Hawaii at 75- to 80-km depth, and are confined to the interior of layer 1. The G is poorly resolved beneath regions of crust older than 130 Ma; these regions are undersampled by the *SS* precursors, with only a few sporadic detections of reflectors beneath the oldest portions of the oceanic plate (*24*). Thus, the G is associated with vertical changes in mantle azimuthal anisotropy.

For a discontinuity arising from anisotropy, the detection of the interface is dependent on the relative orientations of the overlying and underlying fabrics, combined with the strength of the anisotropy in each layer and the azimuthal sampling provided by source-receiver paths. As discussed in (*24*), layered changes in azimuthal anisotropy give rise to *SS* precursor underside reflections of varying amplitude and sign, depending on the relative orientation of anisotropy within each layer. Despite limitations in the resolution near ridges and a lack of data sampling beneath older crust, where observed, the detections of the G reflector are tied to vertical changes in mantle anisotropy at a roughly constant depth (Fig. 2), thus requiring a compositional or dynamical component for the origin of the G over purely thermal mechanisms.

Partial melt in the LVZ can help explain observations of increased shear velocity contrast, attenuation (*10*), and mantle conductivity (*25*). Where the G roughly coincides with the top of layer 2, partial melt also offers a possible explanation for observations of layered anisotropy (*3*). Partial melt will introduce azimuthal anisotropy when mantle flow in layer 2 entrains and segregates a small fraction of melt into en echelon tilted layers (*26*), with fast axes aligned perpendicular to mantle flow (Fig. 3A). The presence of such a feature would result in the formation of the G at the solidus/melt interface or where there is a change in mantle permeability (*5*). In this model of the G, partial melt must be long-lived and/or dynamically renewed to sustain such structures, and thus sheared

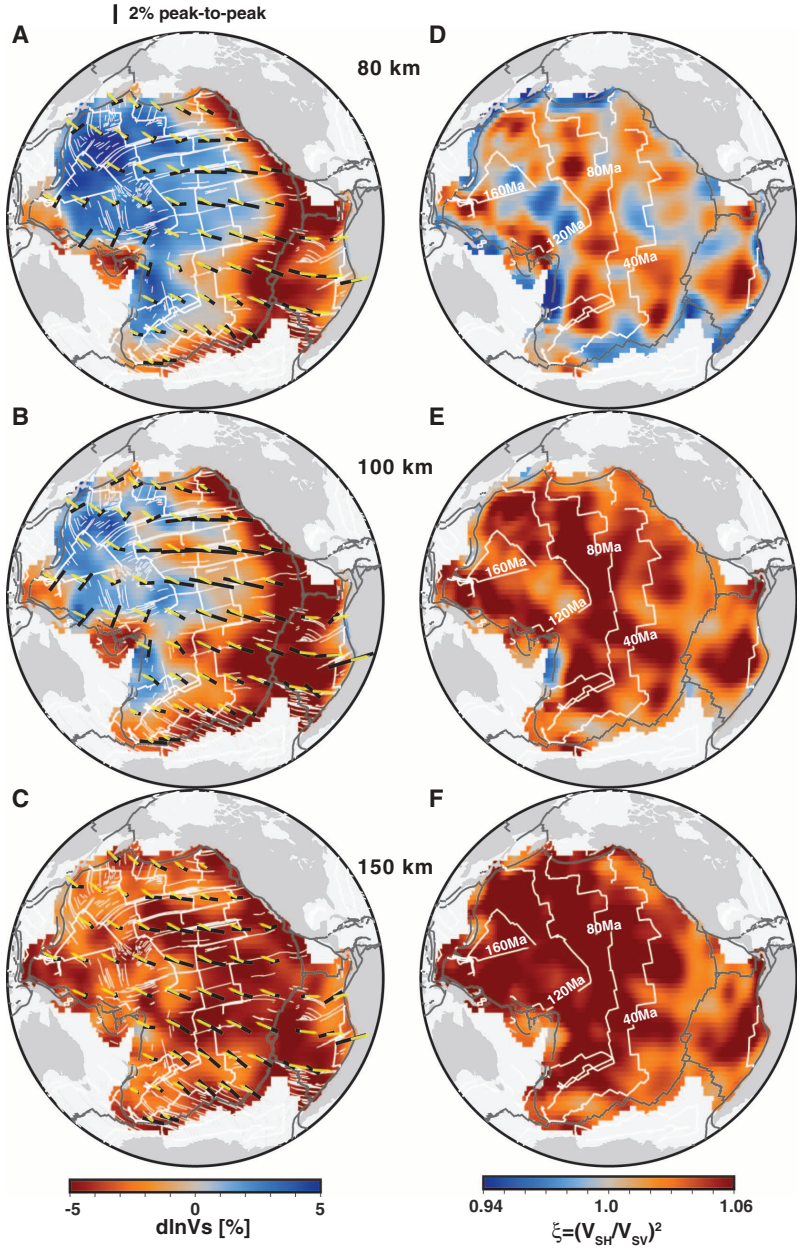

Fig. 1. Lateral variations in wave velocity and anisotropy at different depths. Mantle *S*-wave velocity anomalies (**A** to **C**) are given with respect to the radially anisotropic Preliminary Reference Earth Model, PREM (*16*). Azimuthal anisotropy is plotted on top of the velocity model with black bars representing the fast V_{SV} direction. Yellow arrows represent the APM obtained from no-net-rotation reference frame model NNR-NUVEL 1A (*15*), and thin white lines denote ocean floor fracture zones (*27*). Thick white contour lines denote ocean floor ages at 40-Ma intervals. They are annotated in (**D** to **F**), which display our radial anisotropy model. Other depths are shown in fig. S26. Considering the estimated lateral resolution of the data used, we do not resolve variations in V_S or ξ much smaller than 1600 km (and 5000 km for azimuthal anisotropy).

melt layers would be expected to produce persistent azimuthal anisotropy in the vicinity and downstream of sustained mantle upwellings (*24*), or in the regions of melting produced by small-scale convection. This interpretation is consistent with the observed strong azimuthal anisotropy and well-defined G detections near Hawaii, a long-lived mantle upwelling.

Alternatively, variable hydration with depth offers a subsolidus mechanism for producing anisotropy [e.g., (*7*, *9*), Fig. 3B], although not necessarily in exclusion of tilted melt layers. The presence of 100- to 300-ppm (parts per million) H_2O reduces the viscosity of olivine and modifies the mineral's anisotropic properties (*8*), readily producing fabrics at higher hydration states and elevated temperature. Dehydration of the mantle underlying the mid-ocean ridge generates a chemically depleted, viscous layer of 50- to 80-km thickness (*7*) that subsequently becomes overprinted by lowered temperatures as the plate cools and migrates away from the spreading center. This will produce alignment of the olivine *SV* fast axes with the paleo-spreading direction at the ridge, occurring primarily in the underlying hydrated, and more deformable, layer 2, producing an anisotropic discontinuity at the base of the dehydrated layer. As the lid cools and thickens, this alignment would be frozen and preserved into the part of the lithosphere (layer 1) that lies below the chemical depletion boundary, whereas flow in the warmer underlying asthenosphere (layer 2) would align with present-day APM and potentially deviate from flow at the ridge. This interpretation accounts for the anisotropy of layer 2 and for the frozen-in anisotropy observed below the G in layer 1. In this scenario, both the asthenosphere and the part of the lithosphere located below the G are hydrated, but thermal effects dominate the nature of the lid and underlying LVZ.

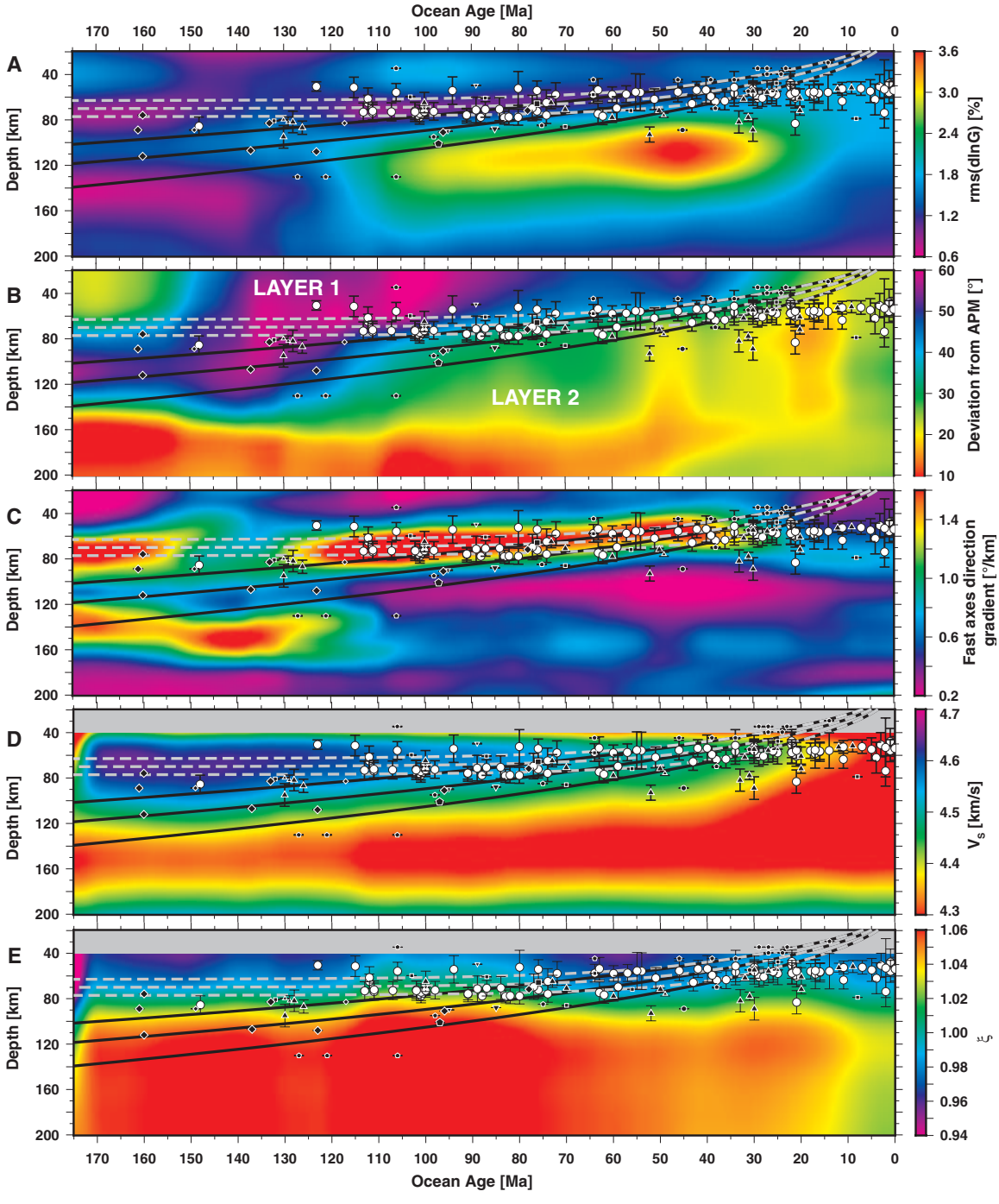

Fig. 2. Anisotropy and velocity models as a function of oceanic crust age. Plate-averaged (**A**) azimuthal anisotropy amplitude, (**B**) angular difference between V_{SV} fast axes and APM directions (*15*), (**C**) vertical gradient of fast *SV* axes orientation, (**D**) *S*-wave velocity, and (**E**) radial anisotropy as a function of ocean sea-floor age beneath the Pacific. The black lines represent HSC models (*28*), assuming $T_m = 1350°C$ for the mantle temperature and $\kappa = 10^{-6}$ m^2 s^{-1} for the thermal diffusivity. Gray dashed lines are for plate models (*29*). The temperature interval is 100°C starting at 900°C for the shallowest isotherm. The white circles and their standard deviations correspond to *SS* precursor detections of the G (*5*). Other symbols correspond to other high-frequency analyses of seismic discontinuities from other groups for whom references can be found in the caption of fig. S10.

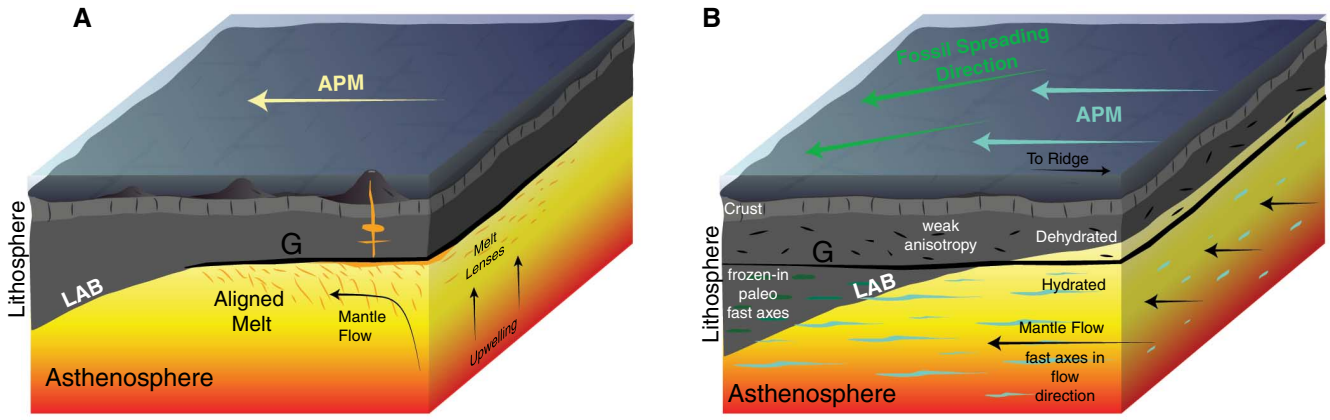

Fig. 3. Proposed models for azimuthal anisotropy beneath the Pacific and detection of the G. (**A**) The G as the top of an anisotropic entrainment and segregation of melt within the asthenosphere. Dynamical upwelling produces melt that is entrained into mantle flow and compacts at the base of the lithosphere from a solidus-induced change in permeability (*10*). The G coincides with the top of the melting zone. In the scenario where the APM and fossil spreading directions are parallel, the G would not be detected. (**B**) The G as a chemical boundary between a weakly anisotropic dry layer and a hydrated region characterized by the fossil frozen-in alignment of olivine. Olivine aligns with the present-day APM in the hydrated, warm asthenosphere. In this scenario, G can be both coincident with and above the thermally defined LAB and is detected by the *SS* precursors where the anisotropy contrast between the two layers is large.

References and Notes

1. B. Gutenberg, *Bull. Seismol. Soc. Am.* **38**, 121 (1948).
2. B. Bagley, J. Revenaugh, *J. Geophys. Res. Solid Earth* **113**, B12301 (2008).
3. H. Kawakatsu *et al.*, *Science* **324**, 499–502 (2009).
4. C. A. Rychert, P. M. Shearer, *J. Geophys. Res. Solid Earth* **116**, B07307 (2011).
5. N. Schmerr, *Science* **335**, 1480–1483 (2012).
6. Y. Tan, D. V. Helmberger, *J. Geophys. Res. Solid Earth* **112**, B08301 (2007).
7. J. B. Gaherty, M. Kato, T. H. Jordan, *Phys. Earth Planet. Inter.* **110**, 21–41 (1999).
8. G. Hirth, D. L. Kohlstedt, *Earth Planet. Sci. Lett.* **144**, 93–108 (1996).
9. S. Karato, *Earth Planet. Sci. Lett.* **321-322**, 95–103 (2012).
10. T. Sakamaki *et al.*, *Nat. Geosci.* **6**, 1041–1044 (2013).
11. Materials and methods are available on *Science* Online.
12. K. Visser, J. Trampert, B. L. N. Kennett, *Geophys. J. Int.* **172**, 1016–1032 (2008).
13. E. Debayle, Y. Ricard, *Earth Planet. Sci. Lett.* **376**, 165–177 (2013).
14. H. Yuan, B. Romanowicz, *Nature* **466**, 1063–1068 (2010).
15. A. E. Gripp, R. G. Gordon, *Geophys. J. Int.* **150**, 321–361 (2002).
16. A. M. Dziewonski, D. L. Anderson, *Phys. Earth Planet. Inter.* **25**, 297–356 (1981).
17. A. Maggi, E. Debayle, K. Priestley, G. Barruol, *Geophys. J. Int.* **166**, 1384–1397 (2006).
18. M. Nettles, A. M. Dziewonski, *J. Geophys. Res. Solid Earth* **113**, B02303 (2008).
19. C. E. Nishimura, D. W. Forsyth, *Geophys. J.* **96**, 203–229 (1989).
20. S. Karato, in *High-Pressure Research in Mineral Physics*, M. H. Manghnani, Y. Syono, Eds. (TERRAPUB/AGU, Tokyo/Washington, 1987), pp. 455–471.
21. T. Miyazaki, K. Sueyoshi, T. Hiraga, *Nature* **502**, 321–326 (2013).
22. B. H. Hager, M. A. Richards, *Philos. Trans. R. Soc. Lond. A* **328**, 309–327 (1989).
23. C. Gaboret, A. M. Forte, J. P. Montagner, *Earth Planet. Sci. Lett.* **208**, 219–233 (2003).
24. C. A. Rychert, N. Schmerr, N. Harmon, *Geochem. Geophys. Geosyst.* **13**, Q0AK10 (2012).
25. S. Naif, K. Key, S. Constable, R. L. Evans, *Nature* **495**, 356–359 (2013).
26. B. K. Holtzman, J. M. Kendall, *Geochem. Geophys. Geosyst.* **11**, Q0AB06 (2010).
27. K. J. Matthews, R. D. Muller, P. Wessel, J. M. Whittaker, *J. Geophys. Res. Solid Earth* **116**, B12109 (2011).
28. R. L. Parker, D. W. Oldenburg, *Nature* **242**, 137–139 (1973).
29. C. A. Stein, S. Stein, *Nature* **359**, 123–129 (1992).

Acknowledgments: C.B. and K.Y. were funded by NSF EAR grants 0838605 and 0949255; N.S. was funded by NSF EAR 1247608. We thank J. Trampert and K. Visser for making their phase velocity maps freely available. Partial derivatives were calculated using fortran code MINEOS (www.geodynamics.org/cig/software/mineos), and figures were made with the Generic Mapping Tools, Gnuplot, and Xmgrace. We thank P. Davis for fruitful discussions. The data used were the phase velocity maps published in (*12*) and are available at www.geo.uu.nl/~jeannot/My_web_pages/Downloads.html. The models are available in the supplementary materials.

Supplementary Materials

www.sciencemag.org/content/343/6176/1237/suppl/DC1
Materials and Methods
Supplementary Text
Figs. S1 to S27
Table S1
References (*30*–*56*)
Model file S1

2 October 2013; accepted 17 February 2014
Published online 27 February 2014;
10.1126/science.1246724

Lethal Interactions Between Parasites and Prey Increase Niche Diversity in a Tropical Community

Marty A. Condon,[1]* Sonja J. Scheffer,[2] Matthew L. Lewis,[2] Robert Wharton,[3] Dean C. Adams,[4,5] Andrew A. Forbes[6]

Ecological specialization should minimize niche overlap, yet herbivorous neotropical flies (*Blepharoneura*) and their lethal parasitic wasps (parasitoids) exhibit both extreme specialization and apparent niche overlap in host plants. From just two plant species at one site in Peru, we collected 3636 flowers yielding 1478 fly pupae representing 14 *Blepharoneura* fly species, 18 parasitoid species (14 *Bellopius* species), and parasitoid-host associations, all discovered through analysis of molecular data. Multiple sympatric species specialize on the same sex flowers of the same fly host-plant species—which suggests extreme niche overlap; however, niche partitioning was exposed by interactions between wasps and flies. Most *Bellopius* species emerged as adults from only one fly species, yet evidence from pupae (preadult emergence samples) show that most *Bellopius* also attacked additional fly species but never emerged as adults from those flies.

Plant and insect diversity both peak in the tropics (*1*) where insect diversity is strongly associated with plant diversity (*2*, *3*) and extreme specialization (*4*). Ecological specialization is often considered a driver of diversification, with increasing specialization reducing niche overlap and promoting speciation (*5*, *6*). Diversification of herbivorous insects, arguably the most diverse group of organisms on Earth (*7*), is often explained by "arms race" or "escape and radiate" hypotheses involving specialized interactions either between two trophic levels—host plants and

specialized herbivores (*8*), or among three trophic levels—plants, herbivores, and their specialized enemies (*9*–*11*). Tritrophic studies emphasize shifts to new host plants as a mechanism that can cause cascading patterns of diversification. Specifically, shifts to new "enemy-free" host plants allow herbivores to escape enemies like parasitoids (lethal parasitic wasps) that often use plant-related cues to find insect hosts (*11*); in turn, selection favors parasitoids that can respond to new plant-related cues to track their prey (*10*, *11*). These models emphasize the lethality of parasitoids; however, parasitoids can also be killed by their hosts (*12*–*14*). We suggest that such "inhospitable" (lethal) hosts may help explain high levels of diversity in some communities.

Specificity to host plants is thought to be a predictor of herbivorous insect diversity (*2*, *4*); however, diversity of some highly specialized herbivorous insect groups far exceeds predictions based purely on host plants' taxonomic diversity and architectural complexity. For example, all species in the species-rich neotropical tephritid genus *Blepharoneura* feed on plants in the family Cucurbitaceae (cucurbits). Unlike most plants, all cucurbits have unisexual flowers, and many cucurbit species are sexually dimorphic: plants bearing female flowers differ architecturally from plants bearing male flowers. Cucurbit flowers are hosts to many species of *Blepharoneura* that feed specifically on particular sex flowers of single species of plants (*15*). To our surprise, we find multiple sympatric cryptic *Blepharoneura* species feeding specifically on exactly the same tissues—the succulent fused sepals (calyces)—of the same sex flowers of the same plant species. This pattern suggests extreme niche overlap among specialists—at least in the "plant-defined dimensions" of their niches (*15*); however, niches can be defined by multiple dimensions representing all environmental factors that affect fitness of individuals (*16*)—including predators and parasites. Species sharing exactly the same food resources may not share the same enemies.

Parasitoids represent an important third trophic level in *Blepharoneura* communities, as in most other communities of herbivorous insects (*9*–*11*, *17*). Parasitoids lay their eggs inside immature *Blepharoneura* (eggs or larvae) hidden within flower tissues. The parasitized fly is not killed immediately but continues to feed on plant host material until larval development is complete and the fly forms a puparium by hardening its larval exoskeleton. The immature parasitoid feeds on the immature fly and completes metamorphosis within the fly puparium. When the wasp reaches adulthood, it emerges from the puparium, leaving behind material ("postemergence puparium") containing both the wasp and host-fly DNA.

To reveal patterns of fly and parasitoid diversity, niche overlap, and tritrophic interactions, we collected 3636 flowers representing four host-plant niches: male flowers and female flowers of two species of cucurbit vines (*Gurania acuminata* and *G. spinulosa*) growing along or near the perimeter of a 1-km-long airstrip at Los Amigos Biological Station in Madre de Dios, Peru, in October 2008 (*18*). Fewer than half of the flowers were infested by flies (Fig. 1). From those flowers, we obtained 1478 fly puparia. We used a traditional approach to individually rear 1085 puparia (*18*): we waited

[1]Department of Biology, Cornell College, Mount Vernon, IA 52314, USA. [2]Systematic Entomology Laboratory, Agricultural Research Service–U.S. Department of Agriculture (ARS-USDA), Beltsville, MD 20705, USA. [3]Department of Entomology, Texas A&M University, College Station, TX 77843, USA. [4]Department of Ecology, Evolution, and Organismal Biology, Iowa State University, Ames, IA 50011, USA. [5]Department of Statistics, Iowa State University, Ames, IA 50011, USA. [6]Department of Biology, University of Iowa, Iowa City, IA 52242, USA.

*Corresponding author. E-mail: mcondon@cornellcollege.edu

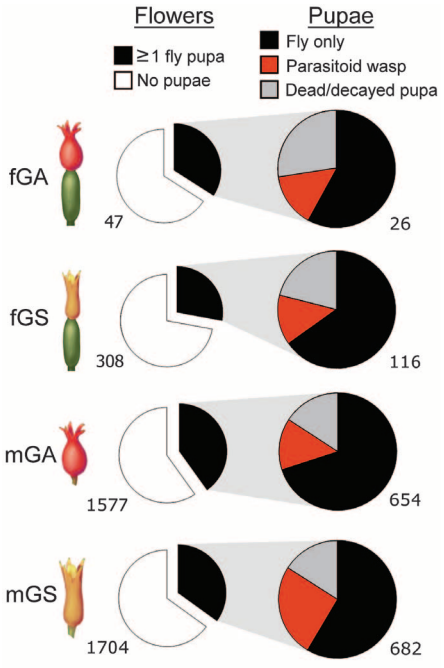

Fig. 1. Percentage of *Gurania* flowers infested by immature *Blepharoneura* flies (left) and survivorship of flies (right) revealing many uninfested flowers and parasitoid-free flies. Fly only: adult flies and preemergence puparia without wasps. Parasitoid wasp: adult wasps and preemergence puparia containing wasps. Dead/decayed puparia: unknown cause of death. Flowers: f, female; m, male, GA, *Gurania acuminata*, GS, *G. spinulosa*.

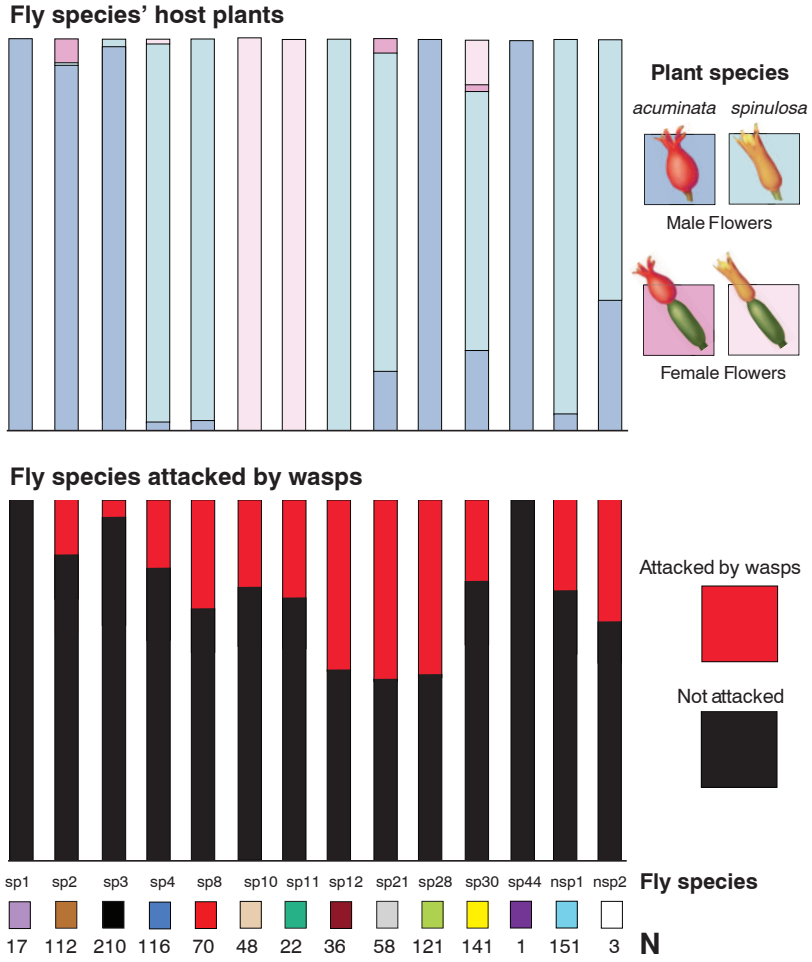

Fig. 2. *Gurania* host plants (top) used by each of 14 fly (*Blepharoneura*) species and percentage of each fly species attacked by wasps (bottom). Samples (*N*) include pre- and postemergence flies. Fly species were color-coded as in Figs. 3 and 4, and figs. S1 to S8.

for adults (either a single fly or a single wasp) to emerge from each puparium. We preserved those adults and associated postemergence puparia in ethanol. Instead of rearing the remaining 393 puparia to adulthood, we used ethanol to kill and preserve newly formed puparia ("preemergence") shortly after pupariation, before adult fly or wasp emergence.

To identify fly species, we used mitochondrial cytochrome oxidase I (mtCOI) sequences (*18*) previously corroborated by nuclear data (*15*). To identify parasitoid species, we sorted wasps into morphospecies, analyzed sequences of mtCOI and nuclear genes 28S and ef1-α, and genotyped a panel of 155 amplified fragment length polymorphism (AFLP) loci (*18*). To determine the host (fly) species killed by each wasp, we extracted DNA from the postemergence puparium of each adult wasp and used fly-specific primers to preferentially amplify fly mitochondrial DNA (mtDNA) (*18*). Postemergence wasp-fly associations represent successful (lethal to flies) host use by wasps. We also used preemergence puparia to assess wasp-fly associations. We extracted preemergence puparial DNA and used taxon-specific mtCOI primers to independently amplify fly mtCOI (always present) and wasp mtCOI (if present). Preemergence wasp-fly data include associations that would have been successful (lethal to flies) as well as "inhospitable" associations that would not have been successful (lethal to wasps). Comparison of post-and preemergence wasp-fly associations can expose virulence at two trophic levels: wasps lethal to flies, and flies inhospitable (lethal) to wasps.

We found extraordinary diversity. In just these two plant species at this single site in Peru, we found 14 fly species (all *Blepharoneura*) and 18 parasitoid species (*18*) (figs. S1 to S7). Most parasitoids were braconid wasps in the subfamily Opiinae (17 species): 14 *Bellopius* species (n = 199 individuals), two *Thiemanastrepha* species (n = 50), and one *Utetes* species (n = 2). We also reared a figitid wasp species (n = 62) (*18*). The level of parasitism of each fly species ranged from zero (*Blepharoneura* sp1) (Fig. 2) to ~50% (sp21 and sp28) (Fig. 2). Although wasp abundance was correlated with host-fly abundance (r = 0.58) (fig. S8a), the relative proportion of each fly species that was parasitized was independent of fly abundance (r = –0.05) (fig. S8b).

Multiple species occupied each of the four host-plant resources (two flower sexes of each of two host-plant species). For example, nine fly species and 12 parasitoid species were discovered in male flowers of *G. spinulosa* (Figs. 2 and 3). Most fly species in this system are extreme specialists: 11 of 14 fly species feed primarily (≥ 90% of individuals) on a single tissue of a single host-plant species (Fig. 2 and fig. S1). Most parasitoid species are even more specific to the host plants of their fly hosts: All but 1 of the 11 species of *Bellopius* represented by more than one specimen exhibited complete (100%) fidelity to a single plant-host species and to a single flower sex (Fig. 3).

Bellopius wasps also discriminate among fly species sharing identical plant resources. As many as 11 *Blepharoneura* fly species infest a single plant resource (Fig. 2) and would be available to parasitoids visiting that plant resource, yet adult *Bellopius* parasitoids revealed a pattern of extreme specialization. Ten of the 11 species of *Bellopius* represented by more than one adult emerged from its "own" single species of *Blepharoneura* (Fig. 3), which revealed a high level of niche partitioning (not niche overlap) among wasps that successfully kill flies. Similarly, mortality suffered by each fly species was usually caused by a single species of *Bellopius*. Of the 10 fly species killed by *Bellopius*, 7 were killed by a single species (Figs. 3 and 4). Such diversity and specificity is especially remarkable because the two vine species grew very close together—often intertwined. Single individual plants served as hosts to as many as six species of flies (table S9), yet all but one species of *Bellopius* (a member of poorly defined *Bellopius* group E1c) (fig. S7 and table S10) visiting those plants successfully parasitized only one species of fly. Such extreme specialization reveals a clear pattern of niche partitioning among the parasitoids, which in turn adds unique dimensions (defined by specific parasitoids) to each fly species' niche (Fig. 4).

A different pattern, however, emerges from analysis of preemergence puparia (Fig. 3). Of the 11 species of *Bellopius* detected within more than one preemergence fly puparium, 8 species were found in puparia of more than one species of *Blepharoneura*. The difference between the pre- and postemergence samples is biologically informative (table S8) (Fisher's exact test, P = 0.0075; confirmed by permutation test, P = 0.0001) (fig. S10): Preemergence puparia show that eight species of *Bellopius* oviposited into more than one species of fly, but reared samples show that adults of each species of *Bellopius* (all but species L) emerged from just a single species of *Blepharoneura.*

Comparison of pre- and postemergence samples suggests that each fly species can defend itself (perhaps immunologically) against most species of *Bellopius*. Offspring of wasps that oviposit into the "wrong" fly are dead offspring (our records show no adults emerging from those fly species) (Fig. 3); thus, selection favors extremely specialized

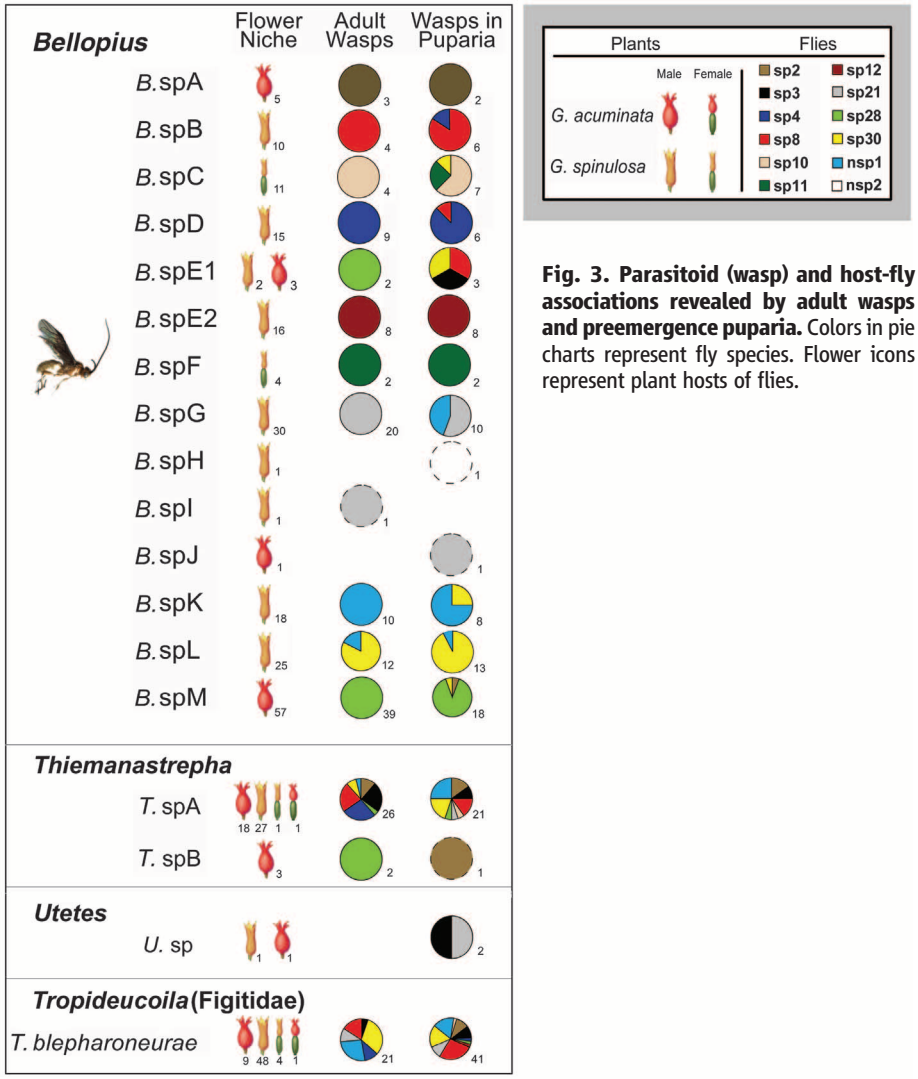

Fig. 3. Parasitoid (wasp) and host-fly associations revealed by adult wasps and preemergence puparia. Colors in pie charts represent fly species. Flower icons represent plant hosts of flies.

host choice by the wasps. Comparison of pre- and postemergence samples also reveals that wasps only oviposit into the "wrong" fly species when their primary host is found on the same flowering branch (table S9) (Fisher's exact test, $P = 0.0155$), which implies that wasps can identify that their host fly is present on a plant but can less accurately discriminate among individual larvae feeding within flowers.

The *Bellopius* pattern contrasts sharply with patterns of specificity shown by other parasitoids reared from *Blepharoneura*. For example, the two species of *Thiemanastrepha* reared from these *Blepharoneura* are generalists and attack 10 species of flies in all four plant-defined niches (Fig. 3); at least seven species of *Blepharoneura* are vulnerable to the most abundant species of *Thiemanastrepha* (Fig. 3). The single figitid species (*Tropideucoila blepharoneurae*) found in this study also attacked 10 different fly species (Fig. 3).

Insects have a well-developed immune system, and the defenses of larval flies against their internal parasitoids are particularly well-studied (*12*–*14*). *Blepharoneura* flies' defenses against *Bellopius* parasitoids represent a "hidden" niche dimension revealed through analysis of preemergence puparia (Figs. 3 and 4). In this tropical system, specialized parasitoids' offspring die in the "wrong" species of fly. Thus, selection favors parasitoids able to discriminate among multiple sympatric species of flies infesting the same host plants. Fidelity to host-plant parts and host-plant species increases *Bellopius* parasitoids' chances of detecting the "correct" host-fly species, but such fidelity also provides opportunities for flies to escape (Fig. 4): Flies on alternate host-plant parts (or alternate host-plant species) escape detection by their specialized lethal parasitoid(s), which oviposit primarily into a particular part and species of plant (Figs. 3 and 4). Yet, in this system, "escape" is not the only defense against parasitoids: Inhospitable flies are lethal to parasitoids.

Instead of representing an example of extreme niche overlap (*15*), this highly diverse community of 14 fly species and 14 *Bellopius* parasitoid species, all occupying flowers of just two species of plants, represents a community with nonoverlapping niches—each distinguished by lethal interactions between parasitoids and vulnerable flies and between parasitoids and inhospitable (lethal) flies (Figs. 3 and 4). Highly specific virulence (lethality) in both parasitoids and their prey adds a previously hidden but highly dynamic dimension to analyses of tritrophic interactions, which typically focus on unidirectional cascading patterns of escape via shifts in host plant use (*10*, *11*, *17*). Discovery of such insect parasitoid-prey interactions in complex communities of cryptic species depends on molecular methods to expose morphologically cryptic species and reveal interactions (*15*, *19*, *20*). Future studies using molecular genetic methods to identify species in other communities throughout the Neotropics are likely to reveal a geographic mosaic (*21*) of highly diverse and dynamic interactions driven by "escape and radiate" mechanisms not only at the level of host plant use, but also at the level of virulent interactions.

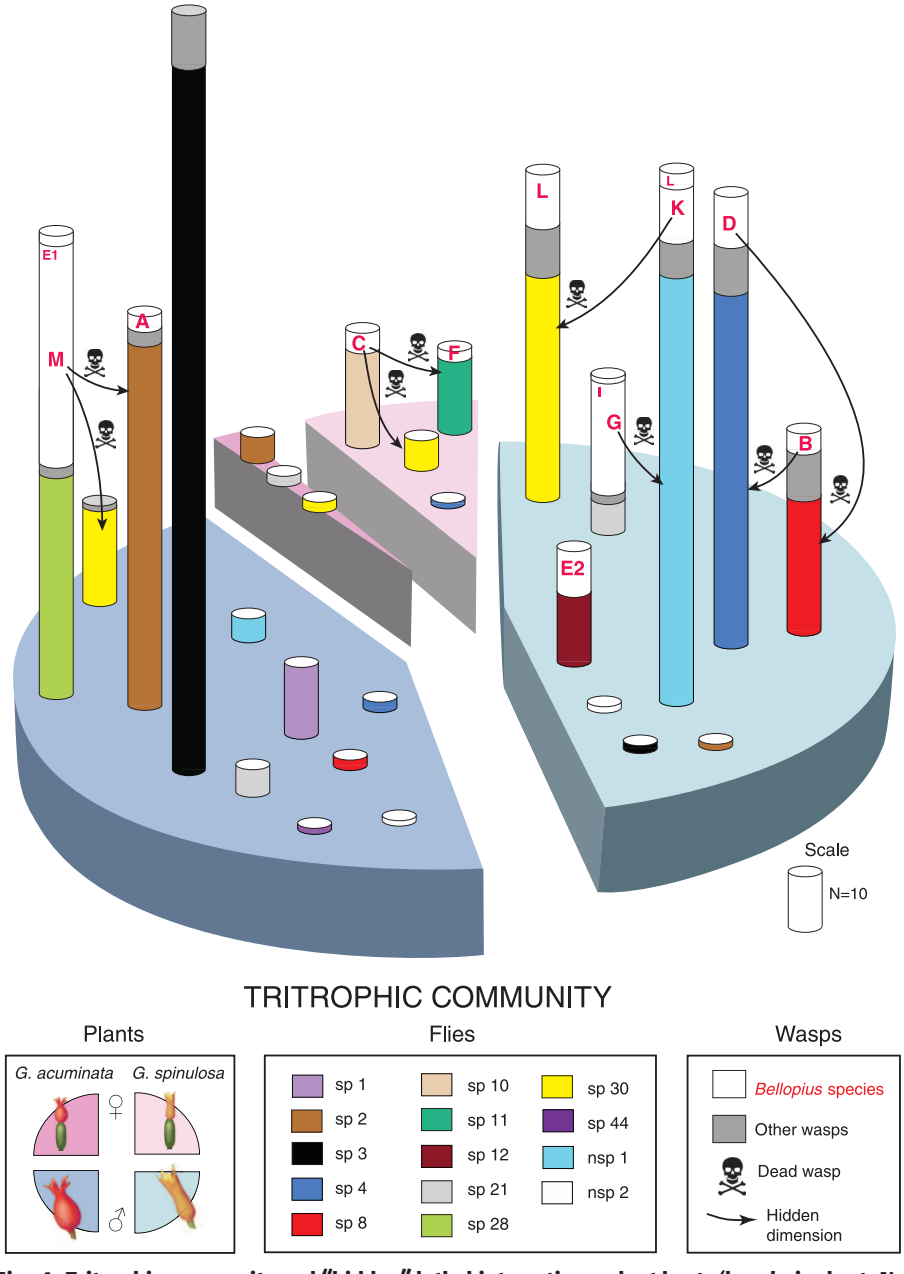

Fig. 4. Tritrophic community and "hidden" lethal interactions: plant hosts (basal pie chart, *N* = 729 host flowers) yielding adult flies and parasitoids. Stacked bars (columns) represent numbers of reared adults: bottom of bars, flies designated by colors; middle, generalist parasitoids (dark gray); and top of bar (white), lethal *Bellopius* species (red letters). (Small letters indicate rare *Bellopius*.) Arrows from *Bellopius* parasitoids indicate host flies from which adult wasps never emerged.

References and Notes

1. E. O. Wilson, *The Diversity of Life* (Norton, New York, 1999).
2. V. Novotny *et al.*, *Science* **313**, 1115–1118 (2006).
3. Y. Basset *et al.*, *Science* **338**, 1481–1484 (2012).
4. L. A. Dyer *et al.*, *Nature* **448**, 696–699 (2007).
5. C. Darwin, *On the Origin of Species by Means of Natural Selection or the Preservation of Favored Races in the Struggle for Life* (J. Murray, London, 1859).
6. D. Schluter, *The Ecology of Adaptive Radiation* (Oxford Univ. Press, Oxford, 2000).
7. D. R. Strong, J. H. Lawton, R. Southwood, *Insects on Plants: Community Patterns and Mechanisms* (Harvard Univ. Press, Cambridge, MA, 1984).
8. P. R. Ehrlich, P. H. Raven, *Evolution* **18**, 586–608 (1964).
9. P. R. Price *et al.*, *Annu. Rev. Ecol. Syst.* **11**, 41–65 (1980).
10. J. O. Stireman III, J. D. Nason, S. B. Heard, J. M. Seehawer, *Proc. Biol. Sci.* **273**, 523–530 (2006).
11. A. A. Forbes, T. H. Q. Powell, L. L. Stelinski, J. J. Smith, J. L. Feder, *Science* **323**, 776–779 (2009).
12. B. Lemaitre, J. Hoffmann, *Annu. Rev. Immunol.* **25**, 697–743 (2007).
13. A. R. Kraaijeveld, H. C. J. Godfray, *Am. Nat.* **153** (s5), S61–S74 (1999).

14. S. A. Mohamed, W. A. Overholt, R. A. Wharton, S. A. Lux, E. M. Eltoum, *Biol. Control* **28**, 155–163 (2003).
15. M. A. Condon, S. J. Scheffer, M. L. Lewis, S. M. Swensen, *Science* **320**, 928–931 (2008).
16. J. M. Chase, M. A. Leibold, *Ecological Niches: Linking Classical and Contemporary Approaches* (Univ. of Chicago Press, Chicago, 2003).
17. M. S. Singer, J. O. Stireman III, *Ecol. Lett.* **8**, 1247–1255 (2005).
18. Materials and methods are available as supplementary materials on *Science* Online.
19. M. A. Smith *et al.*, *Proc. Natl. Acad. Sci. U.S.A.* **105**, 12359–12364 (2008).
20. A. Veijalainen *et al.*, *Proc. Biol. Sci.* **279**, 4694–4698 (2012).
21. J. N. Thompson, *The Geographic Mosaic of Coevolution* (Univ. of Chicago Press, Chicago, 2005).

Acknowledgments: Funding: NSF-0330845, 0949361 to M.A.C.; NSF 0949027 to R.W.; NSF ROA (1145355), University of Iowa to A.A.F. Data are available in supplementary materials and archived at National Center for Biotechnology Information, NIH, GenBank (accession numbers: KF473465 to KF475237). The Instituto Nacional de Recursos Naturales-Intendencia Forestal y de Fauna Silvestre del Perú authorized collections (autorización no. 110-2008-INRENA-IFFS-DCB) and exportation of specimens (permiso no. 011832-AG-INRENA). T. Litwak assisted with illustrations. The authors declare no conflicts of interest. USDA is an equal opportunity provider and employer.

Supplementary Materials

www.sciencemag.org/content/343/6176/1240/suppl/DC1
Materials and Methods
Figs. S1 to S9
Tables S1 to S10
References (*22*–*49*)

21 August 2013; accepted 29 January 2014
10.1126/science.1245007

Structure of Human RNase L Reveals the Basis for Regulated RNA Decay in the IFN Response

Yuchen Han,* Jesse Donovan,* Sneha Rath,* Gena Whitney, Alisha Chitrakar, Alexei Korennykh†

One of the hallmark mechanisms activated by type I interferons (IFNs) in human tissues involves cleavage of intracellular RNA by the kinase homology endoribonuclease RNase L. We report 2.8 and 2.1 angstrom crystal structures of human RNase L in complexes with synthetic and natural ligands and a fragment of an RNA substrate. RNase L forms a crossed homodimer stabilized by ankyrin (ANK) and kinase homology (KH) domains, which positions two kinase extension nuclease (KEN) domains for asymmetric RNA recognition. One KEN protomer recognizes an identity nucleotide (U), whereas the other protomer cleaves RNA between nucleotides +1 and +2. The coordinated action of the ANK, KH, and KEN domains thereby provides regulated, sequence-specific cleavage of viral and host RNA targets by RNase L.

Cells of higher vertebrates respond to pathogens and damage by releasing interferons (IFNs), which activate protective programs in surrounding cells. One of the ubiquitous protective programs in mammalian tissues involves cleavage of intracellular RNA by a protein kinase family receptor, RNase L (*1*). RNase L is a latent endoribonuclease encoded by the hereditary prostate cancer 1 (HPC1) locus and activated by the second messenger, 2-5A (2′,5′-linked oligoadenylates of variable length) (*1*). In human cells, 2-5As are synthesized by IFN-induced 2-5A synthetases, which serve as sensors of pathogen- and damage-associated double-stranded RNA (dsRNA) (*2*, *3*). The activation of RNase L thus depends on the action of IFNs and accumulation of dsRNA.

Here, we report two crystal structures of human RNase L (table S1). These structures and complementary functional studies reveal the mechanism of 2-5A sensing and RNA cleavage by RNase L and suggest that a similar mechanism of RNA cleavage operates during regulated Ire1-dependent decay (RIDD) (*4*). We obtained diffracting crystals of nearly full-length human RNase L using cocrystallization with 2-5A, nucleotides, and an RNA 18-nucleotide oligomer 5′-GGCUUUUGACCUUUAUGC-3′ (RNA18). Cocrystallization with RNA18 was enabled by the use of a catalytically inactive RNase L mutant H672N. The final construct includes residues 21 to 719. A version of this construct with a wild-type (WT) active site is catalytically active in solution.

We determined structures of two RNase L complexes, which crystallized in different space groups (table S1). Both complexes reveal the same crossed homodimer that buries >8000 Å^2 of surface area (Fig. 1A). Previous solution studies indicated that RNase L can form dimers and higher-order oligomers (*5*). Modeling based on the oligomer of Ire1 (*6*) predicts that the homodimers of RNase L could form a similar assembly. The kinase homology (KH) domain of RNase L has a typical protein kinase fold with two globular lobes (Fig. 1B). Adenosine diphosphate (ADP) and β,γ-methyleneadenosine triphosphate are bound to the KH domain in the same conformation as ADP in the catalytically active protein kinase Ire1 (fig. S1, A to C). Nonhydrolyzable nucleotides and ATP exhibit the same effect on RNase L (fig. S1D), indicating that ATP hydrolysis is not involved in RNase L regulation, as suggested previously (*7*).

The KH domain lacks the conserved DFG motif found in most protein kinases and contains the DFD sequence, resembling protein kinases Mnk1/2 (*8*). RNase L does not carry out autophosphorylation (*7*), but it remains unknown whether RNase L phosphorylates nonself targets. To examine this possibility, we assayed phosphorylation of a nonspecific substrate, myelin basic protein (MBP), using Ire1 as a control kinase. Ire1 phosphorylated MBP, whereas RNase L was inactive (fig. S1E), supporting the current consensus that RNase L is a pseudokinase. The activation loop of RNase L contains only 13 amino acid residues and is among the shortest in the human protein kinome (fig. S3). The interlobe hinge and the ATP pocket contact a unique helix from the ankyrin (ANK)/KH linker (Fig. 1B and fig. S2). These attributes of the KH domain likely reflect adaptation to autophosphorylation-independent control as a homodimerization scaffold.

Previous structural studies identified two different 2-5A binding sites in the ANK domain (*5*, *9*). The crystal structure of the entire RNase L now reveals an unanticipated third site in the N lobe of the KH domain (Fig. 1A and fig. S4, A to C). The ANK and KH domains create a composite pocket for 2-5A binding, which exposes the 2′-end to solvent to accommodate long 2-5A molecules and anchors the 5′-end in the ANK domain (fig. S5A). Although RNase L can recognize 5′-p and 5′-ppp groups, at saturating concentrations 2-5pA_3 activates RNase L stronger than 2-5pppA_3 (fig. S5, B and C). The ANK/ANK homodimer binds 2-5A in a configuration that displays the phosphate p1 for recognition by the KH domain (fig. S6). Mutagenesis of the KH/2-5A interface confirms that the N lobe is functionally involved in 2-5A sensing (fig. S4D). The ANK domain contains a characteristic helix αI, which docks to the KH domain in trans upon homodimerization (fig. S7). The αI/N-lobe interaction and an ANK/N-lobe contact mediated by the residue R238 also facilitate RNase L activation by 2-5A (fig. S4, C and D).

The KH/KH and kinase extension nuclease (KEN)/KEN interfaces resemble those in Ire1 (*10*). Mutagenesis confirmed that both interfaces are important for 2-5A–dependent RNase L activation (Fig. 2A) and dimerization (fig. S8). The KEN residues involved in catalysis in Ire1 (*10*, *11*) are structurally invariant in RNase L (Fig. 2B), indicating that these enzymes share the same catalytic mechanism. However, the KEN domains contain different α-helix/loop elements (HLE) (*6*), implicated in RNA specificity (*10*). To examine the HLE function, we shortened this element in RNase L (ΔHLE). The ΔHLE mutant still cleaved RNA but exhibited a decreased rate and a greater preference for single-stranded RNA (ssRNA)

Department of Molecular Biology, Princeton University, 216 Schultz Laboratory, Princeton, NJ 08540, USA.

*These authors contributed equally to this work.
†Corresponding author. E-mail: akorenny@princeton.edu

versus stem loops (Fig. 2C). A chimeric RNase L with the HLE sequence from Ire1 (HLE swap) retained the preference for ssRNA (Fig. 2C), revealing that the HLE of Ire1 is insufficient for directing RNase L to stem loops. Thus, the HLE does not determine the substrate specificity of RNase L (and, by extension, of Ire1) and only facilitates RNA cleavage.

Both complexes of RNase L described here were obtained with an RNA bound in the active site. Two sugar-phosphate groups and one pyrimidine nucleobase are resolved in complex II (fig. S9 and table S1). We modeled uridine based on the preference of RNase L for AU-rich sites (*12*) and biochemical studies of RNA substrates described below. The U residue blocks access of the nearest catalytic histidine H672 to the phosphodiester backbone. Thus, RNA cleavage should be carried out by the symmetry-related histidine H672 provided by homodimerization (Fig. 3A). Distance constraints suggest that cleavage occurs between the nucleotides +1 and +2 relative to the U residue.

To test this model, we employed an in trans complementation assay using a mixture of WT and catalytically inactive RNase L (H672N). The H672N mutation eliminates the proton transfer but preserves the H-bonding and space-filling character of histidine. Thus, the H672N mutant should interact with RNA analogous to the WT protein but without cleaving the RNA. The in trans complementation assay was performed by adding increasing concentrations of the H672N mutant to a fixed and limiting concentration of WT RNase L (2 nM). The H672N mutant was a potent in trans activator for WT RNase L, whereas double H672N mutant was inactive (Fig. 3B). Thus, a single H672 residue per a KEN/KEN dimer is necessary and sufficient for RNA cleavage. The biochemical and structural data converge on a single mechanism of RNA cleavage by RNase L that involves recognition of a U residue by one KEN protomer and catalytic RNA scission by the second KEN protomer. The size of the nucleotide-binding pocket in RNase L can explain the preference for a pyrimidine, whereas U/C discrimination apparently results from H bonding with H672 (fig. S10).

In contrast to other endoribonucleases, such as RNase A and RNase T1, RNase L does not cleave ssRNA randomly. Only a single site is cleaved in 5′-CCCCCCCCCCCUU^UCCCCCCC-3′ ssRNA (RNA21) (^ denotes the cleavage site) (*13*). RNase L has been described as an enzyme that cleaves RNA at dinucleotides UU and UA (*12*), as well as after dinucleotides UN (*14*). Our structural analysis suggests that RNase L recognizes the pattern UN^N, supporting cleavage 3′ of UN sequences. To verify this assignment, we synthesized a series of model RNA substrates. RNase L cleaved these substrates according to the UN^N rule (Fig. 3C). We next designed substrates DI and DII, which use a different RNA backbone and contain the AU, UA and UN^N sequences in mutually exclusive positions. RNase L cleaved these substrates also according to the UN^N pattern (Fig. 3D). The UN^N rule extends to the biological targets of RNase L. Cleavage of 28*S* rRNA within the L1 protuberance occurs at UG^C,

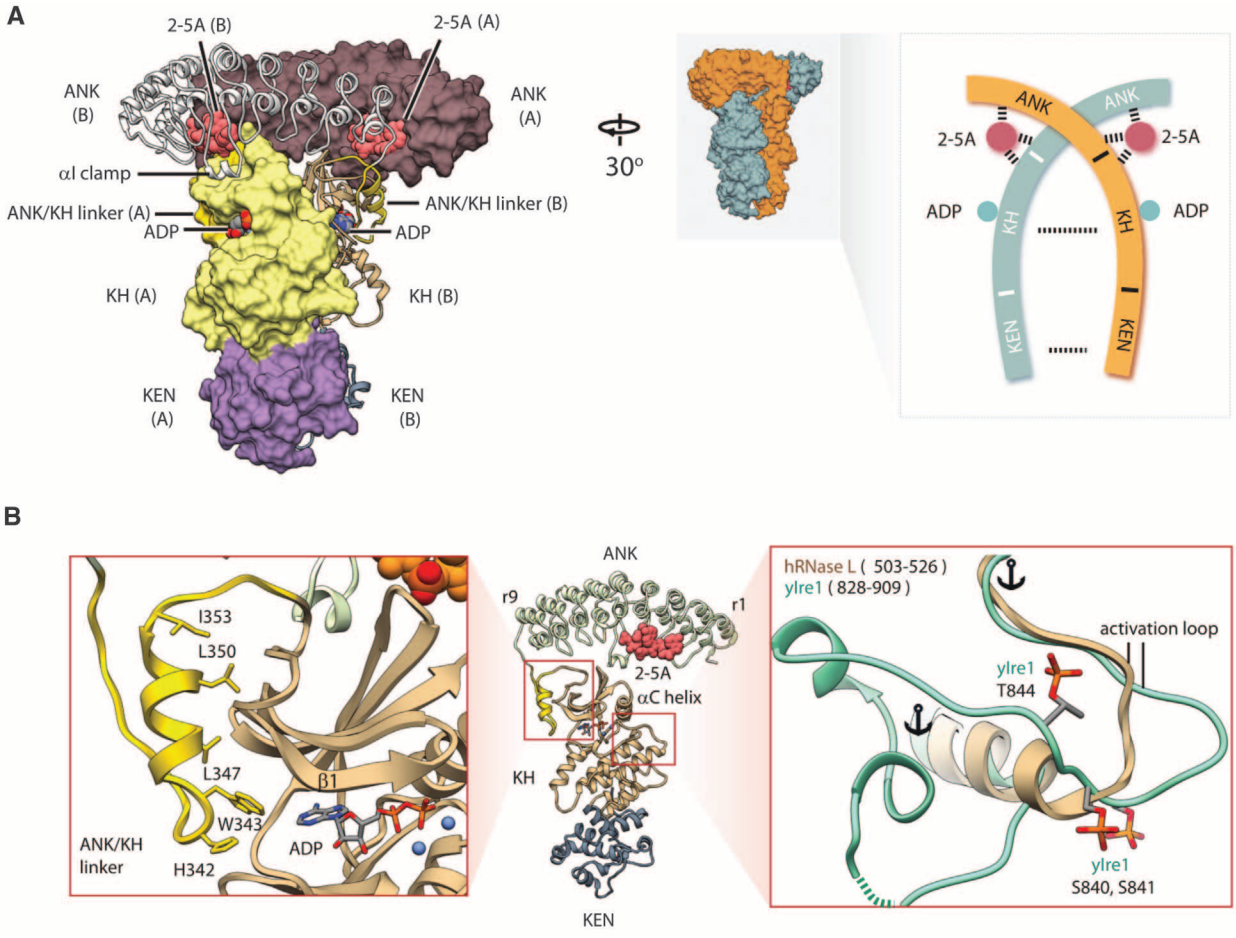

Fig. 1. Structure of human RNase L•2-5pA_3•ADP•RNA18 quaternary complex. (**A**) Crossed homodimer of RNase L. Different protomers are shown as molecular surface and ribbon, respectively. The structured linker connecting the ANK and the KH domains is colored gold. Schematic topology of the RNase L homodimer is shown on the right. (**B**) Structure of the KH domain. The ATP pocket is flanked by the structured linker (left). The activation loop is short and lacks phosphorylation sites (right). Single-letter abbreviations for the amino acid residues are as follows: A, Ala; C, Cys; D, Asp; E, Glu; F, Phe; G, Gly; H, His; I, Ile; K, Lys; L, Leu; M, Met; N, Asn; P, Pro; Q, Gln; R, Arg; S, Ser; T, Thr; V, Val; W, Trp; and Y, Tyr.

CU^G, and UC^G sites (*15*) (Fig. 4A), which do not contain the UU/UA dinucleotides conventionally ascribed to RNase L targets (*12*). However, two of them match the UN^N pattern. Cleavage of hepatitis C virus RNA (*12*) occurs markedly at the UN^N sequences (Fig. 4A).

To confirm that key functional residues identified by our structural and biochemical analyses are important in vivo, we tested the activity of several RNase L mutants in human cells using 28*S* rRNA cleavage readout (*12*). RNase L mutants R163A (αI clamp), R412A (KH/KH interface), R427A (recognition of 2-5A), and H672N (RNA cleavage) were tested and displayed reduced activity compared with WT RNase L. Western blotting confirmed that all mutants were expressed similarly (Fig. 4B).

The mechanism of RNA cleavage by RNase L identified here has implications for understanding RNA decay by a related receptor, Ire1. In addition to cleaving canonical RNA stem loops within Hac1/XBP1 mRNA, Ire1 has a broader second set of RNA targets, which are cleaved during RIDD (*4*). Our review of these targets revealed a surprising agreement between the recently mapped RIDD cleavage sites and the consensus UN^N established for RNase L. This is observed with Angptl3 mRNA (*16*), Cyp1 mRNAs (*17*), and pre-mir-17 microRNA (*18*), all of which are cleaved at UG^C sites. Moreover, Ire1 in fission yeast, which lacks the Hac1 gene, cleaves mRNA at sites NNUG^CNN (*19*) that match both the UN^N pattern and the UG^C pattern in RIDD substrates. Thus, structural similarity between RNase L and Ire1 results in a functional similarity, which hitherto escaped notice.

To examine this functional relationship, we tested cleavage of UN^N motifs by Ire1. Ire1 did not cleave UU^U, UU^A, and UA^A sequences, exhibiting a mutually exclusive specificity with RNase L (fig. S11). However, Ire1 and RNase L

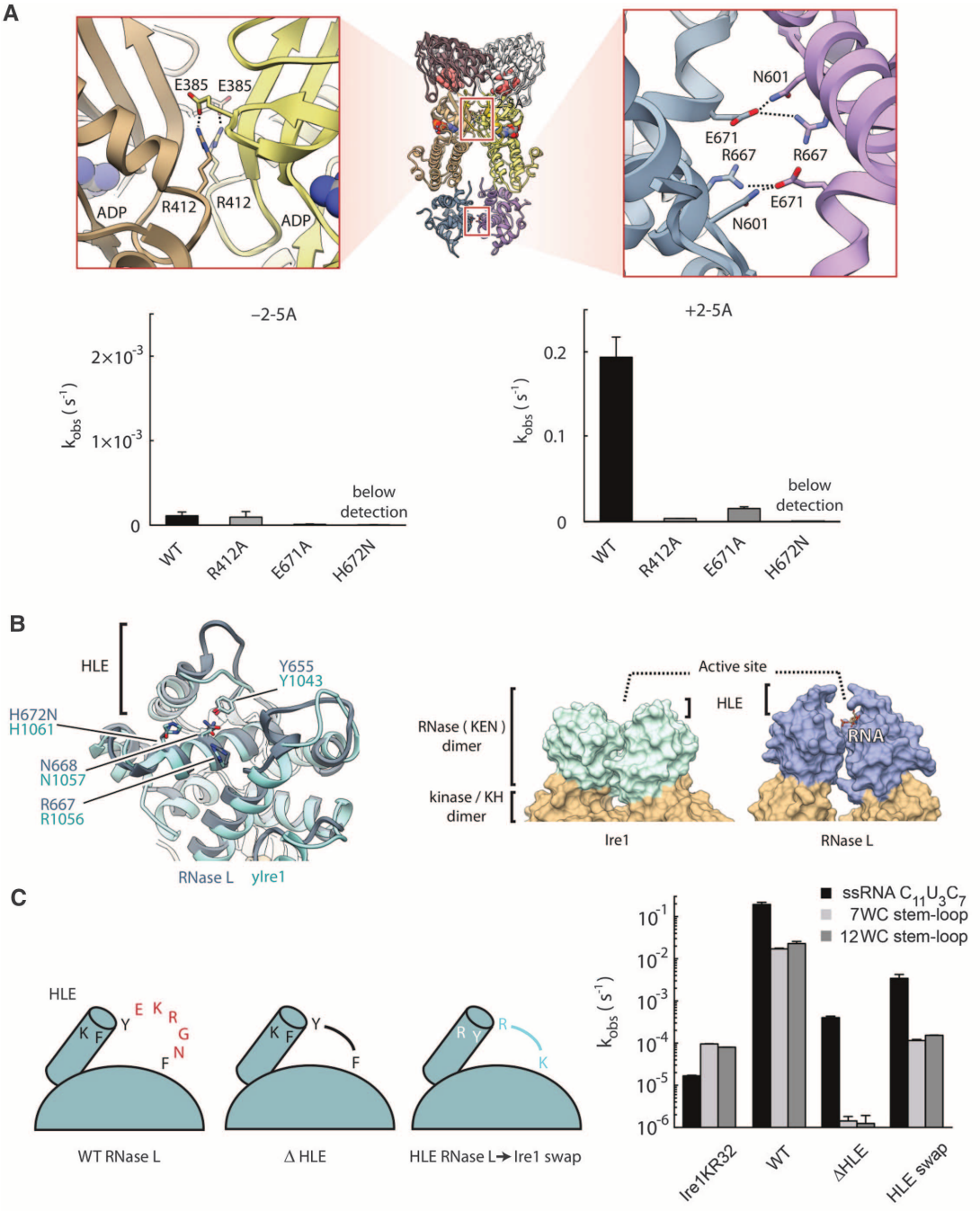

Fig. 2. KH and KEN homodimers. (**A**) Symmetrical salt bridges stabilize the interfaces between the KH (1364 Å^2) and RNase (943 Å^2) domains. Mutations of these salt bridges impair RNase L activity. (**B**) Comparison of KEN domains in RNase L and Ire1. Key active-site residues are indicated. (**C**) Effect of HLE mutagenesis on cleavage of ssRNA and RNA hairpins derived from human XBP1 mRNA. WC indicates the number of Watson-Crick base pairs in the hairpin stem. Ire1KR32 is yeast Ire1 kinase/RNase. Reactions contained 100 nM Ire1KR32 and 5 nM RNase L. Error bars show mean ± SE.

both cleaved the UG^C sequence (DIII) (Fig. 4C) and were sensitive to a U→A mutation (DIV). Ire1 was still able to cleave the G^C site in substrate DIV, indicating that the catalytic KEN protomer of Ire1 provides G^C recognition. Together, our experiments and the studies of RIDD and fission yeast suggest that RNA decay by RNase L and RIDD use related mechanisms of RNA cleavage (fig. S12).

RNase L is expressed in most human tissues, which imposes the requirement for a delicate regulation of this protein to prevent uncontrolled RNA cleavage, growth inhibition, and apoptosis. Here, we describe the mechanism of this regulation. Our findings further the understanding of the IFN response and RIDD and provide a structural basis for designing synthetic 2-5A analogs as molecular probes and modulators of IFN

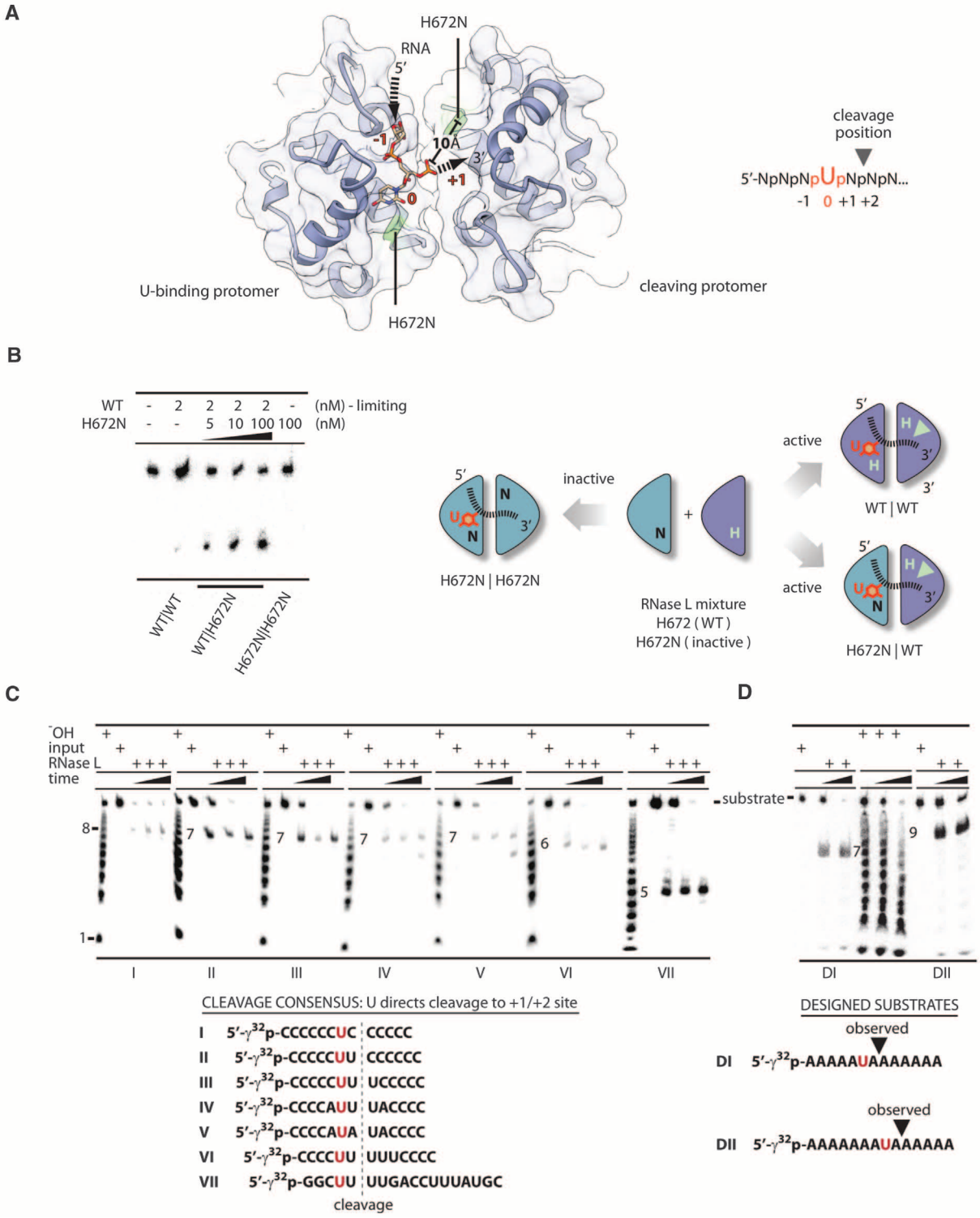

Fig. 3. RNA sequence recognition by RNase L. (**A**) Structure of RNA bound to the KEN homodimer. Arrows show the RNA trace. RNA cleavage is predicted at UN^N sites. (**B**) In trans activation of WT RNase L by the catalytically inactive RNase L mutant H672N. (**C**) RNase L cleavage of substrates I to VII. (**D**) RNase L cleavage of substrates DI and DII.

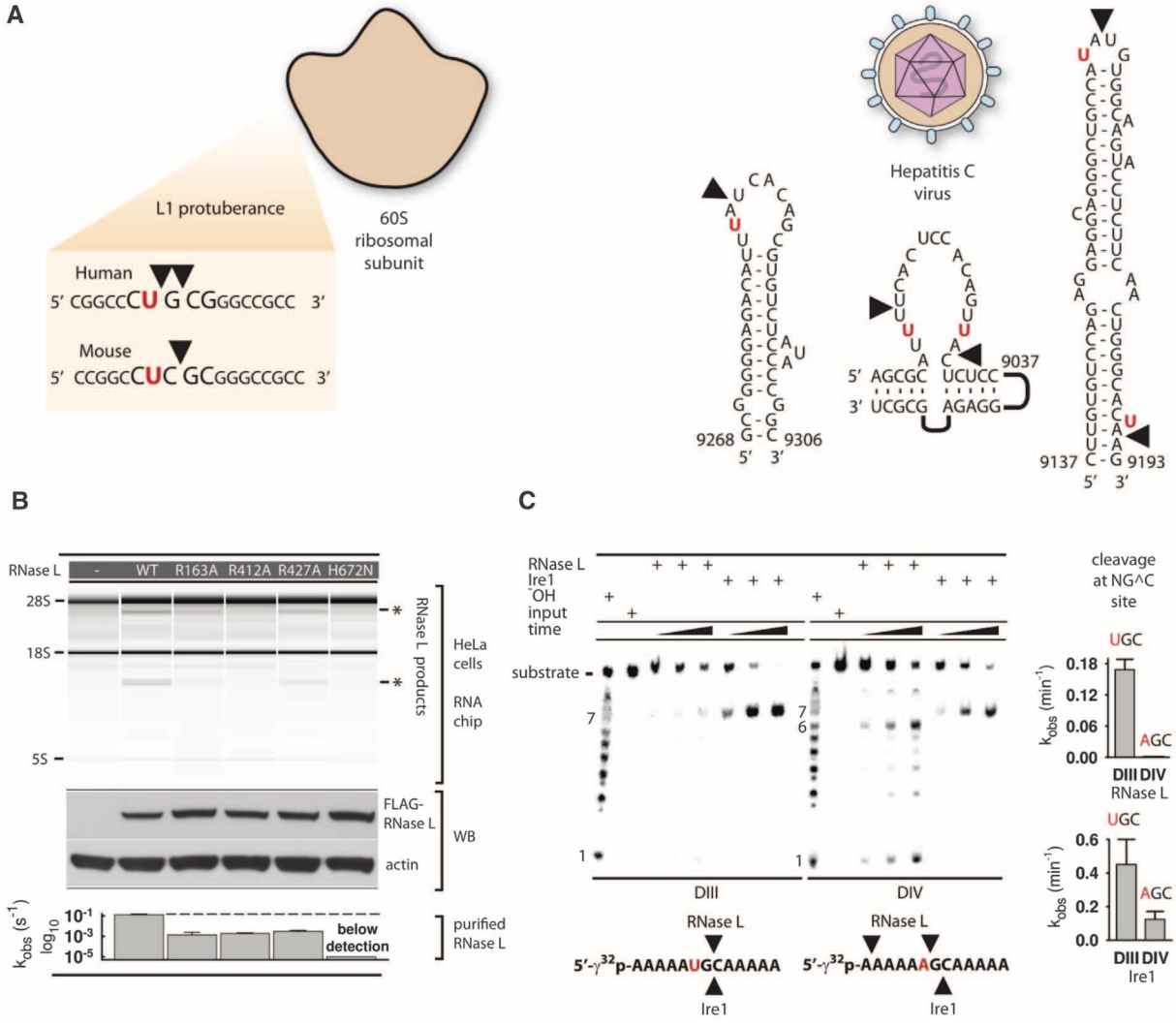

Fig. 4. Cleavage of biological targets. (**A**) Site selection by RNase L in mammalian ribosomes and hepatitis C virus RNA. (**B**) Total RNA from HeLa cells cotransfected with plasmids encoding RNase L mutants or not encoding a protein (–), and 2-5A. Protein expression levels were analyzed by Western blot (WB). The bar graph shows compiled data from in vitro assays in Fig. 2A and fig. S4D. (**C**) Cleavage of substrates DIII and DIV by RNase L and Ire1KR32. Bar charts show quantification of cleavage. Error bars show mean ± SE of a single-exponential fitting (RNase L) and two time courses (Ire1KR32).

action and adjuvants for treating infections and inflammatory diseases.

Note added in proof: After this manuscript was submitted, groups of F. Sicheri and R. Silverman published a structural analysis of porcine RNase L. This work reports a similar crossed homodimer but observes different KEN/KEN interactions (*20*) due to a conformational difference presumably caused by RNA binding.

References and Notes

1. A. Chakrabarti, B. K. Jha, R. H. Silverman, *J. Interferon Cytokine Res.* **31**, 49–57 (2011).
2. J. Donovan, M. Dufner, A. Korennykh, *Proc. Natl. Acad. Sci. U.S.A.* **110**, 1652–1657 (2013).
3. R.-J. Lin *et al.*, *J. Immunol.* **183**, 8035–8043 (2009).
4. J. Hollien, J. S. Weissman, *Science* **313**, 104–107 (2006).
5. Y. Han, G. Whitney, J. Donovan, A. Korennykh, *Cell Rep.* **2**, 902–913 (2012).
6. A. V. Korennykh *et al.*, *Nature* **457**, 687–693 (2009).
7. B. Dong, R. H. Silverman, *Nucleic Acids Res.* **27**, 439–445 (1999).
8. J. P. Turowec *et al.*, *Methods Enzymol.* **484**, 471–493 (2010).
9. N. Tanaka *et al.*, *EMBO J.* **23**, 3929–3938 (2004).
10. K. P. K. Lee *et al.*, *Cell* **132**, 89–100 (2008).
11. A. V. Korennykh *et al.*, *BMC Biol.* **9**, 47 (2011).
12. C. L. Washenberger *et al.*, *Virus Res.* **130**, 85–95 (2007).
13. S. S. Carroll *et al.*, *J. Biol. Chem.* **271**, 4988–4992 (1996).
14. D. H. Wreschner, J. W. McCauley, J. J. Skehel, I. M. Kerr, *Nature* **289**, 414–417 (1981).
15. M. S. Iordanov *et al.*, *Mol. Cell. Biol.* **20**, 617–627 (2000).
16. J. S. So *et al.*, *Cell Metab.* **16**, 487–499 (2012).
17. K. Y. Hur *et al.*, *J. Exp. Med.* **209**, 307–318 (2012).
18. J. P. Upton *et al.*, *Science* **338**, 818–822 (2012).
19. P. Kimmig *et al.*, *eLife* **1**, e00048 (2012).
20. H. Huang *et al.*, *Mol. Cell* **53**, 221–234 (2014).

Acknowledgments: We thank F. Hughson (Princeton University) and A. Korostelev (University of Massachusetts, Worcester) for reading the manuscript and making valuable suggestions. We thank the staff of Brookhaven National Laboratory for providing access to a synchrotron x-ray source. We are grateful to our colleagues at the Department of Molecular Biology for stimulating discussions and an excellent research environment. We thank Princeton University for supporting and funding our work. Coordinates have been deposited to the Protein Data Bank with accession codes 4OAU and 4OAV. Author contributions: Y.H., J.D., and A.K. determined the structures of RNase L. S.R. carried out biochemical studies of model RNA substrates. G.W. and A.C. carried out studies in HeLa cells. Y.H. and A.K. wrote the manuscript. A.K. supervised the work.

Supplementary Materials

www.sciencemag.org/content/343/6176/1244/suppl/DC1
Materials and Methods
Figs. S1 to S12
Table S1
References (*21*–*30*)

17 December 2013; accepted 12 February 2014
Published online 27 February 2014;
10.1126/science.1249845

Selective Methylation of Histone H3 Variant H3.1 Regulates Heterochromatin Replication

Yannick Jacob,[1]* Elisa Bergamin,[2]* Mark T. A. Donoghue,[1] Vanessa Mongeon,[2] Chantal LeBlanc,[1] Philipp Voigt,[3] Charles J. Underwood,[1] Joseph S. Brunzelle,[4] Scott D. Michaels,[5] Danny Reinberg,[3] Jean-François Couture,[2]† Robert A. Martienssen[1,6]†

Histone variants have been proposed to act as determinants for posttranslational modifications with widespread regulatory functions. We identify a histone-modifying enzyme that selectively methylates the replication-dependent histone H3 variant H3.1. The crystal structure of the SET domain of the histone H3 lysine-27 (H3K27) methyltransferase *ARABIDOPSIS* TRITHORAX-RELATED PROTEIN 5 (ATXR5) in complex with a H3.1 peptide shows that ATXR5 contains a bipartite catalytic domain that specifically "reads" alanine-31 of H3.1. Variation at position 31 between H3.1 and replication-independent H3.3 is conserved in plants and animals, and threonine-31 in H3.3 is responsible for inhibiting the activity of ATXR5 and its paralog, ATXR6. Our results suggest a simple model for the mitotic inheritance of the heterochromatic mark H3K27me1 and the protection of H3.3-enriched genes against heterochromatization during DNA replication.

During the S phase of the cell cycle, patterns of histone posttranslational modifications (PTMs) must be reestablished after passage of the replication fork to restore the correct epigenetic status to each region of the genome (*1*). Because many different chromatin states are encountered during replication, the deposition of histone PTMs on newly replicated chromatin must be precisely regulated.

The histone H3 Lys^{27} (H3K27) methyltransferases *ARABIDOPSIS* TRITHORAX-RELATED PROTEIN 5 (ATXR5) and ATXR6 (ATXR5/6) are thought to maintain the heterochromatic mark H3K27me1 during DNA replication in plants (*2*). In *atxr5 atxr6* double mutants, H3K27me1 levels are reduced, heterochromatin is decondensed, some repetitive sequences are transcribed, and heterochromatic overreplication is observed (*3*–*5*). In both animals and plants, chromatin restoration after DNA replication depends on the histone chaperone CAF-1 and involves deposition of the S-phase–expressed histone H3 variant H3.1 (*6*, *7*). In contrast, histone H3.3 is inserted by other histone chaperones, mainly during transcription, and acts as a replacement histone (*7*–*11*). Canonical histone H3.1 and histone H3.3 are >96% identical in most eukaryotes (*12*) and differ only by four and five residues in flowering plants and mammals, respectively (Fig. 1A). H3.1 and H3.3 variants have been shown to contain different histone PTMs, but the mechanisms involved in H3 variant–specific marking are not known (*12*). It is possible that sequence variation between the variants could directly affect their PTMs (*13*, *14*).

One of the conserved differences between H3.1 and H3.3 is at position 31, with alanine (H3.1), threonine (H3.3 *Arabidopsis*), or serine (H3.3 human) (Fig. 1A). Because residue 31 of histone H3 is close to the modifiable and functionally important residue K27 (Lys^{27}), we hypothesized that H3 variants could selectively regulate methylation at K27. To test this, we performed histone lysine methyltransferase (HKM) assays using methyltransferases from *Arabidopsis thaliana* and recombinant chromatin containing either plant histone H3.1 or plant histone H3.3. Our results show that the H3K27 methyltransferases ATXR5/6 have much higher activity on nucleosomes containing H3.1 than H3.3 (Fig. 1B). Furthermore, steady-state kinetic analysis of ATXR5 confirms that the enzyme exhibits strong preference toward the H3.1 variant (Fig. 1C). This ability to favor H3.1 nucleosomes over H3.3 nucleosomes as substrates was not observed for two polycomb repressive complex 2 (PRC2) complexes [MEDEA (MEA) and CURLY LEAF (CLF)], which also methylate K27, or the H3K9 methyltransferases KRYPTONITE (KYP)/SU(VAR)3-9 HOMOLOG 4 (SUVH4) and SUVH5 (Fig. 1B). We tested whether Ala^{31} of H3.1 is required for H3K27 methylation by ATXR5/6. When using H3.3 nucleosomes with Thr^{31} replaced with alanine (T31A), we observed levels of H3K27 methylation similar to levels obtained when H3.1 nucleosomes are used (Fig. 1D). Taken together, these results demonstrate that ATXR5/6 selectively methylate the replication-dependent variant H3.1 in vitro and that Thr^{31} in H3.3 is responsible for inhibiting the activity of ATXR5/6.

To gain a better understanding of how ATXR5/6 specifically methylate H3.1, we solved the crystal structure of an ATXR5-H3.1 complex. We focused on the C-terminal half of ATXR5, which contains the catalytic SET domain preceded by a conserved sequence (hereafter named nSET) of unknown function (fig. S1). The structure of the ATXR5 homolog from the plant *Ricinus communis* [RcATXR5 amino acids 158 to 374] in complex with a histone H3.1 peptide (amino acids 18 to 36, strictly conserved between *A. thaliana* and *R. communis*) and the product cofactor S-adenosylhomocysteine (AdoHcy) was solved at 2.1 Å resolution (fig. S2 and table S1). Collectively, the structure shows that the SET domain comprises two short α helices (α5 and α6) and 10 β strands (β1 to β10), all forming twisted antiparallel β sheets (Fig. 2A). The nSET region folds as four consecutive α helices (α1 to α4) interspersed by loops that pack onto the SET domain. The H3.1 peptide binds in a tight binding cleft in an L-shaped conformation and engages in several hydrogen bonds and hydrophobic contacts (see supplementary text) with RcATXR5 (Fig. 2, A and B). A simulated annealing $F_o - F_c$ omit map revealed electron density for residues 24 to 36 of histone H3.1 (Fig. 2C). A comparative analysis of the ATXR5/H3.1 complex reveals structural divergence in the histone-binding mode (fig. S3 and supplementary text).

The ternary structure shows that both SET and nSET of RcATXR5 are involved in selective H3.1 binding. The residues E212 and M216 (E, Glu; M, Met) of the α3-α4 loop (L1) of nSET, along with R334 (R, Arg) in the SET domain, form a shallow binding pocket (referred to as selectivity pocket) accommodating the small side chain of H3.1 Ala^{31} (Fig. 3A). Accordingly, E212, M216, and R334 are strictly conserved in ATXR5/6 homologs from mosses to flowering plants (fig. S1). The side chain of Ala^{31} makes hydrophobic and van der Waals contacts with the side chains of M216 and R334, and the guanidium group of R334 engages in two short hydrogen bonds with the carboxylate group of E212, which likely rigidify the specificity pocket. Consistent with our HKM assays (Fig. 1D), we found that replacing Ala^{31} with Thr^{31} generates van der Waals clashes between the Thr^{31} Cγ methyl group and the side chain of R334 (fig. S4). In addition, amino acid substitutions at E212 and R334 (*A. thaliana* ATXR6 residues E186 and R309) drastically reduced methylation on nucleosomes (Fig. 3B), suggesting that residues forming the specificity pocket are important for conferring specificity and high affinity binding to H3.1.

Another unique structural feature of ATXR5/6 likely contributes to the selective methylation of histone H3.1. A loop (L3) comprising residues G363, Y364 (Y, Tyr), E365, and E367 folds back on top of H3.1, shielding the peptide from the solvent in a "safety belt" conformation (Figs. 2, A and B, and 3A). Y364 makes hydrophobic

[1]Howard Hughes Medical Institute–Gordon and Betty Moore Foundation, Watson School of Biological Sciences, Cold Spring Harbor Laboratory, 1 Bungtown Road, Cold Spring Harbor, NY 11724, USA. [2]Ottawa Institute of Systems Biology, Department of Biochemistry, Microbiology and Immunology, University of Ottawa, Ottawa, Ontario K1H 8M5, Canada. [3]Howard Hughes Medical Institute, Department of Biochemistry and Molecular Pharmacology, New York University School of Medicine, New York, NY 10016, USA. [4]Feinberg School of Medicine, Department of Molecular Pharmacology and Biological Chemistry, Northwestern University, Chicago, IL 60611, USA. [5]Department of Biology, Indiana University, 915 East Third Street, Bloomington, IN 47405, USA. [6]Institut de Biologie de l'École Normale Supérieure, 75005 Paris, France.

*These authors contributed equally to this work.
†Corresponding author. E-mail: jean-francois.couture@uottawa.ca (J.F.C.); martiens@cshl.edu (R.A.M.)

contact with Pro[30], while the carboxylate group of E365 engages in hydrogen bonds with the guanidium group of Arg[26] and the hydroxyl group of T289. Together, these residues help bind the peptide tightly to the histone H3.1 binding cleft. The role of the L3 loop is likely twofold: (i) locking the peptide in a conformation that forces the side chain of Ala[31] into the specificity pocket and (ii) packing the structurally constrained residue Pro[30] onto the peptide-binding pocket of RcATXR5. This hypothesis is supported by our HKM assays showing that substitution of Y364 (*A. thaliana* ATXR6 Y339) by an alanine residue reduces the specificity of the enzymes for H3.1 by threefold (Fig. 3B).

In *Arabidopsis*, H3K27me1 is enriched on H3.1 (fig. S5) (*15*, *16*), and more than 80% of H3.1 was found to be methylated at K27 by mass spectrometry (*17*). To validate that Thr[31] in histone H3.3 directly interferes with the activity of ATXR5/6 in vivo, we generated transgenic *Arabidopsis* plants expressing the tandem histone H3.1 genes *HTR9* and *HTR13* as wild-type (WT) proteins (H3.1) or with an alanine-to-threonine replacement at position 31 (H3.1 A31T). The transgenes were expressed in H3.1 quadruple mutants (*A. thaliana* contains five H3.1 genes). We quantified by chromatin immunoprecipitation (ChIP) the levels of H3K27me1 at genomic regions enriched in H3.1 (fig. S6) and that have been shown to be dependent on ATXR5/6 for H3K27me1 (*4*), because plant PRC2 complexes also have the ability to monomethylate H3K27 (fig. S7). When we measured H3K27me1 levels in the two sets of transgenic plants, we observed lower levels of the epigenetic mark in plants expressing H3.1 A31T compared to WT (Col), but not in plants expressing H3.1 (Fig. 4A and fig. S8). As in *atxr5 atxr6* double mutants, silencing of *Athila* open reading frame 1 [also known as *transcriptionally silent information* (*TSI*)] was lost in transgenic plants expressing H3.1 A31T (Fig. 4B).

Reactivation of *TSI* and other heterochromatic defects has also been observed when the histone chaperone CAF-1 is mutated in *Arabidopsis* (Fig. 4B) (*18*–*22*). Depletion of CAF-1 in mammalian cell lines leads to H3.1 replacement with H3.3 (*23*). Consistently, *Arabidopsis* CAF-1 mutants show higher expression of H3.3 genes (*18*). On the basis of our finding that ATXR5/6 specifically methylate H3.1, we hypothesized that

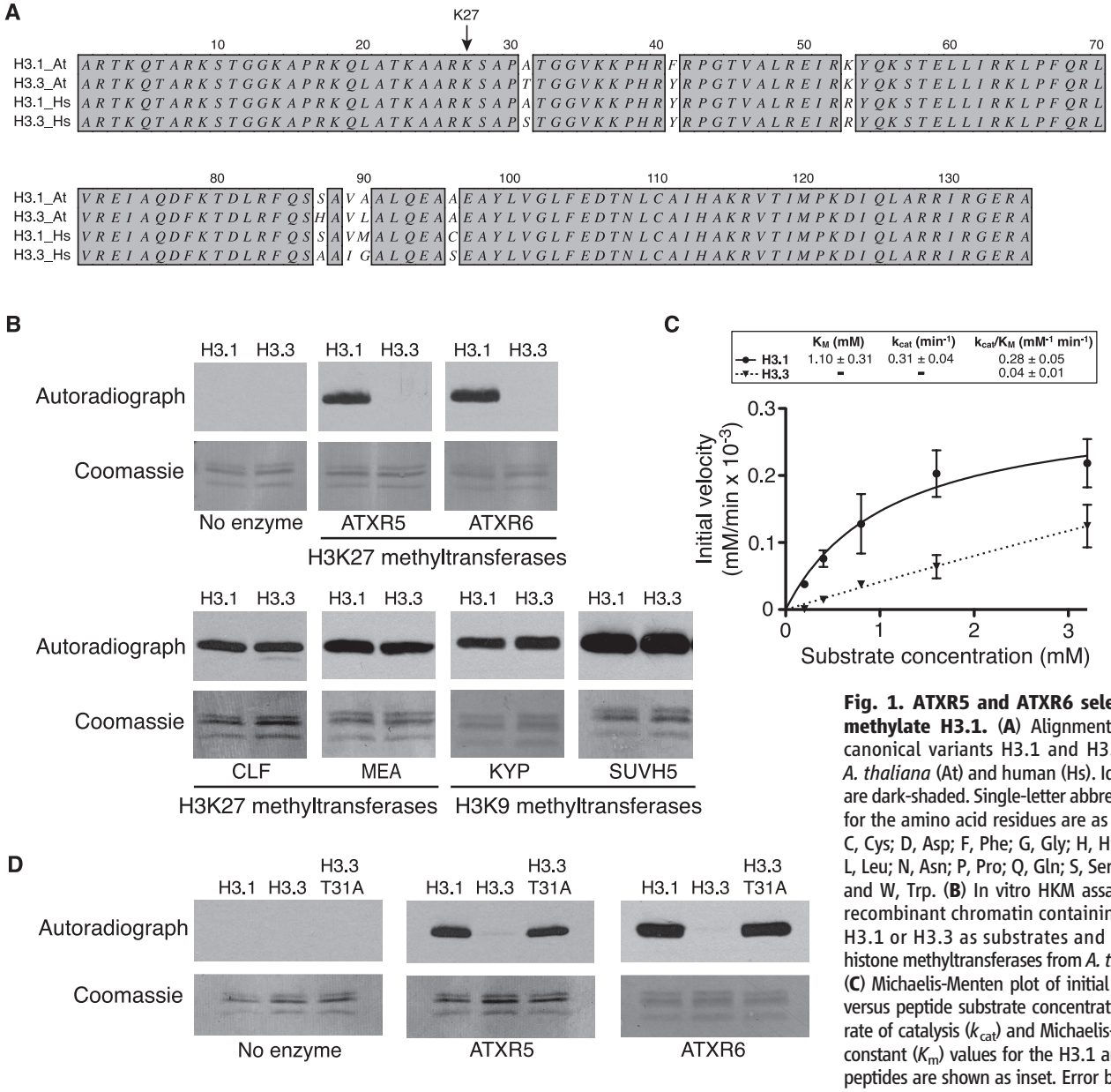

Fig. 1. ATXR5 and ATXR6 selectively methylate H3.1. (**A**) Alignment of the canonical variants H3.1 and H3.3 from *A. thaliana* (At) and human (Hs). Identities are dark-shaded. Single-letter abbreviations for the amino acid residues are as follows: C, Cys; D, Asp; F, Phe; G, Gly; H, His; I, Ile; L, Leu; N, Asn; P, Pro; Q, Gln; S, Ser; V, Val; and W, Trp. (**B**) In vitro HKM assay using recombinant chromatin containing plant H3.1 or H3.3 as substrates and various histone methyltransferases from *A. thaliana*. (**C**) Michaelis-Menten plot of initial velocity versus peptide substrate concentration. The rate of catalysis (k_{cat}) and Michaelis-Menten constant (K_m) values for the H3.1 and H3.3 peptides are shown as inset. Error bars represent the standard deviations of three independent experiments, each performed in triplicates with three different batches of RcATXR5. (**D**) In vitro HKM assays using recombinant chromatin containing plant H3.1, H3.3, or H3.3 T31A.

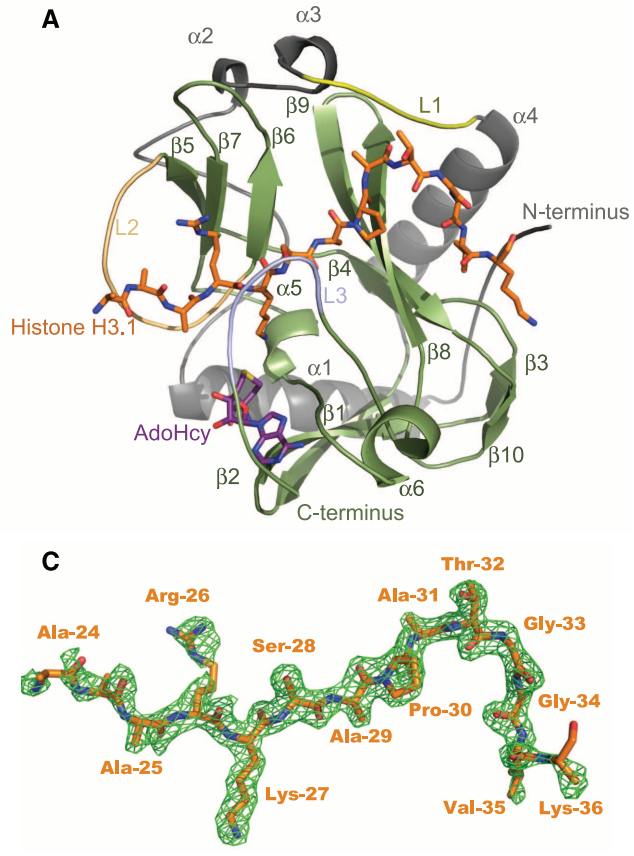

Fig. 2. ATXR5/6 contain a bipartite catalytic domain composed of nSET and SET. (**A**) Ribbon representation of the RcATXR5-H3.1-AdoHcy ternary complex in which nSET and SET are highlighted in gray and green, respectively. Carbon atoms of H3.1 and product cofactor are colored in orange and magenta, respectively. (**B**) Zoomed view of the peptide binding cleft of RcATXR5. Three-letter code refers to H3.1 residues. Carbon atoms of residues found in the L1, L2, and L3 loops are rendered in yellow, beige, and purple, respectively. The carbon atoms of other residues interacting with H3.1 are highlighted in green. Carbon atoms of H3.1 residues are colored in orange, whereas oxygen and nitrogen atoms are highlighted in red and blue. Hydrogen bonds and water molecules are illustrated as red dashed lines and red spheres, respectively. (**C**) Simulated annealing $F_o - F_c$ omit map (green) contoured at 2σ. The H3.1 peptide is rendered as in (A).

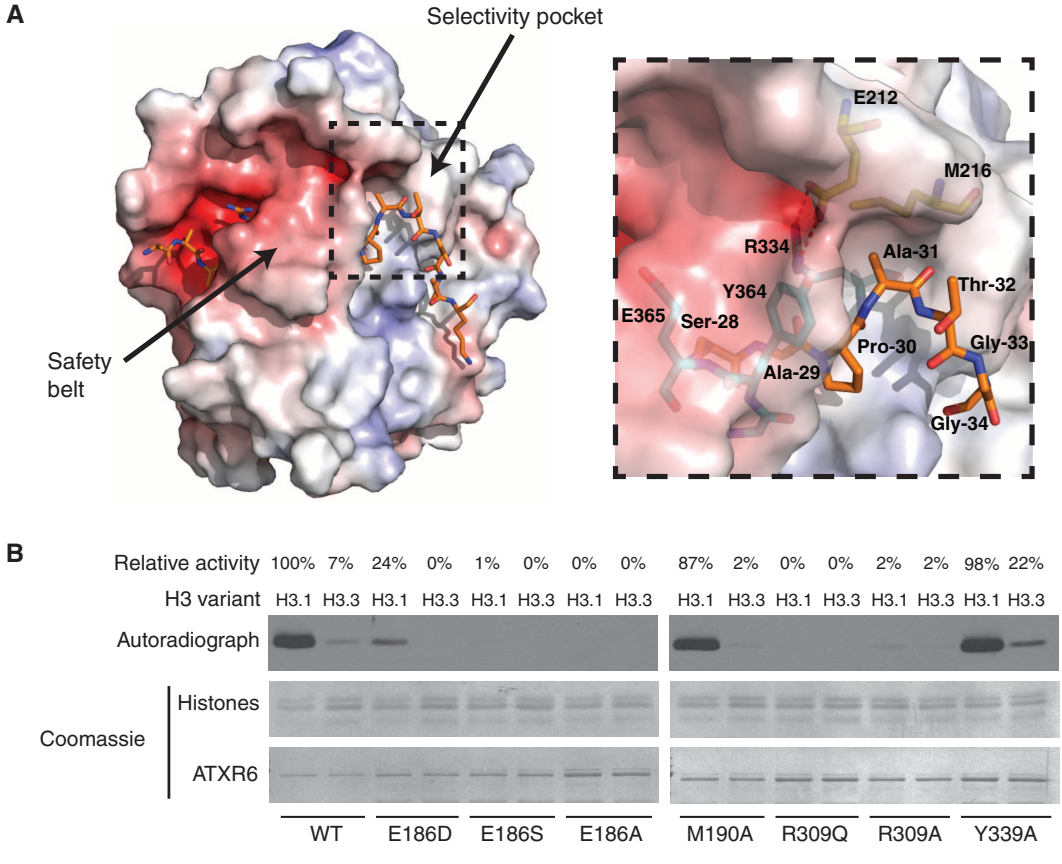

Fig. 3. The selectivity pocket and safety belt of ATXR5/6-type H3K27 methyltransferases are responsible for H3.1 preference over H3.3. (**A**) The structure of the ATXR5-H3.1-SAH complex in electrostatic potential surface representation, with the selectivity pocket and safety belt highlighted. Positive and negative potentials are in blue and red, respectively. Inlet figure shows a zoomed view of the residues forming the surface of the selectivity pocket (three-letter code refers to histone H3.1 residues). Hydrogen bonds are shown as dashed red lines. (**B**) In vitro HKM assay using recombinant chromatin containing plant H3.1 or H3.3 as substrates and WT or point mutants of ATXR6 from *A. thaliana*. The enzymatic activity indicated for each reaction is relative to the activity of ATXR6 (WT) on H3.1 nucleosomes.

the heterochromatic defects of CAF-1 mutants in *Arabidopsis* could be due, at least in part, to depletion of K27me1 when H3.3 replaces H3.1. Our results show that H3K27me1 levels are indeed lower in *fasciata2* (*fas2* encodes a subunit of CAF-1) mutants compared with Col, and this is not caused by defects in nucleosome density or antibody preference for H3.1K27me1 over H3.3K27me1 (figs. S9 and S10).

One of the phenotypes associated with reduced levels of H3K27me1 in *atxr5 atxr6* double mutants is overreplication of heterochromatic DNA (*4*). Lower levels of H3K27me1 in *fas2* mutants or our transgenic lines expressing H3.1 A31T is not accompanied by a similar defect in heterochromatic DNA replication (Fig. 4C and figs. S11 and S12) (*19*, *24*–*26*). This suggests a model in which unmethylated H3 having alanine at position 31 (i.e., H3.1K27me0) allows for heterochromatic overreplication to occur. One prediction from this model is that heterochromatic overreplication should be suppressed in a *fas2* mutant background, because H3.1K27me0 would now be replaced by H3.3K27me0. As predicted, the phenotype is strongly suppressed in *atxr5 atxr6 fas2* triple mutants (Fig. 4C). This model also provides an explanation for the partial suppression of the heterochromatic overreplication phenotype of *atxr5 atxr6* by mutations affecting DNA methylation (*5*). H3.3 is known to replace H3.1 at transcribed genes in plants and animals (*7*–*9*, *11*, *15*, *16*). Because loss of DNA methylation leads to the transcriptional activation of normally silent loci (*27*), DNA methylation mutants (similar to *fas2* mutants) would replace H3.1 with H3.3 in heterochromatin. Accordingly, suppression of overreplication is strongest in the DNA methylation mutants that have the greatest effect on transcriptional reactivation (*5*). Taken together, our results suggest a model in which H3.1K27me0 is the stimulus for heterochromatic overreplication.

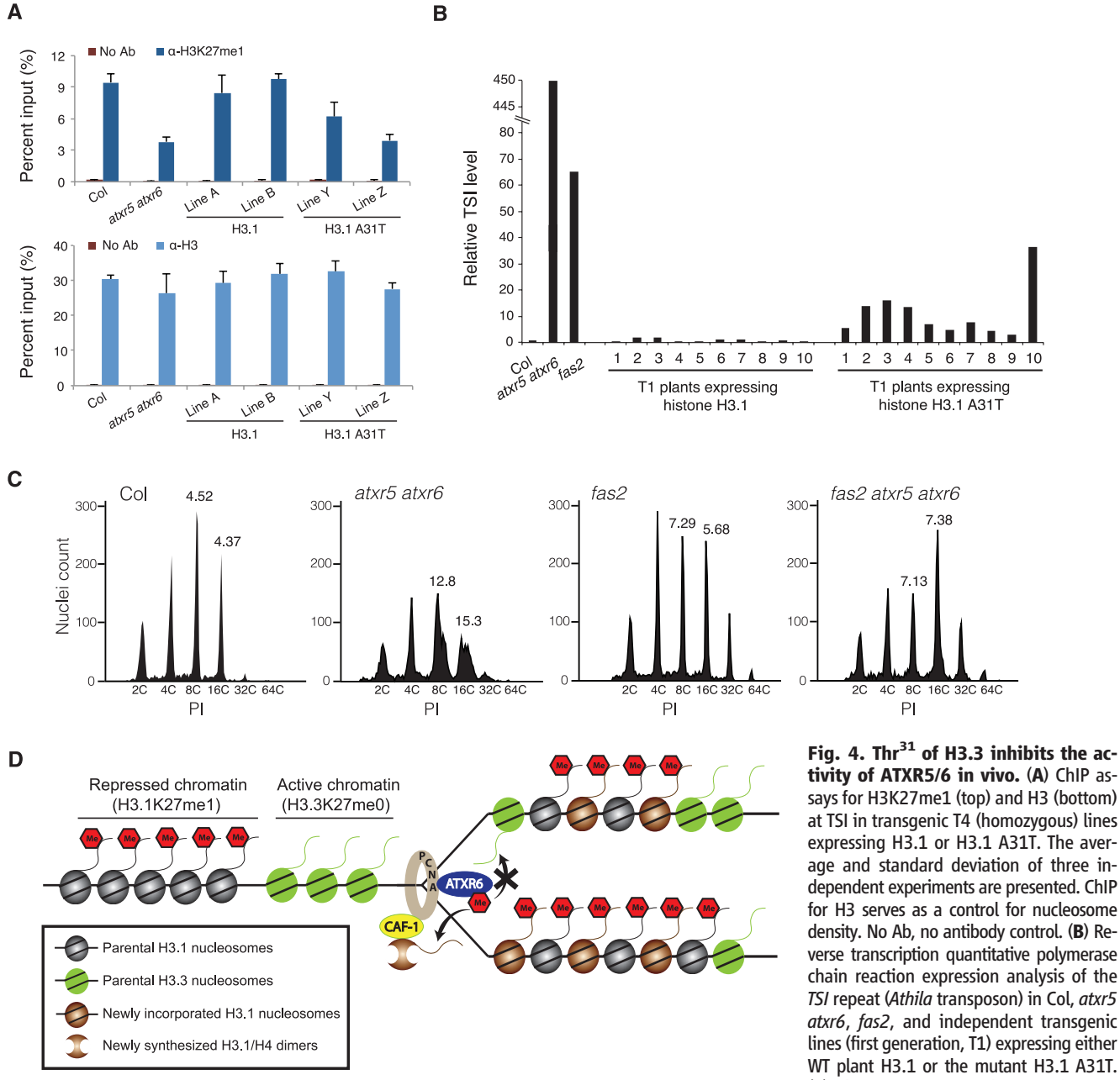

Fig. 4. Thr^{31} of H3.3 inhibits the activity of ATXR5/6 in vivo. (**A**) ChIP assays for H3K27me1 (top) and H3 (bottom) at TSI in transgenic T4 (homozygous) lines expressing H3.1 or H3.1 A31T. The average and standard deviation of three independent experiments are presented. ChIP for H3 serves as a control for nucleosome density. No Ab, no antibody control. (**B**) Reverse transcription quantitative polymerase chain reaction expression analysis of the *TSI* repeat (*Athila* transposon) in Col, *atxr5 atxr6*, *fas2*, and independent transgenic lines (first generation, T1) expressing either WT plant H3.1 or the mutant H3.1 A31T. (**C**) Flow cytometry profiles of Col, *atxr5 atxr6*, *fas2*, and *fas2 atxr5 atxr6* leaf nuclei. The numbers below the peaks indicate the endoreduplication (ploidy) levels of the nuclei. The numbers above the 8C and 16C peaks correspond to the robust CV values [propidium iodide (PI) units that enclose the central 68% of nuclei] for those peaks. High robust CV values at 8C and 16C peaks characterize heterochromatic over-replication (*4*). (**D**) Model for the role of ATXR5/6 during DNA replication in plants. Me, methyl group.

Overall, this study demonstrates how histone variants can determine epigenetic states through direct modulation of chromatin-modifying enzyme activity. Further, the ability of ATXR5/6 to discriminate between the variants H3.3 and H3.1 provides a mechanism for the mitotic inheritance and genome-wide distribution of H3K27me1 in plants. According to this model, ATXR5/6 are recruited to the replication fork during S phase through their interaction with PROLIFERATING CELL NUCLEAR ANTIGEN (PCNA) (*2*), where they specifically monomethylate K27 at newly incorporated, CAF-1–dependent H3.1 to rapidly restore this epigenetic mark (Fig. 4D) and prevent overreplication. This model does not rule out the possibility that some H3.1 might escape DNA replication–coupled K27 monomethylation (fig. S5). The inability of ATXR5/6 to methylate H3.3 may contribute to the protection of transcriptionally active, H3.3-enriched regions against H3K27me1 and repression during DNA replication.

References and Notes

1. C. Alabert, A. Groth, *Nat. Rev. Mol. Cell Biol.* **13**, 153–167 (2012).
2. C. Raynaud *et al.*, *Plant J.* **47**, 395–407 (2006).
3. Y. Jacob *et al.*, *Nat. Struct. Mol. Biol.* **16**, 763–768 (2009).
4. Y. Jacob *et al.*, *Nature* **466**, 987–991 (2010).
5. H. Stroud *et al.*, *PLOS Genet.* **8**, e1002808 (2012).
6. S. Smith, B. Stillman, *Cell* **58**, 15–25 (1989).
7. H. Tagami, D. Ray-Gallet, G. Almouzni, Y. Nakatani, *Cell* **116**, 51–61 (2004).
8. B. E. Schwartz, K. Ahmad, *Genes Dev.* **19**, 804–814 (2005).
9. A. D. Goldberg *et al.*, *Cell* **140**, 678–691 (2010).
10. P. Drané, K. Ouararhni, A. Depaux, M. Shuaib, A. Hamiche, *Genes Dev.* **24**, 1253–1265 (2010).
11. K. Ahmad, S. Henikoff, *Mol. Cell* **9**, 1191–1200 (2002).
12. A. Loyola, G. Almouzni, *Trends Biochem. Sci.* **32**, 425–433 (2007).
13. S. Henikoff, K. Ahmad, *Annu. Rev. Cell Dev. Biol.* **21**, 133–153 (2005).
14. Y. Mito, J. G. Henikoff, S. Henikoff, *Nat. Genet.* **37**, 1090–1097 (2005).
15. H. Stroud *et al.*, *Proc. Natl. Acad. Sci. U.S.A.* **109**, 5370–5375 (2012).
16. H. Wollmann *et al.*, *PLOS Genet.* **8**, e1002658 (2012).
17. L. Johnson *et al.*, *Nucleic Acids Res.* **32**, 6511–6518 (2004).
18. N. Schönrock, V. Exner, A. Probst, W. Gruissem, L. Hennig, *J. Biol. Chem.* **281**, 9560–9568 (2006).
19. A. Kirik, A. Pecinka, E. Wendeler, B. Reiss, *Plant Cell* **18**, 2431–2442 (2006).
20. L. Hennig, P. Taranto, M. Walser, N. Schönrock, W. Gruissem, *Development* **130**, 2555–2565 (2003).
21. T. Ono *et al.*, *Genes Cells* **11**, 153–162 (2006).
22. S. Takeda *et al.*, *Genes Dev.* **18**, 782–793 (2004).
23. D. Ray-Gallet *et al.*, *Mol. Cell* **44**, 928–941 (2011).
24. M. Endo *et al.*, *EMBO J.* **25**, 5579–5590 (2006).
25. V. Exner, P. Taranto, N. Schönrock, W. Gruissem, L. Hennig, *Development* **133**, 4163–4172 (2006).
26. E. Ramirez-Parra, C. Gutierrez, *Plant Physiol.* **144**, 105–120 (2007).
27. M. Rigal, O. Mathieu, *Biochim. Biophys. Acta* **1809**, 452–458 (2011).

Acknowledgments: We thank J. Calarco for critically reading the manuscript and J. Goodrich, C. Kohler, S. E. Jacobsen, D. J. Patel, and T. Schalch for materials and advice. Y.J. was supported by a Louis-Berlinguet postdoctoral fellowship (Fonds Québécois de la Recherche en Santé/Génome Québec). P.V. is supported by fellowships from the Deutsche Akademie der Naturforscher Leopoldina (LPDS 2009-5) and the Empire State Training Program in Stem Cell Research (NYSTEM, contract no. C026880). Work in the Reinberg laboratory is supported by grants from the NIH (GM064844 and R37GM037120) and the Howard Hughes Medical Institute. S.D.M. is supported by a grant from the NIH (GM075060). J.F.C. is supported by grants from the Canadian Institute of Health Research (BMA-355900) and the Natural Sciences and Engineering Research Council of Canada (Discovery Grant 191666) and acknowledges an Ontario Early Research Award and a Canada Research Chair in Structural Biology and Epigenetics. This work was supported by the Howard Hughes Medical Institute–Gordon and Betty Moore Foundation and by grants from the NSF (DBI-1025830) and the NIH (GM067014) to R.A.M. R.A.M. acknowledges a Chaire Blaise Pascal (Region Ile-de-France) at IBENS, Paris. The Protein Data Bank (PDB) accession number for the RcATXR5-H3.1-AdoHcy ternary structure is 4O30.pdb.

Supplementary Materials

www.sciencemag.org/content/343/6176/1249/suppl/DC1
Materials and Methods
Supplementary Text
Figs. S1 to S12
Table S1
References (*28*–*40*)

11 November 2013; accepted 12 February 2014
10.1126/science.1248357

Vertebrate Limb Bud Formation Is Initiated by Localized Epithelial-to-Mesenchymal Transition

Jerome Gros* and Clifford J. Tabin†

Vertebrate limbs first emerge as small buds at specific locations along the trunk. Although a fair amount is known about the molecular regulation of limb initiation and outgrowth, the cellular events underlying these processes have remained less clear. We show that the mesenchymal limb progenitors arise through localized epithelial-to-mesenchymal transition (EMT) of the coelomic epithelium specifically within the presumptive limb fields. This EMT is regulated at least in part by *Tbx5* and *Fgf10*, two genes known to control limb initiation. This work shows that limb buds initiate earlier than previously thought, as a result of localized EMT rather than differential proliferation rates.

In 1971, Searls and Janners found that, at early limb stages (Hamburger-Hamilton stage 17 to 18 in the chick), there is a substantial decrease in proliferation of the flank mesoderm, whereas higher rates are maintained within the emerging vertebrate limb buds. Accordingly, they proposed that localized regulation of proliferation at specific levels along the body axis is responsible for limb initiation (*1*). However, the cellular properties of the somatopleural lateral plate cells that give rise to the limb bud have not been identified.

During gastrulation, the mesodermal germ layer is formed through the generation of mesenchymal cells from the epithelial epiblast. However, shortly after gastrulation a reepithelization occurs such that essentially the entire embryo is epithelial, as defined by apical (F-actin) and basal (laminin) epithelial markers: Not only are the ectoderm, neural tube, and endoderm epithelial, but also the notochord, the somites, the intermediate mesoderm and the lateral plate mesoderm (i.e., splanchnopleural and somatopleural mesoderm, Fig. 1, A and D). At stage 13 in the chick, before any signs of limb bud formation, the somatopleure displays epithelial rather than mesenchymal characteristics. Molecular characterization revealed that, at this stage, F-actin and N-cadherin, as well as β-catenin and atypical protein kinase C (aPKC), localize at the apical end of somatopleure cells (Fig. 1, A and D, and fig. S1, A and D). On the other hand, vimentin is localized at the basal end of somatopleural cells, and laminin is deposited only on the basal side (Fig. 1, A and D, and fig. S1A), demonstrating that at early stages the somatopleure is a single cell layer and highly polarized, pseudostratified columnar epithelium. These observations differ from the previous assumption that limbs originate from a preexisting mesenchymal population. Forelimb bud mesenchyme first becomes apparent at stage 14 to 15, whereas the more posterior hindlimb mesenchyme can be first observed only at stage 15 to 16, as revealed by enrichment of vimentin expression and a concomitant loss of polarized localization of N-cadherin, β-catenin, F-actin, and aPKC within somatopleural cells and basement membrane of laminin breakdown (Fig. 1, B and E, and fig. S1, B, C, E, and F). Furthermore, mesenchyme in the trunk region is only seen at stage 17, long after forelimb and hindlimb mesenchymes have emerged (Fig. 1, C and F, and fig. S2), and thus out of order relative to the general rostral-caudal wave of development

Department of Genetics, Harvard Medical School, 77 Avenue Louis Pasteur, Boston, MA 02115, USA.

*Present address: Department of Developmental and Stem Cell Biology, Institut Pasteur, 25, 28 rue du Docteur Roux, 75724 Paris, Cedex 15, France.

†Corresponding author. E-mail: tabin@genetics.med.harvard.edu

along the body axis, indicating specific regulation is involved in this timing. Similar results were found for the mouse (fig. S3).

Because the somatopleural lateral plate mesoderm of the limb field starts out as an epithelium and ultimately generates limb bud mesenchyme, one would expect that this occurs through an epithelial-mesenchymal transition (EMT) process. To directly demonstrate this, we performed lineage analysis with an electroporated green fluorescent protein (GFP) reporter in chick embryos. We found that, 3 hours after electroporation, each GFP electroporated cell exhibited a bottlelike epithelial shape (Fig. 1G and fig. S4A) and localized expression of apical N-cadherin, β-catenin, aPKC, and basal vimentin (fig. S4, D, E, H, I, L, M, P, and Q). After 12 and 24 hours, although some GFP-labeled cells could still be seen in an epithelial state, the vast majority of GFP-labeled cells had left the epithelium and displayed mesenchymal characteristics (Fig. 1, H and I, and fig. S4, B, C, F, G, J, K, N, O, R, and S), demonstrating that most if not all all mesenchymal cells of the limb bud originate from the epithelial somatopleure (Fig. 1I).

Although EMT is delayed in the trunk relative to the limb-forming regions, ultimately it is necessary to generate the ventral dermis of the body wall. Therefore, we quantified the extent of EMT process occurring in each of these regions. To this end, we electroporated the somatopleure of both the forelimb and the trunk level of stage-13 chick embryos and quantified the number of GFP-positive cells in the epithelial and mesenchymal state. We found that the somatopleure at the forelimb level generates 5.5 times more mesenchymal than epithelial cells, whereas at the trunk level the number of mesenchymal cells that emerge from the somatopleure is nearly equal to the number of epithelial cells (Fig. 1J). These quantifications show that a precocious and sustained EMT process generates the limb primordium, as opposed to the trunk region in which a delayed and less-efficient EMT generates only the minimal amount of mesenchymal cells that will eventually contribute to the dermis of the trunk (*2*).

Limb bud initiation has previously been described to be the consequence of differential proliferation between limb and trunk regions starting at stage 17 (*1*). However, our data indicated that EMT, resulting in localized production of limb mesenchyme, begins before proliferation starts. Therefore, we decided to revisit the timing of proliferative changes in the lateral plate mesoderm using more modern approaches: automated cell counting of proliferative cells labeled by using 5-bromo-2′-deoxyuridine (BrdU) as opposed to manual counting of tritiated thymidine–labeled cells in the Searls and Janners study. Our study confirmed that proliferation starts to decrease at about stage 17 to 18 in the trunk and that it remains sustained at a high level in the limb region (Fig. 1K). However, at stage 15 to 16, as mesenchyme is being generated, proliferation is uniform throughout the lateral plate mesoderm, including both the trunk and limb-forming fields (Fig. 1K).

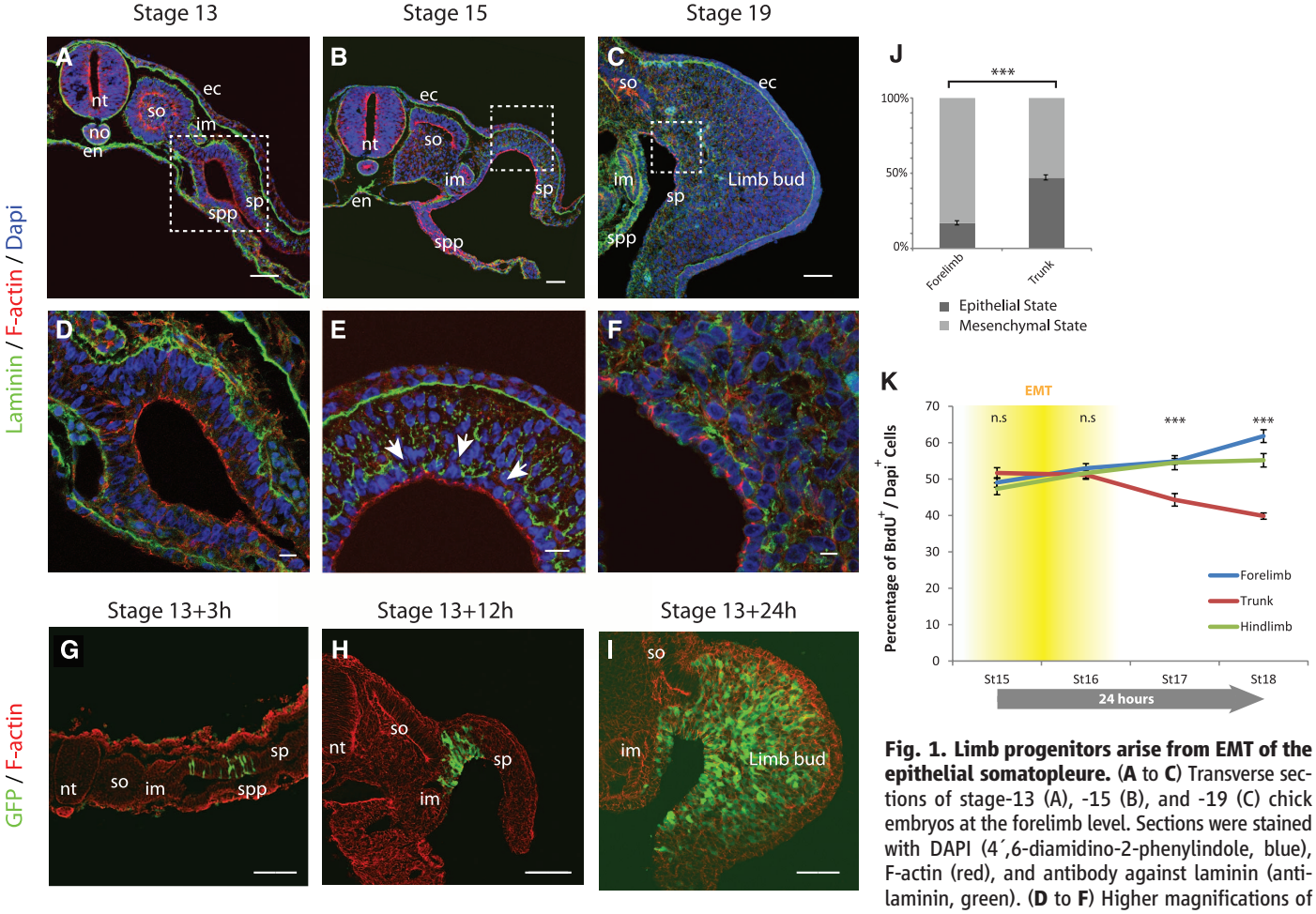

Fig. 1. Limb progenitors arise from EMT of the epithelial somatopleure. (**A** to **C**) Transverse sections of stage-13 (A), -15 (B), and -19 (C) chick embryos at the forelimb level. Sections were stained with DAPI (4′,6-diamidino-2-phenylindole, blue), F-actin (red), and antibody against laminin (anti-laminin, green). (**D** to **F**) Higher magnifications of (A) to (C); arrows point at laminin basement membrane breakdown. (**G** to **I**) Transverse sections of chick embryos electroporated at stage 13 and harvested after 3, 12, and 24 hours. Sections were stained with phalloidin (red) and with anti-GFP (green). (**J**) Proportion of cells in epithelial or mesenchymal state at forelimb and trunk levels ($n = 3723$ cells, five embryos; Mann-Whitney U test $^{***}P = 2.4 \times 10^{-9}$). (**K**) Percentage of proliferating cells (BrdU+/DAPI+) in the somatopleure of chick embryos at stages 15 to 18 at the level of the forelimb (blue), trunk (red), and hindlimb (green) ($n = 5$ embryos for each stage; over 250,000 cells were counted in total; Mann-Whitney U test; n.s, nonsignificant $P > 0.05$; $^{***}P < 10^{-7}$). The timing of EMT in relation to proliferation is represented in yellow. Errors bars indicate SEM. Scale bars represent 10 μm in (D) to (F) and 50 μm elsewhere. nt, neural tube; no, notochord; en, endoderm; so, somite; im, intermediate mesoderm; ec, ectoderm; spp, splanchnopleure; sp, somatopleure.

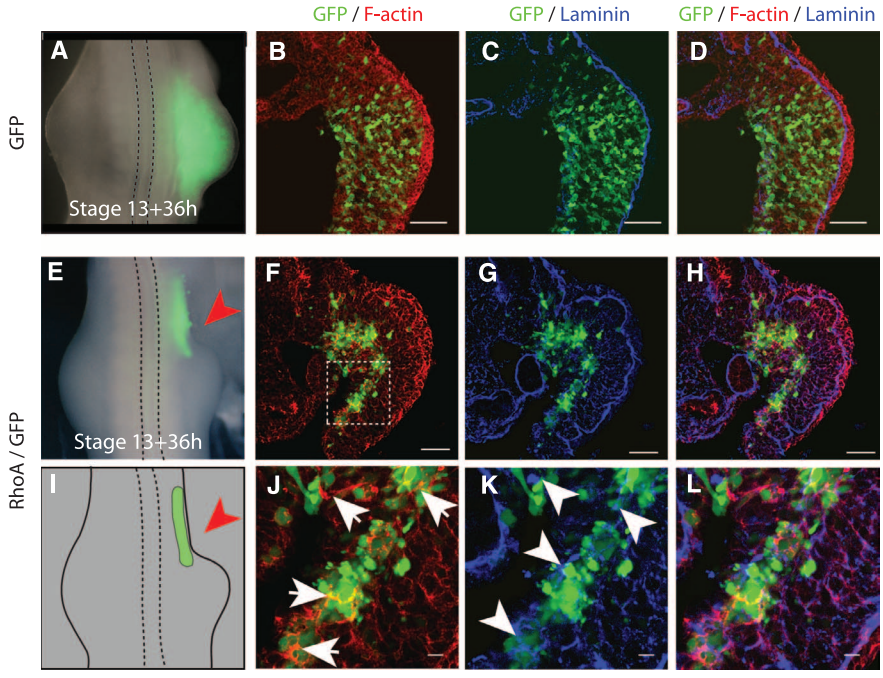

Fig. 2. EMT of the somatopleure is a necessary step in limb bud initiation. (**A** and **E**) Dorsal views of stage-21 chick embryos 36 hours after electroporation of GFP or GFP/RhoA. (**B** to **D** and **F** to **H**) Transverse sections of chick embryos electroporated with GFP or GFP/RhoA at the forelimb level and stained with phalloidin (red), GFP (green), and anti-laminin (blue). (**J** to **L**) Higher magnification of (F) to (L); note the overstabilization of F-actin (arrows) and the presence of large aggregates of laminin (arrowheads). (**I**) Cartoon representing the extent of RhoA/GFP electroporation as shown in (E) and highlighting the absence of limb formation in the RhoA-electroporated region, red arrow. Scale bars, 10 μm in (J) to (L) and 50 μm elsewhere.

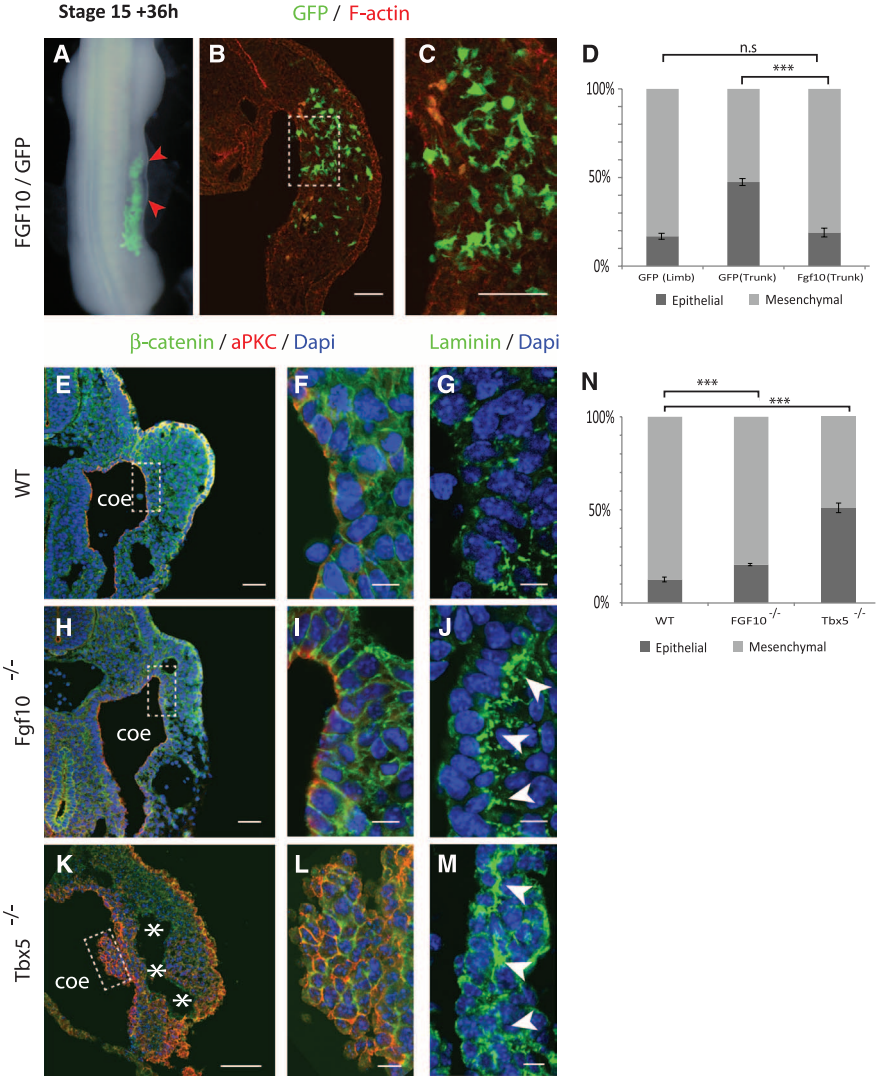

Fig. 3. Tbx5/FGF10 participates in the regulation of the EMT of the somatopleure. (**A**) FGF10/GFP-electroporated chick embryos showing ectopic swellings (red arrowheads). (**B** and **C**) Transverse section of FGF10/GFP electroporated embryo; (C) is a higher magnification of (B). (**D**) Proportion of cells in mesenchymal or epithelial state [$n = 1912$ (FGF10/GFP), three embryos; Mann-Whitney U test $^{***}P < 0.0001$; n.s, non-significant, $P = 0.38$]. (**E**, **H**, and **K**) Transverse sections of mouse embryos at the forelimb level stained with DAPI (blue), β-catenin (green), and aPKC (red) antibody. (**F**, **I**, and **L**) Higher magnifications of boxed areas in (E), (H), and (K). (**G**, **J**, and **M**) Transverse sections stained with DAPI (blue) and anti-laminin (green) focusing on the somatopleure epithelium and basement membrane stabilization (arrowheads). (**N**) Proportion of cells in mesenchymal or epithelial state [$n = 2962$ (WT), 10,894 ($Tbx5^{-/-}$), and 3115 ($FGF10^{-/-}$) cells, three embryos for each genotype; Mann-Whitney U test $^{***}P < 0.0001$]. Scale bars represent 50 μm in (B), (C), (E), (H), and (K) and 10 μm in (F), (I), (L), (G), (J), and (M). Coe, coelomic cavity; asterisks, separation between epithelium and mesenchyme.

Together with the lineage analysis, these observations strongly suggest that the limb bud initiates earlier than stage 17 to 18, through EMT and independent of proliferation rate changes. When the limb bud mesenchyme is generated, it induces a source of fibroblast growth factor (Fgf) activity in the overlying ectoderm, the apical ectoderm ridge, which serves to maintain the limb's high level of proliferation (*3*). This does not occur in the trunk region, which we hypothesize is the reason for its relative decrease in mitotic activity as mesenchyme is generated. We suggest that the difference in proliferation of trunk versus limb bud mesenchyme is a result of limb bud initiation, as opposed to being a cause of it.

To verify that EMT of the somatopleure represents a necessary step of limb initiation, we blocked EMT in the presumptive limb region by RhoA overexpression, which abrogates EMT by inducing strong interaction of cells with extracellular matrix components (*4*). We electroporated RhoA with GFP within the epithelial somatopleure. In control embryos electroporated with GFP alone, limb buds formed normally (Fig. 2A), the basement membrane of laminin broke down, and cells underwent EMT (Fig. 2, B to D). In contrast, coelectroporation of RhoA with GFP completely abrogated limb formation (Fig. 2, E and I). Sections revealed that RhoA electroporated cells were stuck in the epithelial somatopleure and failed to undergo proper EMT (Fig. 2, F to H). These cells were attached to aggregates of laminin (Fig. 2, K and L) and did not exhibit enrichment in vimentin staining (fig. S5, G to L). We found that RhoA-overexpressing cells overexpressed F-actin, maintained adherens junction as revealed by N-cadherin and β-catenin stainings (fig. S5, A to L), and failed to relocalize aPKC from their apical cortex to the cytoplasm (fig. S5, A to F) as observed in control GFP-electroporated cells (fig. S4, N, O, R, and S). RhoA overexpression did not lead to dramatic reduction of proliferation (fig. S6, A to C) or increase in apoptosis in the electroporated cells (fig. S6, D to G), confirming that RhoA acts to prevent epithelial-to-mesenchymal cell state change. Thus as a consequence of this failure to undergo EMT, the electroporated cells did not participate in the initiation and formation of the limb primordium.

To understand how EMT is regulated in this context, we explored the possibility that Snail1, a transcription factor upstream of EMT in other contexts (*5*), plays a similar role here, but (perhaps because of redundancy) we failed to find such a connection. We therefore turned to factors known to be involved in establishing the formation of a limb bud. Ectopic Fgf protein, applied up to stage 17, is sufficient to induce the formation of an entire additional limb from trunk tissue (*6*). To test whether Fgf10 promotes limb formation by inducing EMT, we coelectroporated Fgf10 and GFP into the trunk somatopleure of stage-13 to -14 chick embryos. As expected, 36 hours after electroporation Fgf10 induced swelling of the trunk, indicating ectopic limb initiation (Fig. 3A, red arrowheads). Sectioning through the electroporated region showed that most of the GFP-positive cells had left the epithelium and had acquired a mesenchymal phenotype (81%, Fig. 3, B to D), showing that indeed EMT had taken place. The trunk is only competent to form an ectopic limb up to stage 16 to 17 (*7*, *8*). This was previously interpreted as the time at which the trunk mesenchyme becomes determined and is no longer capable of being redirected to a limb fate. However, our data show that this is precisely the time at which the trunk mesenchyme is first generated. Thus, we would reinterpret those results as indicating that ectopic Fgf activity can induce limb bud formation from epithelial trunk somatopleure cells but not from mesenchymal cells of the same rostrocaudal level.

Targeted mutation of Fgf10 and Tbx5 in mice have demonstrated that these genes are necessary to initiate limb bud formation (*9*–*12*). Transverse sections of embryonic day 9.5 *Fgf10*$^{-/-}$ and *Tbx5*$^{-/-}$ embryos confirmed that neither Tbx5 nor Fgf10 mutant embryos exhibit swellings characteristic of limb bud initiation (Fig. 3, E, H, and K). Both FGF10 and Tbx5 mutant embryos showed the presence of mesenchyme in the forelimb region; however, the proportion of mesenchymal cells compared to the proportion of epithelial cells was significantly lower than that of a wild-type (WT) sibling embryo (Fig. 3N), with a stronger phenotype observed in Tbx5$^{-/-}$ embryos (only 12% of cells were epithelial in WT embryos, whereas 21% and 51% were epithelial in Fgf10- and Tbx5-deficient embryos, respectively). In Tbx5 mutant embryos, the epithelium appeared separated from the mesenchyme (Fig. 3K, asterisks). aPKC and β-catenin staining revealed hyperplasia of the somatopleure epithelium, in support of failure of these cells to undergo EMT (Fig. 3, K and L). Last, in Fgf10$^{-/-}$ as well as in Tbx5$^{-/-}$ embryos, the basement membrane of laminin did not properly break down and appeared overstabilized, as opposed to WT embryos (Fig. 3, F, G, I, J, L, and M). Taken together, these data show that Tbx5 and Fgf10 act on the somatopleure epithelium to regulate, at least partially, the early induction of EMT in the limb fields, the process that is at the heart of limb bud initiation.

References and Notes

1. R. L. Searls, M. Y. Janners, *Dev. Biol.* **24**, 198–213 (1971).
2. A. Mauger, *J. Embryol. Exp. Morphol.* **28**, 313–341 (1972).
3. H. Ohuchi *et al.*, *Development* **124**, 2235–2244 (1997).
4. Y. Nakaya, E. W. Sukowati, Y. Wu, G. Sheng, *Nat. Cell Biol.* **10**, 765–775 (2008).
5. J. P. Thiery, H. Acloque, R. Y. J. Huang, M. A. Nieto, *Cell* **139**, 871–890 (2009).
6. M. J. Cohn, J. C. Izpisúa-Belmonte, H. Abud, J. K. Heath, C. Tickle, *Cell* **80**, 739–746 (1995).
7. H. Ohuchi *et al.*, *Biochem. Biophys. Res. Commun.* **209**, 809–816 (1995).
8. A. Vogel, C. Rodriguez, J. C. Izpisúa-Belmonte, *Development* **122**, 1737–1750 (1996).
9. P. Agarwal *et al.*, *Development* **130**, 623–633 (2003).
10. C. Rallis *et al.*, *Development* **130**, 2741–2751 (2003).
11. H. Min *et al.*, *Genes Dev.* **12**, 3156–3161 (1998).
12. K. Sekine *et al.*, *Nat. Genet.* **21**, 138–141 (1999).

Acknowledgments: We thank F. Constantini for help rederiving the Fgf10 mutant mouse line, B. Bruneau for kindly providing Tbx5 mutant embryos, and J. deMelo and P. Tschopp for help with mouse work. J.G. was a fellow of the Human Frontier Science Program. This work was supported by NIH grant R01-HD045499 to C.J.T.

Supplementary Materials

www.sciencemag.org/content/343/6176/1253/suppl/DC1
Materials and Methods
Supplementary Text
Figs. S1 to S6
Reference (*13*)

7 November 2013; accepted 7 February 2014
10.1126/science.1248228

The *stum* Gene Is Essential for Mechanical Sensing in Proprioceptive Neurons

Bela S. Desai, Abhishek Chadha, Boaz Cook*

Animal locomotion depends on proprioceptive feedback, which is generated by mechanosensory neurons. We performed a genetic screen for impaired walking in *Drosophila* and isolated a gene, *stumble* (*stum*). The Stum protein has orthologs in animals ranging from nematodes to mammals and is predicted to contain two transmembrane domains. Expression of the mouse orthologs of *stum* in mutant flies rescued their phenotype, which demonstrates functional conservation. Dendrites of *stum*-expressing neurons in legs were stretched by both flexion and extension of corresponding joints. Joint angles that induced dendritic stretching also elicited elevation of cellular Ca^{2+} levels—not seen in *stum* mutants. Thus, we have identified an evolutionarily conserved gene, *stum*, which is required for transduction of mechanical stimuli in a specific subpopulation of *Drosophila* proprioceptive neurons that sense joint angles.

Animal locomotion is achieved by coordination of motor activity according to proprioceptive mechanosensory inputs. In *Drosophila*, mechanosensation is mediated either by ciliated or multidendritic receptor neurons. Multidendritic neurons can respond to direct

application of mechanical force to their membranes (*1*, *2*). It is less clear, however, how multidendritic mechanosensory neurons can be tuned to one mechanical modality, such as joint angle, and disregard other mechanical stimuli that may originate from external impacts or changes in the shape of muscles during contraction. In order to identify genes involved in proprioceptive sensation, we screened for uncoordination in a collection of ethyl methanesulfonate–mutagenized *Drosophila* lines (*3*). Lines that exhibited walking impairments were selected, and the phenotype severity was quantified by measuring climbing speed. We identified three lines, 204, 922, and 4487, that showed lack of coordination in homozygous flies and did not complement one another (Fig. 1A), which suggested that they represent alleles of the same gene. Two of the lines, 204 and 4487, showed severe uncoordination, and the phenotype in 922 was mild (Fig. 1A). Deficiency mapping pointed to a gene, *CG30263* (Fig. 1B), predicted to encode a large protein with 1870 or 1959 amino acids (depending on the splice variant). Because the mutants had a walking impairment phenotype, we named this gene *stumble* (*stum*). The *stum* ortholog in humans is *C1orf95*, and it was categorized as a member of the SPEC3 family (UNIPROT, INTERPRO), with unknown function. We sequenced the *stum* gene in the three mutant lines and found that $stum^{204}$, $stum^{4487}$, and $stum^{922}$ had stop codons at amino acid positions 171, 202, and 1081, respectively (Fig. 1C).

We generated transgenic flies that express *stum* cDNA in neurons and found that the *stum*

Department of Molecular and Cellular Neuroscience, The Scripps Research Institute, La Jolla, CA 92037, USA.
*Corresponding author. E-mail: bcook@scripps.edu

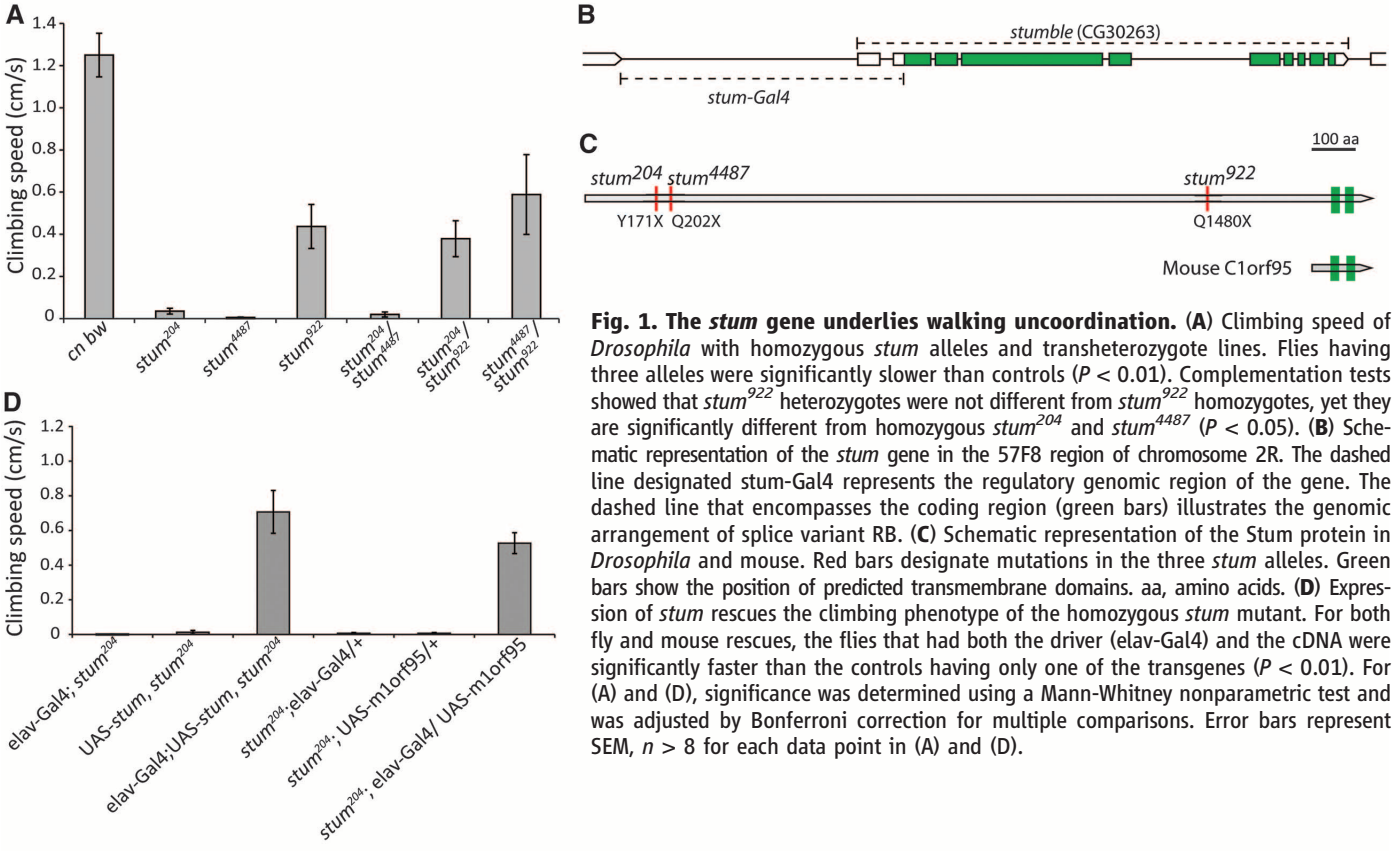

Fig. 1. The *stum* gene underlies walking uncoordination. (**A**) Climbing speed of *Drosophila* with homozygous *stum* alleles and transheterozygote lines. Flies having three alleles were significantly slower than controls ($P < 0.01$). Complementation tests showed that $stum^{922}$ heterozygotes were not different from $stum^{922}$ homozygotes, yet they are significantly different from homozygous $stum^{204}$ and $stum^{4487}$ ($P < 0.05$). (**B**) Schematic representation of the *stum* gene in the 57F8 region of chromosome 2R. The dashed line designated stum-Gal4 represents the regulatory genomic region of the gene. The dashed line that encompasses the coding region (green bars) illustrates the genomic arrangement of splice variant RB. (**C**) Schematic representation of the Stum protein in *Drosophila* and mouse. Red bars designate mutations in the three *stum* alleles. Green bars show the position of predicted transmembrane domains. aa, amino acids. (**D**) Expression of *stum* rescues the climbing phenotype of the homozygous *stum* mutant. For both fly and mouse rescues, the flies that had both the driver (elav-Gal4) and the cDNA were significantly faster than the controls having only one of the transgenes ($P < 0.01$). For (A) and (D), significance was determined using a Mann-Whitney nonparametric test and was adjusted by Bonferroni correction for multiple comparisons. Error bars represent SEM, $n > 8$ for each data point in (A) and (D).

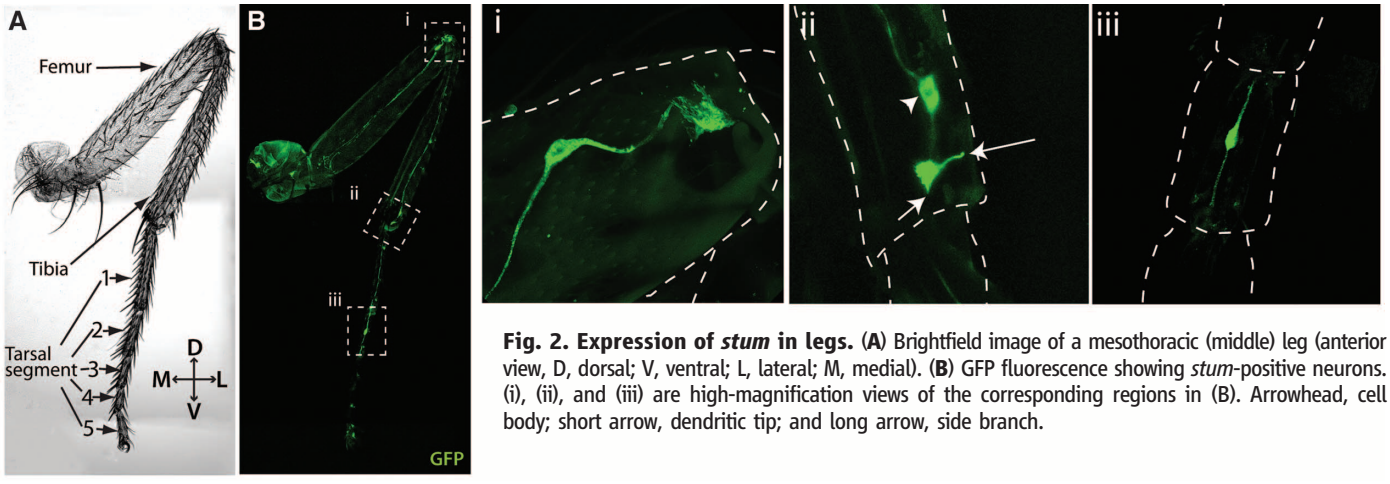

Fig. 2. Expression of *stum* in legs. (**A**) Brightfield image of a mesothoracic (middle) leg (anterior view, D, dorsal; V, ventral; L, lateral; M, medial). (**B**) GFP fluorescence showing *stum*-positive neurons. (i), (ii), and (iii) are high-magnification views of the corresponding regions in (B). Arrowhead, cell body; short arrow, dendritic tip; and long arrow, side branch.

phenotype was partially rescued (Fig. 1D), which indicated that the mutations in *stum* were underlying the uncoordination phenotype. We noted that the mouse ortholog of *stum* (National Center for Biotechnology Information, the U.S. National Institutes of Health, reference sequence: NP_001074696.1), which is only 141 amino acids long and shares 33% sequence identity with *Drosophila stum*, was also able to substantially rescue the uncoordination phenotype (Fig. 1D). Therefore, the function of *stum* appears to be conserved between distant animal species. Moreover, the rescue of the phenotype with such a short form of *stum* suggests that the C-terminal region of the fly protein constitutes the functional core.

Proprioceptive defects in adult flies have been attributed to malfunction of type I (ciliated) mechanoreceptor neurons (*4*–*6*). To test whether such defects also underlie the phenotype in the *stum* mutant, we performed electrophysiological recordings of mechanical responses from the ciliated mechanoreceptor neuron of the anterior notopleural bristle (*6*). Type I neurons of *stum* mutants were indistinguishable from controls (fig. S1). Therefore, unlike known proprioception mutants, the phenotype in *stum* mutants does not arise from a general defect in type I mechanoreceptor neurons. To identify which cells give rise to the phenotype, we used the genomic regulatory region of *stum* to drive a CD8 fused to green fluorescent protein (CD8GFP) reporter [*stum*-Gal4 driving the upstream activation sequence (UAS)–CD8GFP]. We found that *stum* expression in the legs was localized to three labeled neurons: one at the femur-tibia joint, the second at the tibia-tarsus joint, and the third spanning the second tarsal segment (Fig. 2). The cell bodies of these *stum*-expressing neurons were located near the distal end of each leg segment, and their dendrites terminated at the corresponding joints (Fig. 2).

To study whether there are *stum*-expressing cells within the ventral nerve cord (VNC), we examined it in flies that express CD8GFP using *stum*-Gal4. We found that the only fluorescent signal in the VNC originated from the axons of the leg neurons (fig. S2). The axons terminated within the neuropil that corresponds to each particular leg, branching into a bowl shape (fig. S2). This pattern is typical of neurons that take part in proprioception, such as the hair plate neurons (*7*–*9*). Therefore, the *stum*-expressing cells in the *Drosophila* body have characteristics of proprioceptive neurons that sense a property of specific joints.

We performed confocal imaging of the dendritic region of *stum*-expressing neurons and found that, close to its tip, the dendrite branches toward the lateral aspect of the joint, and this side branch terminates at a short distance from the cuticle (Fig. 2). The tips of dendrite were not associated with a cuticular structure or a scolopale. These structural features are typical features of type II (multidendritic) neurons (*10*) but are incompatible with type I mechanoreceptor neurons that terminate with a ciliary structure. Thus, *stum* uncoordination mutations affect type II mechanoreceptor neurons. Furthermore, the entire dendritic terminal of these neurons was located in a region that is devoid of musculature (fig. S3), which suggests that they do not sense the mechanical properties of muscles. Taken together, these data suggest that *stum*-expressing neurons sense a mechanical property of the joint.

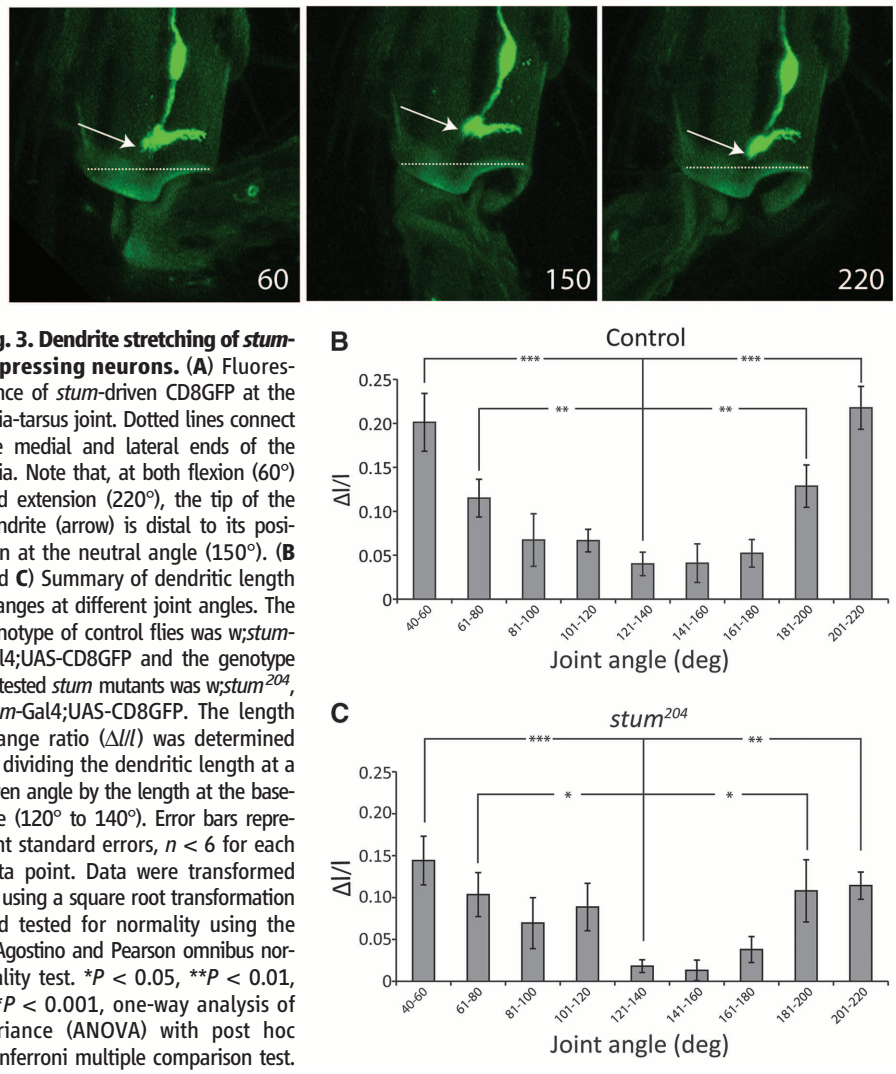

Fig. 3. Dendrite stretching of *stum*-expressing neurons. (**A**) Fluorescence of *stum*-driven CD8GFP at the tibia-tarsus joint. Dotted lines connect the medial and lateral ends of the tibia. Note that, at both flexion (60°) and extension (220°), the tip of the dendrite (arrow) is distal to its position at the neutral angle (150°). (**B** and **C**) Summary of dendritic length changes at different joint angles. The genotype of control flies was w;*stum*-Gal4;UAS-CD8GFP and the genotype of tested *stum* mutants was w;*stum*^{204}, *stum*-Gal4;UAS-CD8GFP. The length change ratio ($\Delta l/l$) was determined by dividing the dendritic length at a given angle by the length at the baseline (120° to 140°). Error bars represent standard errors, $n < 6$ for each data point. Data were transformed by using a square root transformation and tested for normality using the D'Agostino and Pearson omnibus normality test. *$P < 0.05$, **$P < 0.01$, ***$P < 0.001$, one-way analysis of variance (ANOVA) with post hoc Bonferroni multiple comparison test.

To test whether *stum*-positive neurons encode joint angles, we performed high-resolution imaging of the tibia-tarsus joint area at different angles. At each angle of the joint, we measured the total length of the sensory dendrite and its side branch. We found that the total dendrite length had a minimum typically at 130° to 170°, and it increased when the joint was shifted to either more obtuse or more acute angles (Fig. 3). These morphological changes indicate that these neurons are mechanically affected by the position of the joint. Because the tip of the side branch is stationary, it is likely that the change in total length results from the coupling of the tip of the main dendrite to the motion of the distal joint segment. The position of the dendrite and the susceptibility of its morphology to joint angle suggest that the role of *stum*-positive neurons is to sense and encode the angle of the joint.

We measured Ca^{2+} fluorescence while forcing the tibia-tarsus joint to different angles and found that the Ca^{2+} fluorescence in *stum*-expressing neurons correlated with the angle of the joint (Fig. 4). As in the morphological changes, the responses correlated with joint angle in a U-shaped manner, where both acute and obtuse angles induced increasing Ca^{2+} elevations. These results indicate that the *stum*-positive neurons encode proprioceptive information about the angle of joints. It is noteworthy that a similar U-shaped encoding of joint angles was also described in receptor neurons of mammalian joints (*11*), which suggests that sensing the deviations from a neutral joint range is universally critical for motor function.

The walking impairment in the *stum* mutant fly suggests that the gene is necessary for generating the proper proprioceptive responses in *stum*-expressing neurons. To test whether the *stum* mutations affect coupling between joint

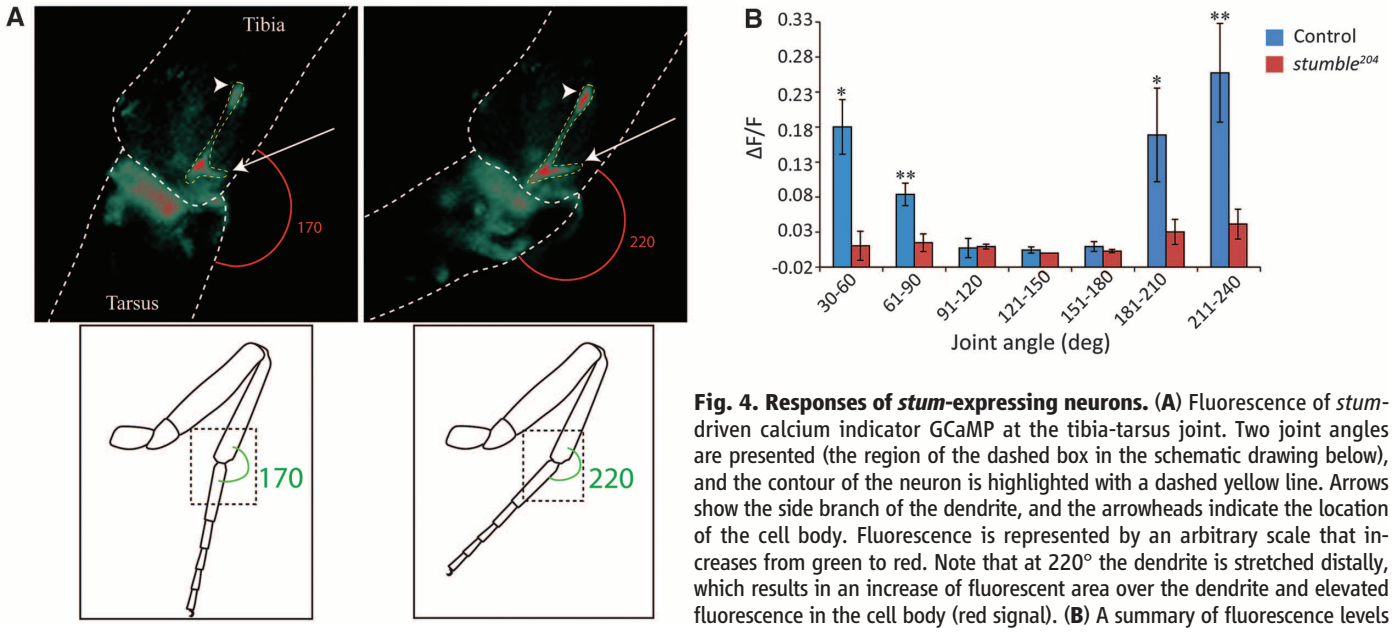

Fig. 4. Responses of *stum*-expressing neurons. (**A**) Fluorescence of *stum*-driven calcium indicator GCaMP at the tibia-tarsus joint. Two joint angles are presented (the region of the dashed box in the schematic drawing below), and the contour of the neuron is highlighted with a dashed yellow line. Arrows show the side branch of the dendrite, and the arrowheads indicate the location of the cell body. Fluorescence is represented by an arbitrary scale that increases from green to red. Note that at 220° the dendrite is stretched distally, which results in an increase of fluorescent area over the dendrite and elevated fluorescence in the cell body (red signal). (**B**) A summary of fluorescence levels of the cell body at different joint angles. The genotype of control flies was w; *stum*-Gal4;UAS-GCaMP3, and the genotype of tested *stum* mutants was w;*stum*^{204},*stum*-Gal4;UAS-GCaMP3. The $\Delta F/F$ was determined by dividing the fluorescence value at a given angle by the fluorescence at the preceding baseline (120° to 150°). Error bars represent standard errors, $n > 6$ for each data point. Baseline and response fluorescence levels were compared pairwise for each data point. *$P < 0.05$, **$P < 0.01$, Wilcoxon signed-rank test.

angles and dendritic stretching, we quantified the stretching in mutant flies that have *stum*-expressing neurons labeled with CD8GFP. We found that, in the *stum* mutant, the dendritic stretching in response to joint angles was comparable to that of control flies (Fig. 3). Thus, *stum* is not required for the mechanical coupling between joint angles and stretching of the sensory dendrites.

Although the dendritic stretching was not significantly affected in the *stum* mutant, we found that the Ca^{2+} responses to both acute and obtuse joint angles were abolished in the mutant (Fig. 4). Therefore, we conclude that *stum* is essential for transducing dendrite stretching into cellular responses.

We examined the morphology of *stum*-expressing neurons and found that, although axons (fig. S2) and cell bodies (fig. S4) of *stum* mutants were indistinguishable from controls, the sensory dendrite in mutants exhibited abnormalities (fig. S4). Most notably, in some of the *stum*-expressing neurons the tip of the dendrite was overgrown and extended into the distal segment of the joint (fig. S4). Thus, the absence of *stum* leads to a morphological defect, possibly because of the lack of mechanical responsiveness. The occasional morphological differences may account for the slight difference in the stretching profile between control and mutant dendrites (Fig. 3, B and C). The fraction of neurons demonstrating the abnormal morphology in the mutant increased from the day of eclosion to the following day (fig. S4C). As the addition of morphological changes takes place after eclosion, it is possible that *stum*-dependent activity is essential for late shape determination that can take place in adult multidendritic neurons (*12*).

We generated transgenic flies that express a GFP fused with the N terminus of Stum under UAS regulation (UAS-GFP-Stum). We found that the Stum fusion protein was specifically localized to the distal part of the sensory dendrite, although it did not accumulate substantially in any other part of the cell (fig. S5). The fluorescent signal started at the region of bifurcation and extended to both distal tips of the dendrite (fig. S5). This specific localization suggests that Stum functions in the part of the dendrite that senses stretching.

Taken together, *stum* expression in mechanosensory neurons, Stum localization to the sensory dendrite, and the abolition of responses to stretching in the *stum* mutant suggest that *stum* has an essential role in mediating mechanical sensing in receptor neurons. Because the Stum protein in most species is very small and because *Drosophila stum* is expressed in limited populations of receptor neurons, we propose that *stum* is not the mechanically activated channel. Rather, *stum* may serve as an accessory module that is essential for the proper localization or function of the transduction channels.

The stretch-receptor neurons that express *stum* present an elegant engineering solution for generating specificity to the modality of mechanical stimulus. The distal part of their dendrite bifurcates into two branches whose tips are anchored to parts of the joint that shift their relative positions. Sensing the stretching only between the two dendritic tips may tune the nerve responses to joint motions and filter out the effect of irrelevant mechanical impacts. This specificity enables the sensory neuron to relay reliable proprioceptive information to the central nervous system.

References and Notes

1. S. E. Kim, B. Coste, A. Chadha, B. Cook, A. Patapoutian, *Nature* **483**, 209–212 (2012).
2. Z. Yan *et al.*, *Nature* **493**, 221–225 (2013).
3. E. J. Koundakjian, D. M. Cowan, R. W. Hardy, A. H. Becker, *Genetics* **167**, 203–206 (2004).
4. T. Avidor-Reiss *et al.*, *Cell* **117**, 527–539 (2004).
5. M. Kernan, D. Cowan, C. Zuker, *Neuron* **12**, 1195–1206 (1994).
6. R. G. Walker, A. T. Willingham, C. S. Zuker, *Science* **287**, 2229–2234 (2000).
7. D. J. Merritt, R. K. Murphey, *J. Comp. Neurol.* **322**, 16–34 (1992).
8. R. K. Murphey, D. Possidente, G. Pollack, D. J. Merritt, *J. Comp. Neurol.* **290**, 185–200 (1989).
9. R. K. Murphey, D. R. Possidente, P. Vandervorst, A. Ghysen, *J. Neurosci.* **9**, 3209–3217 (1989).
10. R. Bodmer, Y. N. Jan, *Roux's Arch. Dev. Biol.* **196**, 69–77 (1987).
11. D. Burke, S. C. Gandevia, G. Macefield, *J. Physiol.* **402**, 347–361 (1988).
12. K. Shimono *et al.*, *Neural Dev.* **4**, 37 (2009).

Acknowledgments: We thank K. Spencer for technical assistance. The *stum* mutants were identified by screening a collection of F3 *Drosophila* lines in the laboratory of C. S. Zuker. We thank L. Stowers and T. Avidor-Reiss for kindly providing reagents. Data for this paper may be found in the supplementary materials.

Supplementary Materials

www.sciencemag.org/content/343/6176/1256/suppl/DC1
Materials and Methods
Figs. S1 to S5
References

28 October 2013; accepted 6 February 2014
10.1126/science.1247761

Complement Is Activated by IgG Hexamers Assembled at the Cell Surface

Christoph A. Diebolder,[1,2]* Frank J. Beurskens,[3]* Rob N. de Jong,[3] Roman I. Koning,[2] Kristin Strumane,[3] Margaret A. Lindorfer,[4] Marleen Voorhorst,[3] Deniz Ugurlar,[1] Sara Rosati,[5] Albert J. R. Heck,[5] Jan G. J. van de Winkel,[3,6] Ian A. Wilson,[7,8] Abraham J. Koster,[2] Ronald P. Taylor,[4] Erica Ollmann Saphire,[9] Dennis R. Burton,[8,9,10] Janine Schuurman,[3] Piet Gros,[1]† Paul W. H. I. Parren[3]†

Complement activation by antibodies bound to pathogens, tumors, and self antigens is a critical feature of natural immune defense, a number of disease processes, and immunotherapies. How antibodies activate the complement cascade, however, is poorly understood. We found that specific noncovalent interactions between Fc segments of immunoglobulin G (IgG) antibodies resulted in the formation of ordered antibody hexamers after antigen binding on cells. These hexamers recruited and activated C1, the first component of complement, thereby triggering the complement cascade. The interactions between neighboring Fc segments could be manipulated to block, reconstitute, and enhance complement activation and killing of target cells, using all four human IgG subclasses. We offer a general model for understanding antibody-mediated complement activation and the design of antibody therapeutics with enhanced efficacy.

Complement activation by antibodies initiates immune protection through the generation of an array of biologically active products including opsonins, anaphylatoxins, chemotactic agents, and membrane attack complexes (*1*, *2*). The classical pathway of complement is triggered when antigen-bound immunoglobulin M (IgM) or IgG antibody molecules bind C1, which consists of the multimeric pattern recognition molecule C1q and a heterotetramer of the proteases C1r and C1s (*3*, *4*). C1q binds a single IgG Fc segment with very low affinity (dissociation constant $K_d \approx 10^{-4}$ M) (*5*, *6*), and physiological C1 binding thus requires an increase in the apparent binding constant—for instance, through antigen-driven antibody clustering, which allows multivalent C1q binding (*7*). The molecular events governing complement activation, including the C1-antibody stoichiometry required for optimal activation, remain poorly understood (*3*, *8*–*13*). Here, we set out to characterize and visualize the first steps in complement activation by IgG at the molecular level.

In the structure of human anti–HIV-1 gp120 antibody IgG1-b12 at 2.7 Å resolution [Protein Data Bank (PDB) entry 1HZH] (*14*, *15*), the IgG Fc segments are arranged in a hexameric ring (Fig. 1A). A similar crystal packing is found for human antibody 2G12 (*16*). The spatial orientation of Lys^{322} (Fig. 1A), a critical residue in the C1q binding site on IgG, suggested a compatibility of the hexamer with the arrangement of the six antibody-binding headpieces in C1q. We hypothesized that IgG antibodies activate complement-dependent cytotoxicity (CDC) via ordered clustering into hexamers through specific noncovalent Fc interactions. To investigate this hypothesis, we used a peptide that has been shown to bind residues in the observed Fc-Fc interface (*17*) (Fig. 1B). The peptide inhibited CDC of human B cell lymphomas by CD20 antibody IgG1-7D8 and CD38 antibody IgG1-005 (Fig. 1C), both of which potently induce CDC by the classical pathway (*18*, *19*). Next, we generated interface mutations designed to weaken Fc-Fc interactions. We confirmed that antigen binding and C1q binding to randomly immobilized IgG1 (fig. S1) were mostly unaffected by the mutations. In contrast, the apparent avidity of C1q for cell-bound IgG1-7D8 mutated at positions Ile^{253}, His^{433}, or Asn^{434} decreased by as much as a factor of 20 (Fig. 1D, fig. S2A, and table S1); this resulted in reduced complement activation and CDC, consistent with other mutations in the Fc-Fc interface (Fig. 1E, fig. S2A, and table S2). Modeling suggested that Lys^{439} and Ser^{440} could be manipulated to test Fc-Fc interactions in a gain-of-function experiment (fig. S2B). In isolation, charge repulsion in mutants K439E (Lys^{439} → Glu) and S440K (Ser^{440} → Lys) indeed inhibited CDC; this inhibition could be overcome with double mutants or mixtures containing both mutants that neutralized this repulsion (Fig. 1, F and G, and tables S1 and S2).

We also identified mutations that resulted in significantly enhanced CDC, as exemplified by E345R (Glu^{345} → Arg), which increased C1q avidity to opsonized cells by a factor of ~5 and CDC by a factor of ~10 when introduced into CD20 antibody IgG1-7D8 (Fig. 2A and tables S1 and S2) (*20*). Similarly, the E345R substitution increased CDC of CD38 antibody IgG1-005 (Fig. 2B) as well as of its IgG2, IgG3, and IgG4 isotype variants (Fig. 2C). A triple mutant, IgG1-005-RGY, combining E345R with two additional enhancing mutations [E430G (Glu^{430} → Gly) and S440Y (Ser^{440} → Tyr)] readily formed hexamers in solution. The presence of monomeric and hexameric species of IgG1-005-RGY, presumably in equilibrium, was demonstrated by native mass spectrometry (Fig. 3A and table S3), high-performance size exclusion chromatography (HP-SEC) combined with multi-angle static light scattering (MALS) (Fig. 3B), and negative-stain electron tomography (ET) (Fig. 3, C to F). Solution-phase hexamers of IgG1-005-RGY directly activated complement when added to human serum, as shown by the generation of C4d (Fig. 2D). This was also observed for IgG1-7D8-RGY, a triple mutant of the CD20 antibody. Together, these findings directly link a biophysically characterized noncovalent IgG1 hexamer with classical pathway complement activation. Finally, IgG1-005-RGY showed a further potency increase when bound to cells, as shown by stronger CDC at low concentrations relative to the single mutant (Fig. 2E), which may be explained by preformed hexamers or enhanced Fc-Fc–mediated assembly on the cell surface.

To image C1 binding to antigen-bound IgG on a membrane, we performed cryo–electron tomography (cryo-ET) using dinitrophenyl (DNP)–labeled liposomes (*20*). In the cryo-ET reconstructions, antibodies on the liposome surface assembled in single-layer patches with maximum density at a distance of 11 nm from the membrane (fig. S3, A and E) (*20*). Addition of purified C1 protein, C4-depleted serum, or normal human serum resulted in C1 binding on top of the antibody layer (fig. S3, F to H). Cryo-ET tomograms of 107 particles representing antibody-C1 complexes were averaged (fig. S4), resulting in an electron density map at low (>6 nm) resolution. The map showed a lower platform at 11 nm (coinciding with the maximum density observed on liposomes with antibody alone), a second platform at 20 nm, and a stalk on top of the upper platform (Fig. 4A). Horizontal sections through the tomogram average indicated that the lower

[1]Crystal and Structural Chemistry, Bijvoet Center for Biomolecular Research, Department of Chemistry, Faculty of Science, Utrecht University, 3584 CH Utrecht, Netherlands. [2]Department of Molecular Cell Biology, Electron Microscopy Section, Leiden University Medical Center, 2300 RC Leiden, Netherlands. [3]Genmab, 3584 CM Utrecht, Netherlands. [4]Department of Biochemistry and Molecular Genetics, University of Virginia School of Medicine, Charlottesville, VA 22908, USA. [5]Biomolecular Mass Spectrometry and Proteomics, Bijvoet Center for Biomolecular Research and Utrecht Institute for Pharmaceutical Sciences, Utrecht University, 3584 CH Utrecht, Netherlands. [6]Department of Immunology, University Medical Center, 3584 CX Utrecht, Netherlands. [7]Department of Integrative Structural and Computational Biology, The Scripps Research Institute, La Jolla, CA 92037, USA. [8]IAVI Neutralizing Antibody Center and Center for HIV/AIDS Vaccine Immunology and Immunogen Discovery, The Scripps Research Institute, La Jolla, CA 92037, USA. [9]Department of Immunology and Microbial Science, The Scripps Research Institute, La Jolla, CA 92037, USA. [10]Ragon Institute of MGH, MIT, and Harvard, Cambridge, MA 02139, USA.

*These authors contributed equally to this work.
†Corresponding author. E-mail: p.parren@genmab.com (P.W.H.I.P.); p.gros@uu.nl (P.G.)

platform was composed of a continuous disk with six poorly resolved densities protruding toward the membrane and four discernible densities on top, arranged as an incomplete hexagon (Fig. 4, B to E). We generated a model of the C1-antibody complex by docking the 1HZH crystal packing [adapted by Fab rotation (fig. S5)] into the lower platform and manually fitting C1q headpieces (Fig. 4F and fig. S6) (*20*). The four densities on top of the lower platform suggested incomplete (4:6) C1q headpiece binding to the antibody hexamer (Fig. 4C) and may reflect flexibility and dynamics of the C1q-IgG interactions.

The model suggested that one Fab arm of each antibody in the hexamer bound the membrane-associated antigen while the other Fab arm was positioned at the height of the platform (Fig. 4F). To test the concept that complement activation might only require monovalent binding, we generated functionally monovalent bispecific antibodies (*20*, *21*) that contained one specific and one innocuous Fab arm (i.e., IgG1-7D8/b12 and IgG1-2F8/b12, monovalently binding CD20 and EGFR, respectively). Both antibodies induced efficient CDC of relevant target cells (Fig. 4, G and H), which for the bispecific antibody 2F8/b12 was strongly enhanced relative to the parental 2F8 antibody. Thus, for this antibody-antigen pair, monovalent binding is better able than (high-affinity) bivalent binding to accommodate the Fc-Fc hexamerization required for efficient CDC.

The hexameric IgG-C1 binding model (Fig. 4, A and F, and fig. S6) revealed geometrical restraints that could explain the strong antigen and epitope dependency of complement activation. Potent complement activation by monoclonal antibodies is restricted to certain antigens and epitopes (*12*, *19*, *22*), presumably because antigen size, density, and fluidity may affect activation (*18*, *22*–*26*) and because IgG orientation resulting from epitope geometry imposes additional structural constraints (*12*, *19*, *22*, *25*, *27*). Polyclonal antibodies appear to be less sensitive than monoclonal antibodies to such constraints (*24*, *28*, *29*), potentially because binding of antibodies to a variety of antigens or epitopes facilitates clustering of Fc segments, thereby allowing efficient Fc-Fc assembly. Monovalent binding of IgG molecules in the platform is consistent with earlier observations (*30*) and could be envisaged to provide more degrees of freedom for the Fc segments, allowing their optimal positioning for C1q recruitment.

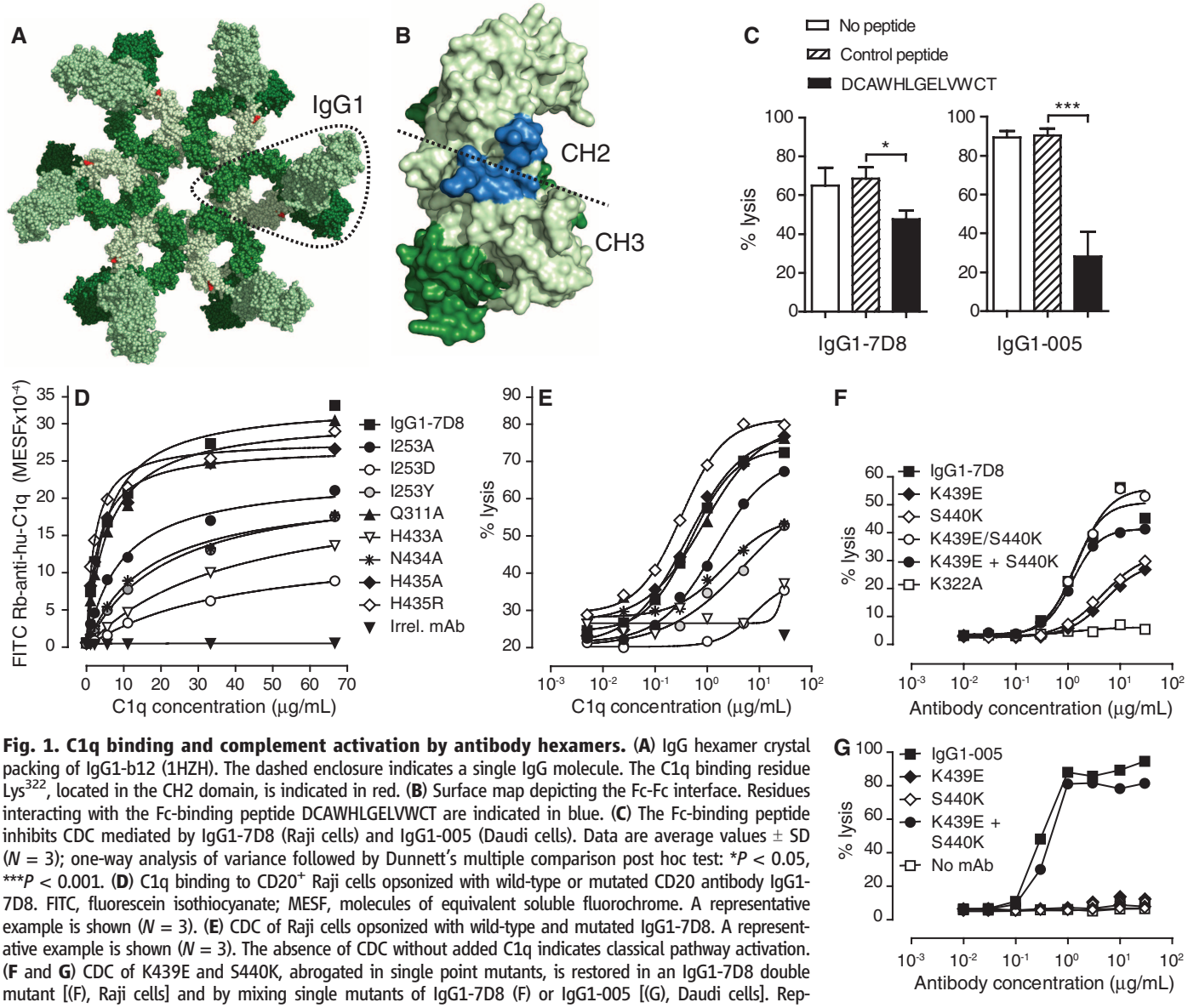

Fig. 1. C1q binding and complement activation by antibody hexamers. (**A**) IgG hexamer crystal packing of IgG1-b12 (1HZH). The dashed enclosure indicates a single IgG molecule. The C1q binding residue Lys^{322}, located in the CH2 domain, is indicated in red. (**B**) Surface map depicting the Fc-Fc interface. Residues interacting with the Fc-binding peptide DCAWHLGELVWCT are indicated in blue. (**C**) The Fc-binding peptide inhibits CDC mediated by IgG1-7D8 (Raji cells) and IgG1-005 (Daudi cells). Data are average values ± SD ($N = 3$); one-way analysis of variance followed by Dunnett's multiple comparison post hoc test: $^{*}P < 0.05$, $^{***}P < 0.001$. (**D**) C1q binding to $CD20^{+}$ Raji cells opsonized with wild-type or mutated CD20 antibody IgG1-7D8. FITC, fluorescein isothiocyanate; MESF, molecules of equivalent soluble fluorochrome. A representative example is shown ($N = 3$). (**E**) CDC of Raji cells opsonized with wild-type and mutated IgG1-7D8. A representative example is shown ($N = 3$). The absence of CDC without added C1q indicates classical pathway activation. (**F** and **G**) CDC of K439E and S440K, abrogated in single point mutants, is restored in an IgG1-7D8 double mutant [(F), Raji cells] and by mixing single mutants of IgG1-7D8 (F) or IgG1-005 [(G), Daudi cells]. Representative examples are shown ($N = 3$). Amino acid abbreviations: A, Ala; C, Cys; D, Asp; E, Glu; G, Gly; H, His; I, Ile; K, Lys; L, Leu; N, Asn; Q, Gln; R, Arg; S, Ser; T, Thr; V, Val; W, Trp; Y, Tyr.

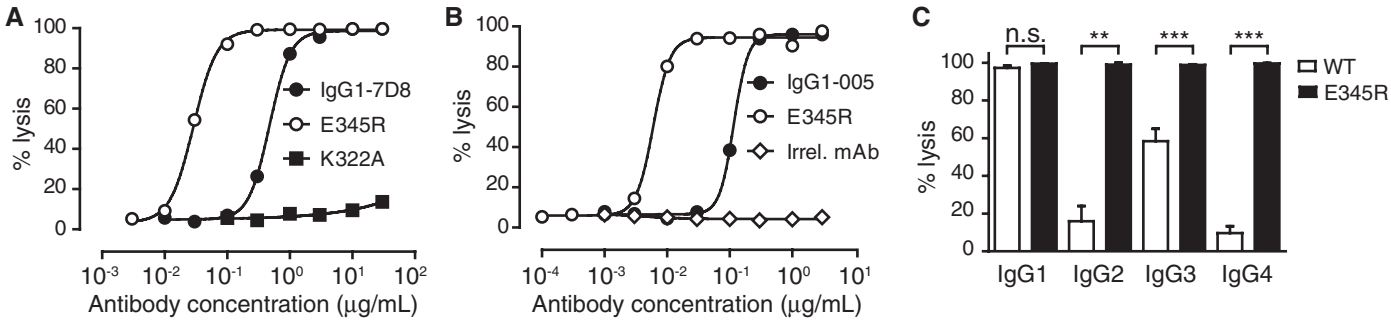

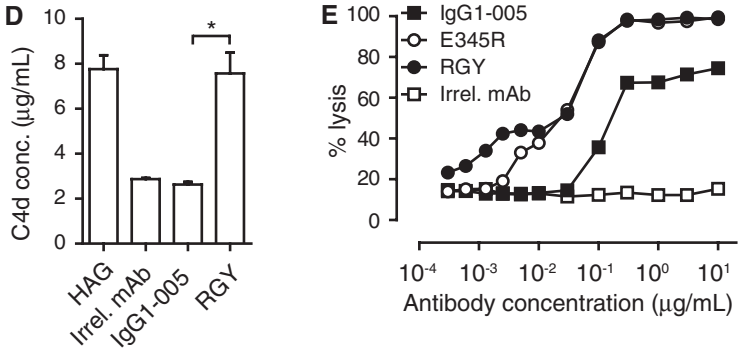

Fig. 2. Increased CDC by enhanced hexamer formation. (**A** and **B**) Increased CDC of Daudi cells by IgG1-7D8-E345R (A) and IgG1-005-E345R (B) relative to wild-type antibodies. Representative examples are shown (N = 4). (**C**) E345R mutants of IgG1-005 isotype variants induce CDC of Daudi cells more potently than wild-type (WT) IgG2, IgG3, and IgG4; IgGs were tested at 10 μg/ml. Data are average values ± SD (N = 3); two-sided unpaired t test with Welch's correction: n.s., not significant; $^{**}P < 0.01$, $^{***}P < 0.001$. (**D**) IgG1-005-RGY induced C4d generation in normal human serum. Data are average values ± SD (N = 3). Two-sided unpaired t test with Welch's correction; $^{*}P < 0.05$. Heat-aggregated IgG (HAG) was used as a positive control. (**E**) IgG1-005-RGY showed enhanced CDC activity of Ramos cells relative to wild-type IgG1-005 and IgG1-005-E345R. A representative example is shown (N = 3).

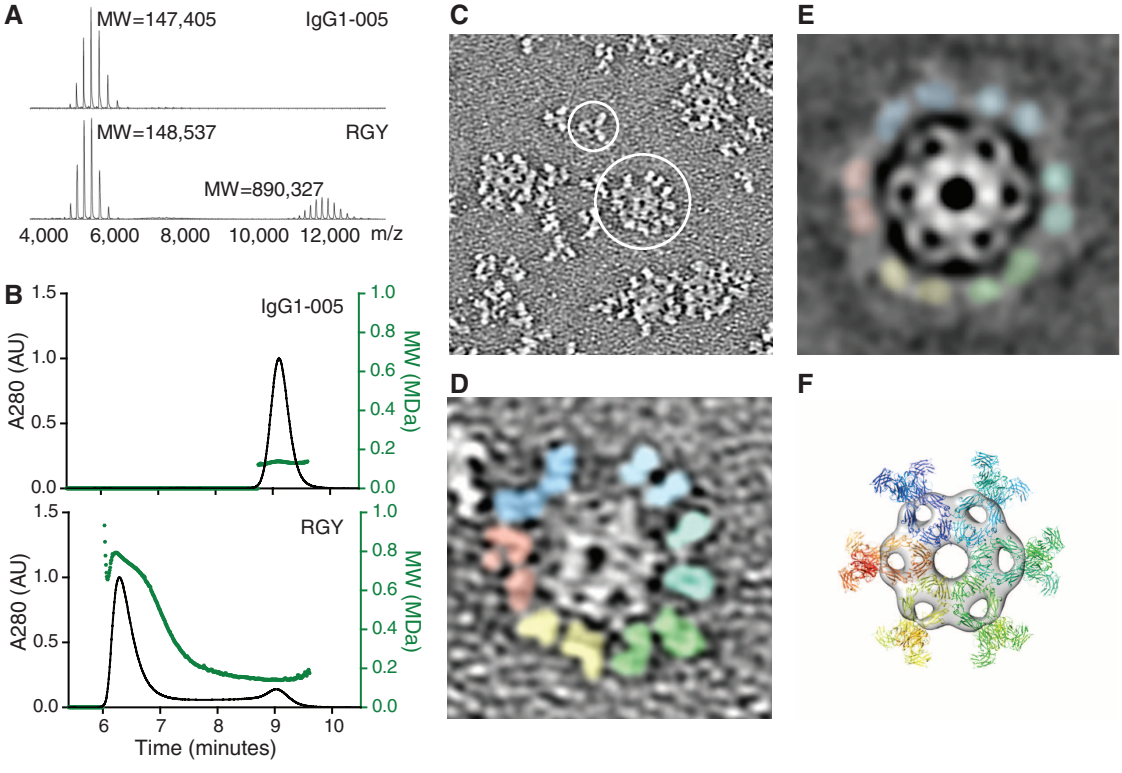

Fig. 3. Solution-phase hexamers formed by triple mutant IgG1-005-RGY. (**A**) Native mass spectrometry of IgG1-005 indicating a molecular weight (MW) of 147,405 daltons and IgG1-005-RGY showing MWs of a monomer (148,537 daltons) and a hexamer (890,327 daltons) (table S3). The hexameric state was confirmed in experiments using different conditions (N = 6); m/z, mass/charge ratio. (**B**) Overlay of HP-SEC–MALS profiles [absorbance at 280 nm (A280), black, left axis; MW, green, right axis] of IgG1-005 (top) and IgG1-005-RGY (bottom) shows that ~79% IgG1-005-RGY eluted as hexamer and ~21% as monomer, whereas >99% of IgG1-005 eluted as monomer. A representative example is shown (N = 3). (**C** to **F**) ET of negatively stained IgG1-005-RGY. (C) ET overview image showing a monomer (small circle) and a hexamer (large circle). (D) Representative hexamer with colored Fab pairs. (E) ET average of 200 subtomograms at a resolution of 2.9 nm. (F) Surface rendering of a symmetrized Fc ring with docked 1HZH hexamer.

Our model is in agreement with an evolutionary relationship between IgM and IgG in triggering complement (*11*). IgM normally exists in a polymeric state, in which C1q binding sites are sequestered and only become exposed when antigen is bound (*6*, *31*), whereas IgG normally exists in a monomeric state in which C1q binding sites are exposed but affinity is too low to allow adequate C1 binding. In our model, sequential antigen and Fc-Fc binding by IgG leads to the formation of hexamers that bind C1q with high avidity and activate complement. The model

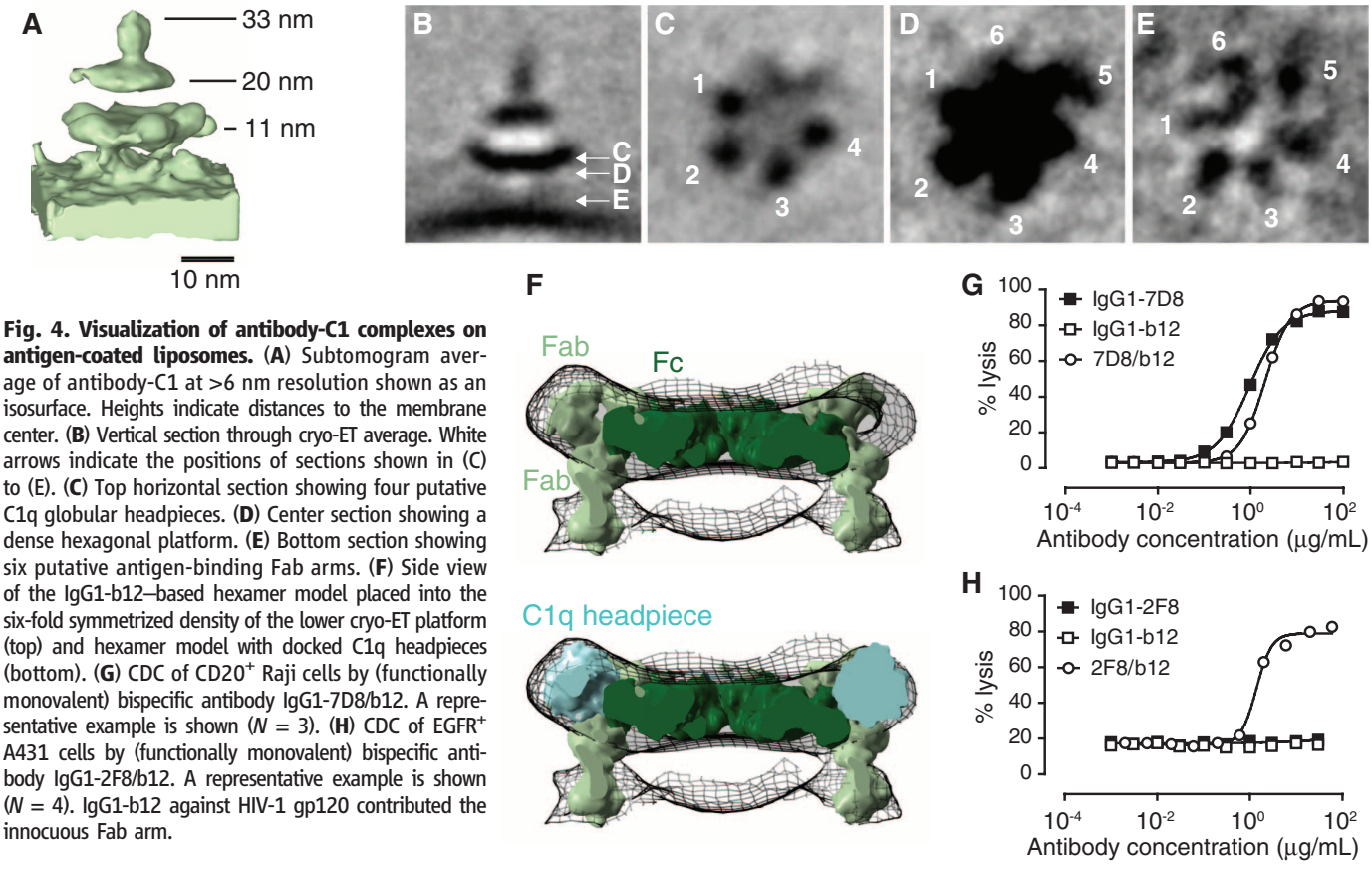

Fig. 4. Visualization of antibody-C1 complexes on antigen-coated liposomes. (**A**) Subtomogram average of antibody-C1 at >6 nm resolution shown as an isosurface. Heights indicate distances to the membrane center. (**B**) Vertical section through cryo-ET average. White arrows indicate the positions of sections shown in (C) to (E). (**C**) Top horizontal section showing four putative C1q globular headpieces. (**D**) Center section showing a dense hexagonal platform. (**E**) Bottom section showing six putative antigen-binding Fab arms. (**F**) Side view of the IgG1-b12–based hexamer model placed into the six-fold symmetrized density of the lower cryo-ET platform (top) and hexamer model with docked C1q headpieces (bottom). (**G**) CDC of $CD20^+$ Raji cells by (functionally monovalent) bispecific antibody IgG1-7D8/b12. A representative example is shown ($N = 3$). (**H**) CDC of $EGFR^+$ A431 cells by (functionally monovalent) bispecific antibody IgG1-2F8/b12. A representative example is shown ($N = 4$). IgG1-b12 against HIV-1 gp120 contributed the innocuous Fab arm.

is nonetheless compatible with observations that smaller IgG complexes may suffice to initiate some complement activation (*8*, *32*). However, low-avidity C1q binding will result in only modest complement activity (*27*), whereas the IgG hexamer will bind C1q most avidly, thus ensuring optimal complement activation when required.

The observation that IgG hexamerization after antigen binding leads to effective complement activation could be exploited by increasing Fc-Fc contact formation. Because the E345R mutation bestowed complement-activating capability on all human IgG subclasses, IgG hexamerization may be a general concept applicable to the engineering of therapeutic antibodies with enhanced activity.

References and Notes

1. D. Ricklin, G. Hajishengallis, K. Yang, J. D. Lambris, *Nat. Immunol.* **11**, 785–797 (2010).
2. J. R. Dunkelberger, W. C. Song, *Cell Res.* **20**, 34–50 (2010).
3. C. Gaboriaud *et al.*, *Trends Immunol.* **25**, 368–373 (2004).
4. U. Kishore, K. B. Reid, *Immunopharmacology* **49**, 159–170 (2000).
5. N. C. Hughes-Jones, B. Gardner, *Mol. Immunol.* **16**, 697–701 (1979).
6. A. Feinstein, N. Richardson, M. J. Taussig, *Immunol. Today* **7**, 169–174 (1986).
7. D. R. Burton, *Mol. Immunol.* **22**, 161–206 (1985).
8. T. Borsos, H. J. Rapp, *Science* **150**, 505–506 (1965).
9. W. F. Rosse, *J. Clin. Invest.* **50**, 727–733 (1971).
10. J. J. Thompson, L. G. Hoffman, *Immunochemistry* **11**, 537–541 (1974).
11. D. R. Burton, *Immunol. Today* **7**, 165–167 (1986).
12. C. I. Bindon, G. Hale, H. Waldmann, *Eur. J. Immunol.* **18**, 1507–1514 (1988).
13. D. R. Burton, *Trends Biochem. Sci.* **15**, 64–69 (1990).
14. E. O. Saphire, P. W. H. I. Parren, C. F. Barbas 3rd, D. R. Burton, I. A. Wilson, *Acta Crystallogr. D* **57**, 168–171 (2001).
15. E. O. Saphire *et al.*, *Science* **293**, 1155–1159 (2001).
16. Y. Wu *et al.*, *Cell Rep.* **5**, 1443–1455 (2013).
17. W. L. DeLano, M. H. Ultsch, A. M. de Vos, J. A. Wells, *Science* **287**, 1279–1283 (2000).
18. J. L. Teeling *et al.*, *Blood* **104**, 1793–1800 (2004).
19. M. de Weers *et al.*, *J. Immunol.* **186**, 1840–1848 (2011).
20. See supplementary materials on *Science* Online.
21. A. F. Labrijn *et al.*, *Proc. Natl. Acad. Sci. U.S.A.* **110**, 5145–5150 (2013).
22. M. S. Cragg *et al.*, *Blood* **101**, 1045–1052 (2003).
23. J. W. Parce, D. Kelley, K. Heinzelmann, *Biochim. Biophys. Acta* **736**, 92–98 (1983).
24. N. C. Hughes-Jones, B. D. Gorick, J. C. Howard, A. Feinstein, *Eur. J. Immunol.* **15**, 976–980 (1985).
25. J. L. Teeling *et al.*, *J. Immunol.* **177**, 362–371 (2006).
26. M. Q. Xia, G. Hale, H. Waldmann, *Mol. Immunol.* **30**, 1089–1096 (1993).
27. A. W. Pawluczkowycz *et al.*, *J. Immunol.* **183**, 749–758 (2009).
28. M. Dechant *et al.*, *Cancer Res.* **68**, 4998–5003 (2008).
29. F. Kushihata, J. Watanabe, A. Mulder, F. Claas, J. C. Scornik, *Transplantation* **78**, 995–1001 (2004).
30. H. F. Watts, V. A. Anderson, V. M. Cole, G. T. Stevenson, *Mol. Immunol.* **22**, 803–810 (1985).
31. D. M. Czajkowsky, Z. Shao, *Proc. Natl. Acad. Sci. U.S.A.* **106**, 14960–14965 (2009).
32. W. F. Rosse, H. J. Rapp, T. Borsos, *J. Immunol.* **98**, 1190–1195 (1967).

Acknowledgments: We thank M. Daha for purified C1, and F. G. A. Faas and W. Vossenaar-Horstman for technical support. Supported in part by European Research Council advanced grant 233229; Cyttron II (Life Sciences Health framework FES0908); the Netherlands Centre for Electron Nanoscopy (NeCEN), Leiden; the Netherlands Organization for Scientific Research (NWO 175.010.2009.001); and the European Regional Development Fund of the European Commission (21Z.014). D.R.B. is supported by National Institute of Allergy and Infectious Diseases (NIAID) grant AI055332. I.A.W. is supported by NIAID grant AI084817. The data presented are tabulated in the main paper and in the supplementary materials. The ET data presented are archived at EMDataBank, entries EMD-2506, EMD-2507, and EMD-2554. F.J.B., R.N.d.J., K.S., M.V., J.G.J.v.d.W., J.S., and P.W.H.I.P. are Genmab employees and own Genmab warrants and/or stock. M.A.L., R.P.T., S.R., and A.J.R.H. received Genmab funding. F.J.B., R.N.d.J., J.S., and P.W.H.I.P. are inventors on Genmab patent applications related to technology to enhance complement activation.

Supplementary Materials

www.sciencemag.org/content/343/6176/1260/suppl/DC1
Materials and Methods
Supplementary Text
Figs. S1 to S6
Tables S1 to S3
References (*33*–*62*)

25 November 2013; accepted 6 February 2014
10.1126/science.1248943

Dlk1 Promotes a Fast Motor Neuron Biophysical Signature Required for Peak Force Execution

Daniel Müller,[1] Pitchaiah Cherukuri,[1] Kristine Henningfeld,[2,3] Chor Hoon Poh,[1] Lars Wittler,[4] Phillip Grote,[4] Oliver Schlüter,[5] Jennifer Schmidt,[6] Jorge Laborda,[7] Steven R. Bauer,[8] Robert M. Brownstone,[9] Till Marquardt[1,3]*

Motor neurons, which relay neural commands to drive skeletal muscle movements, encompass types ranging from "slow" to "fast," whose biophysical properties govern the timing, gradation, and amplitude of muscle force. Here we identify the noncanonical Notch ligand Delta-like homolog 1 (Dlk1) as a determinant of motor neuron functional diversification. Dlk1, expressed by ~30% of motor neurons, is necessary and sufficient to promote a fast biophysical signature in the mouse and chick. Dlk1 suppresses Notch signaling and activates expression of the K^+ channel subunit Kcng4 to modulate delayed-rectifier currents. Dlk1 inactivation comprehensively shifts motor neurons toward slow biophysical and transcriptome signatures, while abolishing peak force outputs. Our findings provide insights into the development of motor neuron functional diversity and its contribution to the execution of movements.

Slow or fast motor neurons respectively synapse with type I muscle fibers responsible for fatigue-resistant low-force contractions or fatigable type IIb muscle fibers eliciting brief high-force outputs (fig. S1A) (*1*–*3*). The biophysical properties of these motor neuron types are exquisitely matched to the muscle fiber contractile properties (*1*, *4*–*9*). For instance, slow motor neurons, which possess low activation thresholds and long afterhyperpolarizations, can sustain long periods of low-frequency firing (*1*, *4*–*9*). Fast motor neurons, in contrast, are larger, exhibit high activation thresholds with shorter afterhyperpolarizations, and can fire in high-frequency bursts (*1*, *4*–*9*). Motor neurons with properties falling between these two extremes (which we call intermediate motor neurons) innervate muscle fibers with similarly intermediate characteristics (*3*–*6*, *9*). We identified molecular markers for these motor neuron types and studied how motor neuron functional diversity is established.

We exploited the distinct fiber type composition of soleus, tibialis anterior, and quadriceps muscles in the early postnatal mouse hindlimb (fig. S1B) to retrogradely label, isolate, and obtain transcriptome profiles of motor pools enriched in motor neurons developing into either slow/intermediate or fast types (fig. S1, C to O). One of the genes associated with a fast motor pool profile encoded Dlk1 (fig. S1P), a type I transmembrane protein related to the Notch ligand Delta, which functions in adipogenesis, postnatal myogenesis, and adult neurogenesis (*10*–*12*). Dlk1 was selectively expressed by large α motor neurons, but not smaller α motor neurons or γ motor neurons, throughout the spinal cord (Fig. 1, A to E, and fig. S2, A to F). Moreover, motor pools innervating predominantly fast or slow/intermediate muscles respectively exhibited either high or low proportions of $Dlk1^+$ motor neurons (Fig. 1, F to H, and fig. S2, C and D), together indicating selective expression of Dlk1 by fast motor neurons (fig. S2G).

To test whether Dlk1 would be involved in motor neuron functional diversification, we performed whole-cell patch clamp recordings of late-gestation chick motor neurons engineered to stably express excess Dlk1 or control fluorescent protein (fig. S3). Excess Dlk1 shifted biophysical properties toward a profile typical of fast motor neurons (Fig. 2, A and B, and fig. S4, A to E), including elevated firing thresholds and frequencies and reduced afterhyperpolarization and firing periods (Fig. 2C and fig. S4, F to I).

We next analyzed motor neuron biophysical properties in acute spinal cord preparations of mice with the *Dlk1* gene knocked out ($Dlk1^{KO}$) (fig. S5A). Motor neurons in $Dlk1^{KO}$ mice showed a shift in biophysical properties opposite to those driven by excess Dlk1 in the chick (Fig. 2C and fig. S5, B to F). In normal mice, the proportion of $Dlk1^+$ motor neurons (34%) matched the proportion of motor neurons with a fast signature (30 to 32%) (Fig. 2, D and E, and fig. S6, A and B). In $Dlk1^{KO}$ mice, a similar proportion (30%) of motor neurons shifted to lower firing thresholds (Fig. 2D and fig. S6, E to G) and slow/intermediate biophysical signatures, resulting in an almost complete lack of motor neurons with a fast signature (Fig. 2F and fig. S6, C and D). Together, these data indicated that Dlk1 is both sufficient and necessary for promoting a fast biophysical signature in motor neurons.

To test how a shift away from fast toward slow/intermediate motor neuron properties would affect neuromuscular function, we analyzed the gait of mice selectively lacking Dlk1 in the motor neuron lineage ($Dlk1^{CKO}$) (fig. S7, A to D). Neither $Dlk1^{CKO}$ nor $Dlk1^{KO}$ mice showed measurable alterations in gait kinematics, posture, cutaneous sensation, rotarod test, or water maze performance (Fig. 3B and fig. S7, E to N). However, $Dlk1^{CKO}$ mice were deficient in braking and, to a lesser extent, propulsion velocities (Fig. 3A and fig. S7O), suggesting an inability to elicit the high forces needed in the extensor phase of the gait cycle (*13*). Consistently, $Dlk1^{CKO}$ mice showed abnormally low maximal limb force generation (Fig. 3C). Loss of a fast motor neuron biophysical signature in these mice thus resulted in deficient peak force outputs.

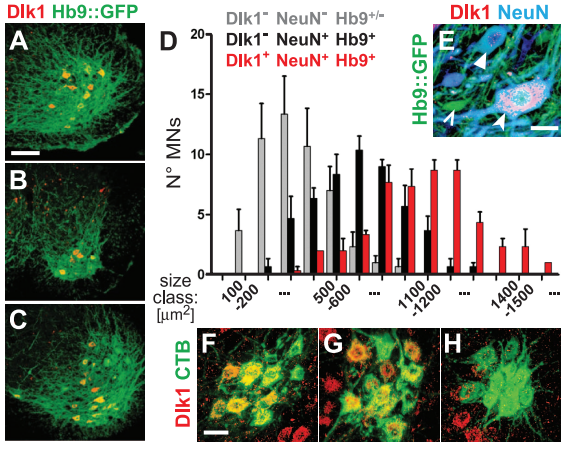

Fig. 1. Dlk1 is expressed by fast motor neurons. (**A** to **C**) Dlk1 expression in subsets of motor neurons colabeled by green fluorescent protein (GFP) in a postnatal day (P10) *Hb9::eGFP* transgenic mouse at brachial (A), thoracic (B), and lumbar (C) levels (scale bar, 150 μm). (**D**) Motor neuron (MN) size distribution in P10 mouse spinal cord: Dlk1 expression by the largest α motor neuron ($NeuN^+$ $Hb9^+$) size classes [n = 450 motor neurons, three P10 mice; error bars indicate the standard error of the mean (SEM)]. (**E**) Dlk1 expression by a subset of $NeuN^+$ α motor neurons, but not $NeuN^-$ putative γ motor neurons (open arrowhead) at P10. Scale bar, 10 μm. (**F** to **H**) High abundance of $Dlk1^+$ motor neurons in rectus femoris (F), tibialis anterior (G), but not soleus (H) motor pools colabeled by cholera toxin B (CTB) (scale bar, 20 μm).

[1]Developmental Neurobiology Laboratory, European Neuroscience Institute (ENI-G), Grisebachstraße 5, 37077 Göttingen, Germany. [2]Institute of Developmental Biochemistry, University Medical Center Göttingen, Justus-von-Liebig-Weg 11, 37077 Göttingen, Germany. [3]Center for Nanoscale Microscopy and Molecular Physiology of the Brain, Göttingen, Germany. [4]Department of Developmental Genetics, Max-Planck Institute for Molecular Genetics, Ihnestraße 63-73, 14195 Berlin, Germany. [5]Molecular Neurobiology Laboratory, ENI-G, Grisebachstraße 5, 37077 Göttingen, Germany. [6]Department of Biological Sciences, University of Illinois at Chicago, 900 South Ashland Avenue, MBRB 4210 Chicago, IL 60607, USA. [7]Departament of Inorganic and Organic Chemistry and Biochemistry, University of Castilla–La Mancha Medical School, 02006 C/Almansa 14, Albacete, Spain. [8]Cellular and Tissue Therapies Branch, Division of Cellular and Gene Therapies, Center for Biologics and Research, U.S. Food and Drug Administration, Bethesda, MD 20892, USA. [9]Medical Staff, QEII Health Sciences Centre, Departments of Surgery and Medical Neuroscience, Dalhousie University, Halifax B3H 4R2, Canada.

*Corresponding author. E-mail: t.marquardt@eni-g.de

Through transcriptome profiling (fig. S8, A to C) we found that the shift of biophysical signatures in Dlk1-deficient motor neurons was accompanied by a shift in the expression of genes related to motor neuron type (Fig. 4A) but not of genes linked to generic or positional motor neuron identities (fig. S8, D and E), nor did we observe altered abundance of γ motor neurons (fig. S8, G to I). 58% of genes normally expressed by predominantly fast tibialis anterior and quadriceps motor pools were down-regulated, whereas genes normally expressed by the slow/intermediate soleus pool were up-regulated in the fast pools (Fig. 4A and fig. S8C).

A Dlk1-dependent gene normally associated with a fast motor pool transcriptome signature was Kcng4 (Fig. 4B and fig. S9, A to D), encoding a β subunit of delayed-rectifier K^+ channels (*14*). Because these channels help tune neuronal firing properties (*15*) and are expressed by early postnatal mouse motor neurons (*16*), we asked whether Kcng4 could influence motor neuron properties. Similar to Dlk1, excess Kcng4 promoted elevation of rheobase and firing frequency, while shortening repetitive firing periods (Fig. 4C and fig. S9, E to H). However, unlike Dlk1, excess Kcng4 did not shift other motor neuron properties (Fig. 4D

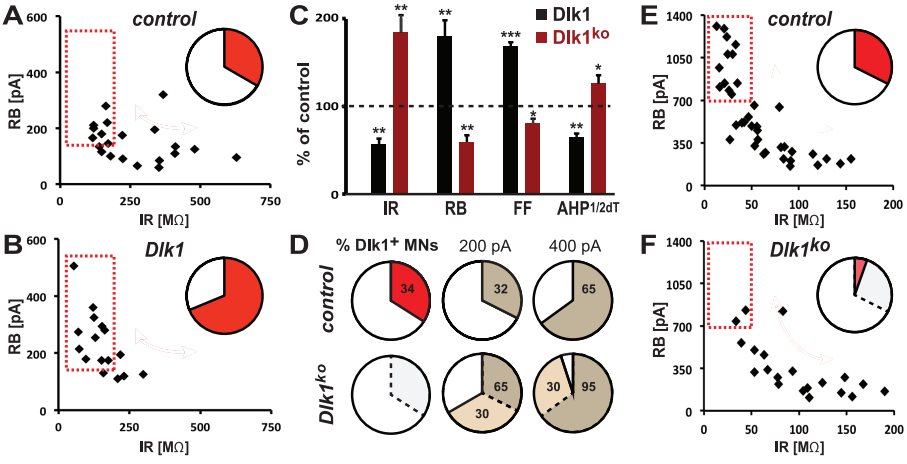

Fig. 2. Dlk1 is sufficient and necessary to promote a fast biophysical signature in motor neurons. (**A** and **B**) Biophysical signatures of control (GFP-transfected) (A) and *Dlk1*-transfected (B) embryonic day E12 to 15 chick motor neurons, based on rheobase (RB) against input resistance (IR) (*4*): Dlk1 promotes a shift toward a fast signature. Pie charts show the proportions of motor neurons inside the "fast quadrant" (arbitrarily delineated in red). (**C**) Black bars show that excess Dlk1 promotes a shift toward a fast biophysical signature: RB^{high}, IR^{low}, firing frequency $(FF)^{high}$, and afterhyperpolarization half-decay time $(AHPdT)^{short}$ ($n = 21$ control, 16 *Dlk1* motor neurons). Red bars indicate a converse shift toward a slow biophysical signature in $Dlk1^{KO}$ ($Dlk1^{-/-}$) as compared to control ($Dlk1^{+/+}$) mice: RB^{low}, IR^{high}, FF^{low}, $AHPdT^{long}$ ($n = 37$ control, 21 $Dlk1^{KO}$ motor neurons; tables S3 to S5). (**D**) Percentage of $Dlk1^+$ motor neurons in P10 mice (34 ± 4% SEM, 340 motor neurons, three P10 mice). A similar percentage (30%) of $Dlk1^{KO}$ motor neurons were prematurely recruited to repetitive firing. (**E** to **F**) Biophysical signatures of control (E) and $Dlk1^{KO}$ motor neurons (F) (boxed quadrant, pie charts: subpopulation with a fast signature): loss of motor neurons with a fast signature in $Dlk1^{KO}$ mice (F). Paired two-tailed *t*-test in (C). $^*P < 0.05$, $^{**}P < 0.01$, $^{***}P < 0.001$. Error bars indicate SEM.

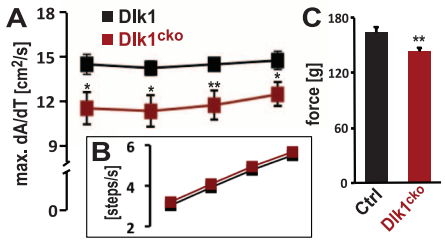

Fig. 3. Reduced peak force generation upon motor neuron–specific Dlk1 elimination. (**A** and **B**) Gait analysis during brief running tasks at 10, 20, 30, and 40 cm/s. (A) Reduced deceleration rates [maximal change of paw area (*dA*) over time (*dT*)] during the extensor phase of the gait cycle in $Dlk1^{CKO}$ ($Dlk1^{fx/fx}$; $Olig2^{Cre}$) as compared to control ($Dlk1^{fx/fx}$) mice ($n = 11$, 9 control $Dlk1^{CKO}$ mice, an average of three runs per condition). (**B**) Indistinguishable adaptation of stride frequency to increased running speeds by control and $Dlk1^{CKO}$ mice. (**C**) Reduced maximal limb force generation in $Dlk1^{CKO}$ mice (n = 11, 9 control $Dlk1^{CKO}$ mice). Paired two-tailed *t* test was used in (A) to (C). $^*P < 0.05$, $^{**}P < 0.01$. Error bars indicate SEM.

Fig. 4. Dlk1 is required for motor neuron type–specific gene expression, including the neural activity modulator Kcng4. (**A**) Motor pool transcriptome signatures (heat maps) showing the loss of fast [quadriceps (QC) and tibialis anterior (TA)] signatures and a shift toward a slow/intermediate [soleus (SL)] signature in $Dlk1^{KO}$ mouse QC/TA pools ($n = 4$ mice per pool, cutoff ≥1.5 fold, $P < 0.05$). (**B**) Loss of differential Kcng4 expression between TA/SL pools in P4 $Dlk1^{KO}$ mouse. (**C**) Excess Kcng4 ($n = 16$ motor neurons) partially recapitulates the promotion of fast properties by Dlk1 ($n = 16$ motor neurons) in chick motor neurons. Noncleavable $Dlk1^{NC}$ ($n = 10$ motor neurons), but not extracellular $Dlk1^{ES}$ ($n = 14$ motor neurons) nor Dll1 ($n = 17$ motor neurons), recapitulates Dlk1 activity. Excess Dlk1 had no effect on adjacent nontransfected motor neurons ($Dlk1^{AD}$, $n = 26$ motor neurons). Notch1 intracellular segment (NICD) abolishes Dlk1 effects on motor neuron properties ($n = 10$ motor neurons) (tables S6 and S7). (**D**) Dlk1 abolishes induction of the *UAS::luciferase* reporter by *Notch1:Gal4* in *Xenopus* embryos. Luciferase normalized to constitutive Renilla fluorescence ($n = 3$ samples per condition in three experiments). Analysis of variance (ANOVA) was used in (A) and two-tailed *t* test in (B) to (D). $^*P < 0.05$, $^{**}P < 0.01$, $^{***}P < 0.001$. Error bars indicate SEM.

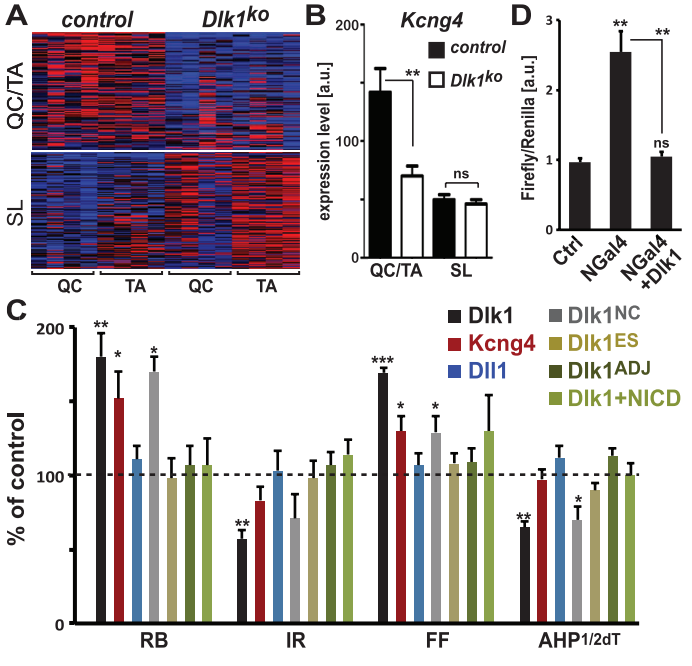

and fig. S9I). Thus, some but not all biophysical properties driven by Dlk1 are mediated by the secondary actor Kcng4.

The Dlk1 isoforms expressed in the mouse spinal cord can give rise to membrane-tethered or cleaved extracellular proteins (fig. S10, A and B) (*11*, *12*). We therefore forcedly expressed a noncleavable form of Dlk1 ($Dlk1^{NC}$) or the extracellular segment of Dlk1 ($Dlk1^{ES}$) (fig. S10B) in chick motor neurons. We observed that $Dlk1^{NC}$, but not $Dlk1^{ES}$, promoted fast properties (Fig. 4C). We further observed that only motor neurons forcedly expressing Dlk1, but not adjacent nontransfected motor neurons (fig. S10C), exhibited altered properties (Fig. 4C), together suggesting that Dlk1 operates cell-autonomously to promote a fast biophysical signature.

In preadipocytes, Dlk1 actions involve the inhibition of Notch signaling (*17*). Indeed, our expression of Dlk1 completely abolished the induction of a reporter for Notch activation in *Xenopus* embryos (Fig. 4D and fig. S10D). Moreover, forced expression of the canonical Notch activator Delta-like 1 (*18*) did not recapitulate the effects of excess Dlk1 on chick motor neuron properties (Fig. 4C). Furthermore, cotransfection of constitutively active Notch1 abolished the ability of excess Dlk1 to alter motor neuron properties (Fig. 4B), suggesting that Dlk1 action in motor neurons relies on Notch inhibition. Because Notch signaling is generally involved in cell fate decisions (*18*), it is likely that Dlk1 action involves additional pathways to promote fast motor neuron identity.

Here we have shown that Dlk1 is both necessary and sufficient for determining fast motor neurons and their corresponding biophysical signature in the mouse and chick (fig. S10E). Dlk1 implements expression of motor neuron type–specific genes such as Kcng4, which modulates a subset of neural activity parameters. The result is a biophysical signature in motor neurons that supports peak neuromuscular outputs. The strategy by which expression of a neural activity modulator is confined to a subset of neurons may similarly drive functional diversity elsewhere in the developing nervous system.

The overall lack of topographic organization for slow or fast motor neurons suggests that motor neuron type is acquired independently of the mechanisms that, before muscle innervation, determine motor neuron positional (column or pool) identities (*19*, *20*). We still do not know when subsets of motor neurons acquire type-specific biophysical signatures, to what extent motor neuron functional diversification involves signals from muscle (*21*), how motor neuron and muscle fiber types are matched (*22*–*24*), or what causes the differential vulnerability of motor neuron types to disease or aging (*25*). However, 57 years after the characterization of fast and slow motor neurons (*1*), we can now have insight into the molecular mechanisms that control their development and function.

References and Notes

1. J. C. Eccles, R. M. Eccles, A. Lundberg, *Nature* **179**, 866–868 (1957).
2. R. E. Burke, D. N. Levine, F. E. Zajac 3rd, P. Tsairis, W. K. Engel, *Science* **174**, 709–712 (1971).
3. D. Kernell, *The Motoneuron and Its Muscle Fibers* (Oxford Univ. Press, New York, ed. 1, 2006).
4. J. E. Zengel, S. A. Reid, G. W. Sypert, J. B. Munson, *J. Neurophysiol.* **53**, 1323–1344 (1985).
5. R. Bakels, D. Kernell, *J. Physiol.* **463**, 307–324 (1993).
6. M. Manuel, C. J. Heckman, *J. Neurosci.* **31**, 15188–15194 (2011).
7. E. Henneman, *Science* **126**, 1345–1347 (1957).
8. D. Kernell, *Science* **152**, 1637–1639 (1966).
9. M. Gustafsson, M. J. Pinter, *Trends Neurosci.* **8**, 431–433 (1985).
10. E. Davis *et al.*, *Curr. Biol.* **14**, 1858–1862 (2004).
11. H. S. Sul, *Mol. Endocrinol.* **23**, 1717–1725 (2009).
12. S. R. Ferrón *et al.*, *Nature* **475**, 381–385 (2011).
13. S. Grillner, in *Handbook of Physiology: The Nervous System, Motor Control,* Vol. 2, V. B. Brooks, Ed. (American Physiological Society, Bethesda, MD 1981), pp. 1179–1236.
14. N. Ottschytsch, A. Raes, D. Van Hoorick, D. J. Snyders, *Proc. Natl. Acad. Sci. U.S.A.* **99**, 7986–7991 (2002).
15. H. Murakoshi, J. S. Trimmer, *J. Neurosci.* **19**, 1728–1735 (1999).
16. J. M. Wilson, J. Rempel, R. M. Brownstone, *J. Comp. Neurol.* **474**, 13–23 (2004).
17. M. L. Nueda, V. Baladrón, B. Sánchez-Solana, M. A. Ballesteros, J. Laborda, *J. Mol. Biol.* **367**, 1281–1293 (2007).
18. K. Hori, A. Sen, S. Artavanis-Tsakonas, *J. Cell Sci.* **126**, 2135–2140 (2013).
19. W. A. Alaynick, T. M. Jessell, S. L. Pfaff, *Cell* **146**, 178, e1 (2011).
20. J. S. Dasen, T. M. Jessell, *Curr. Top. Dev. Biol.* **88**, 169–200 (2009).
21. J. V. Chakkalakal, H. Nishimune, J. L. Ruas, B. M. Spiegelman, J. R. Sanes, *Development* **137**, 3489–3499 (2010).
22. W. J. Thompson, L. A. Sutton, D. A. Riley, *Nature* **309**, 709–711 (1984).
23. T. Fladby, J. K. Jansen, *Development* **109**, 723–732 (1990).
24. V. F. Rafuse, L. D. Milner, L. T. Landmesser, *J. Neurosci.* **16**, 6864–6877 (1996).
25. K. C. Kanning, A. Kaplan, C. E. Henderson, *Annu. Rev. Neurosci.* **33**, 409–440 (2010).

Acknowledgments: We thank A. Klusowski, B. Veith, T. V. Bui, and T. G. Hampton for technical support; S. Schiaffino and K. Kawakami for reagents; P. D'Adamo for phenotyping service; and O. Shomroni and S. Bonn for bioinformatics advice. This research received funding from the European Research Council under the European Union's Seventh Framework Programme (FP/2007-2013)/ERC Grant Agreement 311710-MU TUNING and the Emmy-Noether Program of the Deutsche Forschungsgemeinschaft (MA4278/1-1). S.R.B. was supported by the Center for Biologics Evaluation and Research, Food and Drug Administration, operating funds; O.S. by the Emmy-Noether Program (SCHL592-4); R.M.B. by the Canadian Institutes of Health Research, Canada Research Chairs Program, Canada Foundation for Innovation, and Nova Scotia Research and Innovation Trust; and J.L. by the Ministerio de Educación y Ciencia, Spain, from whom $Dlk1^{ko}$ mice are available through a materials transfer agreement. $Dlk1^{fx}$ mice are deposited at jaxmice.jax.org (no. 019074). Notch1:Gal4 is available from R. Kopan (Cincinnati Children's Hospital Medical Center). ENI-G is a cooperation of University Medical Center Göttingen and the Max-Planck Society.

Supplementary Materials

www.sciencemag.org/content/343/6176/1264/suppl/DC1
Materials and Methods
Supplementary Text
Figs. S1 to S10
Tables S1 to S9
References (*26*–*43*)

25 September 2013; accepted 14 February 2014
10.1126/science.1246448

cell sciences®
cytokine center

www.cellsciences.com

Buy one, get one free

Stock up now on select cytokines, growth factors and chemokines.

Order any two vials from this list for just $235
Enter promo code CYT241 when you place your order on-line or mention the promo code to get your discount when calling our toll-free number 888-769-1246.

These recombinant proteins are low endotoxin, carrier-free, highly pure, biologically active and suitable for cell culture and animal studies. Get two of the same item or pick any two different items from the list.* See our web site for complete product specifications.

Browse our web site of recombinant proteins, including hundreds more cytokines, growth factors, chemokines and neurotrophins. Bulk quantities of these proteins are available at competitive pricing. Call or visit our web site for details. Cell Sciences also carries corresponding antibodies and ELISA kits.

Catalog No:	Item:	Size:
CRB100B	Recombinant Human BMP-2	10 µg
CRC400B	Recombinant Human CNTF	20 µg
CRF000B	Recombinant Human FGF-acidic/FGF1	50 µg
CRF001B	Recombinant Human FGF-basic/FGF2	50 µg
CRK300B	Recombinant Human FGF-7/KGF	10 µg
CRG300B	Recombinant Human G-CSF/CSF3	10 µg
CRG100B	Recombinant Human GM-CSF/CSF2	20 µg
CRG101B	Recombinant Mouse GM-CSF/CSF2	20 µg
CRG500B	Recombinant Human GRO-alpha/CXCL1	25 µg
CRG502B	Recombinant Rat GRO-alpha/KC/CXCL1	25 µg
CRI004B	Recombinant Human IFN-alpha 2b	100 µg
CRI000B	Recombinant Human IFN-gamma	100 µg
CRI001B	Recombinant Mouse IFN-gamma	100 µg
CRI002B	Recombinant Rat IFN-gamma	100 µg
CRI500B	Recombinant Human IGF-1	100 µg
CRI100B	Recombinant Human IL-2	50 µg
CRI153B	Recombinant Human IL-10	10 µg
CRI137B	Recombinant Human IL-15	10 µg
CRI162B	Recombinant Human IL-17	25 µg
CRI172B	Recombinant Human IL-21	10 µg
CRI225B	Recombinant Human IL-33	10 µg
CRM151B	Recombinant Human M-CSF/CSF1	10 µg
CRR000B	Recombinant Human RANTES/CCL5	20 µg
CRS000B	Recombinant Human SDF-1 alpha	10 µg
CRS002B	Recombinant Human SDF-1 beta	10 µg
CRT100B	Recombinant Human TNF-alpha	50 µg
CRT192B	Recombinant Mouse TNF-alpha	20 µg
CRV000B	Recombinant Human VEGF 165	10 µg
CRV014B	Recombinant Mouse VEGF 165	10 µg

* Good on orders in US and Canada only. This offer may not be combined with other offers or discounts. All products for research use only.

CELL SCIENCES INC • 480 NEPONSET STREET, BUILDING 12A, CANTON, MA 02021 • INFO@CELLSCIENCES.COM
TOLL FREE: (888) 769-1246 • TEL: (781) 828-0610 • FAX: (781) 828-0542 • WEB WWW.CELLSCIENCES.COM

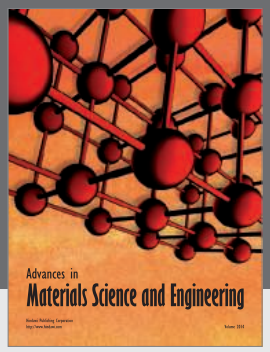

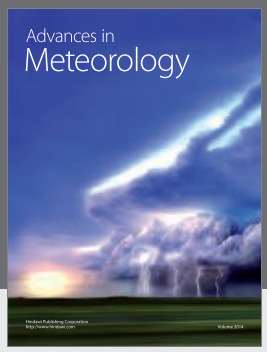

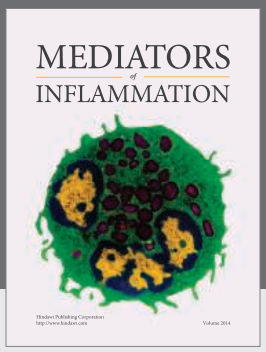

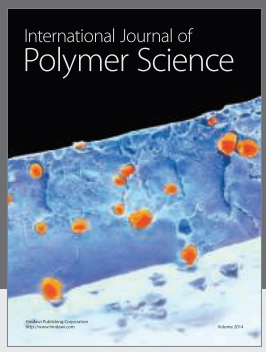

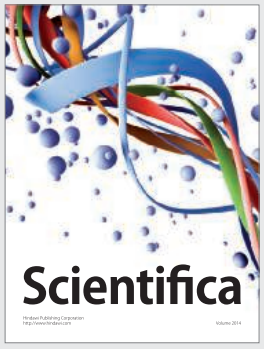

Hindawi
Submit your manuscripts at
http://www.hindawi.com

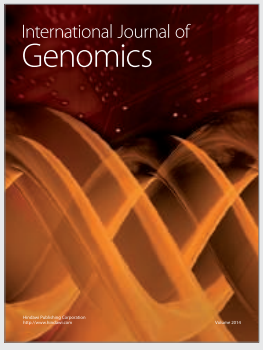

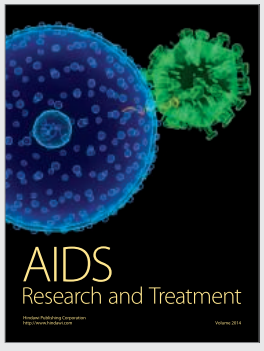

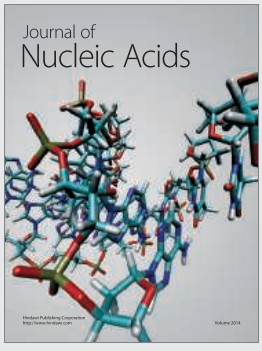

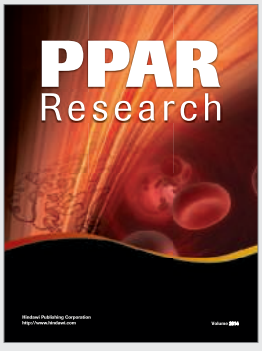

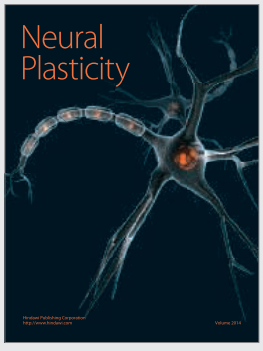

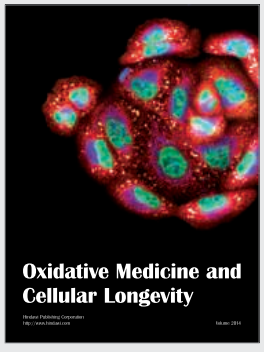

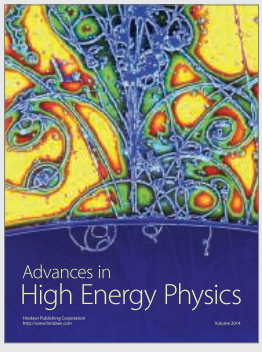

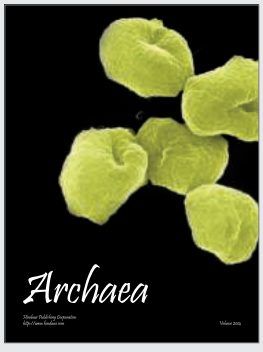

BD Horizon™ Brilliant Ultraviolet™ and the BD LSRFortessa™ X-20

Ultraviolet laser and reagents expand research capabilities and clarify results.

BD

Helping all people live healthy lives

A whole new spectrum of choice.

BD Horizon Brilliant Ultraviolet reagents open a new world of choice and productivity for scientists who use multicolor flow cytometry in their research. By adding the ultraviolet range to panel design, markers can be spread over more lasers, reducing compensation requirements of the experiment.

Use of these new ultraviolet excitable dyes can reduce setup time because there is less need to adjust for compensation.

When the dyes are combined with a dedicated ultraviolet laser position, your options and capabilities are further expanded.

Find out how you can add a whole new spectrum of productivity to your research with BD Horizon Brilliant Ultraviolet dyes and the ultraviolet capable BD LSRFortessa X-20 special order analyzer. Tools and information available at **bdbiosciences.com/go/ultra.**

For Research Use Only. Not for use in diagnostic or therapeutic procedures.
BD, BD Logo and all other trademarks are property of Becton, Dickinson and Company. © 2014 BD
23-15992-00

BD Biosciences
2350 Qume Drive
San Jose, CA 95131
bdbiosciences.com

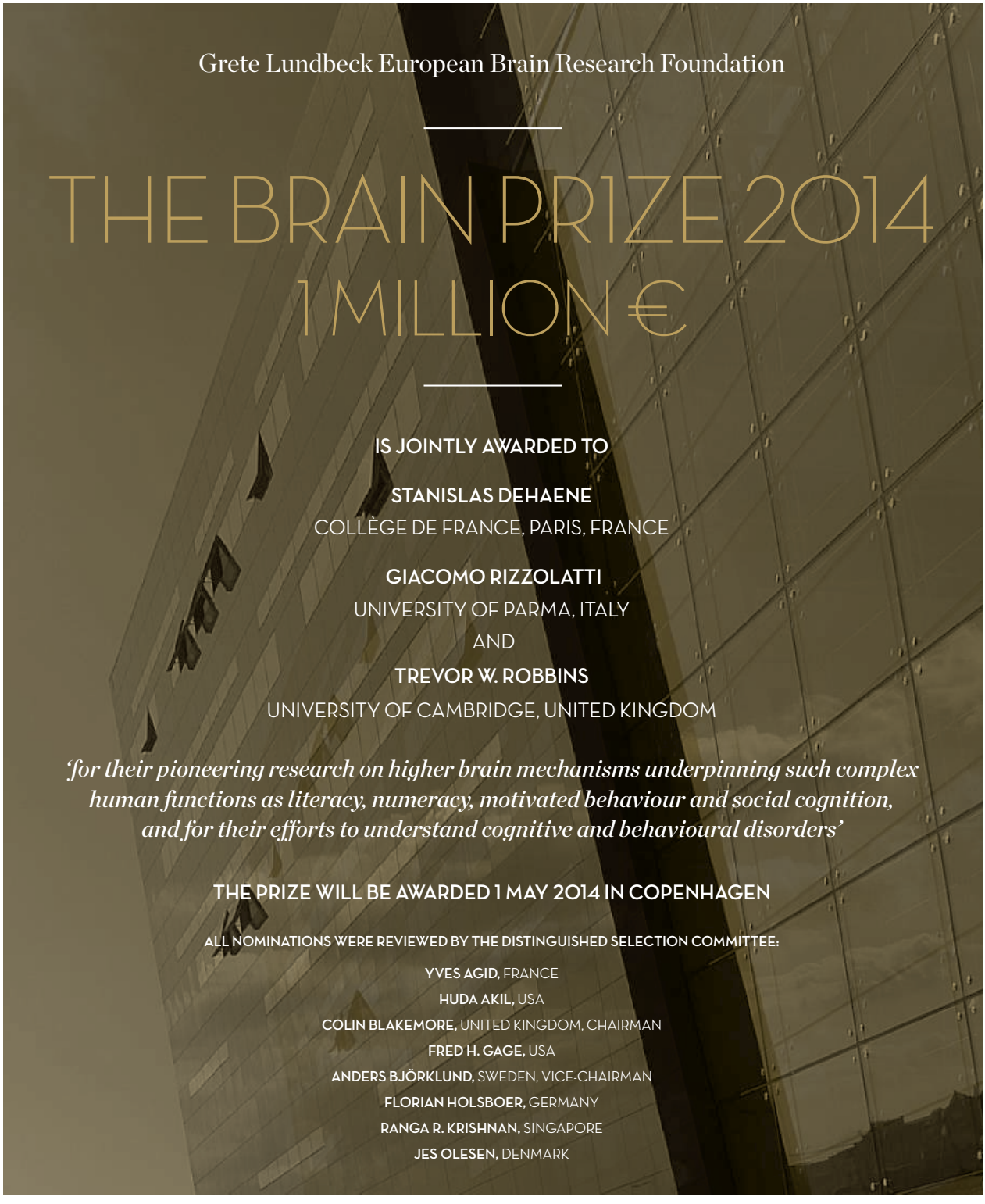

Grete Lundbeck European Brain Research Foundation

THE BRAIN PRIZE 2014
1 MILLION €

IS JOINTLY AWARDED TO

STANISLAS DEHAENE
COLLÈGE DE FRANCE, PARIS, FRANCE

GIACOMO RIZZOLATTI
UNIVERSITY OF PARMA, ITALY
AND
TREVOR W. ROBBINS
UNIVERSITY OF CAMBRIDGE, UNITED KINGDOM

'for their pioneering research on higher brain mechanisms underpinning such complex human functions as literacy, numeracy, motivated behaviour and social cognition, and for their efforts to understand cognitive and behavioural disorders'

THE PRIZE WILL BE AWARDED 1 MAY 2014 IN COPENHAGEN

ALL NOMINATIONS WERE REVIEWED BY THE DISTINGUISHED SELECTION COMMITTEE:

YVES AGID, FRANCE
HUDA AKIL, USA
COLIN BLAKEMORE, UNITED KINGDOM, CHAIRMAN
FRED H. GAGE, USA
ANDERS BJÖRKLUND, SWEDEN, VICE-CHAIRMAN
FLORIAN HOLSBOER, GERMANY
RANGA R. KRISHNAN, SINGAPORE
JES OLESEN, DENMARK

GRETE LUNDBECK EUROPEAN BRAIN RESEARCH FOUNDATION

THE BRAIN PRIZE

The Brain Prize recognizes and rewards outstanding contributions to European neuroscience, from basic to clinical

Science & Diplomacy

Science & Diplomacy provides an open access forum for rigorous thought, analysis, and insight to serve stakeholders who develop, implement, or teach all aspects of science and diplomacy. Learn more about the latest ideas in science diplomacy and receive regular updates by following @SciDip on Twitter and registering for free at **www.sciencediplomacy.org/user/register**.

WWW.SCIENCEDIPLOMACY.ORG

Science & Diplomacy is published by the Center for Science Diplomacy of the American Association for the Advancement of Science (AAAS), the world's largest general scientific society.

Science & Diplomacy

AAAS
ADVANCING SCIENCE SERVING SOCIETY

CALL FOR APPLICATIONS

CHANEL
RECHERCHE ET TECHNOLOGIE
RESEARCH AND TECHNOLOGY

CHANEL - CE.R.I.E.S. RESEARCH AWARD

The CHANEL - CE.R.I.E.S. Research Award of 40,000 € is intended to honor a scientific researcher with a proven track record in fundamental or clinical research work, for a one-year period, on the subject of:

PHYSIOLOGY OR BIOLOGY OF HEALTHY SKIN AND/OR ITS REACTIONS TO ENVIRONMENTAL FACTORS

Previous Research Award Winners:

2013	Robert L. Modlin, M.D., Los Angeles, USA
2012	Martin Röcken, M.D., Ph.D., Tübingen, Germany
2011	Joke A. Bouwstra, Ph.D., Leiden, Netherlands
2010	Howard Y. Chang, M.D., Ph.D., Stanford, USA
2009	Sabine Werner, Ph.D., Zurich, Switzerland
2008	Paul A. Khavari, M.D., Ph.D., Stanford, USA
2007	Richard L. Gallo, M.D., Ph.D., San Diego, USA
2006	Irwin McLean, Ph.D., DSc, FRSE, Dundee, Scotland, UK
2005	Masayuki Amagaï, M.D., Ph.D., Tokyo, Japan
2004	Thomas Schwarz, M.D., Kiel, Germany
2003	Angela M. Christiano, Ph.D., New York, USA
2002	Dennis R. Roop, Ph.D., Houston, USA
2001	Fiona M. Watt, D.Phil., London, UK
2000	Michael Karin, Ph.D., San Diego, USA
1999	Jonathan Rees, M.D., Edinburgh, UK
1998	Jean Krutmann, M.D., Düsseldorf, Germany
1997	Jens-Michael Schröder, Ph.D., Kiel, Germany
1996	Akira Takashima, M.D., Ph.D., Dallas, USA

Deadline for applications: May 16, 2014

http://research-technology.chanel.com/award

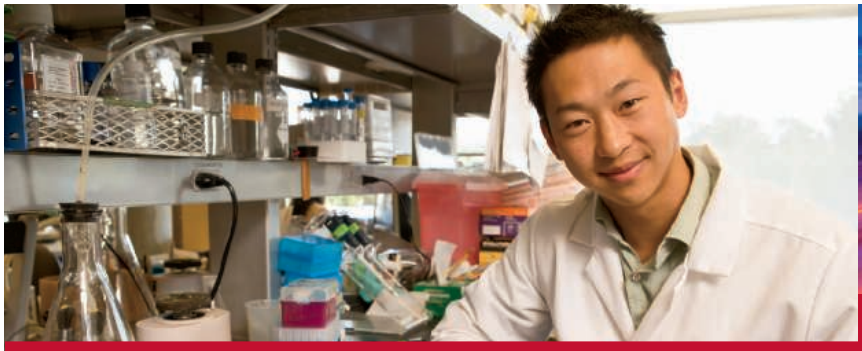

AUTONOMY. SECURITY. AND $1.625 MILLION.

For researchers pursuing promising but high-risk projects, Pathway to Stop Diabetes® provides an accelerated road for research breakthroughs. Now in our second year, we are again offering grants of five to seven years and $1.625 million to attract more brilliant scientists to the field of diabetes research, regardless of their current field of study. Learn more about Pathway today. And secure a more promising future for yourself and those living with diabetes, every day.

PATHWAY SPONSORS

novo nordisk® SANOFI Lilly AstraZeneca

STOP DIABETES®

PATHWAY TO STOP DIABETES®

American Diabetes Association. RESEARCH FOUNDATION

APPLICATIONS BY NOMINATION ONLY.
DEADLINE: JULY 1, 2014.
FIND OUT MORE AT
DIABETES.ORG/PATHWAY

For your career in science, there's only one **Science**

Introducing **myIDP**: A career plan customized *for* you, *by* you.

- The first and only online app that helps scientists prepare their very own individual development plan.
- Recommended by leading professional societies and the NIH.
- Developed by scientists at FASEB, UCSF, and the Medical College of Wisconsin in collaboration with AAAS and *Science* Careers, with support from the Burroughs Wellcome Fund.

my IDP Science Careers

Visit the website and start planning today!
myIDP.sciencecareers.org

AAAS In partnership with: advancing the life sciences 1912-2012 FASEB Federation of American Societies for Experimental Biology

UCSF University of California San Francisco

MEDICAL COLLEGE OF WISCONSIN

BURROUGHS WELLCOME FUND

Patient in a Dish: Toxicologists Embrace Stem Cells

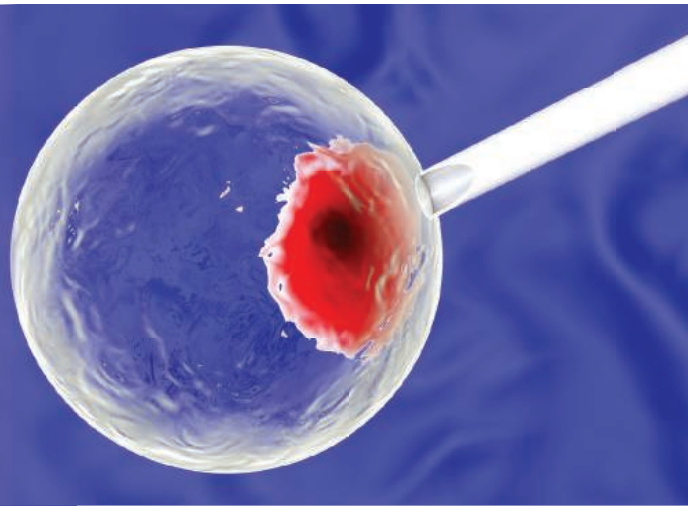

Toxicity assays based on embryonic and adult stem cells could soon replace unreliable cellular and animal testing, helping toxicologists detect which drugs might be dangerous long before they reach the market.

By Alan Dove

Pharmaceutical researchers live with a recurring nightmare. After spending years and billions of dollars developing a new drug, carefully shepherding it through preclinical and clinical trials, and finally receiving government approval to deliver it to patients, the compound suddenly starts hurting some of the people it was supposed to help. The promise of a new therapy collapses instantly into a morass of lost research investments and litigation.

"If you look back over the last 10 to 12 years, this is happening continuously, every year there are several drugs that go all the way [to market] and then have to be withdrawn or have their use significantly curtailed," says Stephen Minger, chief scientist for life sciences at **GE Healthcare** in Cardiff, United Kingdom.

The problem stems from the limitations of toxicology assays. In the standard drug approval process, researchers test a drug's toxicity in animals and relatively small numbers of people. Animal models don't represent human physiology accurately, and clinical trials seldom include a large enough population to identify rare idiosyncratic effects.

The ideal solution would be to grow realistic human tissues and organs in the lab, mimicking the physiology of a large population of patients without the cost and ethical baggage of massive clinical trials. Armed with the latest technologies for culturing embryonic and adult-derived human stem cells, toxicologists and cell biologists are now starting to do exactly that.

HEART LINES

Traditionally, toxicologists have tested compounds in immortalized cell lines and primary tissue cultures. Immortalized lines are effectively lab-adapted tumors that bear only a passing resemblance to cells in the body. Primary cultures represent a tissue's normal physiology more realistically, but don't live long enough for extended experiments.

Stem cells combine the best traits of both types of cultures, as they can be grown continuously and induced to differentiate into realistic tissues of all types. About five years ago, Minger and his colleagues began to exploit those characteristics to develop new assays for drug toxicity. "We've taken human embryonic stem cells and converted them into large populations of adult human cardiomyocytes that in our hands and the hands of our customers are extremely predictive," says Minger, adding that "at least retrospectively, we can show toxicity in compounds that have had to be withdrawn by the [U.S.] Food and Drug Administration that never had a hint of toxicity [in traditional assays]." Several pharmaceutical companies are now using GE's cardiomyocyte assay, called Cytiva, to test drugs in development.

Other companies are also developing stem cell-based assays for cardiac toxicity. **Cellular Dynamics** in Madison, Wisconsin, for example, offers a competing line of cardiomyocytes, called iCell, derived from induced pluripotent stem (iPS) cells. Unlike embryonic stem cells, iPS cells come from adult volunteers. A combination of growth factors reprograms the adult cells into an embryonic-like state, from which they can be directed to differentiate into all major tissue types.

For researchers who want to develop their own stem cell assays, reagent choices abound. General lab supply companies now offer culture media for stem cells, and specialty firms such as **Cellectis** in Paris, France and **Stem Cell Technologies** in Vancouver, British Columbia also cater to the field. Whichever path they choose, assay developers must address several problems to continued>

"We use a stem cell assay to help us identify those compounds that are clearly toxic and clearly don't need to go forward."

— Robert Chapin

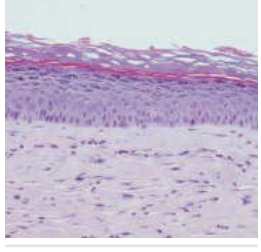

A model of human skin derived from induced pluripotent stem cells by researchers in the SCR&Tox program.

Upcoming Features

Genomics—April 11
Microscopy—May 2
Big Data—June 13

CREDITS: (FROM TOP) JENS GOEPFERT/SHUTTERSTOCK.COM; IMAGE COURTESY VANIA ROSAS.

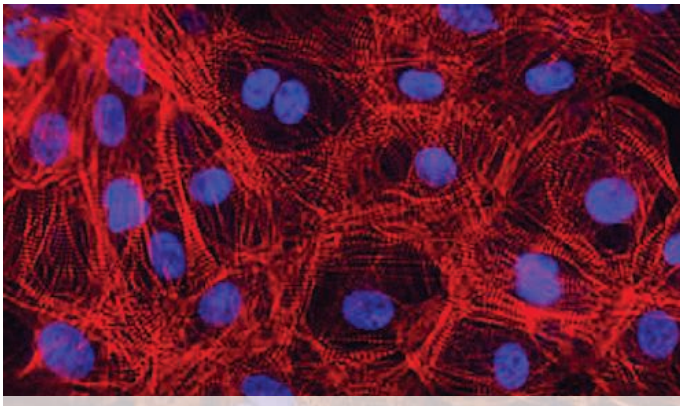

Embryonic Stem Cell-Derived Cardiomyocytes

"We've taken human embryonic stem cells and converted them into large populations of adult human cardiomyocytes that in our hands and the hands of our customers are extremely predictive."

—Stephen Minger

produce useful toxicology tools. While many of the protocols to differentiate stem cells into particular tissues seem straightforward, the resulting cells are often in an im-mature state and mixed with partially differentiated progenitor cells.

Assays for pharmaceutical research also have to be consistent, which is a major challenge in the stem cell field. "A lot of the reagents that we use for the production of [stem] cells … are notoriously variable," says Minger. To address that, his team broke down the process of cardiomyocyte differentiation into discrete steps, then isolated and controlled as many variables as possible. The result is a production line that consistently produces cultures where at least 50% of the cells are mature cardiomyocytes.

DRUGS AND DEVELOPMENT

Generating fully mature adult cells will likely remain a major challenge, given the inherent biology of stem cells. "Stem cells … are really designed to do a good job of getting the fetus set up and structuring the body for its initial stab at life," says Robert Chapin, senior research fellow at **Pfizer** in Groton, Connecticut. However, the immaturity of stem cell-derived tissues is more a feature than a bug for Chapin and his colleagues, who study developmental toxicity.

Indeed, stem cell systems should be nearly ideal for determining whether a compound will be toxic to a developing fetus, especially if researchers can recapitulate the biology of multiple tissues in a single culture. "One of the [goals] is getting multiple cell types derived from stem cells together [in] 3-D cultures, because these cells don't operate in isolation," says Donald Stedman, senior principal scientist at Pfizer.

Pfizer now incorporates its own murine stem cell-based assay into its drug development pipeline to test for developmental toxicity. Regulatory agencies rely heavily on mouse and rabbit preclinical data to predict drugs' developmental effects in humans, rather than insist on clinical trials in pregnant women. A drug that is toxic to mouse embryos won't get approved for use in pregnancy, so companies want to weed out compounds likely to fail in mice.

To validate the assay, Chapin's team tested over 90 compounds that had been studied previously in animals, and found nearly perfect agreement between the stem cell assay and real developmental toxicity results. "We use a stem cell assay to help us identify those compounds that are clearly toxic and clearly don't need to go forward, and if we're lucky and we run an unknown compound through the assay and it comes out very clean, then it's easy to give that one a nice bill of health," says Chapin.

Such extreme results are the exception rather than the rule. More often, the investigators find that new compounds exhibit some toxicity at some doses. "In practice we wind up making judgment calls and talking about probabilities," Chapin explains.

The short track record and probabilistic results of stem cell assays have slowed their adoption. "I would say there's been quite a bit of resistance within the pharma community to [stem cell-based assays], because they're uncertain what [the technology] is telling them," says GE's Minger. For example, he adds, "if you see a compound that's toxic on our [Cytiva] cells that's not toxic on all the other standard tests, what do you believe?"

Early proponents of stem cell assays are confident those concerns will erode as more data come in. Researchers may also be swayed by the unique capabilities of stem cell assays, such as more direct tests of human developmental toxicity. "I'm hoping that from the developmental toxicity side there will be assays developed that are predictive using human embryonic stem cells, and we'll be able to decide whether those have any more or less value than the animal [systems] that we use," says Stedman.

TEAM EFFORTS

Using stem cells to replace animal testing is also a popular idea in Europe. In 2011, the European Commission and a consortium of cosmetics manufacturers jointly funded the Safety Evaluation Ultimately Replacing Animal Testing (SEURAT) program, which encompasses several large projects aimed at developing alternative safety tests for cosmetics and other chemicals. Meanwhile, European authorities began restricting animal testing, culminating in a full Europe-wide ban on the sale of animal-tested cosmetics in March of 2013.

Within the SEURAT cluster, the Stem Cells for Relevant, Efficient, and Normalized Toxicology (**SCR&Tox**) project focuses entirely on developing stem cell-based assays for toxicity in five types of tissues: heart, liver, muscle, skin, and nerves. Though cosmetics companies fund SEURAT, pharmaceutical researchers will likely find many of SCR&Tox's assays useful as well. "The objective of the SEURAT cluster is to replace in vivo repeated dose toxicity testing," says Vania Rosas, project manager for SCR&Tox.

CREDIT: IMAGE COURTESY OF GE HEALTHCARE

Featured Participants

Cellectis
www.cellectis.com

Cellular Dynamics
www.cellulardynamics.com

GE Life Sciences
www.gelifesciences.com

Hoffmann-La Roche
www.roche.com

Nuffield College
www.nuff.ox.ac.uk

Pfizer
www.pfizer.com

SCR&Tox
www.scrtox.eu

StemBANCC
stembancc.org

Stem Cell Technologies
stemcell.com

University of Applied Sciences of Western Switzerland
www.hes-so.ch/en

"At the end of the day we expect to have what we call the petri dish of the 21st century, that's to have a culture embedded in a biochip where all the biosensors ... are integrated." — Luc Stoppini

To do that, SCR&Tox researchers have been working on differentiating iPS cells into the five mature tissue types the project studies. Rosas says they've confronted many of the same problems other investigators have had, especially the tendency of stem cells to retain immature characteristics even after differentiation. Nonetheless, SCR&Tox-developed assays will soon find their way into industry laboratories for testing and validation, and Rosas hopes regulatory agencies will begin accepting stem cell-based toxicity data for cosmetics within a few years.

Another large European research project, **StemBANCC**, is also working to improve the use of stem cells in toxicology assays. While SCR&Tox researchers are developing general-purpose toxicology assays based on iPS cells derived from healthy volunteers, StemBANCC scientists are focusing on iPS cells derived from 500 patients with various diseases. These disease-specific cells will form the basis for a new generation of drug development assays, including toxicological tests.

"The generation of induced pluripotent cells is just a technical goal. More important [is] to then differentiate them into a cell type that is relevant for a disease … and then try to understand the disease in a dish," says Martin Graf, head of the stem cell platform at **Hoffmann-La Roche** in Basel, Switzerland and one of the leaders of the StemBANCC project.

Besides cell samples, StemBANCC will also collect detailed clinical data from the patients. "One of the big things about this project is the depth of the clinical phenotyping that we're going to be doing on these patients, I think the real value of the cell lines subsequently is having that phenotyping information," says Zameel Cader, academic director of StemBANCC and a professor of clinical neurosciences at **Nuffield College** in Oxford, United Kingdom. Besides a diagnosis and history, each StemBANCC line will come with extensive data from diagnostic tests characterizing the patient's disease progression, treatments, and drug reactions.

Ultimately, the project seeks to give pharmaceutical researchers realistic laboratory models of individual patients, yielding more reliable predictions of a new drug's efficacy and toxicity long before it reaches the clinic. "I think in vitro toxicology using patient-derived material is really the first step towards trying to address the fall-off in drugs during their development," says Cader.

THIS IS YOUR BRAIN ON A CHIP

Other researchers are taking the patient-in-a-dish concept a step further by trying to grow multiple tissue types together in organ-like 3-D cultures. Luc Stoppini, professor of tissue engineering at the **University of Applied Sciences of Western Switzerland** in Delemont, Switzerland, began such a project after an initial disappointment with conventional stem cell culture. "People were claiming that they had [stem cell-derived] neurons, because they were expressing beta-3 tubulin which is one of the markers of neurons, but when I looked at them they were like fibroblasts, not really differentiating with axons, neurites, and synapses," says Stoppini.

As a neurobiologist, Stoppini wanted a more realistic neuronal system. Allowing the stem cell-derived "neurons" to grow in a 3-D culture system caused them to develop more neuronal shapes, and the cells also began transmitting electrical signals. The trick was to let the 3-D cultures grow much longer than traditional flat cultures; the neurons often continue developing for several months. "The message here is that we really need time to get human neuron function," says Stoppini. He adds that this slow development may make it hard to scale some assays to the high throughput needs of pharmaceutical companies.

Nonetheless, the payoff for getting such a system working could be huge. In particular, Stoppini says the long-term cultures can develop some of the non-neuronal cell types that are crucial for normal nervous system functions, such as astrocytes and oligodendrocytes. His team can now derive these miniature brains from both embryonic and iPs cells, raising the possibility of mimicking specific neural diseases with patient-derived cells.

The investigators have also taken the process a step further, growing 3-D brain cultures on microfluidic chips dotted with electrical sensors. Microcapillaries bring fresh nutrients to the culture while the sensors record electrical activity.

Stoppini is also connecting the brain chip to other stem cell-derived microfluidic organ cultures. Future pharmaceutical researchers might be able to feed an experimental drug into a patient-derived intestine, which would then deliver its metabolites through a vascular system to a miniature liver, finally affecting the activity of an in vitro brain. "At the end of the day we expect to have what we call the petri dish of the 21st century, that's to have a culture embedded in a biochip where all the biosensors … are integrated," says Stoppini.

The latest iteration of the technology also includes a Wi-Fi transmitter, so researchers can monitor the system without even opening the incubator. Stoppini adds that, "it's an extraordinary period that's opened new avenues of research by combining the biological tools [with electronics] … so we can really have some glimpse of how these things are working."

Alan Dove is a science writer and editor based in Massachusetts.

DOI: 10.1126/science.opms.p1400083

CELL AND BIOCHEMICAL ASSAY DETECTION

GloMax Discover is an integrated multimode detection plate reader system that offers scientists an integrated system to easily study cell signaling and metabolism, while monitoring cell viability, apoptosis, and cytotoxicity, or to study gene expression with a wide variety of reporter assays. The system offers a broad dynamic range for both strong and weak bioluminescence experimental samples, superior luminescence sensitivity and low well-to-well cross talk, enabling users to generate more usable data from each experiment. GloMax Discover provides flexible use of filters for fluorescence intensity, BRET, FRET, filtered luminescence, and ultraviolet-visible absorbance measurements as well as seamless integration with industry-leading bioluminescent assays from Promega. The GloMax Discover software was developed with the goal of designing elegant, easy-to-use, and high-performance systems in mind. The software provides quick and easy navigation through the control options, preloaded assay protocols, and drag-and-drop protocol customization.

Promega

For info: 608-274-4330 | www.promega.com/discover

LABORATORY INFORMATION MANAGEMENT SYSTEMS

The new Laboratory Information Management Systems (LIMS) software is specifically designed for laboratories providing drug screening. The LIMSABC software provides LIMS users with options that have never been available before in labs. With this cloud LIMS, users can track point of care test results, prescribed medications, and create reports as well as manage clients, patients, and projects in addition to many other things. This is the first cloud LIMS available that will handle all of the tasks necessary for running and maintaining an efficient and state-of-the-art toxicology laboratory. The ability to efficiently test and document drug screening results is important in the lab; however, it is equally important to be able to e-mail, text, fax, and have the reports available online as soon as possible for the client. This immediate access to data is not only important for the toxicology lab's clients, but also essential in boosting the reputation of the lab for having the ability to provide reliable results and findings quickly and efficiently.

LIMSABC

For info: 800-834-8618 | www.limsabc.com

GPCR PROTEIN DETECTION

The ClonePix 2 System is proven effective for rapidly assessing endogenous G-protein-coupled receptor (GPCR) target protein expression levels in mammalian cell lines and selecting high-expressing clones. Unlike conventional methods and assays that have significant sensitivity and throughput limitations, the ClonePix 2 System provides a unique solution to identify and select a wide range of expression levels of endogenous GPCRs in situ. The ClonePix 2 System offers the necessary sensitivity to detect endogenous levels of protein limited to cell surface expression by utilizing robust white light and fluorescent imaging, followed by rapid selection of high expressing clones. This technology platform enables high throughput screening and picking of up to 10,000 mammalian clones in three weeks. The ClonePix 2 System thereby maximizes workflow efficiency and increases the probability of finding high-quality GPCR-expressing cells.

Molecular Devices

For info: 800-635-5577 | www.moleculardevices.com/clonepix

TRANSFECTION REAGENT

Lipofectamine 3000 is the company's most efficient and versatile transfection reagent for nucleic acid delivery in the broadest spectrum of cell lines. The product increases efficiency up to 10-fold in difficult-to-transfect cells, which is key for researchers working with more biologically relevant cell models. Its superior transfection efficiency, coupled with the reduction of cytotoxicity-associated cell alteration, provides consistent results and more significant experiments. Working with biologically relevant cell models provides researchers with more meaningful answers to their research questions. The lack of lipid-based transfection products that efficiently transfect these cell types has challenged researchers for many years. To overcome these obstacles, Lipofectamine 3000 is designed to optimize every step in the transfection process and deliver superior performance and improved cell viability in hard-to-transfect cells researchers care about.

Life Technologies

For info: 800-955-6288 | www.lifetechnologies.com/3000

STABLE CELL LINES

The new stable cell lines express endogenous or recombinant proteins and are available in a ready-to-use format to facilitate your research efforts. Using the stable cell lines not only provides an optimized solution for manufacture of therapeutic and diagnostic protein, but also for applications in drug screening, pharmacological research, and toxicological studies. The extensive portfolio of ready-to-use stable cell lines available includes: receptors (RAR α, IGF1 receptor, motilin receptor [MLNR]); ion channels (CFTR, Nav1.7, Kv1.5); cell signaling (Notch, JNK, NF-κB, ERK); phosphodiesterases (aequorin, CNGA2, PDE1B); stem-cell related (LGR5, OCT4, LIN28); fluorescent (GFP, RFP, CFP, YFP); TetR; luciferase; CRE recombinase/reporter; p53 and DNA repair gene knockdown cell lines (PARP1, MUTYH, MSH2, MLH1, XRCC6, BRCA1, NBS1). In addition, AMSBIO scientists can quickly establish an optimized cell line, using a lentiviral system, according to scientists' specification. All custom cell lines are designed specifically to meet client specifications and our own rigorous internal QC criteria.

AMS Biotechnology

For info: +44-(0)-1235-828200 | www.amsbio.com

Electronically submit your new product description or product literature information! Go to **www.sciencemag.org/products/newproducts.dtl** for more information.

Newly offered instrumentation, apparatus, and laboratory materials of interest to researchers in all disciplines in academic, industrial, and governmental organizations are featured in this space. Emphasis is given to purpose, chief characteristics, and availability of products and materials. Endorsement by *Science* or AAAS of any products or materials mentioned is not implied. Additional information may be obtained from the manufacturer or supplier.

immunogenomics 2014

September 29 - October 1, 2014

HudsonAlpha Biotechnology Campus
Huntsville, Alabama, USA

Bringing together preeminent leaders and thinkers at the intersection of genomics and immunology

Our Keynote Speakers:

Christophe Benoist
Professor, Department of Microbiology and Immunobiology, *Harvard Medical School*

Mary Ellen Conley
Federal Express Chair of Excellence and Professor, Department of Pediatrics, *University of Tennessee, College of Medicine, Memphis*

Mark Davis
Investigator, Howard Hughes Medical Institute; Professor, Department of Microbiology and Immunology; Director, Institute for Immunity, Transplantation, and Infections, *Stanford University School of Medicine*

follow @immunogenomics on twitter

Register today at haig.aaas.org

presented by

HUDSONALPHA INSTITUTE FOR BIOTECHNOLOGY

Science AAAS

Promega

Better Biology, Less Work

NAD(P)/NAD(P)H-Glo Assays

The simple add-and-read NAD(P)/NAD(P)H-Glo Assays have unparalleled sensitivity and linearity making them ideal for metabolic research and HTS research applications. These assays enable direct in-well measurement of total and individual NAD/NADH or NADP/NADPH and can be used in either biochemical or cell-based applications.

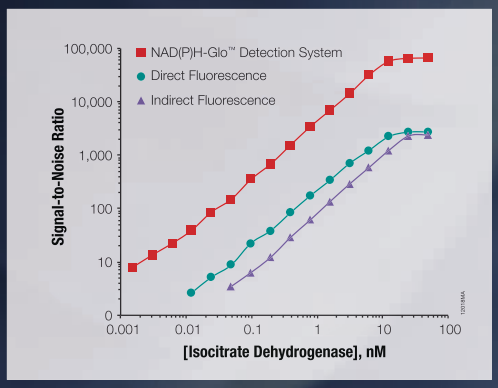

Superior sensitivity compared to fluorescent methods.

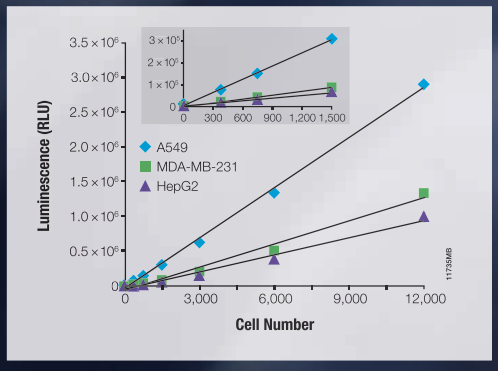

Directly measure total dinucleotide concentrations in multiwell plates using low cell numbers.

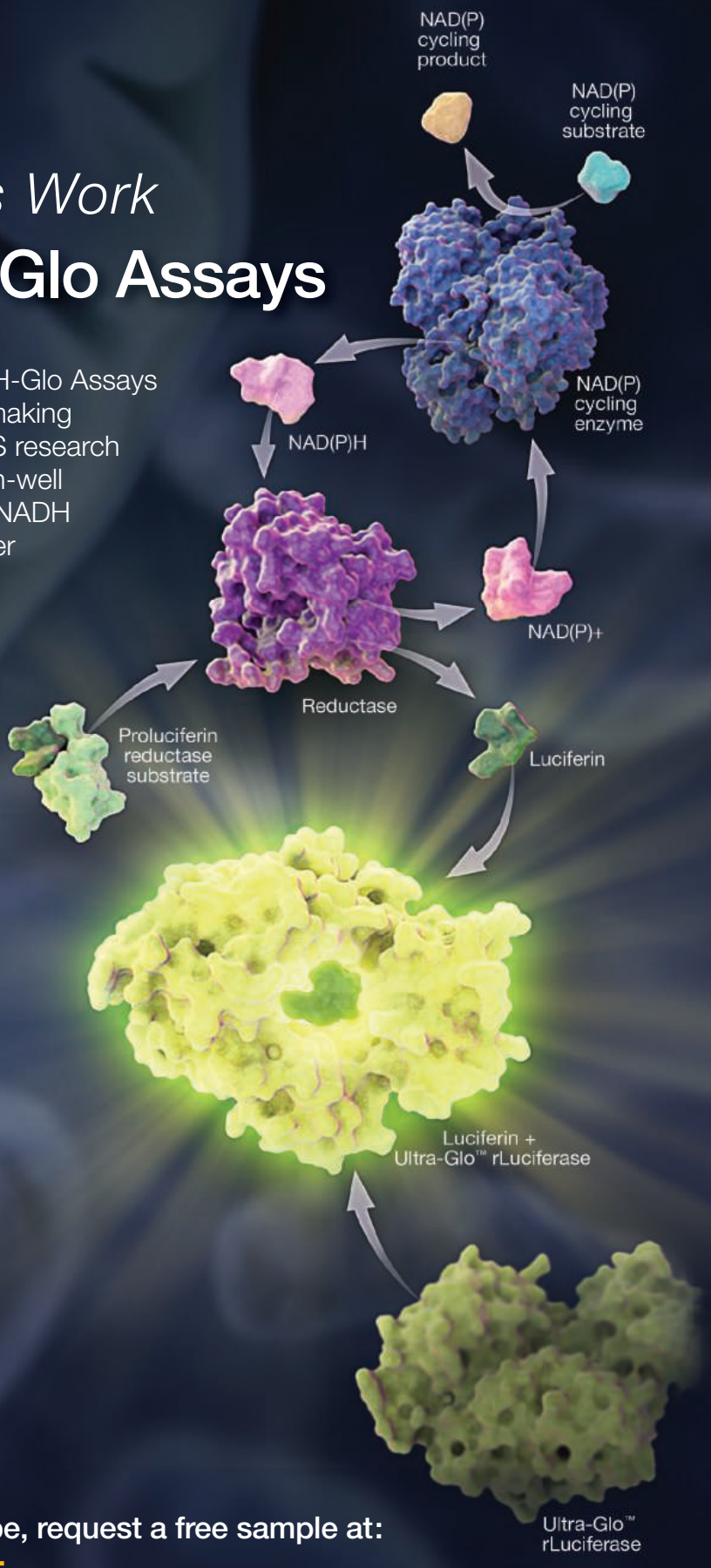

To see how easy better biology can be, request a free sample at:

www.promega.com/metabolism

©2014 Promega Corporation. All rights reserved. 13088558

E.O. WILSON
BIODIVERSITY SYMPOSIUM
April 22-24, 2014
The University of Alabama
Tuscaloosa, AL, USA

Registration: www.biodiversity.ua.edu

Beginning on Earth Day at The University of Alabama

Join Dr. Edward O. Wilson and international biodiversity experts for three days of research briefings and forums on the state and future of biodiversity on our planet.

Featuring the international release of Dr. Wilson's new book, *A Window on Eternity: Gorongosa National Park, Mozambique*.

Distinguished Speakers

E. Virginia Armbrust
P. Dee Boersma
R. Scot Duncan
Ryan Earley
Scott V. Edwards
Harry W. Greene
Juan M. Lopez-Bautista
Jonathan B. Losos
Meg Lowman
D. Bruce Means
Michael B.A. Oldstone
Richard A. Richards
Leslie J. Rissler
Sahotra Sarkar
Diana H. Wall
Edward O. Wilson

Join Dr. Wilson and the College of Arts and Sciences as we explore biodiversity from a range of perspectives: biological, evolutionary, cultural, and philosophical.

Registration: www.biodiversity.ua.edu

THE UNIVERSITY OF ALABAMA
COLLEGE OF ARTS AND SCIENCES

JAXA **Call for Application**

JAXA International Top Young Fellowship (ITYF) in 2014

ITYF application

The Japan Aerospace Exploration Agency (JAXA) International Top Young Fellowship (ITYF) was established as a prestigious new fellowship program in 2009. The ITYF is designed to attract outstanding, highly motivated, early-career researchers in any of the space science fields covered by the Institute of Space and Astronautical Sciences (ISAS) to work in Japan for 3 years. An excellent remuneration package is offered, including research budget (including travel expense) so that the fellow can extend their international profile, as well as developing collaborations within Japan.

The application deadline: May 30, 2014

Please see the below link for further details.
http://www.isas.jaxa.jp/e/researchers/young-fellowship/appli.shtml

Contact Information
E-mail: **ITYF2014@jaxa.jp**

HARVARD MEDICAL SCHOOL

MASTER OF MEDICAL SCIENCES DEGREE in IMMUNOLOGY

A comprehensive program in Basic and Clinical Immunology. Taught by renowned Harvard faculty and intended for biology graduates interested in immunology research and medicine, as well as for research-oriented clinical fellows (MD, MBBS, and equivalent degrees) from all disciplines.

Visit **http://mmscimmunology.hms.harvard.edu/** for information on our comprehensive two-year program, including extensive coursework and laboratory-based research, at Harvard Medical School.

There's only one Science

Science Careers Advertising

For full advertising details, go to ScienceCareers.org and click For Employers, or call one of our representatives.

Tracy Holmes
Worldwide Associate Director
Science Careers
Phone: +44 (0) 1223 326525

THE AMERICAS
E-mail: advertise@sciencecareers.org
Fax: 202-289-6742

Tina Burks
Phone: 202-326-6577

Nancy Toema
Phone: 202-326-6578

Marci Gallun
Sales Administrator
Phone: 202-326-6582

Online Job Posting Questions
Phone: 202-312-6375

EUROPE / INDIA / AUSTRALIA / NEW ZEALAND / REST OF WORLD
E-mail: ads@science-int.co.uk
Fax: +44 (0) 1223 326532

Axel Gesatzki
Phone: +44 (0)1223 326529

Sarah Lelarge
Phone: +44 (0) 1223 326527

Kelly Grace
Phone: +44 (0) 1223 326528

JAPAN
Yuri Kobayashi
Phone: +81-(0)90-9110-1719
E-mail: ykobayas@aaas.org

CHINA / KOREA / SINGAPORE / TAIWAN / THAILAND
Ruolei Wu
Phone: +86-1367-1015-294
E-mail: rwu@aaas.org

All ads submitted for publication must comply with applicable U.S. and non-U.S. laws. *Science* reserves the right to refuse any advertisement at its sole discretion for any reason, including without limitation for offensive language or inappropriate content, and all advertising is subject to publisher approval. *Science* encourages our readers to alert us to any ads that they feel may be discriminatory or offensive.

Science Careers
From the journal *Science* AAAS

ScienceCareers.org

Boosting discovery-driven research in the physics of quantum materials through the Gordon and Betty Moore Foundation's EPiQS initiative.

APPLY TODAY FOR OUR

Experimental Investigator Competition.

Visit moore.org/programs/science/EPiQSinvestigator for details. Deadline is April 21, 2014.

GORDON AND BETTY MOORE FOUNDATION

Moore.org
@MooreScientific

FACULTY POSITIONS AT THE ROCKEFELLER UNIVERSITY

The Rockefeller University seeks exceptional, interactive, and creative scientists to join its faculty. We invite applications from outstanding candidates for tenure-track positions.

The University has a laboratory-based organizational structure that fosters interdisciplinary research. We encourage applications in the following areas:

- **Chemical & Structural Biology**
- **Genetics & Genomics**
- **Immunology, Virology & Microbiology**
- **Medical Sciences, Systems Physiology & Human Genetics**
- **Molecular Cell Biology**
- **Neurosciences & Behavior**
- **Organismal Biology & Evolution**
- **Physical, Mathematical & Computational Biology**
- **Stem Cells, Development, Regeneration & Aging**

Details about specific subjects of research can be found at:
http://www.rockefeller.edu/facultysearch.

The Rockefeller University provides strong support for the research work of its faculty. The positions offer competitive salary, benefits and start-up funds, renovated laboratory space, access to state-of-the-art core facilities and extensive opportunities for collaboration both within the University and with neighboring institutions.

Applications are being accepted electronically through our **Online Application System** at **http://oas.rockefeller.edu**. Applicants should follow the online application procedure.

The deadline for application submission is April 18, 2014.

If you have questions regarding submitting an application, please contact our Administrator at **facultysearch@rockefeller.edu.**

The Rockefeller University is an Affirmative Action/Equal Opportunity/VEVRAA Employer and solicits applications from women and under-represented minorities.

THE UNIVERSITY OF HONG KONG
香港大學

Lecturer in Common Core Curriculum (Ref.: 201400158)

Applications are invited for appointment as Lecturer in Common Core Curriculum in the Faculty of Science, from as soon as possible, on a two-year fixed-term basis, with the possibility of renewal.

The University has established a Common Core Curriculum for all undergraduates since September 2012. The Faculty of Science offers courses in the area of Scientific and Technology Literacy to students from all ten Faculties. A senior Professor in the Faculty of Science will lead the teaching of these courses and work with the Lecturer in the relevant area who will serve primarily as a tutor for small groups of students from multiple disciplines. The medium of instruction is English. Information about the Common Core Curriculum can be viewed at http://tl.hku.hk/common-core-curriculum.

Applicants should have a Ph.D. degree, preferably in Physical Sciences, and substantial teaching experience in subjects related to general education at the university level. Strong candidates with a background in Biological Sciences are also welcome. The appointee's duties include conducting small-group tutorials for two courses per semester, marking assignments/examination scripts, preparing teaching materials, supervising student work, developing new courses, and undertaking other tasks related to science education. He/She will meet regularly with the Centre for the Enhancement of Teaching and Learning to reflect on and refine the teaching activities in Common Core courses.

A globally competitive remuneration package commensurate with qualifications and experience will be offered. At current rates, salaries tax does not exceed 15% of gross income. The appointment will attract a contract-end gratuity and University contribution to a retirement benefits scheme, totalling up to 15% of basic salary, as well as annual leave, and medical benefits. Please note that the University is not able to offer a relocation assistance package (including housing accommodation and a passage and baggage allowance) to the successful candidate recruited from overseas.

For enquiries about the specific job requirements, please write to Professor Sun Kwok, Dean of Science (e-mail: deansci@hku.hk). Applicants should send a completed application form, together with an up-to-date C.V. and a statement on teaching philosophy, which includes a portfolio of syllabi and descriptions of courses they have taught or co-taught by e-mail to sciappt@hku.hk. They should also arrange for submission of three references from senior academics who are familiar with their teaching approaches, skills and experience to sciappt@hku.hk. Please indicate clearly "Ref.: 201400158 (Lecturer in Common Core Curriculum)" in the subject of the e-mail. Application forms (341/1111) can be obtained at http://www.hku.hk/apptunit/form-ext.doc. Further particulars can be obtained at http://jobs.hku.hk/. **Closes April 30, 2014.**

The University thanks applicants for their interest, but advises that only shortlisted applicants will be notified of the application result.

The University is an equal opportunity employer and is committed to a No-Smoking Policy

Faculty Positions in Pharmacology

Northwestern University Feinberg School of Medicine has committed substantial resources toward expanding interdisciplinary research in the pharmacological sciences. A new Department of Pharmacology, to be commissioned in Spring 2014 with founding faculty members from the current Department of Molecular Pharmacology and Biological Chemistry, will be led by Dr. A. L. George, an internationally recognized authority on ion channels. We are now seeking candidates to fill several new full-time, tenure track faculty positions at the Assistant, Associate and full Professor ranks. We are especially interested in candidates who investigate basic and translational topics of modern pharmacology applied to any of a wide range of molecular targets and diseases including cardiovascular disorders, pain, neurological disorders including but not limited to epilepsy, cancer, addiction, and psychiatric disease. Expertise in pharmacogenomics, developing novel disease models including stem cell-derived platforms, drug discovery, proteomics and other cutting edge methodologies is highly desirable. Northwestern University offers a collegial and collaborative scientific environment that is rich with core facilities, robust cross-disciplinary graduate training programs, and diverse expertise.

Candidates should have a Ph.D., M.D./Ph.D. or M.D. degree, significant research experience, and evidence of sustainable extramural funding. Salary is Commensurate with experience. Start date will be for the 2014-2015 academic year. Applications will be accepted until the positions are filled. Please submit by email (as a single PDF) a cover letter, curriculum vitae, summary of research experience and future plans along with names and contact information for three references to:

Pharmacology Faculty Search
Feinberg School of Medicine
Northwestern University
Chicago, IL 60611
NUpharm@northwestern.edu

NORTHWESTERN UNIVERSITY FEINBERG SCHOOL OF MEDICINE

Northwestern University is an Affirmative Action, Equal Opportunity Employer. Women and minorities are encouraged to apply. Hiring is contingent upon eligibility to work in the United States.

IMP
Research Institute of Molecular Pathology

Senior Scientist Position at the IMP

We invite applications for a senior scientist position at the Research Institute of Molecular Pathology (IMP), Vienna, Austria.

The IMP is one of the world's leading basic biomedical research institutes, located in the thriving and interdisciplinary Vienna Biocenter Campus (VBC). Researchers at the IMP conduct curiosity-driven research across a wide range of topics including molecular and cell biology, differentiation and disease, neurobiology and computation and bioengineering.

We aim to recruit a senior scientist with a strong and innovative research programme, in the areas of molecular and cellular biology, and differentiation and disease.

Senior scientist positions are comparable to HHMI or Max Planck director's positions. The IMP offers internationally competitive salaries and generous funds for student, postdoc and technician positions, investments and running costs. Research groups enjoy full access to state-of-the-art core services including mass spectrometry, next generation sequencing, biooptics, bioinformatics, histology, electron microscopy, and a 2,000m^2 mouse house with core funding of all associated costs.

The IMP participates in the VBC International PhD programme and VBC Summer School, which are amongst the most competitive graduate and undergraduate research programmes in Europe.

Applications, including a CV, a brief summary of research achievements and future research plans, should be submitted to Christopher Robinson at robinson@imp.ac.at

The IMP is home to scientists of over 30 different nationalities. Vienna offers a lively multicultural environment with high living standards, consistently ranking in the top 5 cities worldwide for the quality of living. Child care facilities are available on campus.

For further information, see our website: **www.imp.ac.at**

AAAS
ADVANCING SCIENCE, SERVING SOCIETY

Senior Program Associate
Grant #4693 (Science for Seminaries)

The American Association for the Advancement of Science (AAAS) seeks a Senior Program Associate to work within the AAAS Dialogue on Science, Ethics, and Religion (DoSER) Program . The position involves a project in partnership with select seminaries throughout the US to integrate science into their core curricula, with a goal of promoting a positive understanding of science among religious leaders and eventually the communities they serve.

This position is anticipated to extend for an initial period of one year with the possibility of renewal.

Major duties and responsibilities:

- Works with partners including Association of Theological Schools, religious leaders, and prominent scientists on seminary science curricula development and implementation
- Facilitates planned workshops and events
- Writes and edits project-related materials
- Represents and speaks on behalf of the project and supervises project interns

Minimum requirements:

- Extensive university or college level training leading to a Master's degree or PhD in the biological or physical sciences or theology, with coursework in theology or seminary based training, or similar relevant experience
- Experience or familiarity with theological seminaries and curricula administration
- Strong technology skills in contemporary software packages, particularly in Microsoft Office
- Ability to travel at least twice annually
- Experience organizing public events

Please visit our job information website **http://www.aaas.org/page/employment-aaas** to get more information, and to apply to AAAS online.

AAAS is an Equal Opportunity Employer.

Science | Careers

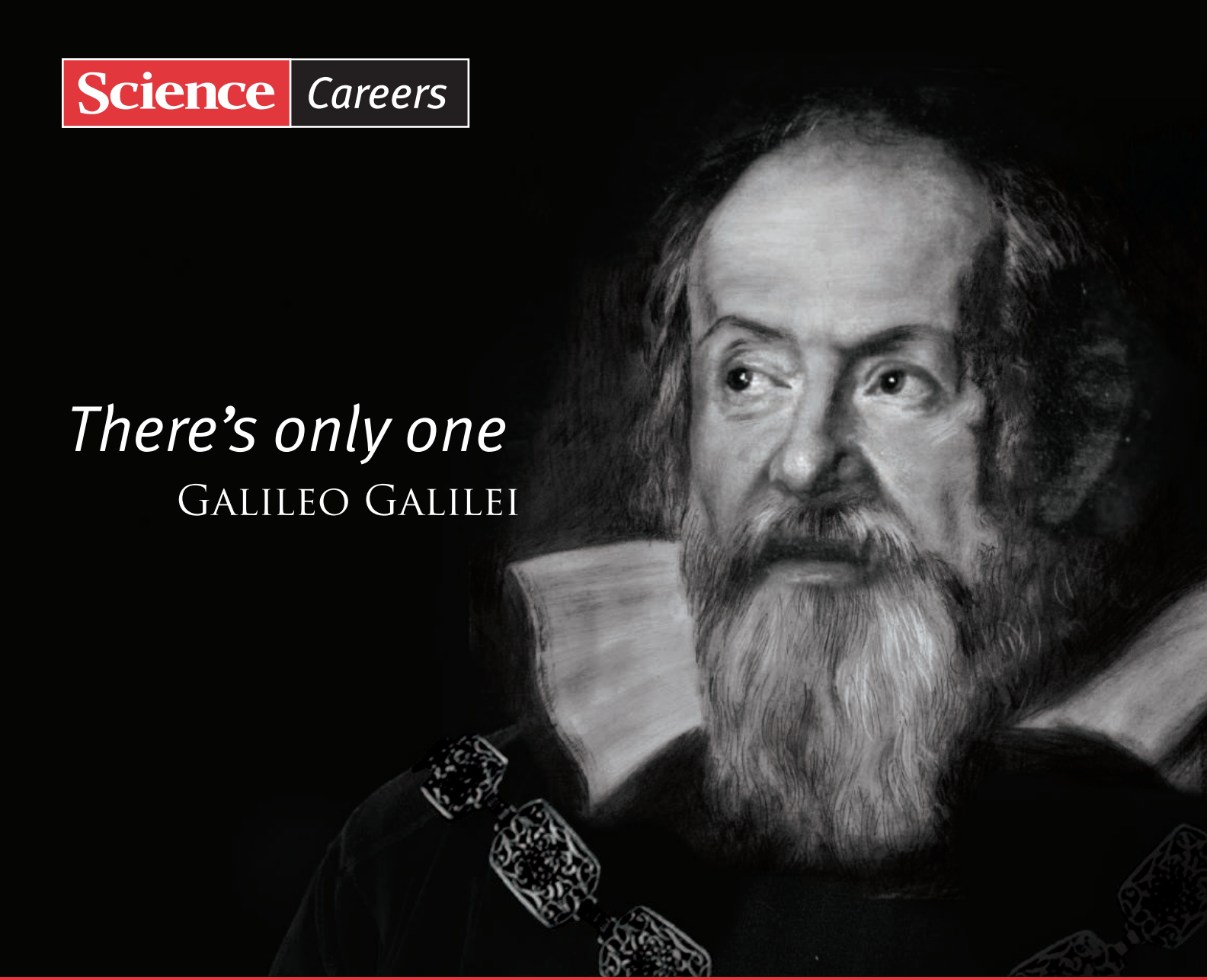

There's only one
Galileo Galilei

Born in 1564, Galileo Galilei once contemplated a career in the priesthood. It's perhaps fortunate for science that upon the urging of his father, he instead decided to enroll at the University of Pisa. His career in science began with medicine and from there he subsequently went on to become a philosopher, physicist, mathematician, and astronomer, for which he is perhaps best known. His astronomical observations and subsequent improvements to telescopes built his reputation as a leading scientist of his time, but also led him to probe subject matter counter to prevailing dogma. His expressed views on the Earth's movement around the sun caused him to be declared suspect of heresy, which for some time led to a ban on the reprinting of his works.

Galileo's career changed science for all of us and he was without doubt a leading light in the scientific revolution, which is perhaps why Albert Einstein called him the father of modern science.

Want to challenge the status quo and make the Earth move? At *Science* we are here to help you in your own scientific career with expert career advice, forums, job postings, and more — all for free. For your career in science, there's only one *Science*. Visit **ScienceCareers.org** today.

For your career in science, there's only one Science

ScienceCareers.org

Career advice | Job postings | Job Alerts | Career Forum | Crafting resumes/CVs | Preparing for interviews

We are one of the youngest universities in Germany and think in terms of possibilities, not limitations. In the heart of the Ruhrregion, we develop ideas of the future at our 11 faculties. We are strong in research and teaching, live diversity, support potential and are highly committed to an educational equality that has earned this name.

UNIVERSITÄT DUISBURG ESSEN

***Offen** im Denken*

The University of Duisburg-Essen invites applications for the following position at the Faculty of Biology:

University professorship (salary grade W 2/W 3) for

"Aquatic Ecosystems Research"

The successful candidate has an excellent track record in molecular ecosystems research and/or ecosystem modelling. Applicants should complement and extend the existing strengths of the Center for Water and Environmental Research (ZWU, http://www.uni-due.de/zwu) and the Faculty of Biology (http://www.uni-due.de/biologie).

Candidates have an international reputation in experimental and/or field studies proven by peer-reviewed publications, a broad international research network and experience in acquisition and management of research projects. They are expected to establish an independent, extramurally funded, competitive research program and to participate in teaching in the Biology programs of the faculty. These include undergraduate and graduate courses for teacher trainees and BSc biology students as well as students of the international MSc programmes "Transnational Ecosystem-based Water Management", "Environmental Toxicology", or "Biodiversity". Teaching will be in German and English. The professor will be involved in the organisation of study programmes, in course guidance and in academic self-administration.

According to §36 of the NRW Act (Institutions of Higher Learning) the requirements for this position are a university degree, doctorate, and additional scientific achievements attained in the context of a junior professorship, post-doctoral thesis, scientific work at a university, research institution, in business, administration or in another relevant area.

The University of Duisburg-Essen seeks to increase the number of female academic staff and encourages women with the necessary qualifications to apply for this position.

Given equal suitability for the appointment, applications of disabled candidates will be given priority.

Applications, including the usual supporting documents (curriculum vitae, list of scientific publications, present and future research plans, information on teaching experience to date, involvement in academic self-administration and information about third-party funding) and the application form (available at http://www.uni-due.de/biologie/fakultaet/stellen.php) should be submitted within 6 weeks after publication of this advertisement to **Prof. Daniel Hoffmann, Dean of the Faculty of Biology, University of Duisburg-Essen, Universitätsstr. 2, 45117 Essen, Germany, preferably by e-mail to dekanat@biologie.uni-due.de**.

Further information can be obtained from the vice-dean of the faculty, Prof. Daniel Hering, Tel. +49 201 183-3084, e-mail: daniel.hering@uni-due.de. Or visit http://www.uni-due.de/biologie/dekanat/stellen.php.

www.uni-due.de

Are you conducting research into the sustainable use of natural resources? Do you want to contribute to the solution of urgent environmental, developmental and social problems, especially in developing and emerging countries?

If yes, then we would like to invite you to apply for the

Robert Bosch Junior Professorship Research into the Sustainable Use of Natural Resources

together with a German university or research institution of your choice. Applicants of all nationalities are welcome.

Areas addressed

We are looking for an outstanding young scientist whose research areas concern the sustainable use of natural resources. Research approaches may be based in the natural sciences as well as in the social, developmental, political, medical and public health sciences.

The research should focus on developing and emerging countries. We expect that research results should contribute to the solution of urgent environmental problems.

Scope

The successful applicant will be awarded a grant worth up to 1 million euros for a five year period, in order to set up a research group in a German research institution or university. The funds can be allocated flexibly towards covering salaries and research costs.

Candidate profile

:: excellent doctorate degree, completed no more than 5 years prior to the application deadline of 18 May 2014 (adjusted for documented parental leave)
:: compelling independent past scientific achievements and publications in peer-reviewed journals
:: international research experience
:: excellent proficiency in English
:: potential to obtain a leading position in his/her research field
:: non-German applicants should be prepared to learn German.

The application deadline is **18 May 2014.**

For further information and to apply please visit **www.bosch-stiftung.de/juniorprofessorship**

Robert Bosch Stiftung

Science Careers online @sciencecareers.org

Women in Science Booklet

Science and the L'Oréal Foundation present

Read inspiring profiles of women making a difference in biology.

Free download at ScienceCareers.org/LOrealWIS

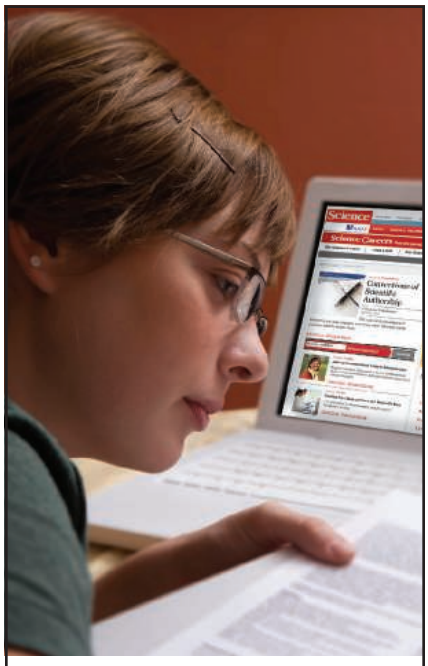

AAAS is here –
helping scientists achieve career success.

Every month, over 400,000 students and scientists visit ScienceCareers.org in search of the information, advice, and opportunities they need to take the next step in their careers.

A complete career resource, free to the public, *Science* Careers offers a suite of tools and services developed specifically for scientists. With hundreds of career development articles, webinars and downloadable booklets filled with practical advice, a community forum providing answers to career questions, and thousands of job listings in academia, government, and industry, *Science* Careers has helped countless individuals prepare themselves for successful careers.

As a AAAS member, your dues help AAAS make this service freely available to the scientific community. If you're not a member, join us. Together we can make a difference.

To learn more, visit
aaas.org/plusyou/sciencecareers

AAAS + U = Δ

TENURE TRACK FACULTY POSITIONS IN CANCER RESEARCH
Case Western Reserve University School of Medicine
Case Comprehensive Cancer Center

The Case Comprehensive Cancer Center (**http://cancer.cwru.edu/**), a National Cancer Institute-designated Comprehensive Cancer Center at CWRU, with affiliates University Hospitals Case Medical Center and Cleveland Clinic, invites applications for tenure track faculty positions at the level of Assistant and Associate Professor in cancer biology. Candidates should have an MD, PhD, or MD-PhD, post-doctoral research experience, and some faculty experience. Candidates at the Assistant Professor level are encouraged to apply and should provide a record of funding and scholarly activity and the potential to advance in cancer research. Candidates at the Associate Professor level should have a nationally-funded program and an outstanding record of cancer research achievements. We are particularly interested in the following research areas: immunotherapy, cancer cell metabolism, molecular basis of lymphoid malignancies, ovarian or gastrointestinal cancer. Priorities include innovative discovery research coupled with an interest in translational disease-oriented cancer research.

The successful candidate will have a primary appointment in the cancer center or a basic science department at the medical school such as Pathology (**http://www.cwru.edu/med/pathology/**), Genetics and Genome Sciences (**http://genetics.case.edu/**), or Pharmacology (**http://pharmacology.case.edu/**).

Please send curriculum vitae, a list of three or more references, and a cover letter outlining your research interests electronically to: **Stanton L. Gerson, MD, Director, Case Comprehensive Cancer Center, cancersearch@case.edu**. Please include "Cancer Research Faculty Search" in the subject line.

In employment, as in education, Case Western Reserve University is committed to Equal Opportunity and Diversity. Women, veterans, members of underrepresented minority groups, and individuals with disabilities are encouraged to apply.

Case Western Reserve University provides reasonable accommodations to applicants with disabilities. Applicants requiring a reasonable accommodation for any part of the application and hiring process should contact the Office of Inclusion, Diversity and Equal Opportunity at 216-368-8877 to request a reasonable accommodation. Determinations as to granting reasonable accommodations for any applicant will be made on a case-by-case basis.

CASE WESTERN RESERVE UNIVERSITY EST. 1826

TENURE TRACK FACULTY POSITION IN CANCER GENETICS
Case Western Reserve University School of Medicine
Case Comprehensive Cancer Center

The Case Comprehensive Cancer Center (**http://cancer.cwru.edu/**), a NCI-designated Comprehensive Cancer Center, at CWRU, with affiliates University Hospitals Case Medical Center and Cleveland Clinic, invites applications for a tenure track faculty position at the level of Assistant or Associate Professor with a research program in cancer genetics, genomics, statistical genetics, or tumor pharmacogenetics/genomics. Qualified individuals should have an MD, MD-PhD, or PhD. Candidates at the Assistant Professor level should have cancer research experience in the study of genes, genomics, targets, and pathways and in working with human cancer samples with clinical correlates. Candidates at the Associate Professor level should also have a nationally funded program and an outstanding record of cancer research activities.

Successful candidates will be expected to interact closely with ongoing basic and translational research, particularly research using human tissue. Candidates with interests in Gastrointestinal Cancers (colon cancer, esophageal cancer, pancreas cancer) that could align with the Case GI SPORE are particularly encouraged, as are candidates with interests in glioma, breast cancer, ovarian cancer, or hematologic malignancies would align with cancer center scientific programs. Physician scientists are particularly encouraged to apply. Primary appointment will be in the department of training, the cancer center or the department of Genetics.

Please send curriculum vitae, a list of three or more references, and a cover letter outlining your research interests, electronically to: **Stanton L. Gerson, MD, Director, Case Comprehensive Cancer Center, cancersearch@case.edu**. Please include "Cancer Genetics" in the subject line.

In employment, as in education, Case Western Reserve University is committed to Equal Opportunity and Diversity. Women, veterans, members of underrepresented minority groups, and individuals with disabilities are encouraged to apply.

Case Western Reserve University provides reasonable accommodations to applicants with disabilities. Applicants requiring a reasonable accommodation for any part of the application and hiring process should contact the Office of Inclusion, Diversity and Equal Opportunity at 216-368-8877 to request a reasonable accommodation. Determinations as to granting reasonable accommodations for any applicant will be made on a case-by-case basis.

CASE WESTERN RESERVE UNIVERSITY EST. 1826

POSITIONS OPEN

Wake Forest School of Medicine

NEUROBIOLOGY POSITION

The Department of Neurobiology and Anatomy is initiating a search for a tenure-track faculty member working in Sensorimotor Neurobiology. The selected candidate will interact with a large and cooperative group of sensory neurobiologists that direct funded projects spanning the visual, auditory, and somatosensory systems as well as training grant and program-project grants emphasizing integrative function and development. Candidates should have a doctoral degree, extramural funding, at least two years of postdoctoral research, a strong record of research accomplishments, and a commitment to developing an independent as well as collaborative research program. Teaching responsibilities will be commensurate with experience and background. A competitive recruitment package will include salary and fringe benefits, setup funds, laboratory space and shared equipment facilities.

Applications should include full curriculum vitae and a statement of research interests. Applicants should also arrange for three letters of recommendation to be sent to the Search Committee. The earliest start date for the position is July 1, 2014; applications will be accepted until a suitable candidate is recruited. Information about the position, individual faculty and research interests, and graduate programs can be found at **website: http://www.wakehealth.edu/nba/nba.html.** All application materials should be sent to: **Faculty Search Committee, Department of Neurobiology and Anatomy, Wake Forest School of Medicine, Medical Center Boulevard, Winston-Salem, North Carolina, 27157-1010.** *Affirmative Action/Equal Opportunity Employer.*

FACULTY POSITIONS - MEDICAL SCHOOL

The Saint James School of Medicine, an international medical school (**website: http://www.sjsm.org**), invites applications from candidates with teaching and/or research experience in any of the basic medical sciences for its Caribbean campuses. Faculty positions are currently available in Pathology, Genetics, Neuroscience, and Biochemistry. Applicants must be M.D., and/or Ph.D.

Teaching experience in the U.S. system is desirable but not required. Retired persons are encouraged to apply. Attractive salary and benefits. Submit curriculum vitae to **e-mail: jobs@mail.sjsm.org** or mail to: **HRDS Inc., 1480 Renaissance Drive, Suite 300, Park Ridge, IL 60068.**

Find your future here.

↓

Science Careers
From the journal *Science* AAAS

www.ScienceCareers.org

POSITIONS OPEN

UIC Center for Cardiovascular Research
COLLEGE OF MEDICINE

TENURE-TRACK FACULTY POSITION

Center for Cardiovascular Research
University of Illinois at Chicago College of Medicine

The University of Illinois at Chicago (UIC) Center for Cardiovascular Research (CCVR) in the College of Medicine seeks outstanding faculty candidates with expertise in cardiac mitochondrial biology, metabolism, non-coding RNA, or heart failure. Consideration will be given to applicants at all ranks (**ASSISTANT, ASSOCIATE, FULL PROFESSORS**).

Successful candidates will demonstrate the ability to garner extramural grant support and are expected to lead comprehensive and innovative research programs that focus on heart failure, diabetes, obesity, metabolic syndrome, and hypertension. A commitment to excellence in teaching is also required. Minimum degree requirements are a Ph.D. or M.D. degree with three or more years of postdoctoral training. Attractive startup packages are available, commensurate with experience.

Applicants will submit a letter of interest, stating a research plan, curriculum vitae, and names of at least three references. For more information on the CCVR visit **website: http://www.ccvr.uic.edu.**

Apply online only at: **website: https://jobs.uic.edu/job-board/job-details?jobID=39340&job=assistant-associate-professor-ccvr.**

The UIC is an Affirmative Action/Equal Opportunity Employer.

Your career is our cause.

Get help from the experts.

www.sciencecareers.org

- Job Postings
- Job Alerts
- Resume/CV Database
- Career Advice
- Career Forum

Science Careers
From the journal *Science* AAAS

Nontraditional Careers: Opportunities Away From the Bench

Webinar

Want to learn more about exciting and rewarding careers outside of academic/industrial research? View a roundtable discussion that looks at the various career options open to scientists and strategies you can use to pursue a nonresearch career.

Now Available On Demand
www.sciencecareers.org/webinar

Produced by the *Science*/AAAS Business Office.

Science Careers
From the journal *Science* AAAS